A STUDY OF MOVING GROUPS OF STARS IN OUR GALAXY

by

Jovan Skuljan

A THESIS

SUBMITTED IN PARTIAL FULFILMENT

OF THE REQUIREMENTS FOR THE DEGREE OF

DOCTOR OF PHILOSOPHY IN ASTRONOMY

IN THE UNIVERSITY OF CANTERBURY

University of Canterbury

1999

Abstract

Numerous observations over the past decades have confirmed that the distribution of stellar velocities in the solar neighbourhood is not uniform. Certain concentrations of stars in the velocity field mean that there exist groups of stars moving in parallel orbits, with practically the same space velocities, even if the stars are spread all over the sky and appear to be gravitationally unbound. These stellar streams are called moving groups. Their precise nature is still not very well understood.

Many authors have contributed to this field, but it is Olin Eggen who deserves special mention. According to Eggen, about one dozen moving groups can be detected, both in the young and old disk populations. He has noted that moving groups are a result of cluster evaporation. According to this hypothesis, many stars are formed together in a relatively small volume in space, and they initially move together as a gravitationally bound cluster. In time, they evaporate from the cluster spreading along the orbit, but keeping their original velocities in the direction of galactic rotation. This hypothesis has not been generally accepted. It implies that the stars from a moving group will all have the same age, and the same chemical composition, which has not been confirmed by observations. It is also hard to believe that the original stellar velocities could stay preserved over many orbital cycles, which puts the existence of the older moving groups into doubt.

The aim of this thesis is to study the reality of moving groups, by examining the space velocities of over 800 stars mentioned in Eggen's papers. The list of stars was included in the Hipparcos project in order to get precise parallaxes and proper motions, while an extensive ground-based observing programme has been undertaken at the University of Canterbury to collect precise radial velocities for the same stars. By combining the Hipparcos astrometry with the ground-based radial velocities, the total space velocities have been obtained and the corresponding velocity distributions studied. In addition, a numerical model of the galactic potential has been developed, so that the orbits of stars could be examined.

The radial velocities have been obtained in the IAU standard system for more than 400 programme stars. A precision of $20 - 30$ m s^{-1} has been achieved for stars with intrinsically constant radial velocities, using the fibre-fed échelle spectrograph on the 1-m telescope at Mt John University Observatory. A precision of about 100 m s^{-1} has been obtained for some northern stars observed from the Dominion Astrophysical Observatory, using the coudé

spectrograph and the radial velocity spectrometer on the 1.2-m telescope.

The distribution of the programme stars in the galactic UV-plane demonstrates that the grouping is better (i.e. with less dispersion) when the Hipparcos data are used, compared to the ground-based pre-Hipparcos astrometry. However, there are indications that this might only be a result of the improved parallaxes, as they tend to make the overall velocity distribution more compact. A separate analysis using a general sample of about 4600 Hipparcos stars in the solar neighbourhood has revealed a branch-like structure in the velocity plane. The branches are probably generated by the galactic spiral structure itself, or by some other global characteristic of the galactic gravitational field. In such a picture, the moving groups may be regarded as shorter fragments and concentrations along the branches.

Numerical simulations based on a model including both the axisymmetric and spiral components of the galactic gravitational potential show that certain concentrations and elongated features in the velocity plane might be a result of galactic spiral structure. In that case, a moving group can be composed of stars having different origins. The most commonly accepted membership criterion of constant V was found to be a good first approximation, although both velocity components (U and V) have to be considered in a more realistic approach.

The results presented in this thesis do not discard Eggen's hypothesis, but they open some new possibilities in understanding the origin and nature of moving groups.

Contents

1 Introduction **1**

1.1 Moving groups of stars 1
1.2 Scientific goal of this thesis 4
1.3 Galactic velocity components 4
1.4 Group parallaxes 6
1.5 Hipparcos satellite mission 8
1.6 Programme stars 9
1.7 About this thesis 14

2 Radial velocity observations **15**

2.1 Observing programme 15
2.2 Observing equipment 16
2.2.1 MJUO instrument description 16
2.2.2 DAO instrument description 18
2.3 Observing statistics 19
2.4 MJUO échelle reduction procedure 24
2.4.1 Line shapes and the extraction process 29
2.4.2 The wavelength calibration 32
2.4.3 Synthetic spectra and the cross-correlation process 38
2.5 Radial velocities and photon counts 47
2.5.1 Problem of thorium intensities 48
2.5.2 Problem of stellar intensities 51
2.6 Testing the PM3000 CCD camera 53
2.7 Other MJUO configurations 55
2.8 The IAU standard radial velocity stars 57
2.9 The DAO RVS observations 60
2.9.1 Data re-reduction 61
2.9.2 Results 64
2.10 Comparing the measured and published velocities 68

3 Analysis of Hipparcos data **71**
3.1 High precision parallaxes and stellar kinematics 71
3.2 Eggen's groups 71
3.3 Stellar velocities in the solar neighbourhood 79
3.4 The sample 80
3.5 Velocity distribution 83
3.6 The wavelet transform 87
3.7 Confidence levels 90
3.8 The data analysis 91
3.8.1 Early-type stars 92
3.8.2 Late-type stars 92
3.9 The Fourier transform 95
3.10 Geneva photometry and metal abundances 97

4 Galactic orbits **107**
4.1 Coordinates and basic parameters 107
4.2 A numerical model 109
4.3 The Sun's orbit 115
4.4 Orbits of stars in the solar neighbourhood 116
4.5 Simulating the observed velocity distribution 120
4.6 Evolution of a moving group 127

5 Conclusions **139**
5.1 Aim of this thesis 139
5.2 Radial-velocity measurements 140
5.3 Hipparcos data 140
5.4 Galactic orbits 141
5.5 Eggen's moving groups: fact or fiction? 142

Appendices **145**

A Coordinate systems **145**
A.1 Equatorial and local coordinates 145
A.2 Galactic coordinates 147

B Error propagation **151**
B.1 Univariate and multivariate statistics 151
B.2 General error propagation 153
B.3 Errors in galactic positions and velocities 154

C An example: position and velocity of Arcturus **159**
C.1 Galactic position and velocity 160
C.2 Standard errors 160

D Reduction of celestial coordinates **163**
D.1 Precession 163
D.2 Nutation 165
D.3 Positions of stars 169
D.4 Sidereal time 170
D.5 Earth's shape and rotation 171

E Rotation of axes using matrices **175**
E.1 Rotation matrix 175
E.2 Elementary rotations 175
E.3 Successive rotations 176

F Radial velocity correction **177**
F.1 Measured radial velocities 177
F.2 JPL planetary and lunar ephemerides 178
F.3 Barycentric correction 178
F.4 The radial velocity of the Sun 181
F.5 Approximate corrections and the problem of residuals 182

Acknowledgements **187**

References **189**

List of Figures

1.1 *The local galactic reference frame used to express stellar velocities with respect to the Sun. An image of M31 is used to represent the Milky Way galaxy.* . . 5

1.2 *Moving groups in the UV-plane as suggested by various authors (Eggen, Asiain et al. and Agekyan & Orlov). The observed stellar velocities in the solar neighbourhood (see Chapter 3, Figure 3.12) are shown grey in the background. The names of the moving groups are taken from Eggen.* 7

1.3 *Equatorial positions of 830 programme stars included in the Hipparcos Catalogue. The sinusoidal line represents the galactic equator.* 11

1.4 *Apparent visual magnitudes for the same sample of stars as in Figure 1.3.* . . 11

1.5 *Proper motions of the programme stars plotted against the parallaxes on a logarithmic scale. A grid of lines representing the loci of constant transverse velocity (V_t = [constant]) and of constant uncertainty in transverse velocity (σ_{V_t} = [constant]) is over-plotted. The grid line spacing is also logarithmic and the values are given in* $\mathrm{km\,s^{-1}}$. *The uncertainties σ_π and σ_μ are assumed to be equal to* 1 mas *and* 1 $\mathrm{mas\,yr^{-1}}$ *respectively.* 13

2.1 *Schematic diagram of the MJUO observing equipment.* 16

2.2 *Schematic diagram of the échelle spectrograph.* 17

2.3 *Distribution of the twenty eight MJUO observing runs, and three DAO runs (shaded peaks) over the three-year observing period.* 19

2.4 *MJUO échelle reduction procedure. Two-dimensional CCD images of the thorium, stellar and white-lamp spectra are used to produce the one-dimensional stellar spectrum (Stage I), which is then cross-correlated with a synthetic spectrum (Stage II). The radial velocity is found from the positions of the peaks in the cross-correlation function.* 25

2.5 *The clean stellar image (left) with the fitted orders shown as horizontal black lines, and the remaining cosmic-ray image (right).* 26

2.6 *Basic reduction steps after the one-dimensional spectrum has been extracted. An image of β Corvi is used. Only order 42 is shown.* 27

2.7 *An enlarged portion of the thorium image (ECHCCD$_R$) illustrating the extraction process. The central line through an échelle order is followed pixel by pixel, and at each position an average value is taken of a number of pixels above and below the central line.* 29
2.8 *Spectral line shapes and tilts depending on the instrument configuration. These four plots (a–d) show the same thorium line $\lambda = 5504.3018$ Å in order 42.* 30
2.9 *Determination of an optimal extraction slit. Both the S/N ratio and RV scatter (σ_{V_r}) are used as suitable indices. The maximum is found at about 2.2 × FWHM (shaded region). This corresponds to a cut-off level of about 3.5 per cent, in case of a gaussian profile (inserted diagram).* 32
2.10 *Th-Ar spectrum (FIBCCD) used for the wavelength calibration. The order numbers (41–46) increase from top to bottom. The wavelengths (Å) are shown for 72 lines involved in the selection process described in the text.* 35
2.11 *Some properties of spectral lines selected for the wavelength calibration: (a) intensity scatter for thorium (black dots) and argon (open circles), (b) position scatter, and (c) residual positions. Only spectral lines represented as black dots in (c) are actually used for wavelength calibration.* 36
2.12 *Two examples illustrating the stability of the dispersion solution. The dots represent the radial velocity of the same stellar image, when combined with different thorium images during the same observing night. The zero point of the relative velocity scale is set to the first thorium image. The r.m.s. error of the polynomial fit (σ) is a measure of the uncertainty of the wavelength calibration.* 37
2.13 *The stellar models used in this thesis, as they appear in the H-R diagram. The spectral types and absolute magnitudes have been computed from the effective temperatures and surface gravities (see Table 2.6).* 41
2.14 *Comparison between the observed solar spectrum (black) and the corresponding synthetic spectrum 'fsun' (red).* 42
2.15 *Comparison between the observed stellar spectra (black) and the corresponding synthetic spectra (red). Only order 43 is shown.* 43
2.16 *Variations in the stellar radial velocity when different synthetic spectra are used. A single sky image has been correlated with the models listed in Table 2.6. The zero point has been set at the solar model.* 44
2.17 *Several different spectral lines from all over the synthetic spectrum, illustrating the rounding of the central wavelengths to the nearest bin. The line centres are used as common zero points.* 45
2.18 *Preparing a spectrum for the cross-correlation. The image has already been rebinned into a logarithmic scale. The mean pixel value is subtracted from the image and the result is then multiplied by a cosine bell function.* 46

2.19 *Typical cross-correlation peaks for each of the six échelle orders. Only the shaded central portions of the profiles are used for the radial-velocity determinations. The cut-off intensity is fixed at a level where the observed profile departs from a regular gaussian shape.* 46
2.20 *Systematic radial velocity differences between the échelle orders. The zero point of the relative velocity scale corresponds to the arithmetic mean of all six orders. The standard deviation (σ) is given for each order.* 47
2.21 *Average thorium intensities (FIBCCD configuration only) over a longer period of time. Only the 180-second exposures are shown. Each group of points is labelled with the corresponding observing run number.* 49
2.22 *Radial velocity of β Hydri depending on the average thorium intensity.* . . . 50
2.23 *Radial velocity shift produced by the thorium spectrum for different signal levels. The relative velocity scale has been centred at 10^3 ADU.* 50
2.24 *Radial velocities of the Sun (blue sky) and β Leporis depending on the signal level in the continuum for a small range of observations during one or two days.* 51
2.25 *Radial velocities of the Sun (blue sky) over a longer period of time depending on the signal level (run corrections applied).* 52
2.26 *Run corrections derived from the sky velocities.* 52
2.27 *Some effects of the PM3000 CCD camera rotation on (a) the radial velocities, and (b) the line profiles, when the camera is rotated by 180° from its normal position.* 54
2.28 *A typical behaviour of the Th-Ar lines in the SITCCD spectra, with (a) the scatter in the pixel position being correlated with the central intensities, and (b) the residuals after the dispersion solution showing an even distribution around the zero line.* 56
2.29 *Residual velocities (measured minus standard) for the IAU standard stars, as obtained at Mt John Observatory (ECHCCD excluded). Each dot corresponds to a single observation. The arithmetic mean is represented by a horizontal dashed line.* 57
2.30 *Radial velocities for some IAU standard stars, with corresponding standard deviations (σ), as measured at Mt John Observatory (ECHCCD excluded). A horizontal dashed line is used to represent the mean value.* 58
2.31 *Radial velocities for some IAU standard stars, with corresponding standard deviations (σ), as measured at Mt John Observatory (ECHCCD excluded). A horizontal dashed line is used to represent the mean value.* 59
2.32 *Some cross-correlation dips produced by the RVS using the K mask (June-July 1997). A gaussian function is fitted to the ratio between the raw profile and the flux monitor record.* 62
2.33 *Barycentric correction error (RVS minus JPL).* 63

2.34 *Difference in radial velocities between the F and K masks. Only the stars measured with both masks are shown. Filled dots represent the standard stars, and open circles represent the programme stars. The arithmetic mean is shown as a horizontal dashed line.* 65

2.35 *Residual velocities (measured minus standard) for the IAU standard stars, as obtained using the RVS. Each dot corresponds to a single observation. The arithmetic mean is shown as a horizontal dashed line.* 65

2.36 *Measured radial velocities for some standard stars (June–July 1997). The mean value is marked by a horizontal dashed line.* 66

2.37 *Measured radial velocities for some standard stars (March–April 1998). The mean value is marked by a horizontal dashed line.* 67

2.38 *Distribution of the residual velocities (measured minus published) for 1217 radial velocity measurements involved in this project (blue sky excluded), presented (a) as a standard histogram, and (b) as a cumulative distribution, showing a percentage of residuals less than a given value.* 68

3.1 *The largest moving groups in the UV plane.* 72

3.2 *The Hyades moving group in the UV plane. Open circles represent the velocities based on the observations before the Hipparcos mission, as taken from the Hipparcos Input Catalogue (HIC). Some of the points fall outside the bounds of the plot. Filled dots correspond to the Hipparcos data (HIP). Solid lines are used to connect the HIC and HIP positions for some of the stars that are moved into the core of the group when the Hipparcos data are used. Dashed lines indicate when the HIP position pulls a star away from the core.* 73

3.3 *Comparison between the group parallaxes ($\pi_{\rm gr}$) and old trigonometric ones ($\pi_{\rm tr}$), relative to the Hipparcos values (π). Only the stars with previously known parallaxes are considered.* 75

3.4 *The Hipparcos H-R diagrams for Eggen's moving groups.* 76

3.5 *The Hipparcos H-R diagrams for Eggen's moving groups.* 77

3.6 *Some Wolf 630 stars in the (M_I,$R-I$) plane, with three different sources of parallaxes used to compute M_I. Filled dots are Eggen's data based on group parallaxes, while circles and crosses correspond to Hipparcos and pre-Hipparcos, respectively. Standard deviations around a mean locus have been computed for dwarfs and giants separately.* 78

3.7 *Seven Eggen's moving groups in the UV plane, with each star presented as a straight line, corresponding to a $\pm\sigma$ change in the parallax.* 79

3.8 *(a) H-R diagram of the 4597 Hipparcos 'survey' stars within 100 pc, with known radial velocities and colours, and (b) the distribution of the $B-V$ colour index. The spectral classes in (a) correspond to the main sequence (Allen 1991).* 81

3.9 *Kinematic bias, presented as a ratio between two distributions: stars with known radial velocities (n_{V_t}) out of the total sample of Hipparcos 'survey' stars within 100 pc (N_{V_t}), where V_t is the transverse velocity. Radial velocities are predominantly known for high-V_t stars, but the effect is important only at $V_t > 70 - 80$ km s^{-1}.* 82

3.10 *The distribution of the uncertainties in all three velocity components: σ_U (thin line), σ_V (bold line) and σ_W (dotted line). The uncertainties are less than 2 km s^{-1} for about 80 per cent of stars (shown as the shaded area under the σ_V histogram).* 83

3.11 *Kernel function $K(r)$ used for the probability density estimation.* 84

3.12 *The distribution of stellar velocities in the UV-plane, shown as (a) a scatter plot, and (b) a contour plot of the probability density function on a logarithmic scale. The density function has been obtained using the adaptive kernel method (see text). The three main moving groups are marked as filled circles in (a). The three hypothetical branches and the 'edge line' are shown as dashed lines.* 86

3.13 *The Mexican hat in two dimensions.* 88

3.14 *Wavelet transforms of the smooth UV-distribution at several different scales. Solid black lines represent positive contours, while grey lines are used for negative values.* 89

3.15 *(a) The velocity distribution of early-type stars, together with (b–d) the corresponding wavelet transforms (90 per cent confidence) at several different scales. The dashed lines are used to mark the branches and the edge line (see text for equations of lines).* 93

3.16 *The one-dimensional velocity distribution of early-type stars along an axis perpendicular to the branches (the direction indicated in the inserted image).* 93

3.17 *(a) The velocity distribution of late-type stars, and (b-d) the corresponding wavelet transforms (90 per cent confidence) at several different scales. The dashed lines are used to mark the branches and the edge line (see text for equations). Two of Eggen's old-disk moving groups are presented in (d), for reference only.* 94

3.18 *The one-dimensional velocity distribution of late-type stars along an axis perpendicular to the branches (the direction indicated in the inserted image).* . 94

3.19 *The two-dimensional power spectrum $Q(f_U, f_V)$ of the velocity distribution for the whole sample of stars, at several levels of significance. The strongest peaks are aligned at $\gamma \approx 74°$, as indicated by the dashed line in (a).* 96

3.20 *The seven filters used in the Geneva photometric system.* 98

3.21 *A typical colour-colour diagram for the 29397 stars measured in the Geneva photometric system. The reddening effect is clearly seen, and the luminosity classes V and III appear well separated.* 99

3.22 *A typical plot of the parameter m_2 (see Equations 3.11) against $B_2 - V_1$. The reddening lines appear horizontal. The reference loci V and III (see Equations 3.13) are shown as solid lines.* 100

3.23 . *Calibration of the blanketing parameter Δm_2 in terms of the metal abundances* [Fe/H], *for (a) the main-sequence stars, and (b) the giants of the luminosity class III. The linear least-square fit is indicated by a dashed line (see Equations 3.14). The stars actually used for the fit are represented by the full dots, while the open circles are used for the rejected stars (with the residuals greater than 3σ).* 101

3.24 *Distribution of metal abundances in the solar neighbourhood as derived from the Geneva photometry of 2666 stars of luminosity classes V and III. The bottom diagram shows an enlarged portion of the histogram including frequencies less than 20.* 102

3.25 *Statistical properties in metal abundances at different velocities. The UV-plane has been divided into circular zones, 20 $\mathrm{km\,s^{-1}}$ wide.* 103

3.26 *Metallicity distributions for moving groups (bold lines) compared with a total sample of stars at the same value of the space velocity (thin lines). The results of the F-tests are given as explained in the text.* 104

3.27 *(a–c) Metallicity distributions for the UV-branches (bold lines) compared with the total sample of stars (thin lines). (d) The three main branches in the UV-plane (the dashed lines are explained in the text).* 105

4.1 *Galactocentric coordinates (xyz), and heliocentric (local) coordinates (XYZ). The two reference frames are translated relative to each other along the x-axis by an amount equal to the Sun's distance from the galactic centre.* 108

4.2 *Rotation curves for the galactic potential model by Flynn et al. (1996).* . . . 110

4.3 *(a) A logarithmic spiral, defined by an arbitrary reference point (R_s, ϑ_s) and the pitch angle i relative to a circle at any point. (b) A two-arm galactic spiral pattern at $t = 0$. The Sun is located in between the arms. The arrows indicate the direction of galactic rotation.* 112

4.4 *Gravitational forces $\vec{F}$ and $\vec{f}$ due to the axisymmetric and spiral potentials.* . 113

4.5 *(Top) The Sun's orbit about the galactic centre, as integrated using (a) the total potential (axisymmetric plus spiral) and (b) the axisymmetric potential only (with no spiral component). A circular orbit at $R = 8.5$ kpc is shown as a dotted line. (Bottom) The difference between the two orbits (a) and (b) as a function of time, shown as (c) the difference in radius and (d) difference in longitude.* 116

4.6 *Stars from the solar neighbourhood as they were distributed in the galactic plane in the past (part I).* 118

4.7 *Stars from the solar neighbourhood, as they were distributed in the galactic plane in the past (part II).* 119

4.8 *Deriving the initial space velocity $\vec{V}_*$ of a star that has just been formed from the interstellar gas inside a spiral arm.* 121

4.9 *Stars formed in a spiral arm* 100 Myr *ago (solid line at $t = -100$* Myr*) with an initial velocity dispersion of $\sigma = 10$ km s^{-1} will appear scattered around the mean locus at $t = 0$.* 122

4.10 *The model distribution of stellar velocities in the solar neighbourhood (within 200 pc of the Sun) presented as (a) a scatter plot and (b) a contour plot, assuming that stars are formed only in spiral arms, with initial velocities given by Equation 4.28.* 124

4.11 *The model distribution of stellar ages in the solar neighbourhood, using the same model as in Figure 4.10. Shaded peaks (marked as A and B) correspond to the inner arm. The remaining two peaks (P and Q) correspond to the outer arm. Black dots represent the ages of 16 moving groups found by Asiain et al. (1999a) in a sample of early-type stars.* 124

4.12 *The model distributions of stars of different ages corresponding to individual peaks (A, B, P and Q) in the age histogram (Figure 4.11).* 125

4.13 *An alternative model distribution of stellar velocities in the solar neighbourhood assuming a larger pitch angle of $i = 20°$: (a) a scatter plot, (b) regions covered by stars of different ages and from different spiral arms, as defined in Figure 4.14. Open circles represent the stars corresponding to the inner arm at about* 800 Myr *(peak C).* 126

4.14 *The age distribution of stars in the solar neighbourhood for the model presented in Figure 4.13. Shaded peaks (marked as A, B and C) correspond to the inner arm, while the remaining peaks (P, Q, R and S) correspond to the outer arm.* 126

4.15 *The place of formation of the Hyades cluster (open circle) in the galactic plane at $t = -625$ Myr. The spiral pattern at the same moment is shown in grey. A portion of the orbit of the cluster before and after the creation is given in a reference frame rotating with the spiral pattern. Numbers in brackets are times in* Myr *relative to the present time.* 129

4.16 *A hypothetical Hyades supercluster evolving in time as it orbits around the galactic centre.* 131

4.17 *(Top) The model Hyades supercluster as it appears in the galactic plane at present, when three different ages are used to compute the initial position and velocity. (Bottom) The supercluster in the velocity plane for the same three ages. The Hyades cluster is marked in each plot as a small circle. The velocity of the Sun is also marked as a circled dot in the bottom plots.* 132

4.18 *The model Hyades supercluster in the XY-plane for various ages. The solar neighbourhood is represented by two different circles ($r_1 = 200$ pc and $r_2 = 300$ pc).* 133

4.19 *The model Hyades moving group in the UV-plane for various ages, assuming a solar neighbourhood radius of* 200 pc. 134

4.20 *The model Hyades moving group in the UV-plane for various ages, assuming a solar neighbourhood radius of* 300 pc. 135

4.21 *Velocity dispersions for the model Hyades moving group at various ages and for two different solar neighbourhoods ($r_1 = 200$ pc, $r_2 = 300$ pc). Open circles (σ_U) represent the standard deviation in U and filled dots (σ_V) represent the standard deviation in V.* 136

A.1 *Equatorial coordinate system, with local vectors $\vec{p}$, $\vec{q}$, $\vec{r}$ for a star at (α, δ).* . 145

A.2 *Galactic coordinate system.* 148

D.1 *Precession from the mean equator of fixed epoch to the mean equator of date.* 164

D.2 *Nutation from the mean equator of date to the true equator of date.* 165

D.3 *Transformation of stellar positions from one epoch to another.* 170

D.4 *The Earth's ellipsoid rotating with an angular velocity ω around the polar axis ζ. An observer P at the geocentric position $\vec{\rho}$ rotates with a velocity vector $\vec{\mu}$.* 172

F.1 *Barycentric correction. A star is observed from the Earth, in a direction $\vec{e}_*$. All vectors are referred to the true equator and equinox of date $(x'y'z')$.* . . . 180

F.2 *The Sun is observed from the Earth, in a direction $\vec{e}_\odot$. All vectors are referred to the true equator and equinox of date $(x'y'z')$.* 181

F.3 *The barycentric correction as a sum of three components: $f_\oplus$, $f_\otimes$, and $f_\odot$.* . . 183

F.4 *The Sun's orbit around the solar system barycentre projected onto the plane of the ecliptic (left) and the magnitude of the Sun's velocity vector (right).* . 184
F.5 *The Earth's orbit around the Earth-Moon barycentre projected onto the plane of the ecliptic (left) and the magnitude of the Earth's velocity vector (right).* 184
F.6 *Residual radial velocity correction when both the Sun's orbit around the solar-system barycentre and the Earth's orbit around the Earth-Moon barycentre are ignored.* 185

List of Tables

1.1 *Eggen's moving groups included in the sample of 880 programme stars (Hipparcos Scientific Proposal No. 61). The number of stars in each group is given separately for the original proposal (PROP), the Hipparcos Input Catalogue (HIC) and the Hipparcos Catalogue (HIP). The moving groups are listed in the same order as they appear in the proposal.* 10

2.1 *MJUO observation summary.* 21
2.2 *DAO observation summary (RVS + CCD).* 21
2.3 *DAO RVS observation summary.* 21
2.4 *CCD characteristics and typical widths (FWHM) of the slit image on the chip (as measured from the thorium spectra).* 22
2.5 *Basic parameters for different instrument configurations.* 23
2.6 *Basic parameters of the stellar models used in this thesis.* 40

3.1 *Standard deviations for velocity distributions in U and V for some moving groups when pre-Hipparcos (HIC) or Hipparcos (HIP) data are used.* 74

C.1 *(First row) Spherical parameters for Arcturus (HIP 69673), as taken from the Hipparcos Catalogue. (Second row) Standard errors for the spherical parameters. (Third row) Correlation coefficients between the astrometric parameters.* 159

D.1 *Nutation in longitude and obliquity (periodic terms 1–53).* 167
D.1 *Nutation in longitude and obliquity (periodic terms 54–106).* 168

F.1 *Notation convention for the position and velocity vectors.* 179

Chapter 1

Introduction

1.1 Moving groups of stars

The idea of *moving groups* of stars in our Galaxy is now more than a century old. In order to illustrate this statement, a reference will be made to an early work by Proctor (1869), who was probably the first astronomer to note that some stars in the sky seemed to share their space motions:

> "I find that in parts of the heavens the stars exhibit a well-marked tendency to drift in a definite direction. In the catalogues of proper motions, owing to the way in which the stars are arranged, this tendency is masked; but when the proper motions are indicated in maps, by affixing to each star a small arrow whose length and direction indicate the magnitude and direction of the star's proper motion, the star-drift (as the phenomenon may be termed) becomes very evident."

The Hyades and Ursa Major groups were mentioned by Proctor in this paper. This idea of "star-drifting" has evolved over many years. At the beginning of this century, Hertzsprung (1909) demonstrated that a search for new members of already existing groups should cover much larger areas of the sky. For example, he found that *Sirius* (α Canis Majoris), as well as some other stars, shared the same motion as the Ursa Major group, in spite of the enormous angular separation between the stars. Hertzsprung based his results not only on proper motions, but also on parallaxes and radial velocities[1], so that a full study of the stellar space velocities was involved, including the now well known *convergent-point method*, developed by Boss (1908), only a year before.

Subsequently, several other moving groups of stars had been suggested by various authors during the first half of the century (see e.g. Eggen 1965a for a more detailed review). It was in late fifties when Olin J. Eggen started publishing his papers on this subject (Eggen 1957). His contribution to the development of the moving group idea was enormous, so that today

[1] Unfortunately, not very many stars had their parallaxes and radial velocities known at the beginning of the 20^{th} century.

the term *Eggen's moving groups* is often used to emphasize this fact. Eggen's papers on this subject span several decades.

Numerous other authors have also provided important contributions, as cited throughout this thesis. Some of the authors choose to work with the stellar proper motions alone, searching for certain convergent points in the celestial sphere (e.g. de Bruijne et al. 1997; de Bruijne 1999; Hoogerwerf & Aguilar 1999), while the majority of other papers involve a complete analysis of the space velocity vectors. A more detailed review of various methods used for the identification of moving groups can be found e.g. in Hoogerwerf & Aguilar (1999). However, no matter what method is used, there seems to exist an undoubted agreement between the authors about the existence of moving groups, or some grouping effects in velocity space.

Simultaneously with this extensive work of Eggen and other authors on detecting moving groups and developing various membership selection criteria, attempts have been made to provide explanations and physical reasons for the fact that there are stars in the solar neighbourhood that move in almost parallel orbits. The most commonly accepted hypothesis (referred to as *the moving group hypothesis* throughout this thesis) has been suggested by Eggen (see e.g. Eggen 1965a) and can be summarized in the following way:

- **The moving group hypothesis**

  Stars are formed in batches out of the material found in the interstellar clouds orbiting the Galaxy. A single batch may include a large number of stars formed approximately at the same point in space and time. The stars acquire the same initial space velocity, corresponding to the original motion of the interstellar cloud. Each star will also have an additional random velocity component, in accordance with a total velocity dispersion inside the batch.

  At first, all the stars stay together after the creation as a single cluster. In time, due to various influences[2], the cluster evaporates so that some stars gradually become free of the gravitational connection with the core of the cluster. Those stars that move faster will go ahead, and those stars that move slower will lag behind. The original cluster will spread along the orbit creating a stellar *supercluster*, i.e. a tube-like structure[3] that will grow longer as time passes. Random velocity components perpendicular to the orbit will only produce some oscillations in stellar motions.

  When the supercluster partially enters the solar neighbourhood, the stars are seen all over the sky, but they all move in almost parallel orbits with roughly the same velocity component *along the orbit* and with some fluctuations in the perpendicular directions. These stars form a *moving group* in the solar neighbourhood.

[2]These influences include close stellar encounters, galactic tidal effects, etc.

[3]The original orbit of the cluster is replaced by a *tube of orbits* of individual stars.

This hypothesis, although providing a basic frame for the explanation of moving groups, has not been generally accepted by all authors. The idea of 'cluster evaporation' has been re-examined, e.g. by Agekyan & Belozerova (1979), and it has been demonstrated that an open cluster can indeed develop an extensive *corona* of weakly bound stars surrounding the core of the cluster, while keeping the velocity vectors the same. The main point of disagreement is that it is probably not very likely that the stars can keep their parallel motions for a long time. Alternative ideas have been proposed, such as the possibility of "trapped" orbits (e.g. Mülläri et al. 1994). That is the reason why one can still find in the literature statements emphasizing some 'controversy about moving groups' (e.g. Asiain et al. 1999a). Nevertheless, the assumption that all stars belonging to a moving group should have almost the same velocity component in the direction of galactic rotation is frequently in use and is normally called *Eggen's membership criterion.*

The terminology used in this thesis is based on Eggen's papers (e.g. Eggen 1994) so that a *supercluster* is a system obtained when the original stellar cluster dissipates and the stars become spread along the orbit. The whole supercluster is not normally seen from the Earth. On the other hand a *moving group* is a small portion of the supercluster composed only of the stars that fall inside the solar neighbourhood and therefore which can be easily observed.

Moving groups are usually named after one star (or a star cluster) belonging to the group and with a well known space velocity (i.e. the *principal* star). About one dozen moving groups have been suggested by Eggen, the most important ones being the Hyades, Sirius, Wolf 630, Arcturus, 61 Cygni, ζ Herculis, σ Puppis, ε Indi, η Cephei and γ Leonis groups. Some of these groups have been studied extensively by other authors, e.g. the Sirius group (Palouš & Hauck 1986; Soderblom & Mayor 1993) and the Hyades group (Bubeníček et al. 1985). In some of Eggen's papers (Eggen 1964a, 1983a, 1983b, 1983c) evidence can be found that several young galactic clusters share their space motions with the Pleiades cluster, so that the Pleiades moving group can be defined.

There have been attempts to detect moving groups in an independent way using various samples of stars in the solar neighbourhood. Agekyan & Orlov (1984) have found nine moving groups (numbered using the roman numerals I–IX) in a sample of 1132 stars within $\sim$ 20 pc. The same groups have been studied by other authors (e.g. Mülläri et al. 1994; Popović et al. 1995). On the other hand, Figueras et al. (1997) analysed a sample of 2588 early-type (B5–F5) main-sequence stars based on the Hipparcos measurements (an improved version of a previous paper by Chen et al. 1997) and reported 5–7 moving groups, depending on the method used. This work was continued by Asiain (1998), Asiain et al. (1999a) and Asiain et al. (1999b).

Using a somewhat different method involving the Hipparcos astrometric data alone, Chereul et al. (1999) find an even larger number of moving groups, depending on the scale parameter used in the wavelet transforms. A cross-identification is also given using the results of Palouš et al. (1977), Chen et al. (1997), as well as various results by Eggen.

1.2 Scientific goal of this thesis

This thesis is a result of a research project undertaken at the University of Canterbury in order to test the reality of the concept of moving groups of stars in our Galaxy. High quality astrometric data collected by the Hipparcos satellite (see Section 1.5) are combined with new ground-based spectroscopic measurements obtained at the University of Canterbury (as the observational part of this project) so that accurate space motions can be derived for over 800 stars found in Eggen's papers as probable or possible members of various moving groups. The main hypothesis to be tested is the existence of moving groups as a result of cluster evaporation (see the "moving group hypothesis" in the previous section), as well as the assumption of constant space velocity in the direction of galactic rotation (Eggen's membership criterion). This becomes particularly interesting for older groups, where stars seem to have managed to preserve their parallel motions over long periods of time (many of Eggen's moving groups belong to the old-disk population, with ages comparable to the age of the Sun, i.e. about $4 - 5$ Gyr).

In the absence of reliable stellar trigonometric parallaxes for most of the stars, Eggen has introduced the concept of *group parallaxes* (see Section 1.4). If a star belongs to a moving group, then the group parallax for this star corresponds to such a distance at which the space velocity component in the direction of galactic rotation (usually denoted as V, see Section 1.3) takes the same value as for the rest of the group. If this hypothesis is correct, then the group parallax provides a relatively easy way of computing the distances when other methods are not efficient. As an additional test, the H-R diagram of the group (when the group parallaxes are used to compute the absolute stellar magnitudes) must resemble that of a stellar cluster, with a well-defined locus of stars corresponding to an isochrone. Eggen has claimed that the H-R diagrams computed in this way for the old-disk moving groups are very similar to that of the old galactic cluster M67 (Eggen 1971c; Eggen et al. 1973). This result can also be tested using the Hipparcos parallaxes.

More details about the main research areas involved in this project, and how they are organized in this thesis, are given at the end of this chapter, in Section 1.7. But first, various important points related to the moving-group hypothesis introduced above will be discussed in the next few sections.

1.3 Galactic velocity components

All stars in our Galaxy move around the galactic centre in orbits following the global galactic rotation. To a first approximation, the orbits can be regarded as circular and mostly concentrated in the galactic plane (galactic disk). A typical circular velocity at the Sun's distance ($R_0 = 8.5$ kpc) is $V_0 = 220$ km s^{-1}, which gives a period of about 240 million years. A more detailed study of galactic dynamics will be presented in Chapter 4. At this stage,

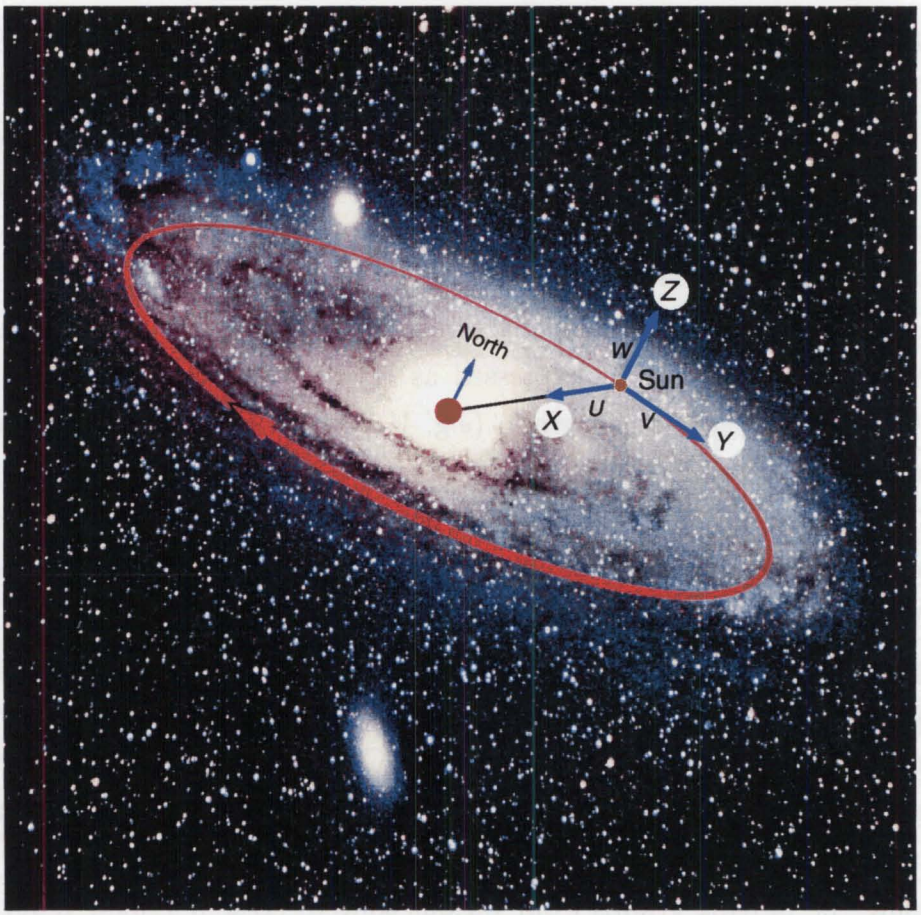

Figure 1.1: *The local galactic reference frame used to express stellar velocities with respect to the Sun. An image of M31 is used to represent the Milky Way galaxy.*

only the basic ideas will be used to illustrate the way in which stellar velocities are studied in the vicinity of the Sun.

A typical spiral galaxy (M31 in the constellation of Andromeda) is shown in Figure 1.1 as a model of the Milky Way. The Sun is also shown in its orbit and a local reference frame is constructed at the Sun, with the X-axis pointing towards the galactic centre[4], Y-axis in the direction of galactic rotation (clockwise, when seen from the north galactic pole) and Z-axis towards the north galactic pole.

The small portion of the galactic disk in the immediate vicinity of the Sun is called the *solar neighbourhood*. The actual radius of the solar neighbourhood can vary from one study to another, but a typical value is about $100 - 200$ pc, which is well inside the Sun's symbol (yellow circle) in Figure 1.1. Nevertheless, most of the present knowledge about the Milky Way galaxy (particularly with respect to optical astronomy) comes from this small volume around the Sun.

[4]Some authors, including Eggen himself, use an X-axis pointing *away* from the galactic centre, but keeping the other two axes the same as in Figure 1.1 so that a left-handed coordinate system is produced.

For the majority of stars in the solar neighbourhood the stellar space velocities are of the same order of magnitude as the velocity of the Sun ($\sim 220\ \mathrm{km\,s^{-1}}$). Therefore it makes sense to calculate the *relative velocities* with respect to the Sun (i.e. the heliocentric velocities), so that they are all distributed around zero. When projected onto the coordinate axes, the stellar heliocentric velocities produce the three galactic velocity components: U, V and W, corresponding to the X, Y and Z axes respectively.

In terms of the three galactic components of the space velocity vector, Eggen's moving group membership criterion can be expressed as $V = [\text{constant}]$. The actual value of the velocity will depend on the moving group (e.g. $V = -19\ \mathrm{km\,s^{-1}}$ for the Hyades[5] group). This criterion will be tested in Chapter 4 (see Section 4.6) by examining the evolution of a hypothetical moving group, using a numerical model of the galactic gravitational potential. Although the criterion of constant V can serve as a good first approximation, simulations show that there are situations when this is not entirely adequate.

Moving groups are typically studied in the galactic UV velocity plane. The third component of the space velocity (W) is often ignored, although there exist papers that include all three velocity components (e.g. Dehnen 1998b; Chereul et al. 1999; Asiain et al. 1999a). However, the W component stays close to zero for the disk stars and the main information about a moving group is derived from the UV-plane. An illustration is presented in Figure 1.2 using the moving groups from various sources (Eggen 1959a, 1960, 1969, 1971c, 1971d; Asiain et al. 1999a; Agekyan & Orlov 1984). Most authors work only with early-type stars, which are concentrated in the central parts of the UV-distribution. However, in Eggen's papers moving groups are also found in the old-disk population at higher velocities (i.e. in the peripheral parts of the diagram).

1.4 Group parallaxes

In order to compute the total space velocity of a star, both the *radial* and *transverse* components have to be obtained from observations. The radial velocity is the projection of the space velocity onto the line of sight (i.e. the direction towards the star). This is measured from the stellar spectrum using the Doppler effect ($V_\mathrm{r} = c\,\Delta\lambda/\lambda$) and does not depend on the distance. On the other hand, the transverse velocity is the projection of the space velocity onto the plane of the sky (i.e. perpendicular to the direction towards the star). This is obtained from astrometry by combining the proper motion and parallax ($V_\mathrm{t} = 4.74\,\mu/\pi$). Transverse velocities can be measured in this way well enough only for the closest stars. According to the above formula for V_t, the relative error in transverse velocity ($\sigma^2_{V_\mathrm{t}}/V_\mathrm{t}^2 = \sigma^2_\mu/\mu^2 + \sigma^2_\pi/\pi^2$) cannot be less than the relative error in parallax. And the relative error in parallax is still large for most of the stars that can be observed. Even with a very high precision of 1 mas

[5]Derived from the Hipparcos measurements (Perryman et al. 1998).

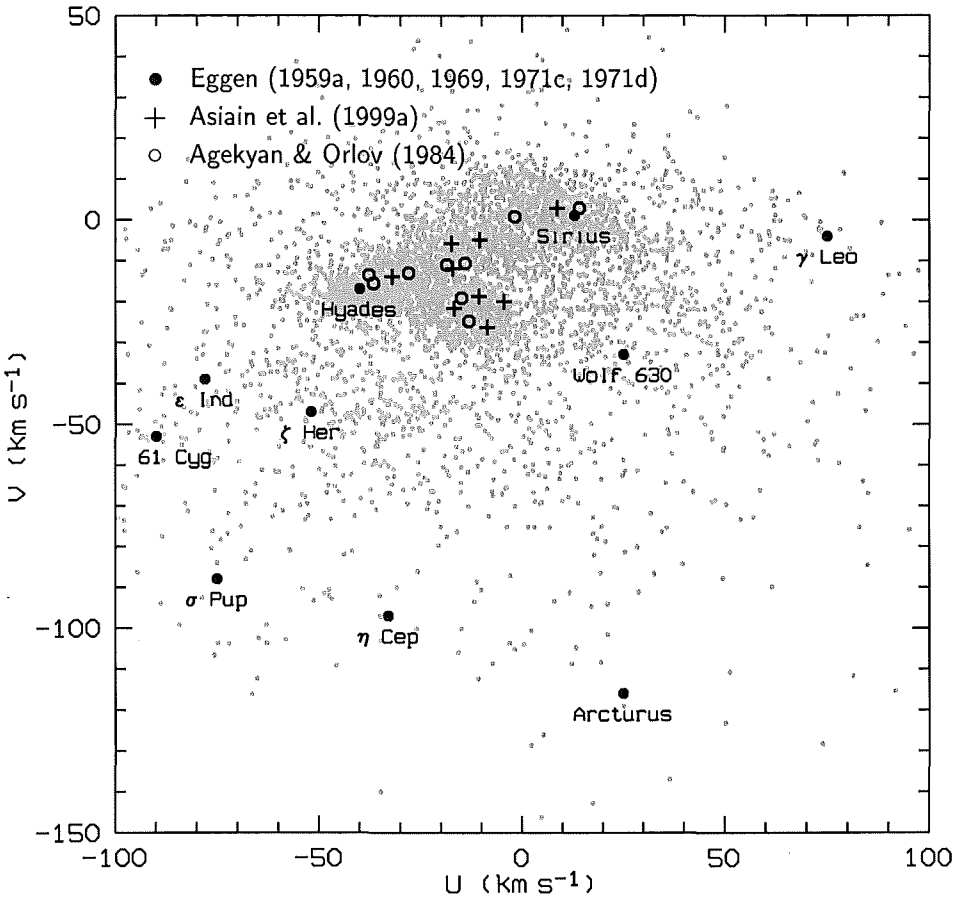

Figure 1.2: *Moving groups in the UV-plane as suggested by various authors (Eggen, Asiain et al. and Agekyan & Orlov). The observed stellar velocities in the solar neighbourhood (see Chapter 3, Figure 3.12) are shown grey in the background. The names of the moving groups are taken from Eggen.*

obtained by the Hipparcos satellite mission (see Section 1.5) the parallax error becomes as large as 20 per cent at 200 pc and 50 per cent at 500 pc, which makes all transverse velocity determinations at those distances unreliable.

In his papers dealing with moving groups Eggen has adopted a different approach in order to overcome this difficulty with stellar parallaxes. Instead of using the parallaxes obtained from observations, he determines the parallaxes so that all stars in a moving group have exactly the same V component of the space velocity (Eggen's membership criterion). The parallax obtained in this way is called the *group parallax.*

This process of deriving the group parallax for a star that is suspected of belonging to a moving group assumes that at least one star from the group (the principal star) has a reliable parallax, so that the V velocity can be computed. For example, the parallax of Arcturus is known within an error of about 1 per cent (see Appendix C) and the V velocity ($V = -119$ km s^{-1}) can be computed with roughly the same precision. Any other star in the Arcturus moving group might have an unreliable parallax leading to a velocity that is only

close to this value. If one assumes that the velocity must be exactly $V = -119\,\mathrm{km\,s^{-1}}$ (as for Arcturus), the group parallax can be computed for this star. Of course, some other criteria have to be used in order to distinguish between a real group member and a field star of the same V velocity, for example by checking if both stars have the same chemical composition and age, assuming that the moving group is a result of a stellar cluster evaporation. In particular, the group parallax must give such a value of the stellar absolute magnitude that places the star on an isochrone corresponding to the actual age of the group, as already discussed in Section 1.2. Eggen's group parallaxes will be compared with the Hipparcos measurements in Chapter 3 (see Figure 3.3).

1.5 Hipparcos satellite mission

Although the basic principle of measuring the distances towards stars is relatively simple and straightforward (by observing the parallactic displacement of a star at various positions of the Earth in its orbit around the Sun), in practice the measurements are more difficult, owing to the extremely small angles involved. The largest stellar parallax (that of α Centauri C) is only $0''.772$ and the vast majority of stars have parallaxes much less than that. This is the reason why the parallaxes had always been a restraining factor in any astronomical analysis at larger distances. The situation has changed dramatically with the Hipparcos project.

The acronym *HIPPARCOS* stands for *HI*gh *P*recision *PAR*allax *CO*llecting *S*atellite. The project was developed and conducted by the *European Space Agency* (ESA) in order to obtain positions, parallaxes and proper motions (i.e. the so-called five astrometric parameters: α, δ, μ_α, μ_δ and π) from space for a large number of stars ($\sim 120\,000$) with a previously unattainable precision of about 2 mas in the position and parallax, and 2 $\mathrm{mas\,yr^{-1}}$ in the proper motion. Some basic photometry was included as well. More details about the project can be found in various ESA publications (e.g. ESA 1985, 1989). Only some of the most important details will be repeated in this section.

The satellite was launched on an Ariane-4 rocket from Kourou, French Guyana on August 8^{th}, 1989 (a year later than previously planned). It was designed to be operated in a geostationary circular orbit and visible from one ground station continuously for 24 hours. However, due to a major failure of the apogee boost motor at an early stage of the mission (36 hours after the launch) the satellite never reached the circular orbit and it ended up trapped in a highly eccentric geostationary transfer orbit with a period of only 10.5 hours. In such conditions, the most optimistic estimate of the lifetime of the mission was about 9 months, with a completeness of only 5 to 10 per cent when compared with the original mission objectives.

Fortunately, this prediction did not come to realization. In spite of the extremely bad

conditions for normal operation, the satellite continued successfully to collect data during the following four years. The mission was terminated on August 15th, 1993, with the results even better than originally planned. For example, the median precision in parallax turned out to be just under 1 mas (0.97 mas precisely). The results have been published in the Hipparcos and Tycho[6] Catalogues (ESA 1997).

1.6 Programme stars

In 1982 John Hearnshaw and Peter Cottrell (Department of Physics and Astronomy, University of Canterbury) made a successful proposal (Hipparcos Scientific Proposal No. 61) to the European Space Agency for 880 moving group stars[7] to be observed by the Hipparcos satellite. The list contained the stars that had been mentioned by Olin Eggen in his papers as probable or possible members of various moving groups (see Table 1.1). Out of these 880 stars, which were all included in the Hipparcos Input Catalogue (ESA 1992), 830 stars were finally included in the Hipparcos Catalogue (ESA 1997) and only 822 of them had meaningful parallaxes (i.e. those greater than zero).

Simultaneously with the Hipparcos astrometric measurements, a ground-based spectroscopic observing programme has been carried out at the University of Canterbury in order to acquire precise radial velocities for the same list of stars (see Chapter 2). By combining the radial velocities obtained in this way (and also using the published values when necessary) with the transverse velocities derived from the Hipparcos astrometry, the stellar space velocities can be computed and the galactic orbits can be studied.

The distribution of the programme stars in the sky is shown in Figure 1.3 using the Hipparcos equatorial coordinates. The stars are spread evenly all over the sky, confirming that moving groups are really 'grouped' in velocities and not in space (see Chapter 3 for a presentation of the programme stars in the galactic UV-plane). The apparent visual magnitudes are distributed as shown in Figure 1.4. The median is at about $6^m.2$ and 80 per cent of the stars are brighter than 8^m.

It should be pointed out that the total number of stars included in this project was too large for a three-year long radial-velocity observing programme, bearing in mind the equipment and observing time available. Ideally, each star should be observed several times over a given period of time so that any variability in the radial velocity could be detected. In a stellar sample of this size one might expect to find many binaries and some of them still to be discovered. Only by repeating the observations of these stars can the radial velocity be obtained with confidence. However, given the large number of stars, some compromise must be found in order to complete the project.

[6]The Tycho Catalogue contains the astrometric and photometric data from the satellite's star mapper for more than 1 000 000 objects, but with less precision.

[7]The original proposal contained 895 stars as given in Table 1.1.

Table 1.1: *Eggen's moving groups included in the sample of 880 programme stars (Hipparcos Scientific Proposal No. 61). The number of stars in each group is given separately for the original proposal (PROP), the Hipparcos Input Catalogue (HIC) and the Hipparcos Catalogue (HIP). The moving groups are listed in the same order as they appear in the proposal.*

Moving Group	*U*	*V*	*Number of Stars*			*References*
	($\mathrm{km\,s^{-1}}$)		PROP	HIC	HIP	
Wolf 630	+25	−33	174	174	170	Eggen (1965b); Eggen (1969); Eggen (1971a); Eggen (1971b); Eggen (1971c); Eggen (1971e); Eggen (1971f); Eggen (1973); Eggen (1974a); Eggen (1974b); Eggen (1976); Eggen (1978)
Arcturus	+25	−116	76	75	75	Eggen (1971d); Eggen (1974b); Eggen (1976); Eggen (1977a); Eggen (1977b); Eggen (1978); Eggen (1979)
Hyades	−40	−17	287	283	264	Eggen (1970); Eggen (1972a); Eggen (1974a); Eggen (1977a)
61 Cygni	−90	−53	76	74	72	Eggen (1959b); Eggen (1969); Eggen (1971a); Eggen (1971b); Eggen (1971e); Eggen (1972b); Eggen (1978)
ζ Herculis	−52	−47	33	33	27	Eggen (1971c)
σ Puppis	−75	−88	29	28	28	Eggen (1971c)
ε Indi	−78	−39	18	17	16	Eggen (1971c)
η Cephei	−33	−97	31	31	26	Eggen (1971c)
γ Leonis	+75	−4	28	25	22	Eggen (1959a)
Groombridge 1830	+230	−156	5	5	4	Eggen (1977a)
Kapteyn's	+20	−289	25	25	25	Eggen (1977a)
Anonymous	+60	−175	5	5	4	Eggen (1979)
Anonymous	+150	−320	5	5	5	Eggen (1977a)
Sirius	+13	+1	103	100	92	Eggen (1960); Eggen (1964b)
Total			895	880	830	

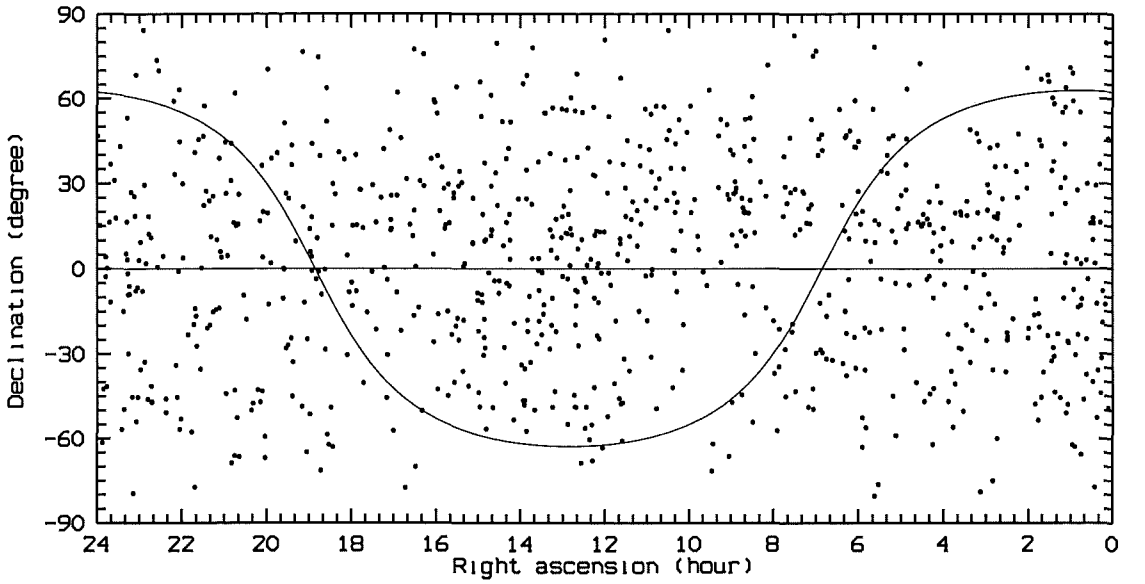

Figure 1.3: *Equatorial positions of 830 programme stars included in the Hipparcos Catalogue. The sinusoidal line represents the galactic equator.*

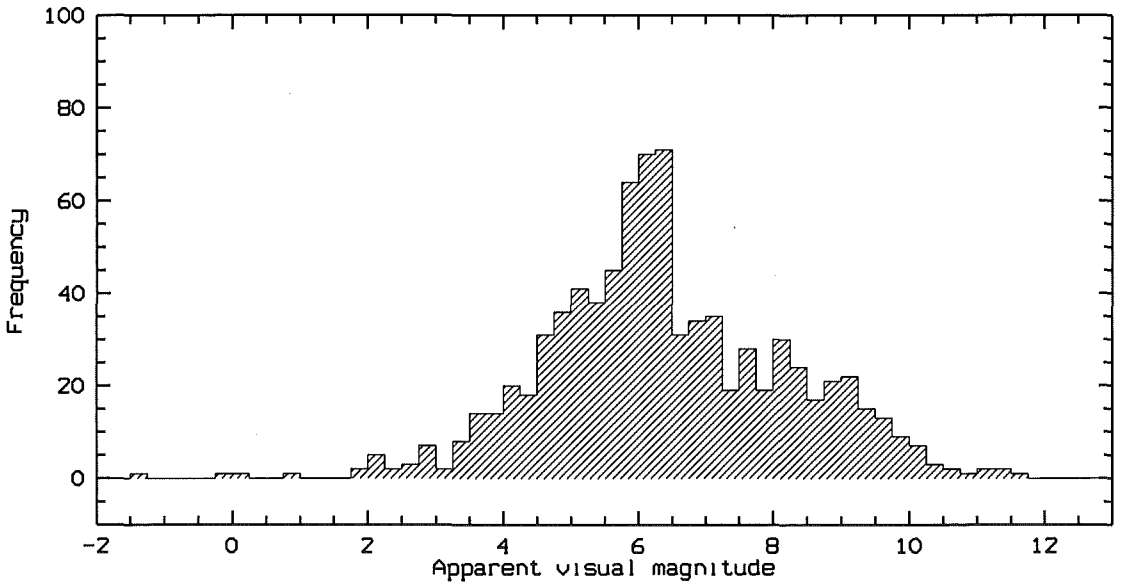

Figure 1.4: *Apparent visual magnitudes for the same sample of stars as in Figure 1.3.*

The main question concerning the efficiency of the radial-velocity measurements in this project is: what sort of precision in radial velocity is really needed? As will be explained in Chapter 2, an uncertainty of 100 $\mathrm{m\,s^{-1}}$ was predicted to be achievable using the échelle spectrograph at Mt John University Observatory. In fact, an uncertainty of about 20 $\mathrm{m\,s^{-1}}$ was achieved for some stars, but this high precision might not be necessary for all the stars. One factor involved in this problem is a typical velocity dispersion in moving groups, since there is no sense in measuring the velocities with much better precision than that. A

dispersion of about 10 $\mathrm{km\,s^{-1}}$ can be derived from some of Eggen's papers (e.g. Eggen 1969). Of course, this is too large to be acceptable as a lower limit to the precision of velocity measurements, but it demonstrates that a study of moving groups is possible even with poor velocities.

Another factor is the precision in transverse velocities derived from the Hipparcos astrometry. Again, there is no need to have radial velocities much better than transverse ones. A typical precision in published radial velocities is about $1-2$ $\mathrm{km\,s^{-1}}$. For example, more than 80 per cent of 14 000 stars with existing estimates for the quality of the radial velocity found in the Hipparcos Input Catalogue (ESA 1992) are labelled as "b" or "c", which corresponds to a standard error of 1.2 $\mathrm{km\,s^{-1}}$ and 2.5 $\mathrm{km\,s^{-1}}$ respectively. On the other hand, a typical precision in transverse velocities tends to be higher. In order to illustrate this the programme stars are plotted in a diagram involving both the parallaxes and proper motions using the Hipparcos measurements (Figure 1.5). A logarithmic scale is used on both axes. All stars having the same transverse velocity (V_t) appear aligned along a straight line at an angle of $\alpha = 45°$ ($\tan\alpha = 1$) with respect to the parallax axis, as easily found from:

$$V_\mathrm{t} = 4.74\,\frac{\mu}{\pi} \Rightarrow \mu = \pi\,\frac{V_\mathrm{t}}{4.74} \Rightarrow \log\mu = \log\pi + C_1, \tag{1.1}$$

where C_1 is a constant depending only on V_t ($C_1 = \log V_\mathrm{t} - \log 4.74$). On the other hand, all stars with the same uncertainty σ_{V_t} belong to a steeper line at an angle of $\beta \approx 63°$ ($\tan\beta = 2$). To be more precise, the line is slightly curved (see the line at $\sigma_{V_\mathrm{t}} = 0.1$ $\mathrm{km\,s^{-1}}$ for example) and the condition $\tan\beta = 2$ applies only at higher values of π or σ_{V_t} ($\pi\,\sigma_{V_\mathrm{t}} \gg 4.74\,\sigma_\mu$), as found from:

$$\frac{\sigma^2_{V_\mathrm{t}}}{V_\mathrm{t}^2} = \frac{\sigma^2_\mu}{\mu^2} + \frac{\sigma^2_\pi}{\pi^2} \Rightarrow \mu^2 = \frac{\pi^2}{\sigma^2_\pi}\left(\frac{\pi^2\sigma^2_{V_\mathrm{t}}}{4.74^2} - \sigma^2_\mu\right) \approx \left(\pi^2\,\frac{\sigma_{V_\mathrm{t}}}{4.74\,\sigma_\pi}\right)^2 \Rightarrow \log\mu = 2\log\pi + C_2, \tag{1.2}$$

where C_2 is another constant ($C_2 = \log\sigma_{V_\mathrm{t}} - \log\sigma_\pi - \log 4.74$) assuming that σ_π is the same for all stars.

A typical uncertainty in V_t (around the central parts of the distribution in Figure 1.5, i.e. close to $\pi \approx 10$ mas and $\mu \approx 100$ $\mathrm{mas\,yr^{-1}}$) is about $4-5$ $\mathrm{km\,s^{-1}}$ (with $\sigma_\pi = 1$ mas and $\sigma_\mu = 1$ $\mathrm{mas\,yr^{-1}}$). In fact, more than 80 per cent of the stars have uncertainties greater than 1 $\mathrm{km\,s^{-1}}$ and more than 60 per cent greater than 2 $\mathrm{km\,s^{-1}}$. Therefore, for the majority of stars there seems to be no reason for acquiring high-precision radial velocities at a level of 100 $\mathrm{m\,s^{-1}}$ or lower, since the total precision of the space velocity will not be much better than $1-2$ $\mathrm{km\,s^{-1}}$ anyway. However, this does not mean that the high-precision radial-velocity measurements are not important for a moving group study. Although the total velocity dispersion of a moving group cannot be improved significantly by improving only the radial-velocity measurements, there are many individual stars for which the transverse velocities are known with uncertainties small enough so that better radial velocities are needed.

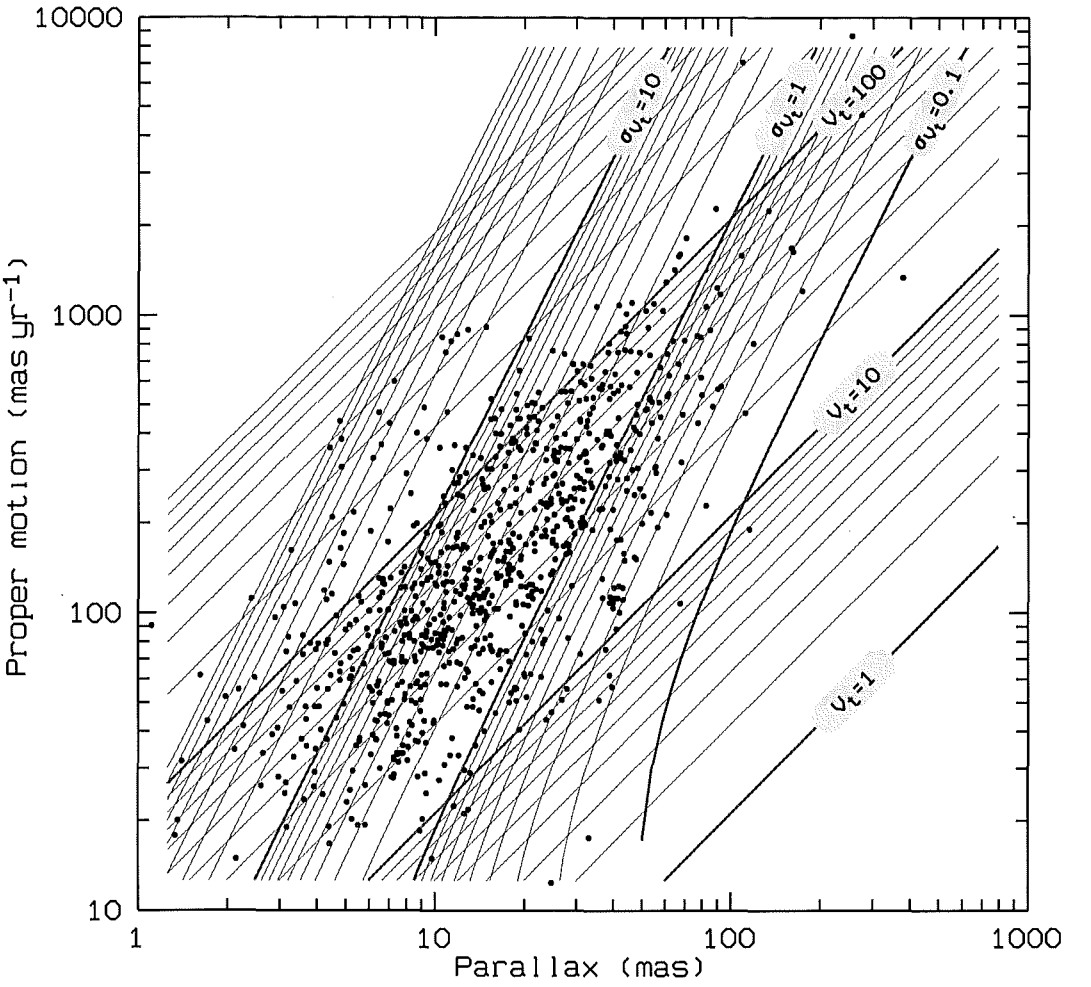

Figure 1.5: *Proper motions of the programme stars plotted against the parallaxes on a logarithmic scale. A grid of lines representing the loci of constant transverse velocity* (V_t = [constant]) *and of constant uncertainty in transverse velocity* (σ_{V_t} = [constant]) *is overplotted. The grid line spacing is also logarithmic and the values are given in* km s^{-1}. *The uncertainties* σ_π *and* σ_μ *are assumed to be equal to* 1 mas *and* 1 mas yr^{-1} *respectively.*

In a situation where a large number of stars is to be observed, a plot like the one presented in Figure 1.5 can be used to create a 'priority list' of stars that need high-quality radial velocities more than others. However, one has to be aware that the quality of the radial velocity can sometimes become important for a certain *component* of the space velocity (U, V or W), even if it does not affect the total space velocity by the same amount. For example, stars observed in the galactic plane at longitudes around $l = 90°$ and $l = 270°$ (along the Y-axis in Figure 1.1) will have their V-components determined only by the radial velocities. On the other hand, the other two components (U and W) will depend only on the transverse velocities. Therefore, the 'priority list' might be modified depending on the velocity component under consideration. Normally it is the V-component (Eggen's membership criterion), although the other two components are studied as well.

1.7 About this thesis

This project was undertaken at the University of Canterbury in order to test the reality of moving groups, using the Hipparcos astrometry and new ground-based radial-velocity measurements, as already explained in Section 1.2. There are three major research areas involved in this work and they are presented in the following chapters:

- **Chapter 2.** High-precision measurements of absolute stellar radial velocities for the stars introduced in Section 1.6 are described. The observations were made from two observatories (Mt John University Observatory in New Zealand and the Dominion Astrophysical Observatory in Canada). The chapter contains a detailed description of the instrumentation, data acquisition, data reduction and analysis of the radial velocities obtained.

- **Chapter 3.** An analysis of the Hipparcos measurements is made, with an emphasis on stellar velocities in the solar neighbourhood. The programme stars included in Hipparcos Proposal No. 61 (Eggen's moving groups) are presented first and then a study of a general sample of about 4600 stars within 100 pc of the Sun is given. An analysis of stellar metallicities derived from the Geneva Observatory seven-colour photometry is also included.

- **Chapter 4.** A numerical model of the galactic gravitational potential is developed, including a static axisymmetric part as well as a rotating spiral component. The stellar orbits are examined using this model and the evolution of moving groups is analysed.

The results from these three research areas are combined in order to understand better the reality, origin and nature of moving groups of stars in our Galaxy.

Chapter 2

Radial velocity observations

2.1 Observing programme

As it was already explained in Chapter 1, this project was based on a list of 880 stars mentioned by O. Eggen in his papers as possible members of various moving groups (for a detailed list of citations, see Section 1.6). The list was included in the Hipparcos Input Catalogue (Proposal No. 61 by J. B. Hearnshaw and P. L. Cottrell) in order to obtain precise *parallaxes* and *proper motions*, as a result of the satellite mission. At the same time, a parallel ground-based observing programme has been undertaken at the University of Canterbury, to acquire precise *radial velocities* for the same stars.

During the three-year observing period from 1995 April 24$^{\text{th}}$ till 1998 May 3$^{\text{rd}}$, covering 31 observing runs, a total number of 1536 radial velocity observations were collected, for 432 different objects. Most of the observing time was spent at Mt John University Observatory (MJUO), Lake Tekapo, New Zealand. With a latitude of $\varphi_{\text{MJUO}} = -43^\circ\,59\farcm2$, this observatory offers an excellent coverage of southern declinations, with a northern limit of about $\delta_{\text{lim}} \approx +30^\circ$, depending on the stellar magnitude. However, this is only about 75 per cent of the sky[1], so that many of the stars cannot be observed.

In addition to the MJUO observations, a significant number of RV measurements were made at the Dominion Astrophysical Observatory (DAO), Victoria, B.C., Canada ($\varphi_{\text{DAO}} = +48^\circ\,31\farcm2$), providing an opportunity to cover the northern declinations.

Some of the results presented in this chapter, in particular the radial velocity measurements of the IAU standards made both at MJUO and the DAO, were also presented in a preliminary form at the IAU Colloquium No. 170, 'Precise stellar radial velocities', held in Victoria, B.C., Canada in June 1998 (Skuljan et al. 1999a, 1999b).

---

[1] A solid angle covered by the declinations from -90° to $+\delta_{\text{lim}}$ is $\Omega = 2\pi\,(1 + \sin\delta_{\text{lim}})$, as can be easily computed from $\Omega = \int_0^{2\pi} d\alpha \int_{-\pi/2}^{+\delta_{\text{lim}}} \cos\delta\, d\delta$. A corresponding fraction of the sky is: $\Omega/\Omega_{\text{tot}} = \Omega/4\pi = (1 + \sin\delta_{\text{lim}})/2 = 0.75$.

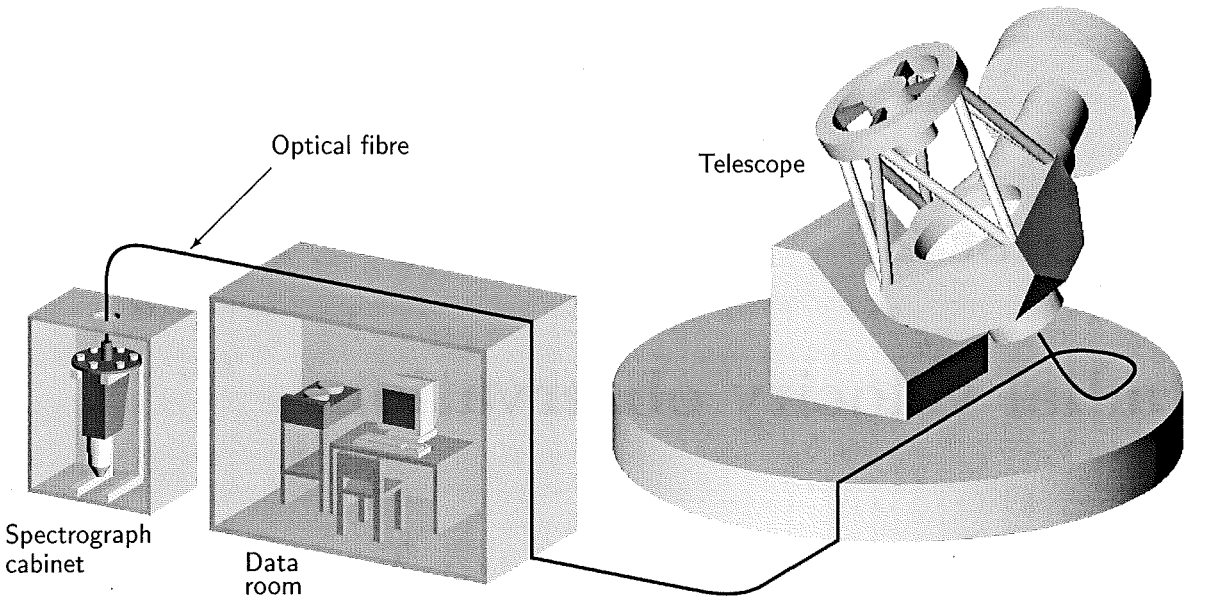

Figure 2.1: *Schematic diagram of the MJUO observing equipment.*

2.2 Observing equipment

2.2.1 MJUO instrument description

The MJUO observing equipment for this project was based on the one-metre McLellan[2] telescope and the échelle spectrograph. In a typical configuration, the spectrograph is placed in a separate temperature-controlled room next to the dome, rather than being mounted directly onto the telescope. The stellar light collected by the telescope is transferred to the spectrograph by a 25-metre long and 105-micrometre thick optical fibre. For more details about the equipment see e.g. Hearnshaw (1977) and Kershaw & Hearnshaw (1989). A CCD camera is used to record a two-dimensional image of several (typically six) diffraction orders in the focal plane of the spectrograph.

A schematic diagram of the equipment with the optical-fibre option is shown in Figure 2.1. This same configuration was also successfully exploited by Irene Cummings, a former PhD student at the University of Canterbury, for her precise radial velocity observations of late-type giants (Cummings 1998). It was also used by Kaylene Murdoch several years before (Murdoch & Hearnshaw 1991b), although with a different detector (a linear diode array). The telescope is set in the f/8 Cassegrain focus, so that the fibre input (diameter) corresponds to $2\rho_{\rm fib} \approx 2.7$ arc seconds of sky. The fibre tips are not polished, but a *glycerine drop* is inserted between the fibre input and the quartz window in the focal plane of the telescope. The presence of the glycerine drop ensures a uniform illumination of the fibre entrance, which in turn produces a uniform illumination of the fibre exit, at the spectrograph slit. In other

[2]In honour of Professor Alister G. McLellan, the former Head of the Physics Department.

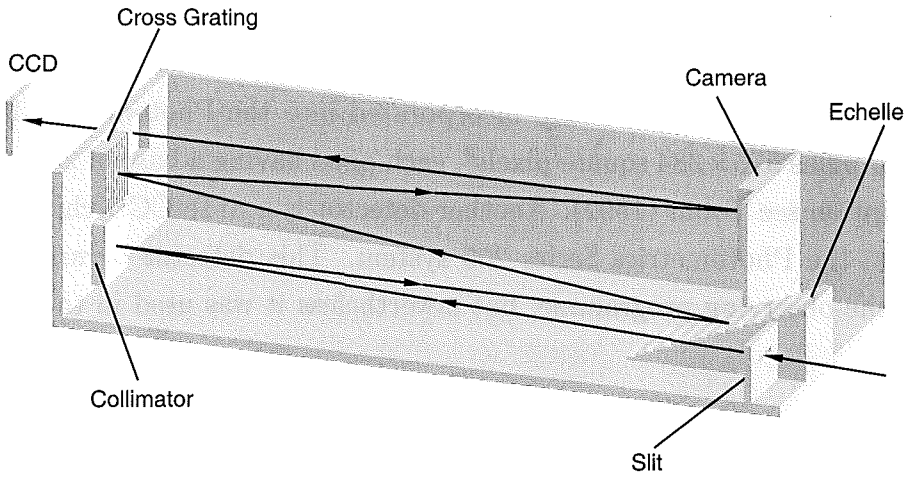

Figure 2.2: *Schematic diagram of the échelle spectrograph.*

words, the resulting image of the fibre on the slit is a stable, uniformly illuminated circle. However, the glycerine drop evaporates slowly, so that it has to be reinserted on a regular basis (typically once a year). At the output end of the fibre, the beam emerges at a focal ratio of f/5.2 and is reconverted back to f/8 by a 50-mm focal length camera lens focusing the fibre image on the slit. The diameter of the image is 180 μm.

The observations are normally done from the data room, using the computer equipment to control both the telescope and the CCD camera. The spectrograph is kept at a stable temperature of $25\overset{\circ}{.}0 \pm 0\overset{\circ}{.}1$ (Cummings 1998). The calibration (Th-Ar) and flat-field (white) lamps are placed inside the fibre feed module on the telescope. This is to ensure that both the stellar light and light from the lamps follow the same optical path before entering the spectrograph.

The spectrograph is based on an échelle grating having 79 grooves per millimetre. Although the nominal value of the blaze angle is $\theta_{\rm B}^{\rm nom} = \arctan(2) = 63\overset{\circ}{.}5$, the actual value seems to be somewhat larger. This was detected by examining some early photographic spectra of Procyon (F5IV), where a maximum intensity in the stellar continuum in order 39 was found at about $\lambda = 5902$ Å. This corresponds to a blaze angle of $\theta_{\rm B} \approx 65\overset{\circ}{.}4$ ($n\lambda = 2d \sin\theta_{\rm B}$), and a blaze wavelength of $\lambda_{\rm B} = 5480$ Å in order 42.

As a cross disperser (to separate the échelle orders) another diffraction grating is used, having 150 grooves per millimetre, and blazed at a wavelength of $\lambda_{\rm B} = 5000$ Å in the first order. The collimator is a parabolic mirror (focal length $f_{\rm col} = 54$ cm) and the camera is a spherical mirror (focal length $f_{\rm cam} = 75$ cm).

A schematic view of the échelle spectrograph is shown in Figure 2.2. The light from an object being observed through the telescope enters the spectrograph through a 100-μm slit and falls onto the collimator. The parallel beam from the collimator then gets dispersed by the échelle grating, and again by the cross grating. Finally, the spectrum is focused onto the

CCD chip by the camera mirror.

Two CCD detectors have been available with the one-metre telescope at Mt John. First, there is a Thomson TH7882 CDA chip incorporated into the Photometrics PM3000 CCD system. The chip has 576×384 square pixels[3], each pixel having a base of 23 μm. For a more detailed description see Tobin (1992). Another detector is a SITe CCD chip of 1024×1024 24-μm pixels in the Photometrics Series 200 system. This detector became available only at the end of the observing programme, but nevertheless it was used in the later observing runs.

2.2.2 DAO instrument description

At the Dominion Astrophysical Observatory, the 1.2-metre telescope was used, equipped with the coudé spectrograph. More details about this telescope can be found on the DAO Internet site, *http://www.dao.nrc.ca.*

The telescope and dome are under computer control from the observer's room. The telescope optical elements (all except the primary mirror) are covered with high-reflectance coatings to improve the performance. For this project, the 'super blue' set of mirrors was selected, optimized for 3500–5300 Å.

The telescope focal ratio of f/145 is converted to f/30 before entering the coudé spectrograph. At the focus, an *image slicer* ensures that most of the stellar light is sent into the spectrograph through the slit.

When the Radial Velocity Scanner (RVS) is used, then an additional piece of equipment called the Guiding Error Minimizer (GEM) is installed. This consists of an image-rotating prism, located just after the spectrograph slit, allowing a rotation of the slit image by 180°. During the RVS observations, the prism is rotated periodically after every five scans in order to compensate for poor guiding, when the star is not centred on the slit.

The spectrograph itself is based on the '9682M' mosaic grating, having 830 grooves per millimetre. It is used in the blue (second order) at 2.4 Å mm^{-1}. The spectrum is focused onto the detector by a large 244-cm focal length camera mirror.

Two different detectors were used for this project at the DAO. The more important one (i.e. that more often used) is the RVS (see e.g. McClure et al. 1985), allowing up to 50–70 radial velocity determinations during a good observing night. The second one is a SITe 1752×532 CCD camera with 15-μm pixels. The CCD observations are much slower than the RVS ones, and need further reduction, but as an advantage the spectra are recorded for future analysis.

[3]Strictly speaking, it is 384×576 pixels, since the physical CCD rows are of 384 and columns of 576 pixels (physical rows are defined by the CCD read-out process). However, in spectroscopic observations, the CCD image is always rotated by 90°, so that the longer side becomes horizontal, and the image rows during the data reduction are 576 pixels long.

2.3 Observing statistics

As already mentioned in Section 2.1, the three-year observing period covers 31 observing runs. The observing runs were quite evenly distributed over time, as presented in Figure 2.3, where each run is shown as a rectangular peak covering the actual number of observing nights. The observing runs are enumerated as 1–28 at MJUO, and again as 1–3 at DAO (shaded peaks).

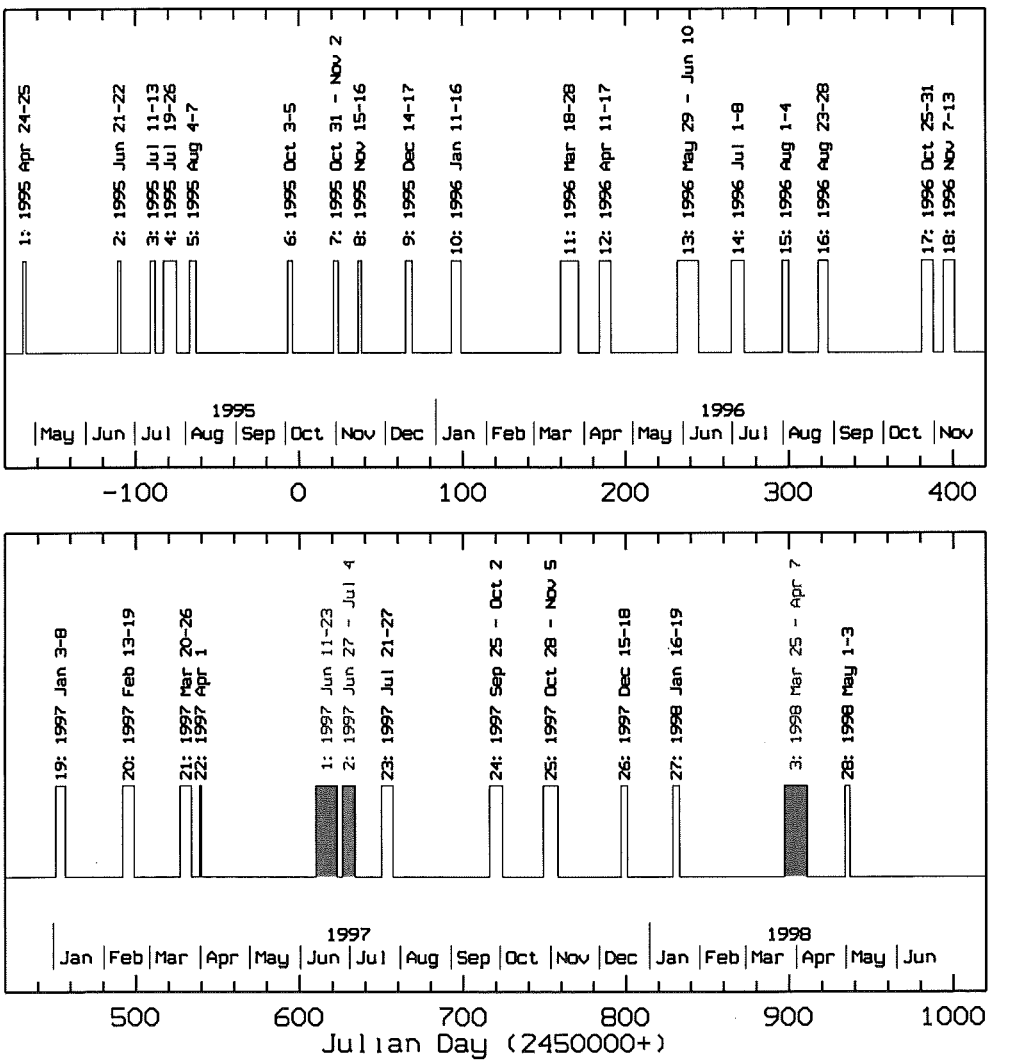

Figure 2.3: *Distribution of the twenty eight MJUO observing runs, and three DAO runs (shaded peaks) over the three-year observing period.*

A variety of instruments and detectors were used, not because it was essential for the observing programme (rather, it was making the reduction procedure more complicated), but simply because it was what the observatories could offer at the particular moment. Sometimes, of course, a different instrument/detector configuration was tried in an attempt to improve the observations.

The observing programme was started at MJUO in 1995 April using the Photometrics PM3000 CCD system with the spectrograph directly mounted on the 1-m McLellan telescope. It was expected that this configuration, combined with a careful data reduction, could yield a radial velocity precision of about 100 $\mathrm{m\,s^{-1}}$. Although the optical fibre was also an available item of equipment at the time, the option without the fibre was thought to be more appropriate for this moving-group project, having in mind the large number of targets not always bright enough (stars fainter than about 6^{th} or 7^{th} magnitude appeared not to be very suitable for the optical fibre configuration).

After some time spent on observations without the optical fibre (observing runs 1–5), it became obvious that the desired precision of 100 $\mathrm{m\,s^{-1}}$ could not be achieved. The main problems were the flexure of the spectrograph during the exposure, sometimes combined with occasional sudden jumps (not very well understood), that moved the spectrum across the CCD chip, producing unwanted shifts in the radial velocity itself. Another problem, of course, was the guiding error (and the focusing error too) making it almost impossible to have the same stellar image at the same position on the spectrograph slit at all times. Different illumination of the slit results in a different radial velocity.

In order to improve the precision of the radial velocities, the optical fibre configuration was then used for the rest of the observing period at MJUO (runs 6–27). The majority of observations were made with the same PM3000 CCD, without any change in the optics (runs 6–21). Then a major change occurred in April 1997, when the *focal reducer* was installed into the spectrograph, in order to put more échelle orders onto the chip, as demanded by some other research projects. Unfortunately, the installation of the focal reducer made it very difficult to use the PM3000 CCD any more, since it was necessary to remove the *shutter ring*, together with the *preflashing diodes*, from the camera. Without the preflashing, the charge transfer efficiency of the chip becomes significantly reduced (Tobin 1992). Only two observing runs (22 and 23) were spent using this CCD with the focal reducer, and then a change was made to the 1024×1024 SITe camera, for the rest of the observing period (runs 24–27).

The last observing run at Mt John (No. 28) was an extra run spent completely on testing the PM3000 camera, as will be described later (see Section 2.6). The telescope was not used, and in fact the tests were made in the daylight by simply exposing the optical fibre input to the blue sky.

The three DAO observing runs were basically reserved for the RVS observations, where the radial velocity is measured by cross-correlating the observed spectrum with a standard mask. The spectrum itself is not recorded. The RVS observations will be discussed in more detail later (see Section 2.9). During the first two DAO runs, however, some CCD observations were also done, but these spectra have been treated independently from the MJUO échelle spectra, since they consist of a single diffraction order.

In order to handle all these different instrument configurations, a set of simple six-letter

Table 2.1: *MJUO observation summary.*

Configuration Name	Optical Fibre	Focal Reducer	Rotation Reading	Observing Runs	Nights Total	Number of observations Sky	Std	Prg	SP	X	Tot
$ECHCCD_R$			−1	1	2	3	0	9	0	0	12
$ECHCCD_N$			−2.8	2 – 5	17	3	15	51	2	0	71
$FIBCCD_R$	✓		−4.5	6	3	9	1	0	0	0	10
$FIBCCD_N$	✓		−2.8	7 – 21	98	220	133	248	30	8	639
FOCCCD	✓	✓	−4.5	22 – 23	8	3	6	19	3	0	31
$SITCCD_R$	✓	✓	0	24	2	1	3	13	0	0	17
$SITCCD_N$	✓	✓	−3.5	24 – 27	23	23	16	34	5	0	78
				TOTAL:	153	262	174	374	40	8	858

Table 2.2: *DAO observation summary (RVS + CCD).*

Configuration Name	Detector Used	Observing Runs	Nights Total	Number of observations Sky	Std	Prg	SP	Tot
DAORVS	RVS	1, 2, 3	28	49	94	367	45	555
DAOCCD	CCD	1, 2	7	8	23	83	9	123
		TOTAL:	35	57	117	450	54	678

Table 2.3: *DAO RVS observation summary.*

Observing Run	Nights Total	Number of observations Sky K *F* **T**	Std K *F* **T**	Prg K *F* **T**	SP K *F* **T**	Tot K *F* **T**
1	9	18 *0* **18**	26 *0* **26**	153 *0* **153**	8 *0* **8**	205 *0* **205**
2	5	5 *2* **7**	13 *9* **22**	37 *26* **63**	4 *5* **9**	59 *42* **101**
3	14	24 *0* **24**	46 *0* **46**	151 *0* **151**	28 *0* **28**	249 *0* **249**
TOTAL:	28	478 *2* **49**	85 *9* **94**	341 *26* **367**	40 *5* **45**	513 *42* **555**

mnemonics will be used here to denote each particular arrangement. The abbreviation ECHCCD is used for the spectrograph on the telescope (i.e. with no fibre), and FIBCCD for the configuration involving the fibre. In a similar manner, FOCCCD is used for the case with the focal reducer installed. All these configurations assume the PM3000 CCD. On the other hand, there is the SITCCD configuration, using the SITe chip, with the optical fibre and

Table 2.4: *CCD characteristics and typical widths (FWHM) of the slit image on the chip (as measured from the thorium spectra).*

Configuration Name	CCD Type	CCD size (pix)	Pixel size (μm)	FWHM (pix)
$ECHCCD_R$	Thomson	576×384	23	3.35
$ECHCCD_N$	Thomson	576×384	23	3.33
$FIBCCD_R$	Thomson	576×384	23	3.13
$FIBCCD_N$	Thomson	576×384	23	3.28
FOCCCD	Thomson	576×384	23	2.32
$SITCCD_R$	SITe	1024×1024	24	2.32
$SITCCD_N$	SITe	1024×1024	24	2.30
DAOCCD	SITe	1752×532	15	2.36

focal reducer installed. Finally, the two mnemonics for the DAO observing configurations are DAOCCD (using a SITe chip) and DAORVS (using the radial velocity spectrometer). Sometimes, a subscript N or R is added to the mnemonics (MJUO observations only) to denote if the configuration is 'normal' or 'rotated'. This is due to the fact that with any instrument-detector combination described above, a variety of possible CCD rotation angles are possible. In an optimal position, the spectral lines on a CCD image should appear vertical, in which case the reduction is the simplest. However, before this optimal position is found, a set of observations is done with a slightly different rotation. The qualifier R (rotated) usually corresponds to the initial set of test observations for the particular configuration, before the correct rotation of the CCD is determined. All subsequent observations are then marked as N (normal). This difference in the rotation angle, however, is not critical for the radial velocity determinations. The observational data clearly demonstrate that the CCD rotation does not introduce any systematic errors, so that it is possible to omit the subscript from the configuration names. For example, when FIBCCD is used, it means both $FIBCCD_R$ and $FIBCCD_N$.

A summary of the whole observing programme is presented in Tables 2.1–2.3. For each observing configuration, the total number of nights is given, as well as the numbers of objects observed. Several classes of objects are treated separately: Sun (Sky), standard radial velocity stars (Std), programme stars (Prg), stars that are both standards and programme stars at the same time (SP), other extra objects (X) and total count (Tot). In addition, Table 2.3 gives separate columns for each of the two masks used with the RVS (K and F), plus the total count for both masks (T).

Basic information on various CCD detectors used with different configurations is presented in Table 2.4. The column 'FWHM' gives the measured full width at the the half

Table 2.5: *Basic parameters for different instrument configurations.*

Configuration Name	Order Number	Wavelength Range (Å)	Central Wavelength (Å)	Window Width (Å)	Mean Dispersion (pix Å^{-1})	Mean Resolution (mÅ)
FIBCCD	46	5008.3–5030.9	5019.6	22.6	25.4	129
&	45	5119.5–5142.7	5131.1	23.2	24.8	132
ECHCCD	44	5235.8–5259.5	5247.6	23.7	24.3	135
	43	5357.5–5381.7	5369.6	24.2	23.7	138
	42	5485.0–5509.8	5497.4	24.8	23.2	141
	41	5618.7–5644.1	5631.4	25.4	22.6	145
FOCCCD	46	5010.2–5044.4	5027.3	34.1	16.8	138
	45	5121.6–5156.5	5139.1	34.9	16.5	141
	44	5238.1–5273.7	5255.9	35.7	16.1	144
	43	5359.9–5396.4	5378.1	36.5	15.8	147
	42	5487.6–5524.9	5506.2	37.3	15.4	151
	41	5621.4–5659.7	5640.5	38.2	15.0	154
	40	5762.0–5801.2	5781.6	39.2	14.7	158
	39	5909.8–5949.9	5929.8	40.2	14.3	162
SITCCD	49	4681.5–4741.5	4711.5	60.1	17.0	135
	48	4779.0–4840.3	4809.7	61.3	16.7	138
	47	4880.7–4943.3	4912.0	62.6	16.3	141
	46	4986.9–5050.8	5018.8	63.9	16.0	144
	45	5097.7–5163.0	5130.4	65.3	15.7	147
	44	5213.6–5280.4	5247.0	66.8	15.3	150
	43	5334.9–5403.2	5369.1	68.3	15.0	154
	42	5462.0–5531.9	5496.9	69.9	14.6	157
	41	5595.3–5666.8	5631.0	71.6	14.3	161
	40	5735.2–5808.5	5771.9	73.4	13.9	165
DAOCCD	2	5008.4–5069.3	5038.9	60.9	28.6	83

maximum of sharp emission lines, as measured from the thorium spectra. This is the width of the slit image projected onto the CCD chip, and defines the effective *resolution* of the spectrograph.

The actual wavelength regions and other characteristics of the configurations mentioned above are given in Table 2.5. The *dispersion* is defined as the ratio between the measured number of pixels on the CCD chip and the corresponding wavelength interval, and is ex-

pressed in pix Å^{-1}. Some authors often use the inverse ratio (i.e. the wavelength interval divided by the linear distance in the spectrum), which is then expressed in Å pix^{-1}, and also in Å mm^{-1}. This inverse definition is not used in this thesis. The *resolution* has been calculated by dividing the mean FWHM values (Table 2.4) with the actual dispersions. The *resolving power*, $R = \lambda/\Delta\lambda$, can be easily calculated by dividing the central wavelengths and mean resolutions from Table 2.5, taking an average of all diffraction orders for a given configuration. A typical resolving power of $R_{\mathrm{MJUO}} \approx 35\,000 - 39\,000$ is obtained from the MJUO échelle observations, depending on the actual configuration. On the other hand, a value of $R_{\mathrm{DAO}} = 60\,700$ is found for the DAO CCD observations.

2.4 MJUO échelle reduction procedure

In this section, the reduction procedure will be described in more detail. Attention will be concentrated mainly on the most important FIBCCD configuration, since it covers about 75 per cent of all observations (see Table 2.1), although the procedure is very similar for the other configurations. The reductions were basically done in MIDAS (ESO-MIDAS is the acronym for the *E*uropean *S*outhern *O*bservatory – *M*unich *I*mage *D*ata *A*nalysis *S*ystem). However, many other additional programs in C and Fortran were also developed (e.g. for the cross-correlation, barycentric correction, galactic components of the velocity vector etc.).

A schematic diagram of the reduction procedure is shown in Figure 2.4. It starts with the two-dimensional raw CCD images of the stellar, thorium and white spectra. Normally, there are two thorium spectra, taken immediately before and after the stellar exposure, but only one is shown in Figure 2.4.

The reduction procedure can be divided into two main stages (the two circles in the diagram), involving numerous individual steps that cannot be displayed. During the first stage, the one-dimensional stellar spectrum is produced, with each échelle order showing a normalized relative intensity as a function of the wavelength. The second stage is a cross-correlation procedure between the stellar spectrum and the corresponding theoretical (synthetic) spectrum. The radial velocity is finally derived from the positions of the peaks in the cross-correlation functions, by averaging all échelle orders.

In a more detailed form, the reduction procedure involves the following basic steps:

• Stage I

1. **Rotation.** The original two-dimensional CCD images are rotated so that the wavelength axis appears horizontal, with the wavelengths increasing from left to right, and the échelle orders appear separated vertically, one below another, with the order numbers increasing from top to bottom. This requirement is essential for the standard échelle reduction in MIDAS.

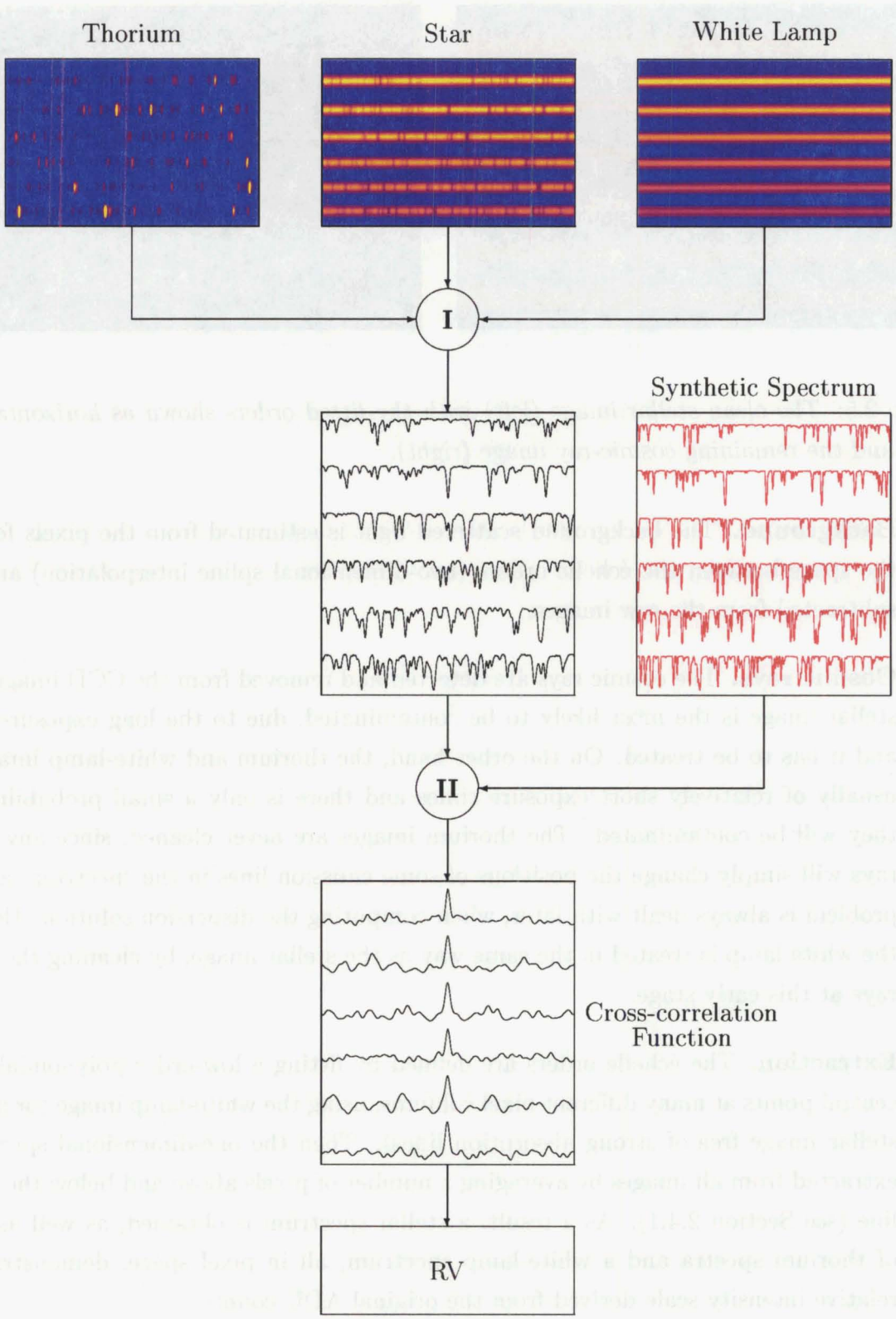

Figure 2.4: *MJUO échelle reduction procedure. Two-dimensional CCD images of the thorium, stellar and white-lamp spectra are used to produce the one-dimensional stellar spectrum (Stage I), which is then cross-correlated with a synthetic spectrum (Stage II). The radial velocity is found from the positions of the peaks in the cross-correlation function.*

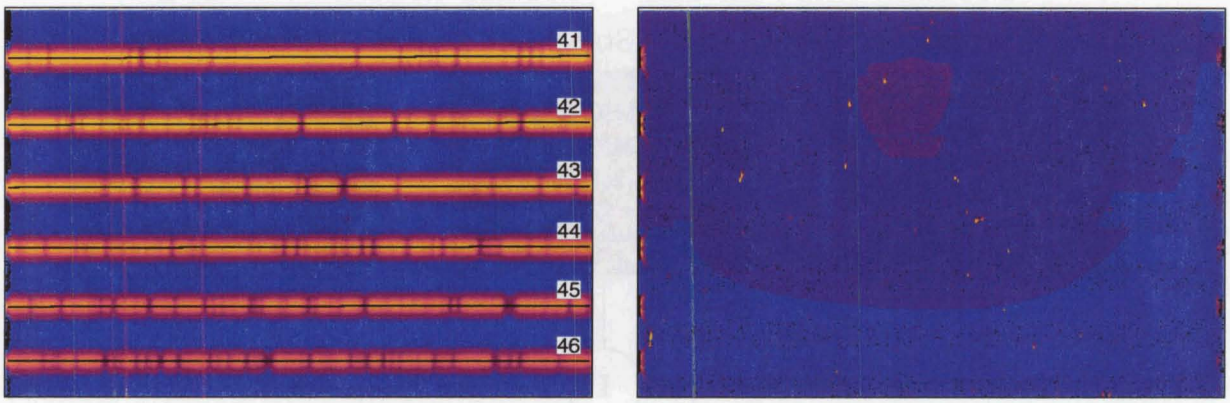

Figure 2.5: *The clean stellar image (left) with the fitted orders shown as horizontal black lines, and the remaining cosmic-ray image (right).*

2. **Background.** The background scattered light is estimated from the pixels found in the space between the échelle orders (two-dimensional spline interpolation) and then subtracted from the raw images.

3. **Cosmic rays.** The cosmic rays are detected and removed from the CCD images. The stellar image is the most likely to be contaminated, due to the long exposure times, and it has to be treated. On the other hand, the thorium and white-lamp images are usually of relatively short exposure times and there is only a small probability that they will be contaminated. The thorium images are never cleaned, since any cosmic rays will simply change the positions of some emission lines in the spectrum, and this problem is always dealt with later, when computing the dispersion solution. However, the white lamp is treated in the same way as the stellar image, by cleaning the cosmic rays at this early stage.

4. **Extraction.** The échelle orders are defined by fitting a low-order polynomial to the central points at many different pixel columns, using the white-lamp image (or a bright stellar image free of strong absorption lines). Then the one-dimensional spectra are extracted from all images by averaging a number of pixels above and below the central line (see Section 2.4.1). As a result, a stellar spectrum is obtained, as well as a pair of thorium spectra and a white-lamp spectrum, all in pixel space, demonstrating a relative intensity scale derived from the original ADU counts.

5. **Flat-fielding.** The stellar and thorium spectra are divided by the white-lamp spectrum in order to eliminate possible pixel-to-pixel variations. This step is usually called the *flat-field* correction, and should normally be performed on 2-D images. However, with the optical-fibre configuration, when the white-lamp image has the same profile as the stellar one, one cannot successfully divide the two images, because the signal

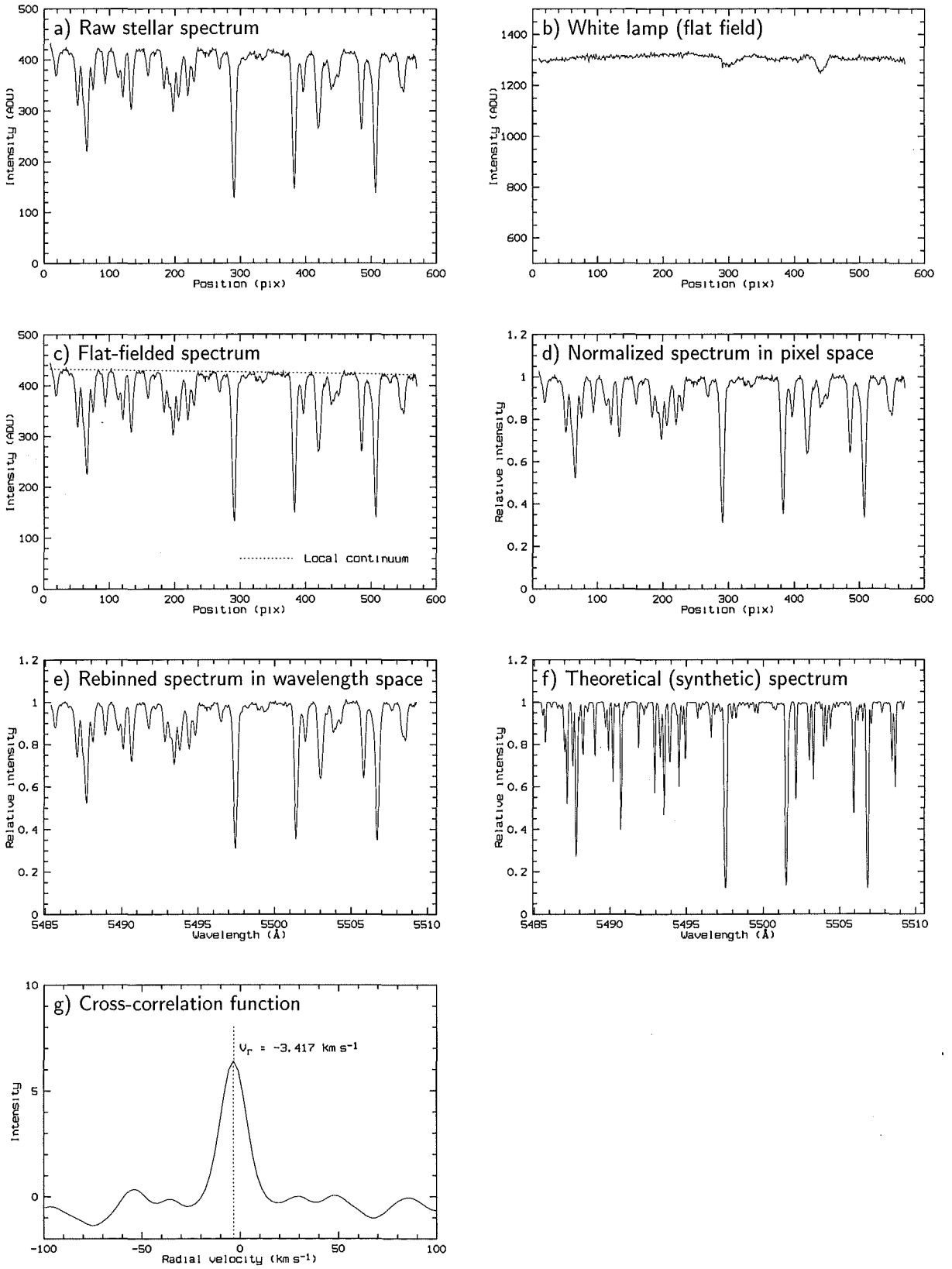

Figure 2.6: *Basic reduction steps after the one-dimensional spectrum has been extracted. An image of β Corvi is used. Only order 42 is shown.*

falls down rapidly (approaching zero) at the edges of the diffraction orders.

6. **Dispersion solution.** A mean dispersion solution (wavelength calibration) is computed using the two thorium spectra (see Section 2.4.2). A linear interpolation is done between the two solutions, using the exact times when the images were taken. The pixel positions of the selected emission lines are expressed as a two-dimensional polynomial depending both on the order numbers and wavelengths.

7. **Normalization.** The stellar spectrum is normalized so that the intensity scale is in the range from zero to one, where one corresponds to the continuum. The normalization is done by setting some points in the stellar continuum first, using the flat-fielded spectrum, as described above. A least-square linear fit to the points is used to define the continuum at every pixel position. Then the stellar image is simply divided by the continuum image.

8. **Rebinning.** The normalized stellar spectrum is rebinned into the wavelength scale, using the dispersion solution derived from the thorium spectra. As a result, a spectrum representing a relative intensity between 0 and 1 over a range of wavelengths is obtained.

• Stage II

1. **Model.** A theoretical (synthetic) spectrum is chosen, according to the spectral type and the luminosity class of the star (see Section 2.4.3).

2. **Rebinning.** Both the stellar and synthetic spectra are rebinned into a logarithmic scale, to make sure that the radial-velocity shift is the same at every pixel position[4].

3. **Cross-correlation.** A cross-correlation function between the stellar and synthetic spectra is computed for each échelle order separately (see Section 2.4.3).

4. **Peaks.** Cross-correlation peak centres are estimated by fitting a gaussian profile to the central parts of the distribution (see Section 2.4.3). The positions of the peaks are then transformed into radial velocities.

5. **Radial velocity.** The final radial velocity is computed as the arithmetic mean of all échelle orders. A corresponding *barycentric correction* (see Appendix F) is applied so that the radial velocity is expressed relative to the solar system barycentre.

6. **Zero-point adjustment.** Numerous spectra of the blue sky (scattered light from the Sun), as well as of the IAU standard radial velocity stars, frequently collected during

[4]From $\Delta\lambda/\lambda = (\lambda' - \lambda)/\lambda = V_r/c$, one obtains $\lambda'/\lambda = 1 + V_r/c$, or $\log\lambda' - \log\lambda = \log(1 + V_r/c) \neq f(\lambda)$.

the whole observing programme, are used for the final determination of the zero point. (see Sections 2.5.2 and 2.8).

Figures 2.5 and 2.6 illustrate some of the reduction steps. An observation of β Corvi is used here, made on April 15th, 1996, the same as in Figure 2.4. The stellar image after the background subtraction and cosmic-ray elimination is shown in Figure 2.5, together with the differential image containing only the scattered light and the cosmic rays. From the clean stellar image, six échelle orders have been extracted, but only one of them (order 42) is shown in Figure 2.6, demonstrating the flat-fielding, normalization and cross-correlation with the synthetic spectrum.

2.4.1 Line shapes and the extraction process

In a perfect case, a two-dimensional spectrum on the CCD should consist of straight and vertical spectral lines coinciding with the pixel columns. The extraction of one-dimensional spectra is done by averaging the pixel values at every pixel column. The actual number of pixels taken above and below the central line depends on the slit height. To illustrate this, a portion of a thorium image is presented in Figure 2.7. In general, the échelle orders do not have to appear horizontal in order to have the spectral lines vertical, since the angle between the spectral lines and the dispersion axis is not 90°.

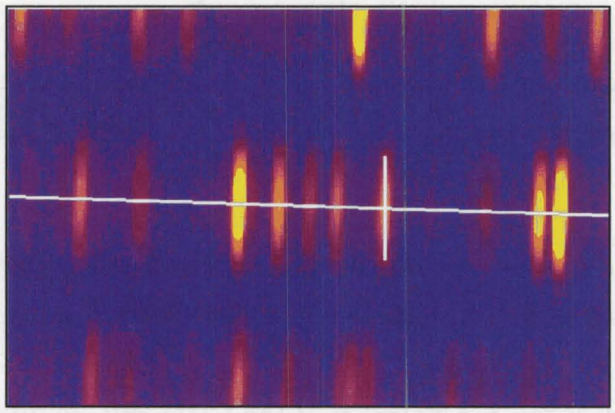

Figure 2.7: *An enlarged portion of the thorium image (*ECHCCD$_R$*) illustrating the extraction process. The central line through an échelle order is followed pixel by pixel, and at each position an average value is taken of a number of pixels above and below the central line.*

There is an objective way to determine if a spectral line is vertical or not, by simply cutting the line at different pixel rows (up and down across the slit), and then computing the centres of the gaussian fits for each profile. As a result, a set of points is obtained, describing the actual shape and tilt of the spectral line in pixel space. More spectral lines across the CCD image can be treated in this way, and an average profile can be derived.

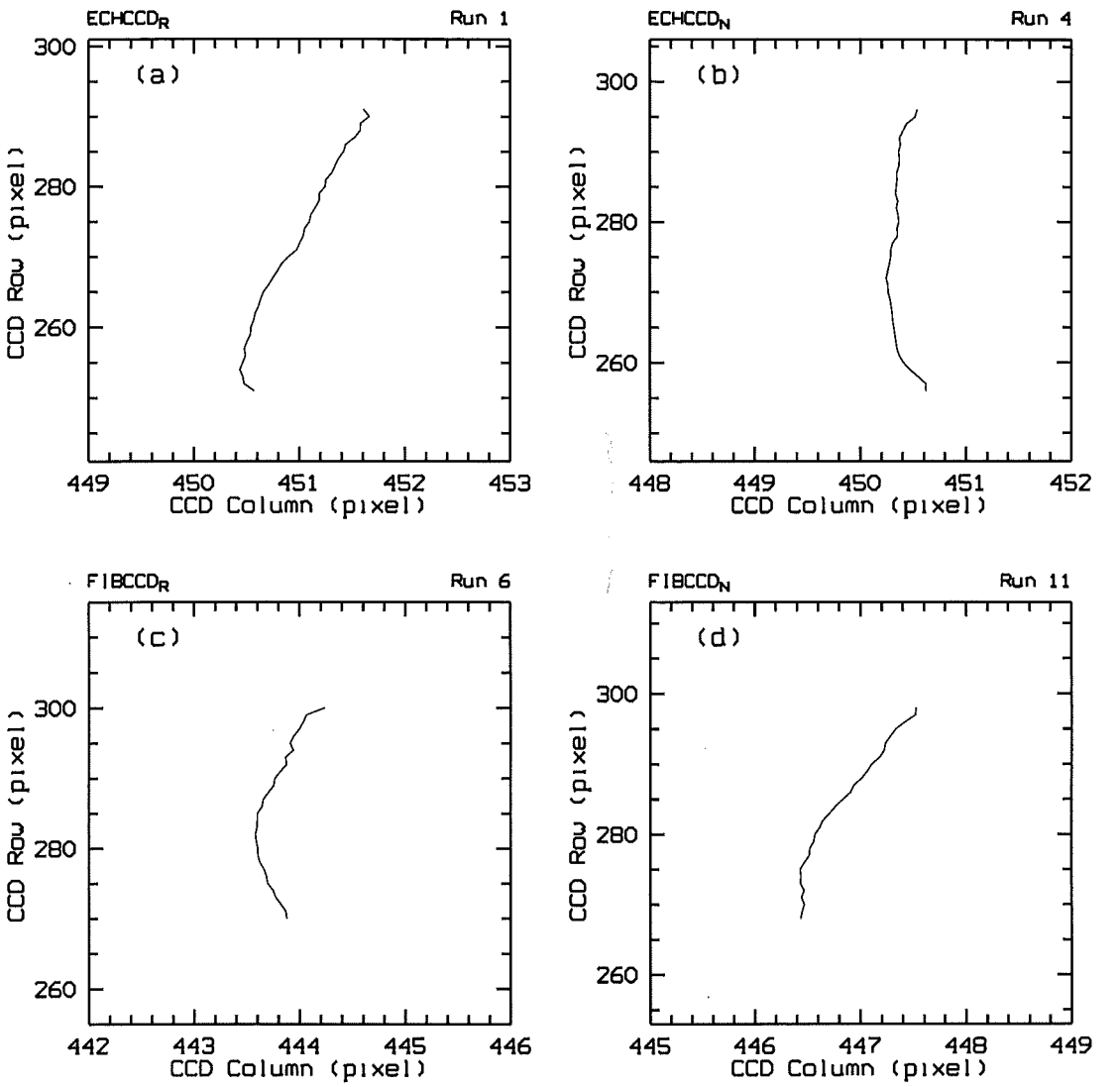

Figure 2.8: *Spectral line shapes and tilts depending on the instrument configuration. These four plots (a–d) show the same thorium line* $\lambda = 5504.3018$ Å *in order 42.*

From such a profile, a decision can be made if the CCD chip should be rotated or not, and the corresponding rotation angle can be computed.

This method is illustrated in Figure 2.8, by analysing a single thorium line, as it appears on different CCD images. The first two plots (2.8a and 2.8b) correspond to the ECHCCD configuration (without the fibre). The spectral lines appear longer (about 40 pix long), because the whole slit is illuminated when the fibre is not used. There is a difference of about 1°.7 in the CCD rotation angle between the two images, causing a different line tilt. The line is practically vertical in Figure 2.8b.

The two bottom plots (2.8c and 2.8d) involve the optical fibre (FIBCCD). The spectral lines now appear shorter (only about 30 pix long), as determined by the diameter of the fibre. There is also a notable *curvature* in the line shapes, making the process of finding the

best CCD rotation angle less effective. The curvature is especially well seen in Figure 2.8c. This was an indication that the glycerine drop at the fibre input had evaporated and had to be reinserted. The fibre was fixed at the end of this observing run and the improvement is seen in Figure 2.8d, although some curvature still remains. An interesting detail is that both the $ECHCCD_N$ (Figure 2.8b), and $FIBCCD_N$ (Figure 2.8d) settings are at the same CCD rotation angle (see Table 2.1), but the line tilts are quite different. An additional rotation of the CCD would be necessary to make the spectral lines appear more vertical when the fibre is used. However, for the sake of uniformity of the data reduction, it was decided to keep the angle as it was, using the value already derived from the ECHCCD images. The line tilt and curvature are both within one pixel, so that any fine adjustments in the tilt would not change almost anything in the extraction process.

Another point of interest concerning the extraction itself is the *optimal slit height* used in the procedure, i.e. the actual number of pixels taken above and below the central line. The échelle orders have gaussian profiles (to a first approximation), with the intensity falling down on each side of the central position. The profile can be described by its full width at the half maximum, FWHM, which is about 14 pix (FIBCCD configuration). This will be used as a unit length for the optimal slit determination.

One can expect that taking more pixels will improve the final signal-to-noise ratio. However, if this is done too far from the profile centre (perpendicular to the échelle orders), only noise will be collected (the signal must fall down to zero at some stage). So, precisely how far is it sensible to go up and down from the central pixel? In order to answer this question, a check was made to see how the extraction slit size affects both the final signal-to-noise ratio and the radial velocity dispersion. A set of solar spectra, taken sequentially over a short time interval ($\sim$ 1 hour), have been used here to determine an optimal slit size[5]. The extraction has been performed at several different slit heights, and the resulting signal-to-nose ratio, as well as the dispersion in radial velocities have been examined at each slit height. Two corresponding normalized *indices* have been constructed, both taking values from zero (at a slit of 0.6 $\times$ FWHM) to one (at the maximum). The corresponding plots are shown in Figure 2.9. The behaviour of the two indices is almost identical, demonstrating an initial steep rise, at slits less than about 1.5 $\times$ FWHM, followed by an extended plateau, and then a slow decay at slits above 2.5 $\times$ FWHM. The maximum is estimated to be at about 2.2 $\times$ FWHM. This value has been adopted as an *optimal slit* and used throughout the data reduction. In the case of a gaussian profile, the corresponding cut-off point is at about 3.5 per cent of the maximum intensity.

[5]Here 'slit' means the *extraction slit*, not the real spectrograph slit.

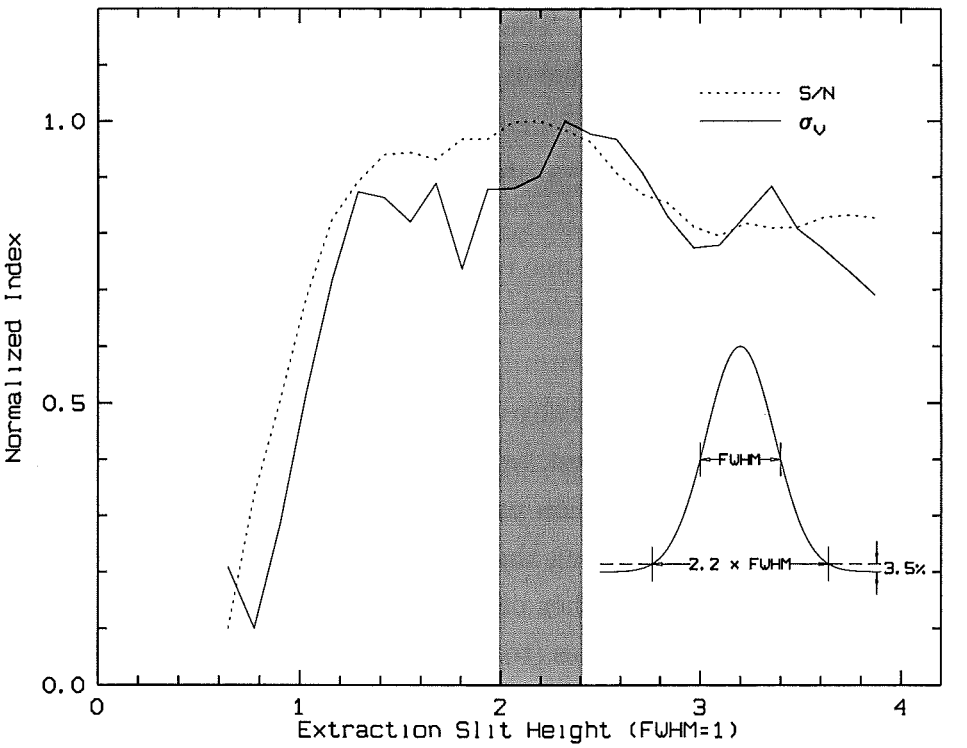

Figure 2.9: *Determination of an optimal extraction slit. Both the S/N ratio and RV scatter (σ_{V_r}) are used as suitable indices. The maximum is found at about 2.2 × FWHM (shaded region). This corresponds to a cut-off level of about 3.5 per cent, in case of a gaussian profile (inserted diagram).*

2.4.2 The wavelength calibration

The wavelength calibration is the process of finding the correspondence between the wavelengths and pixel numbers on the CCD image. It is done from a spectrum of a calibration source producing a set of known spectral lines, such as the thorium-argon lamp. The calibration spectra are taken immediately before and after the stellar exposure and these images are then used to compute the *dispersion solution*, i.e. to define the relation $x = f(\lambda)$, where x represents the pixel position and λ is the wavelength.

If one wants to measure the radial velocities with high precision, then the dispersion solutions have to be computed with high precision too. For example, an uncertainty of 100 $\mathrm{m\,s^{-1}}$ in radial velocity in order 42 corresponds to a shift of only $\Delta\lambda = 1.8$ mÅ at $\lambda = 5500$ Å ($V_r = c\,\Delta\lambda/\lambda$), which is about 0.04 pix at a typical dispersion of 23 $\mathrm{pix\,\AA^{-1}}$.

In principle, a dispersion solution for a single échelle order is computed from a set of known emission lines, using their laboratory wavelengths λ_i, taken from a suitable table, and also measuring their central pixel positions x_i from the observed spectrum. A low-order polynomial (typically a parabola) is then fitted to the points in a form $x = f(\lambda)$, so that for any given wavelength a corresponding pixel position can be computed. However, some

software packages (MIDAS in particular) insist on an inverse solution in a form $\lambda = g(x)$, providing a direct way of computing the wavelengths for given pixel positions. Although sometimes useful, this approach does not strictly treat the data points in a proper way, since the wavelength should be regarded as an *independent* variable, having a negligible uncertainty, while the pixel position is a measured (*dependent*) variable with an associated random error.

One should also keep in mind the fact that an échelle spectrum is made up of many diffraction orders. Although it is always possible to treat the individual orders as if they were completely independent spectra, this would not be a sensible choice, since there is an obvious correlation between the positions of spectral lines in different orders. It follows directly from the grating equation, $n\lambda = d(\sin\alpha + \sin\beta)$, that at any given diffraction angle β a series of wavelengths are found, having different order numbers n, but the same products $n\lambda$. After the orders have been separated by a cross-grating, the positions of spectral lines still remain the same in the direction of the dispersion. Therefore, it makes sense to look for a dispersion solution in a form $x = f(n, \lambda)$, combining all the échelle orders together.

In order to maintain the highest possible stability of the dispersion solutions in the thorium spectra, the following points have been adopted:

- Only well defined and stable spectral lines are used (i.e. ones that give reliable stable centres when measured repeatedly).
- The same set of spectral lines is always used. Numerous tests performed on the thorium spectra demonstrate that even a small change in the line selection criteria (i.e. rejecting some lines and accepting some others) can result in a different dispersion solution.
- Exactly the same portions of the spectral lines are always used to define the line centres. A gaussian profile is fitted to every spectral line, but the first and last pixels for the fit are set for each line separately, depending on other lines in the nearest neighbourhood.

For these reasons it was necessary to abandon the standard MIDAS wavelength calibration procedure, and a new one was developed, using a fixed table of carefully selected spectral lines. The selection process consists of three major steps:

1. From many thorium spectra, taken on the same observing night, the mean central intensity for each line is defined, and those lines that show unacceptable scatter from one image to another are rejected.
2. The mean central pixel position is defined for each spectral line, using the same set of images, and those lines that show unacceptable scatter are rejected.
3. The dispersion solution is computed, and those lines that deviate significantly from the fitted position (heavily blended lines) are rejected.

A result of this selection process for the FIBCCD configuration is presented in Figures 2.10 and 2.11. There are 72 preliminary lines in all six échelle orders together. It is evident from Figure 2.11a that weaker lines are more scattered in their intensities than the stronger ones. The scatter (standard deviation) has been computed from many thorium images, after the images have been rescaled to the same mean intensity. In this way, any real fluctuations in the thorium lamp brightness from one image to another have been eliminated, and only the random errors of the fitting process have remained. It is interesting how all thorium lines (black dots) follow the same general trend, with a scatter decreasing slowly, as the line strength increases. On the other hand, all argon lines (open circles) seem to exhibit a different behaviour, with a much higher scatter for the same central intensity. It is possible that the argon source is actually less stable compared to the thorium source within the same lamp.

Apart from being an interesting plot, Figure 2.11a is not used to reject any spectral lines. The central positions are used instead, as shown in Figure 2.11b. The scatter (standard deviation) has been computed from many thorium images, but any global shifts from one image to another have been eliminated first. The correlation between the scatter and the intensity is even more obvious and regular then in the previous case. All spectral lines (argon included) stronger than about 300 ADU (2.5 in logarithmic units) are extremely stable in their positions, with a standard deviation of only about *one hundredth* of a pixel. However, weaker lines demonstrate a steep increase in the scatter, up to about 0.1 pix. If one excludes the weakest lines from the wavelength calibration process, the stability of the dispersion solution will be improved, as well as the precision of the radial velocities, later in the reduction procedure.

The third plot (Figure 2.11c) demonstrates the residuals as computed from a two-dimensional parabolic fit, $x = P_{2,2}(n, \lambda)$, to the spectral lines. As a source of the thorium laboratory wavelengths, the Atlas of the Thorium Spectrum by Palmer & Engleman (1983), at eight significant digits, was used. A limited number of strong argon lines have been taken from Reader & Corliss (1980), at seven significant digits. Each point in Figure 2.11c represents a difference between the measured pixel position and the fitted pixel position. Only 50 strongest lines (full dots) have been used for the least-square fit. The r.m.s error of the fit for these 50 lines is about 0.07 pix, which corresponds to about 3 mÅ in the central parts of the spectrum (assuming a dispersion of 24 pix Å^{-1}), or about 170 m s^{-1} in the radial velocity units.

Several important points can be drawn out from a careful examination of the residuals in Figure 2.11c:

1. The scatter is not random at all. Each point in the plot will *keep its position* relative to the zero line, as one goes from one thorium image to another. Thousands of thorium spectra, taken over years, demonstrate always the same distribution of the residuals as

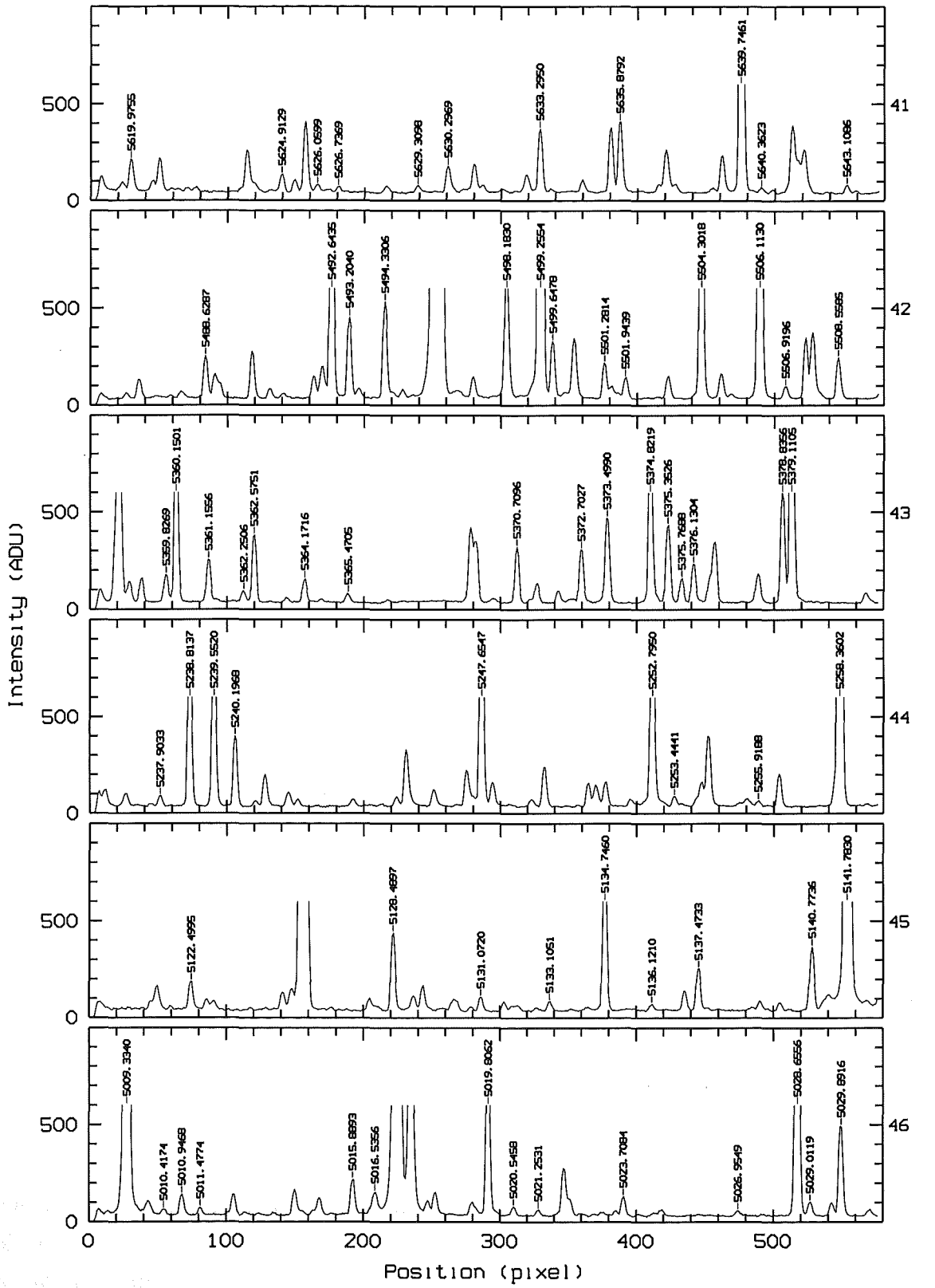

Figure 2.10: *Th-Ar spectrum (FIBCCD) used for the wavelength calibration. The order numbers (41–46) increase from top to bottom. The wavelengths (Å) are shown for 72 lines involved in the selection process described in the text.*

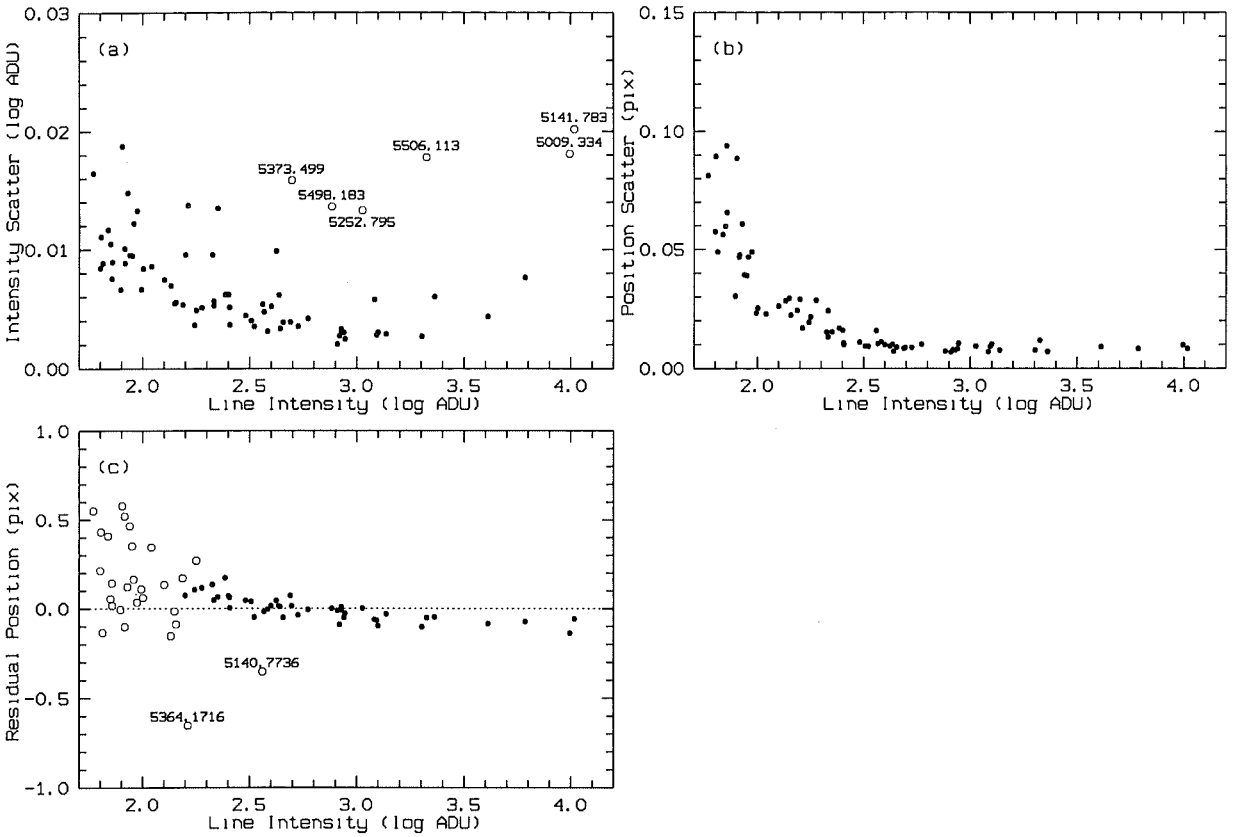

Figure 2.11: *Some properties of spectral lines selected for the wavelength calibration: (a) intensity scatter for thorium (black dots) and argon (open circles), (b) position scatter, and (c) residual positions. Only spectral lines represented as black dots in (c) are actually used for wavelength calibration.*

shown in Figure 2.11c. Of course, there are some random fluctuations in line positions, but they are much less (typically by a factor of ten for strong lines). It has just been demonstrated (see Figure 2.11b) that the strongest lines show a random scatter in the position of only about 0.01 pix. The residuals, on the other hand, are of the order of 0.1 pix and more. One can conclude that the residuals are not a result of the measurement errors. They can be caused by some uncertainties in the laboratory wavelengths, or by the fact that the spectral lines are blended.

2. The fact that the residuals are not random implies another important conclusion, namely that the r.m.s. error of the dispersion solution (as derived from the least-square fit) *does not* contribute in that amount to the total uncertainty of the radial velocity measurements. The actual contribution is much less and it is determined by the uncertainties in the line positions (Figure 2.11b), rather than by the residuals themselves.

3. A surprising result is also an evident *systematic trend* of the residuals depending on

the intensities of spectral lines: the weaker the line, the larger the residual. While the strongest lines remain below the fit at about −0.1 pix, the weakest lines seem to prefer the positive values of up to +0.5 pix or so. The scatter amongst the weakest lines is much bigger, most certainly due to their increased sensitivity to the blending effects. The correlation between the residuals and the line intensities means that a different line selection necessarily leads to a different dispersion solution. A change of only 0.1 pix in the fit, caused by the inclusion or exclusion of some weak spectral lines, will produce a velocity shift of about 240 $\mathrm{m\,s^{-1}}$. This is another strong reason why one should always use exactly the same set of spectral lines for the wavelength calibration.

While the first two points listed above are easy to understand, the third one is somewhat more puzzling and certainly not expected. It should be emphasized here that the effect is seen *only* in the FIBCCD and ECHCCD images using the PM3000 CCD system (Thomson chip). This result will be discussed in more detail later (see Section 2.6). It seems that the systematic trend in the residuals (Figure 2.11c) is neither a property of the thorium spectrum nor a result of a bad data reduction. Its origins can be traced deeper into the data acquisition process, and perhaps connected to the charge-transfer problems during the read-out cycle of the chip itself. At this stage, the result can be simply used to improve the reduction procedure.

To conclude this discussion on the wavelength calibration, a test of stability of the dispersion solution is presented in Figure 2.12 for two typical observing nights. The radial velocity of β Hydri (a bright programme star) has been computed using many thorium spectra taken during the same night. If the thorium spectra had all been projected exactly at the same

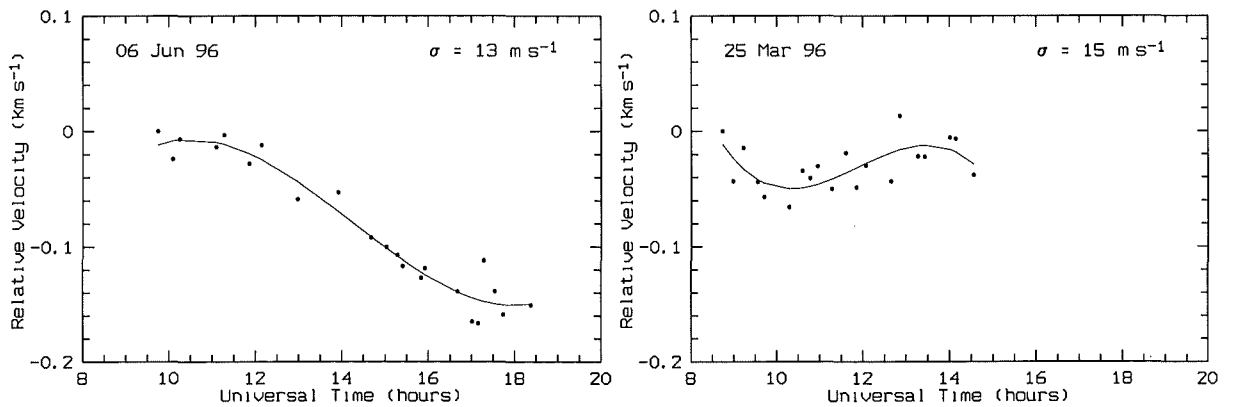

Figure 2.12: *Two examples illustrating the stability of the dispersion solution. The dots represent the radial velocity of the same stellar image, when combined with different thorium images during the same observing night. The zero point of the relative velocity scale is set to the first thorium image. The r.m.s. error of the polynomial fit (σ) is a measure of the uncertainty of the wavelength calibration.*

position on the CCD image, the radial velocities would have been identical, and the two plots in Figure 2.12 would have appeared as horizontal lines. However, the thorium spectra drift slowly during the night, mainly due to the changes in the atmospheric pressure and temperature. This is especially well seen in the first plot (June 6^{th}). Some other observing nights (such as March 25^{th}, in the second plot) are obviously less unstable. This global thorium drift does not normally affect the radial velocity measurements, since two thorium exposures are always taken, before and after the stellar image. However, it is evident from Figure 2.12 that there are random deviations from the smooth drift, and these deviations directly affect the uncertainty of the radial velocity measurements. The standard deviations shown in Figure 2.12 are the r.m.s. errors of the polynomial fits to the data points. They show a typical value of about $(10 - 15)\ \mathrm{m\,s^{-1}}$ and this is the lower limit to the precision of the radial velocities.

It would also be interesting to compare these results with a recent paper by De Cuyper & Hensberge (1998) dealing with the blending effects between close components of the thorium spectral lines, and introducing a list of *adjusted wavelengths* to be used for the wavelength calibration purposes. With a dispersion of about 24 $\mathrm{pix\,\AA^{-1}}$ at $\lambda = 5300$ Å, the FIBCCD images have an R-factor[6] of about 130 000. If the adjusted wavelengths at an R-factor of 100 000 are taken from Table 6 of De Cuyper & Hensberge, one will end up with only 32 lines in the present wavelength region (instead of 50 that are normally found). Of those 32 lines, only 10 have their adjusted wavelengths different from their standard values, and the differences are all *less* than 1 mÅ. The r.m.s. error of the dispersion solution, when these 32 lines are used, is about 0.06 pix, not very much different from the usual value of 0.07 pix. Finally, the stellar radial velocities stay almost unchanged when the new set of thorium lines is used (the differences are typically less than $10\ \mathrm{m\,s^{-1}}$). For these reasons, as well as the fact that adopting a new list of wavelengths would mean a complete re-reduction of the data, it was decided to keep the line tables unchanged.

2.4.3 Synthetic spectra and the cross-correlation process

The stellar radial velocities[7] are measured from the *Doppler shift* in their spectra, using the well known formula:

$$V_{\mathrm{r}} = \frac{\Delta\lambda}{\lambda}\, c, \tag{2.1}$$

where V_{r} is the radial velocity, λ is the laboratory wavelength, $\Delta\lambda = \lambda' - \lambda$ is the difference between the measured and laboratory wavelengths, and c is the speed of light. However, any result obtained from (2.1) includes many different effects, not only the space motion

[6]The R-factor is defined by De Cuyper & Hensberge as a ratio between the wavelength (measured in Å) and the pixel-scale (measured in $\mathrm{Å\,pix^{-1}}$). This is not the same as the *resolving power*, which is defined as $R = \lambda/\Delta\lambda$.

[7]The radial velocity is the projection of the three-dimensional space velocity vector onto the line of sight.

of the star's centre. First of all, the radial velocity is always measured relative to the observer, therefore it includes the Earth's motion. Second, there are some effects in the stellar atmosphere, such as the *gravitational red shift* and the *convectional blue shift*, that are indistinguishable from the motion of the star as a whole, when measuring the Doppler shift $\Delta\lambda$. More comments on these effects will be made when the radial velocities are presented, later in this chapter.

There are various possibilities of obtaining the shift $\Delta\lambda$. In principle, it is possible to take one single line from the spectrum and calculate the radial velocity from its measured position alone, but the precision of such a result would not be very high. A much better result can be obtained by averaging the velocities obtained from many different individual lines. However, it turns out that one can find very few spectral lines suitable for this purpose due to blending effects.

In this thesis, the *cross-correlation* technique is used to derive the radial velocity. The stellar spectrum is cross-correlated with a *synthetic spectrum* of a similar spectral type and the velocity is derived from the position of the cross-correlation peak. In this way the whole spectrum is used and there is no need to measure the positions of any individual spectral lines. The total precision of radial-velocity determinations by cross-correlation depends on many factors, but this subject will not be discussed in this thesis (see e.g. Murdoch & Hearnshaw 1991a for more details). The final uncertainties obtained empirically are presented in Section 2.8.

The synthetic spectra have been computed especially for this project by Robert L. Kurucz, at the Harvard-Smithsonian Center for Astrophysics (Kurucz 1996). There are seven different models, as listed in Table 2.6. They have been computed for the standard solar metallicity, zero turbulence, and no rotation. All model names are given in a form "f*tt gg*", where the first letter "f" has no special meaning, *tt* are the first two digits of the stellar effective temperature, and *gg* are another two digits representing the surface gravity[8]. For example, a model at $T_{\rm eff} = 4500$ K, and $\log g = 2.5$, is named as "f4525". The only exception from this is the *solar model*, which is simply "fsun".

Using the basic parameters ($T_{\rm eff}$, $\log g$) from Table 2.6, the spectral types and absolute magnitudes (the last two columns) have been derived, by interpolating the data from Allen (1991). The corresponding positions of the models in the H-R diagram are shown in Figure 2.13. The models are distributed relatively evenly over the area covered by the late-type stars, from the main-sequence dwarfs (luminosity class V) to the yellow and red giants (luminosity classes II and III). This is also the part of the H-R diagram where most of the

[8]The stellar surface gravity g is the acceleration of the gravitational force at the stellar surface, $g = G\mathfrak{M}/R^2$, where G is the gravitational constant, $\mathfrak{M}$ is the mass of the star, and R is the radius. In the case of the Sun ($\mathfrak{M}_\odot = 1.989 \times 10^{30}$ kg, $R_\odot = 6.96 \times 10^8$ m), and with $G = 6.672 \times 10^{-11}$ m^3 kg^{-1} s^{-2}, one obtains $g_\odot = 274$ m s^{-2}. Usually the logarithm of the surface gravity ($\log g$) is used, in which case the surface gravity must be expressed in cm s^{-2}. For example, $\log g_\odot = \log 27400 = 4.44$.

Table 2.6: *Basic parameters of the stellar models used in this thesis.*

		Defining Parameters		*Derived Parameters*	
Model Number	Model Name	Effective Temperature $T_{\rm eff}$ (K)	Surface Gravity $\log g$	Spectral Type	Absolute Magnitude
1	f7545	7500	4.5	F0V	+3.0
2	f6535	6500	3.5	F3III	+1.3
3	f5525	5500	2.5	G1II	−1.4
4	fsun	5770	4.4	G2V	+4.8
5	f5045	5000	4.5	G9V	+5.8
6	f4525	4500	2.5	K0III	+0.1
7	f3520	3500	2.0	K8III	+0.8

programme stars are situated. For every programme star a suitable model can be selected, which is not far from the star itself in the H-R diagram.

As one might expect, the models do not match the observed spectra exactly. The actual level of agreement between the synthetic spectra and the observed stellar spectra is demonstrated in Figures 2.14 and 2.15. In general, the models are quite good for F and early G spectral types, but not quite adequate for K and M stars. The absence of the molecular lines in the late-type synthetic spectra makes the situation even worse, especially for M stars. However, the great majority of the atomic lines are included, so that a reliable cross-correlation process and final radial velocities can be obtained.

An interesting question regarding the stellar synthetic spectra is *how critical* (in terms of the final radial velocity) the actual choice of the model is for a particular star. In order to find an answer to this question a simple test was made, by using several different models to determine the radial velocity of the same stellar image. The result is shown in Figure 2.16. The differences between the models are less than 100 $\mathrm{m\,s^{-1}}$ for similar spectral types, but can be up to $(200 - 300)$ $\mathrm{m\,s^{-1}}$ if the spectral types are very much different.

The synthetic spectra cover a fixed wavelength range between $\lambda_{\rm start} = 5000$ Å and $\lambda_{\rm end} = 5651$ Å divided into 61197 bins. The actual scale is logarithmic, so that the wavelength at any particular bin ($1 \leq m \leq 61197$) is given by: $\lambda_m = q_0\,\lambda_{m-1}$, where $q_0 = 1 + 2 \times 10^{-6}$ is the step factor. Since q_0 is very close to one, the wavelength scale is almost linear, with a step of $\Delta\lambda_{\rm start} = 10.0$ mÅ at the beginning and $\Delta\lambda_{\rm end} = 11.3$ mÅ at the end of the spectral range.

A closer examination of the synthetic spectra reveals an interesting detail concerning the average precision of the laboratory wavelengths. Every spectral line appears to be centred *exactly on a bin*, as demonstrated in Figure 2.17. This is probably a consequence

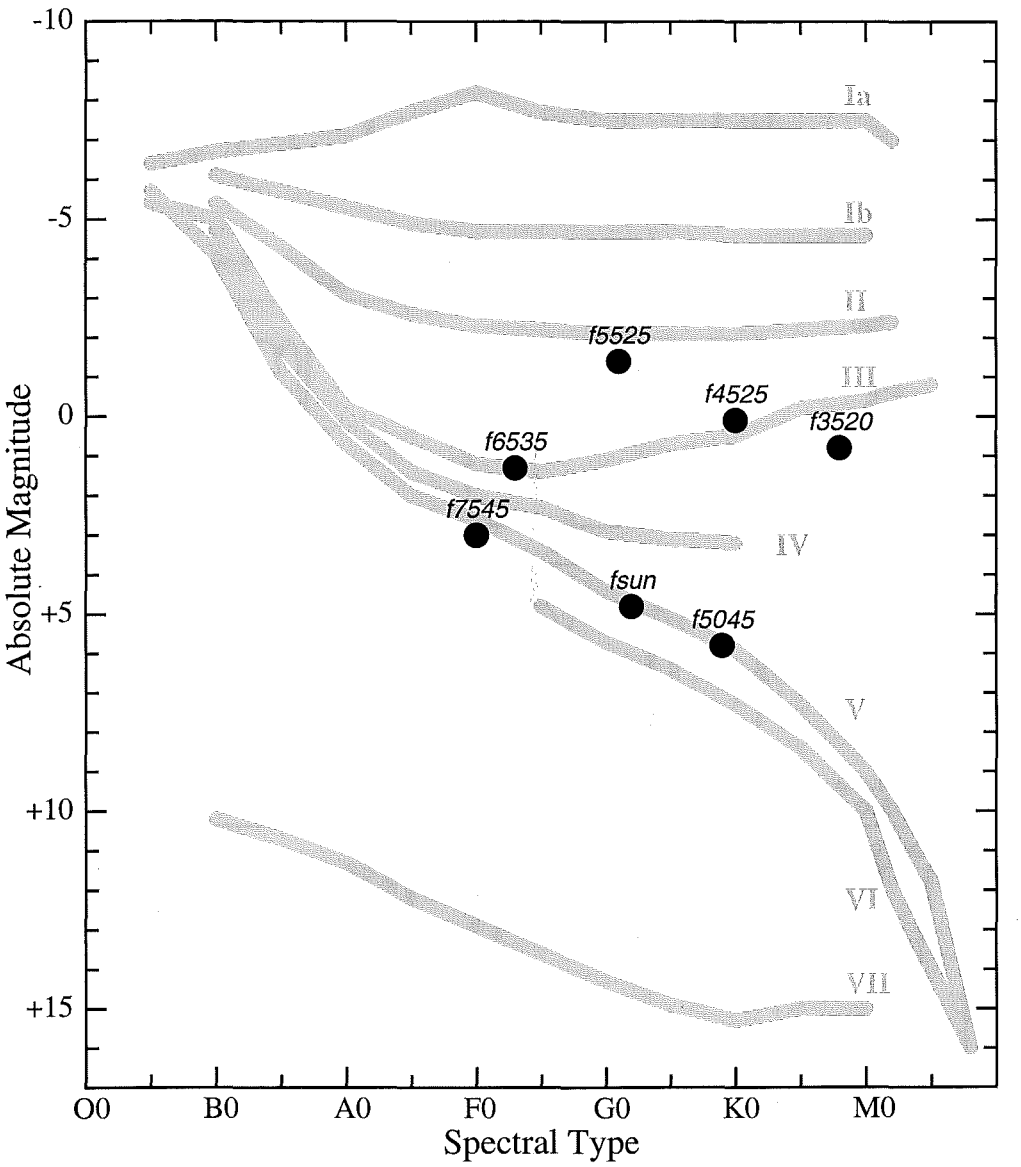

Figure 2.13: *The stellar models used in this thesis, as they appear in the H-R diagram. The spectral types and absolute magnitudes have been computed from the effective temperatures and surface gravities (see Table 2.6).*

of a particular algorithm increasing the speed of the model synthesis. As a result, the wavelengths are rounded to the nearest hundredth of an angstrom (the bin size), which is about 600 $\mathrm{m\,s^{-1}}$ in velocity units. This is not a serious problem, since there are always many lines involved in the reduction process. On average, one can expect that there will be no significant systematic error in radial velocities due to the rounding effect of the synthetic line positions.

The original bin size in the synthetic spectra of about 0.01 Å is too small compared to the actual pixel size on the CCD images ($\sim$ 0.04 Å). In order to keep the same pixel size throughout the reduction procedure the synthetic spectra have been rebinned by combining

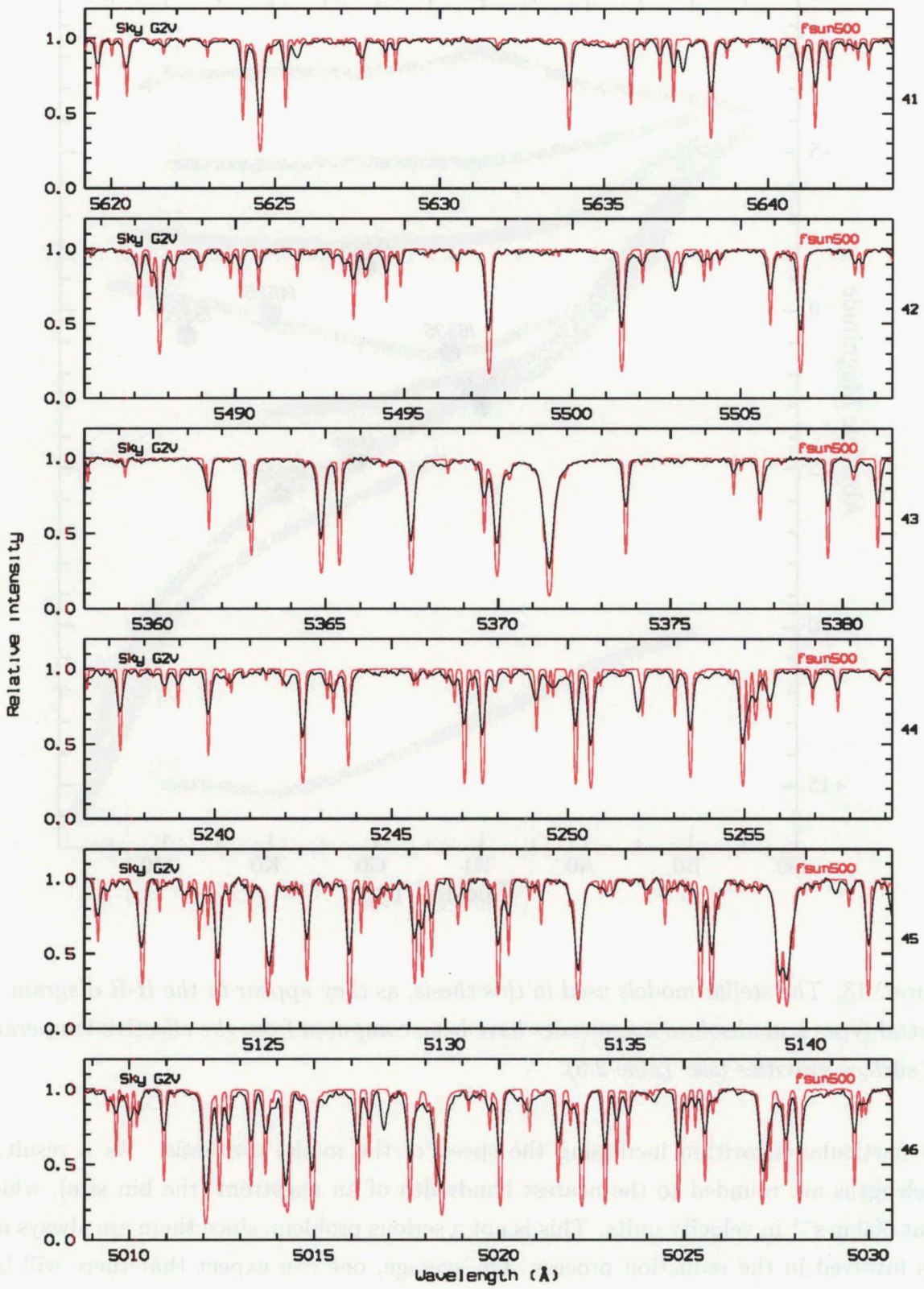

Figure 2.14: *Comparison between the observed solar spectrum (black) and the corresponding synthetic spectrum 'fsun' (red).*

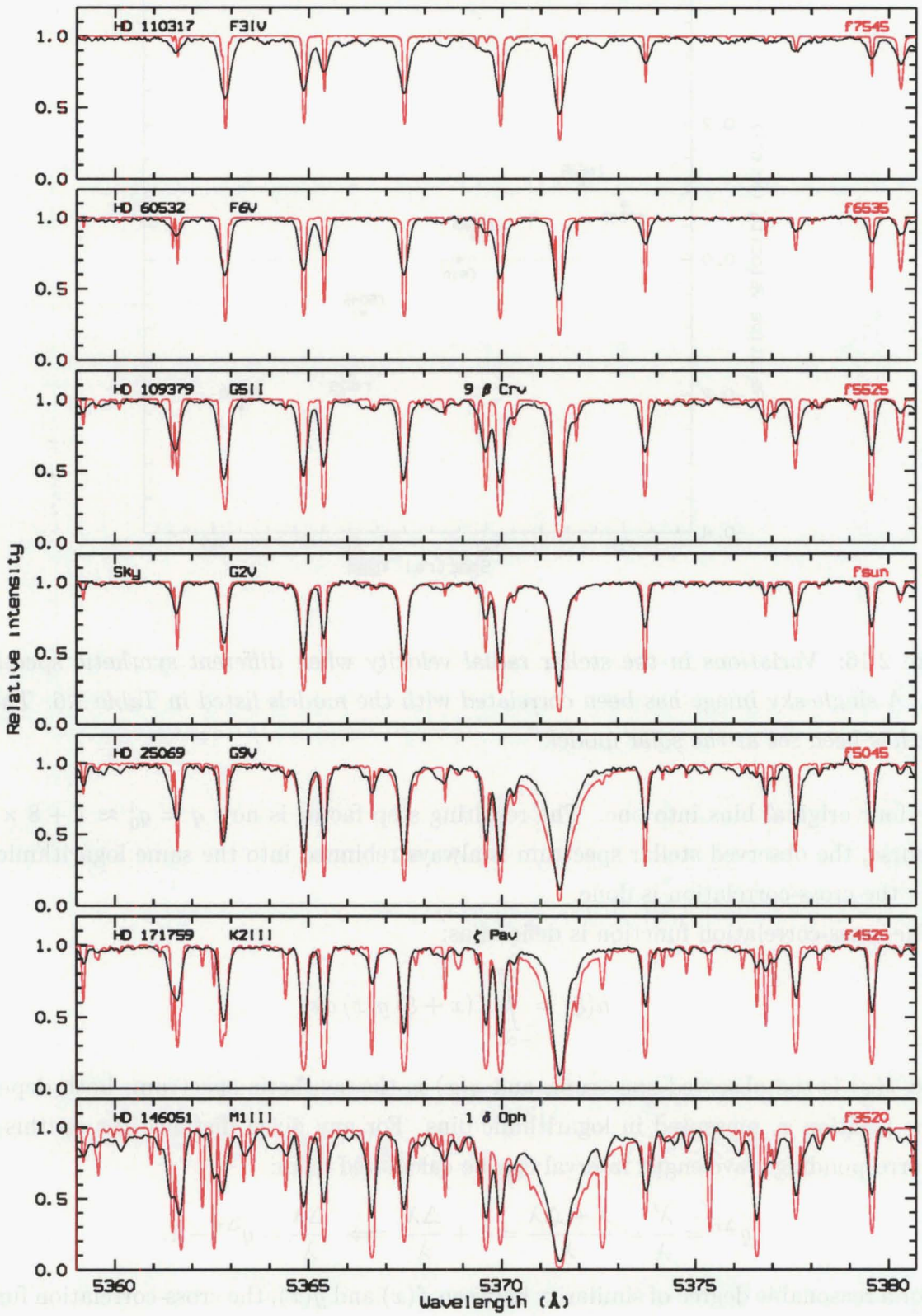

Figure 2.15: *Comparison between the observed stellar spectra (black) and the corresponding synthetic spectra (red). Only order 43 is shown.*

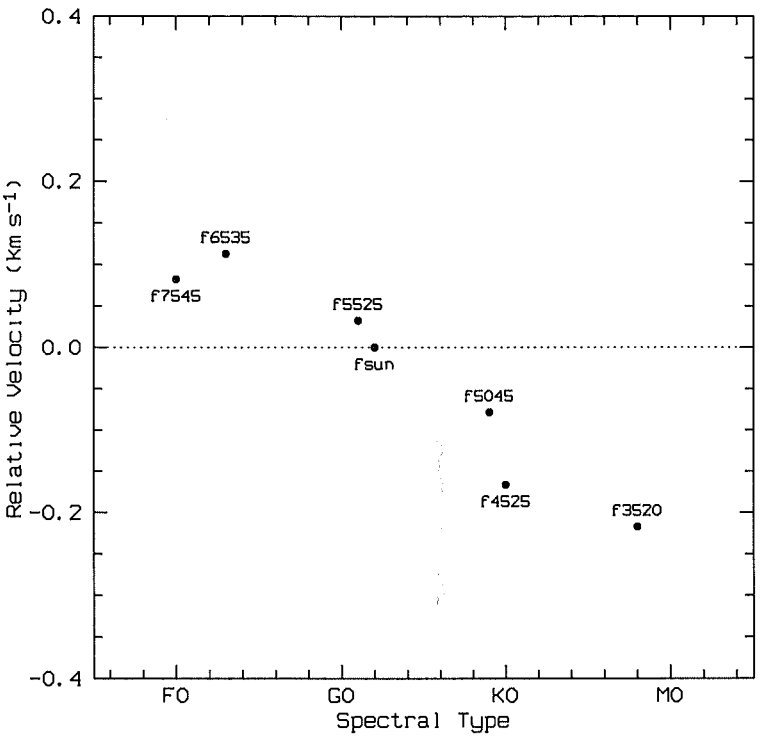

Figure 2.16: *Variations in the stellar radial velocity when different synthetic spectra are used. A single sky image has been correlated with the models listed in Table 2.6. The zero point has been set at the solar model.*

every four original bins into one. The resulting step factor is now $q = q_0^4 \approx 1 + 8 \times 10^{-6}$. Of course, the observed stellar spectrum is always rebinned into the same logarithmic scale before the cross-correlation is done.

The cross-correlation function is defined as:

$$h(\xi) = \int_{-\infty}^{\infty} f(x+\xi)\, g(x)\, dx, \tag{2.2}$$

where $f(x)$ is the observed spectrum, and $g(x)$ is the synthetic spectrum, both depending on the position x, measured in logarithmic bins. For any given distance Δx on this scale, the corresponding wavelength interval can be calculated from:

$$q^{\Delta x} = \frac{\lambda'}{\lambda} = \frac{\lambda + \Delta\lambda}{\lambda} = 1 + \frac{\Delta\lambda}{\lambda} \implies \frac{\Delta\lambda}{\lambda} = q^{\Delta x} - 1. \tag{2.3}$$

For a reasonable degree of similarity between $f(x)$ and $g(x)$, the cross-correlation function $h(\xi)$ will have a well defined peak at $\xi_{\max}$ equal to the *actual shift* between the two spectra. Using the previous result (2.3), the radial velocity is then simply:

$$V_r = c\,(q^{\xi_{\max}} - 1). \tag{2.4}$$

The cross-correlation function is computed using the fast Fourier transform (Press et al.

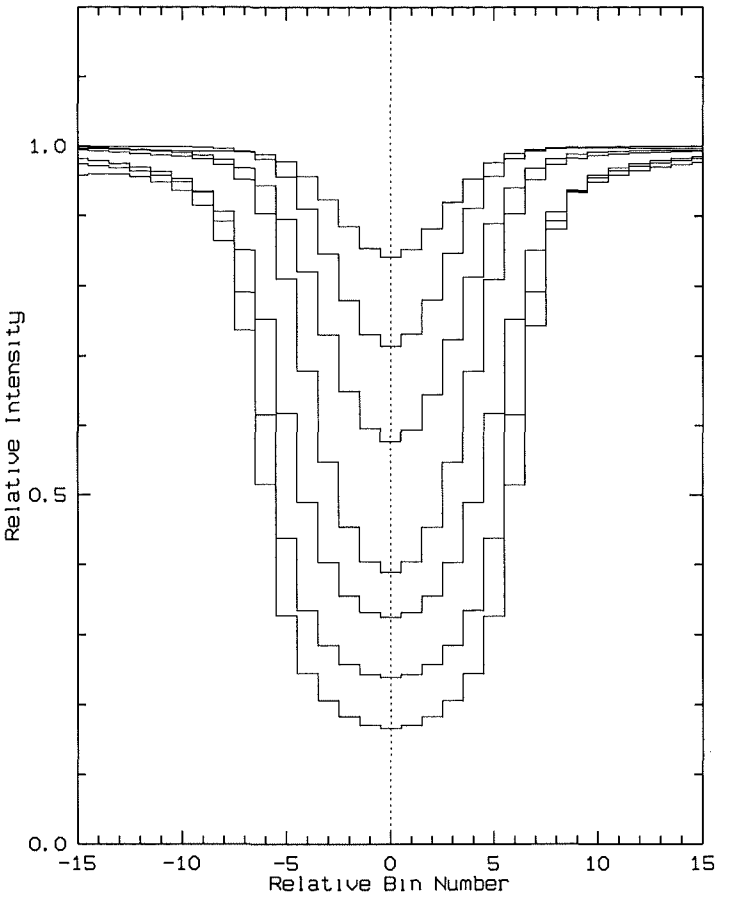

Figure 2.17: *Several different spectral lines from all over the synthetic spectrum, illustrating the rounding of the central wavelengths to the nearest bin. The line centres are used as common zero points.*

1994). Before the actual computation, both the synthetic and observed stellar spectra are prepared in the following way (Brault & White 1971; Simkin 1974):

1. The *arithmetic mean* of all pixels is computed and the mean value is subtracted from the original spectrum, so that the resulting spectrum has a zero mean.

2. A *cosine bell* window is applied to the spectrum, so that the intensity gradually falls towards zero at the edges. Only 10 per cent of the pixels are affected by this procedure at each end.

These two reduction steps are schematically presented in Figure 2.18. The final cross-correlation functions are shown in Figure 2.19. A gaussian is fitted to the central part of a cross-correlation profile. The actual cut-off level is determined for each échelle order separately, at a point where the profile starts departing from a gaussian shape. This will not affect the final precision of the radial velocities, as long as the cut-off levels are kept exactly the same in all measurements.

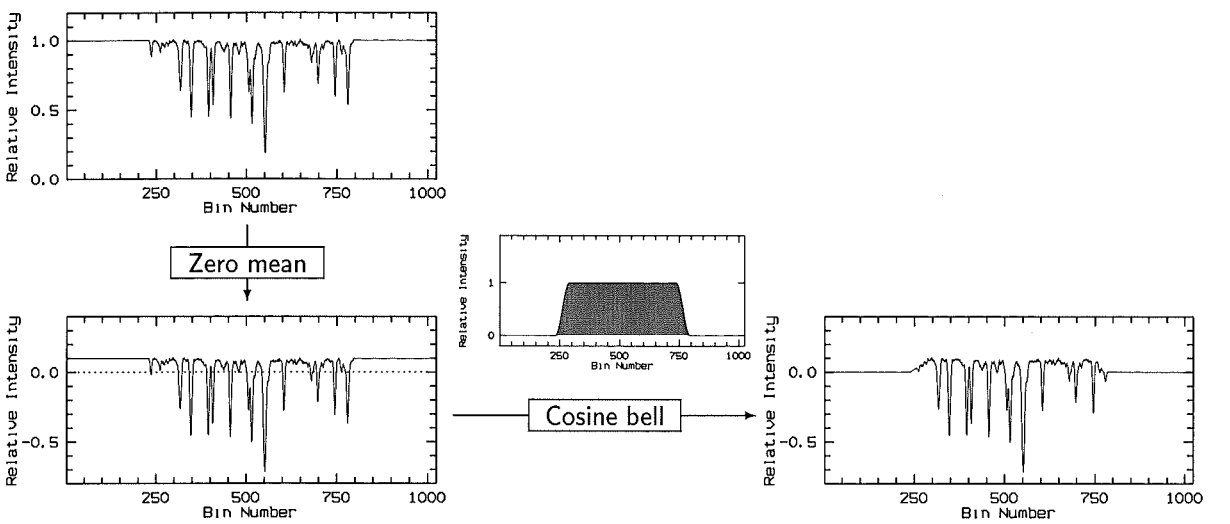

Figure 2.18: *Preparing a spectrum for the cross-correlation. The image has already been rebinned into a logarithmic scale. The mean pixel value is subtracted from the image and the result is then multiplied by a cosine bell function.*

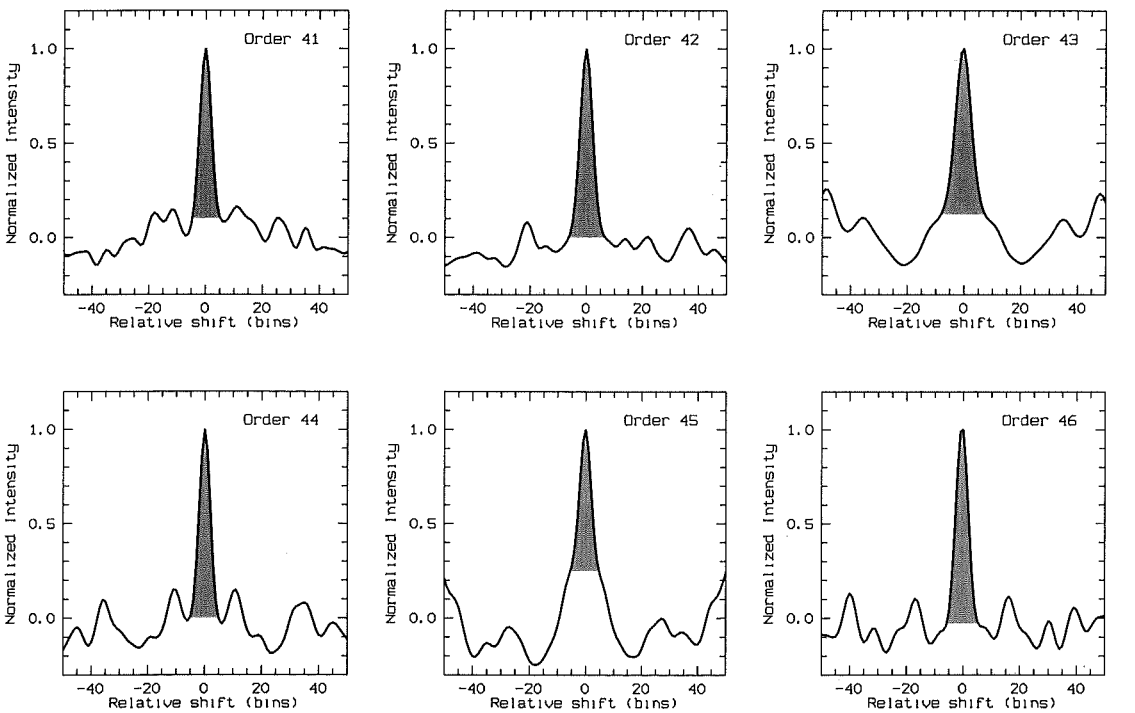

Figure 2.19: *Typical cross-correlation peaks for each of the six échelle orders. Only the shaded central portions of the profiles are used for the radial-velocity determinations. The cut-off intensity is fixed at a level where the observed profile departs from a regular gaussian shape.*

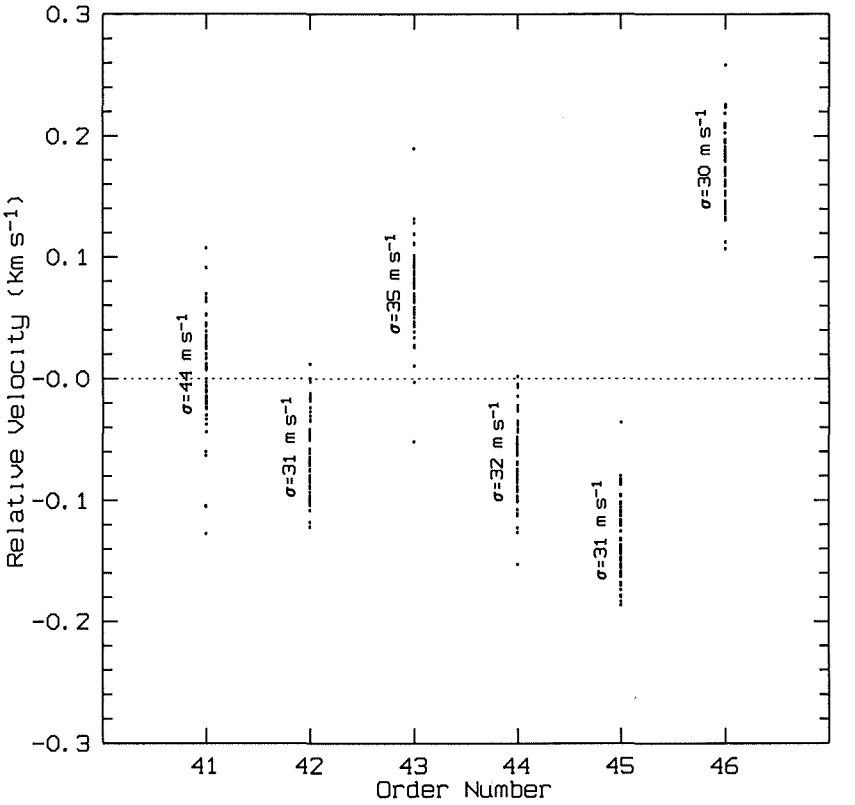

Figure 2.20: *Systematic radial velocity differences between the échelle orders. The zero point of the relative velocity scale corresponds to the arithmetic mean of all six orders. The standard deviation (σ) is given for each order.*

There is a systematic difference between the radial velocities derived from different échelle orders. In order to illustrate this, many observations of β Hydri (spectral type G2IV, synthetic spectrum *fsun*) have been combined and are presented in Figure 2.20. Any global variation in the radial velocity has been eliminated from each observation by subtracting the mean value from all six échelle orders. There are small random fluctuations within each order, typically around $\sigma \sim (30 - 40)$ m s^{-1}, but the systematic shifts can be larger, up to $(200 - 300)$ m s^{-1} between some orders. This is probably caused by systematic differences between the synthetic and observed spectra in different orders.

2.5 Radial velocities and photon counts

The reduction procedure described in Section 2.4 should ideally lead to a radial velocity affected only by some random measurement errors, and a possible systematic error, that would shift all values by the same fixed amount with respect to the standard system. However, a surprising effect has been discovered during the data analysis in the case of the PM3000 CCD camera. It turns out that the measured radial velocities depend strongly on the actual *signal*

levels both in the stellar and thorium spectra! For example, if several thorium spectra of different intensities (different exposure times) are used to reduce the same stellar spectrum, a set of different velocities will be obtained, following always the same regular pattern: the stronger the thorium spectrum, the larger the velocity. It seems that the additional photons tend to move the thorium spectrum to the left, producing an unwanted *blue shift*. In a similar way, if several stellar spectra of different signal levels are reduced using the same thorium image, the radial velocity will again differ, depending on the signal level, this time demonstrating an opposite behaviour: the stronger the stellar spectrum, the less the velocity. This, again, means that the additional photons tend to produce a *blue shift*, but this time in the stellar spectrum. However, one should be more careful at this stage, and allow another possibility, namely that it might be the *photon deficiency* in the lower-signal spectra tending to produce an unwanted *red shift* instead. More comments on these two alternatives will be given in Section 2.6.

The problem can be approached from two different directions. First, one could concentrate only on developing a method to correct the velocities by simply using the data set available, and not get deeper into the possible causes. Alternatively, one could investigate the camera (and spectrograph) in more detail, in order to find the cause for such a behaviour, and possibly introduce a new data reduction step that should be performed on raw 2-D images at an early stage. This, of course, would mean a complete re-reduction of the data. Therefore, the first option has been chosen, i.e. to eliminate the apparent correlation between the measured velocities and the signal levels using the measurements alone. Nevertheless, some additional tests have been performed on the PM3000 CCD camera during an extra observing run (run 28, May 1998) in order to get at least some explanation of why all this is happening (see Section 2.6).

2.5.1 Problem of thorium intensities

In this section the correlation between the measured radial velocities and the thorium signal levels will be analysed. First of all, it is worth pointing out the reason why the thorium signal levels vary at all. This is certainly an interesting question, especially if one keeps in mind the fact that a great majority of the thorium spectra have been collected using always the same 180-second exposure. Therefore, one would only expect some small random variations in the recorded intensities. However, the reality is quite different, as presented in Figure 2.21.

There is an obvious jump in the average thorium intensity from one observing run to another. Within a single run, the fluctuations are smaller, and mostly random. What happens between the runs is the slow evaporation of the glycerine drop at the fibre tip (see Section 2.2.1), significantly affecting the way in which the spectrograph slit is illuminated. There are also some slight differences in the actual position of the fibre output on the slit. A

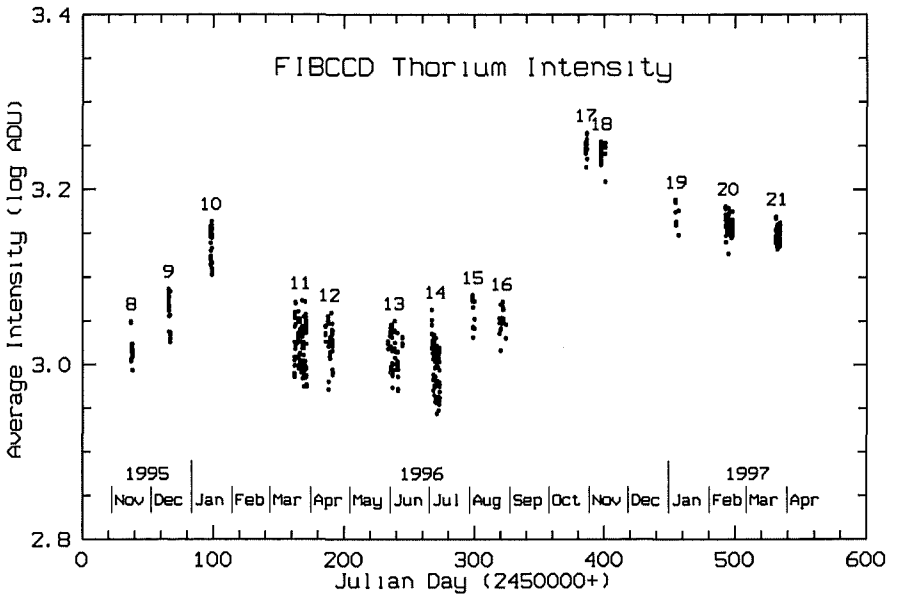

Figure 2.21: *Average thorium intensities (FIBCCD configuration only) over a longer period of time. Only the 180-second exposures are shown. Each group of points is labelled with the corresponding observing run number.*

major jump in the thorium intensity occurs after a regular maintenance of the optical fibre (about once a year).

The 180-second thorium exposures have been used for almost all of the stars in this observing programme. Only one star from the list, β Hydri, has been observed using 120-second thorium exposures, in order to keep a homogeneity with some other MJUO observers, who have observed the same star as part of a different observing programme. There are also a few 60-second and 240-second thorium exposures, mainly to accompany the blue sky (solar) spectra. As a result, there is a range of thorium intensities, sufficient enough to investigate their influence on the stellar velocities.

As an example, three sets of data points are shown in Figure 2.22, each set representing the radial velocities of β Hydri, taken on three different nights, using several different thorium images and only one stellar image. The average thorium intensity is defined here as an arithmetic mean of the central intensities of all spectral lines used for the dispersion solution. There is an obvious correlation between the radial velocity and the thorium intensity, with a slope practically the same in all data sets. At this stage it is not important that the three lines show different offsets. This can be either due to the fact that the star had really got different radial velocities on those days or due to some other systematic effect. In any case, the data sets can be simply shifted vertically relative to each other, until the data points show the smallest possible scatter around a common straight line. This straight line can then be regarded as a transformation law to subsequently correct all stellar radial velocities by bringing them to a same standard thorium intensity.

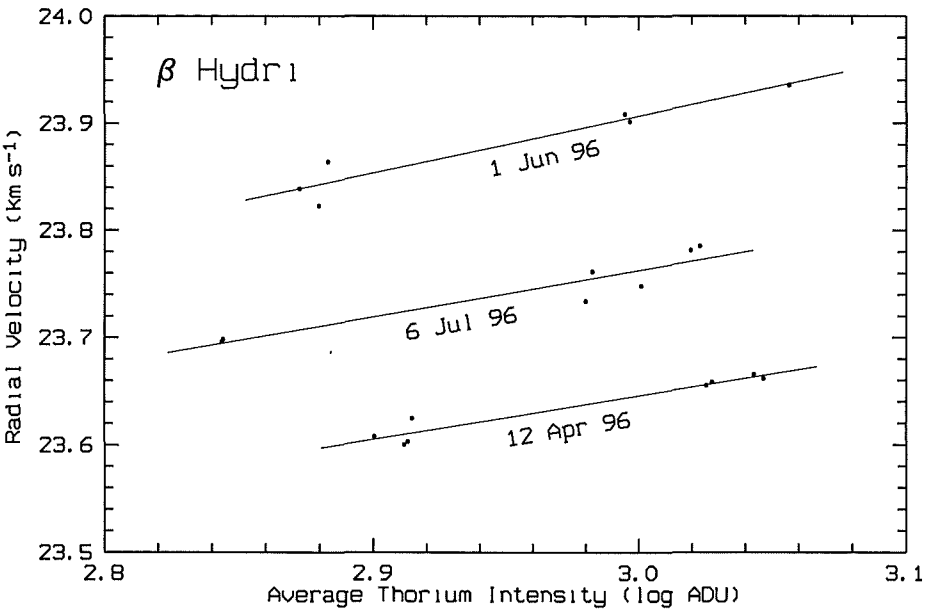

Figure 2.22: *Radial velocity of β Hydri depending on the average thorium intensity.*

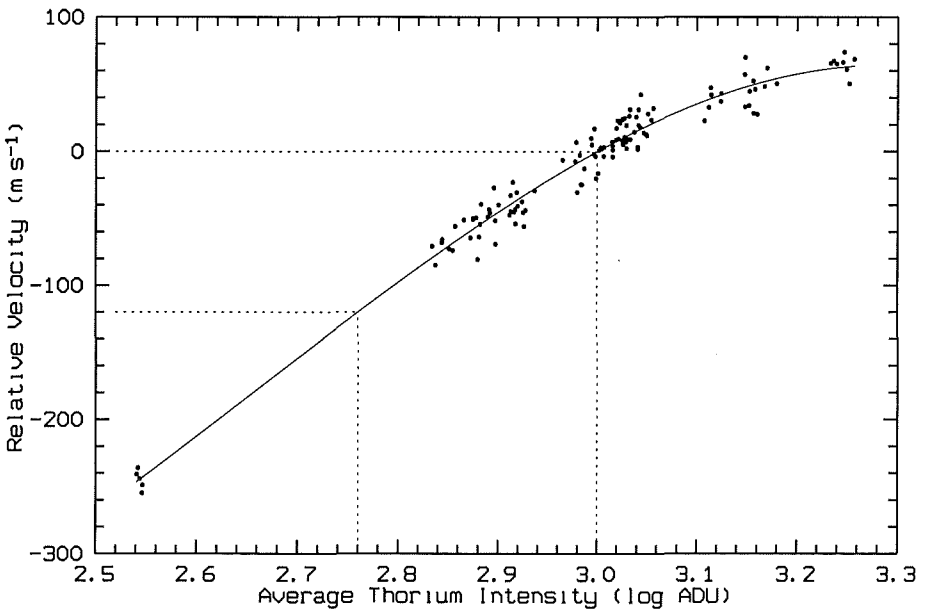

Figure 2.23: *Radial velocity shift produced by the thorium spectrum for different signal levels. The relative velocity scale has been centred at* 10^3 *ADU.*

Apart from the three examples shown in Figure 2.22, many other velocity determinations have actually been used, involving both β Hydri and the blue sky spectra, covering a longer period of time (nine runs over twelve months), as shown in Figure 2.23. The data points have been shifted in a vertical direction in order to get the smallest possible scatter around a common parabolic line (a straight-line model is obviously not good any more, having now a wider range in thorium intensities). The relative velocity scale has been centred arbitrarily

at 10^3 ADU, which is simply a choice for the standard thorium intensity. Figure 2.23 will be used to adjust the measured radial velocities, by adding an appropriate correction, depending on the actual thorium intensity. For example, if a thorium spectrum of only 580 ADU ($\log 580 = 2.76$) is obtained, a correction of $+120\ \mathrm{m\,s^{-1}}$ should be added to compensate for the difference between 580 and 1000 ADU. As a result of this procedure, all radial velocities will be brought to a level where they would normally be if all the thorium spectra were at 10^3 ADU. The procedure does not have anything to do with the stellar spectrum itself, so it will be the same for all spectral classes.

An arbitrary choice of 1000 ADU for the standard thorium intensity could mean that the radial velocities will all have an unknown systematic error, since a different intensity level would change the results. Although this is true, one does not have to worry about it at this stage, since there is still another effect to be taken into account, namely the remaining correlation between the radial velocity and an average signal in the stellar continuum.

2.5.2 Problem of stellar intensities

As has been pointed out earlier, all observations also demonstrate a correlation between the observed velocities and the photon counts in the stellar continuum. This time, the photon counts depend very much on the weather conditions, atmosphere transparency and seeing, all combined with the exposure times and guiding accuracy. The resulting range in signal levels for a single star turns out to be much wider than in the case of the thorium spectra. The 'signal level' is defined here as an average ADU count in the continuum for the whole

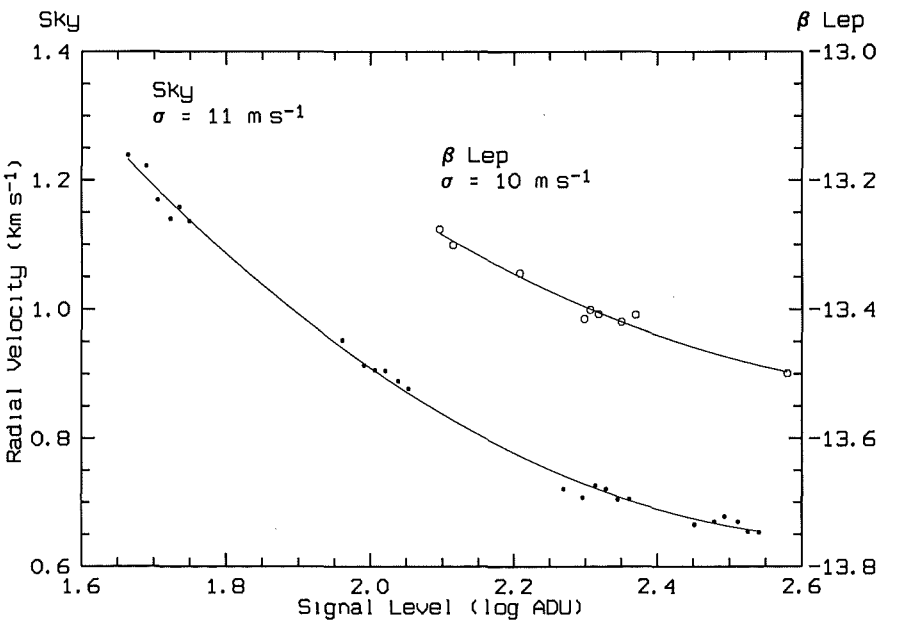

Figure 2.24: *Radial velocities of the Sun (blue sky) and β Leporis depending on the signal level in the continuum for a small range of observations during one or two days.*

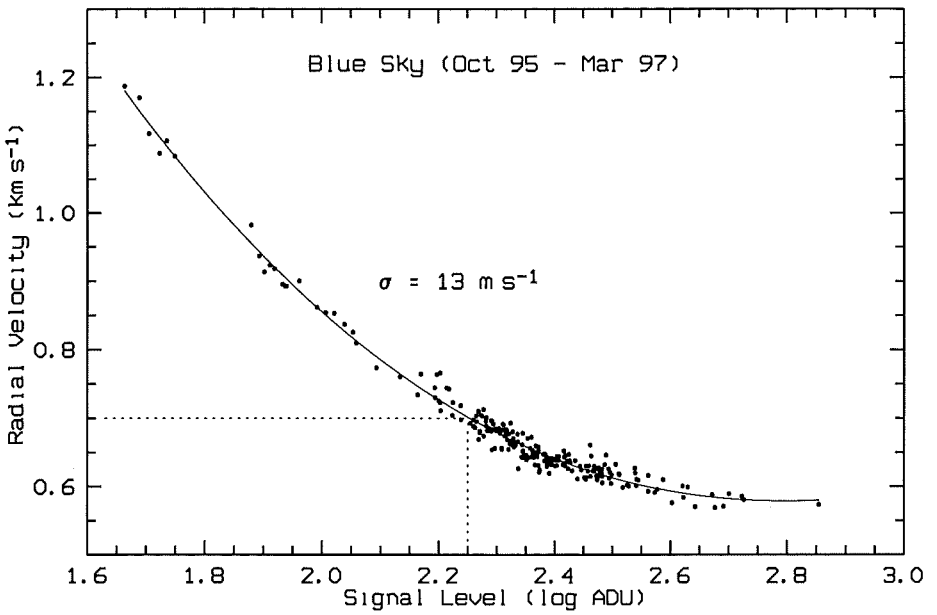

Figure 2.25: *Radial velocities of the Sun (blue sky) over a longer period of time depending on the signal level (run corrections applied).*

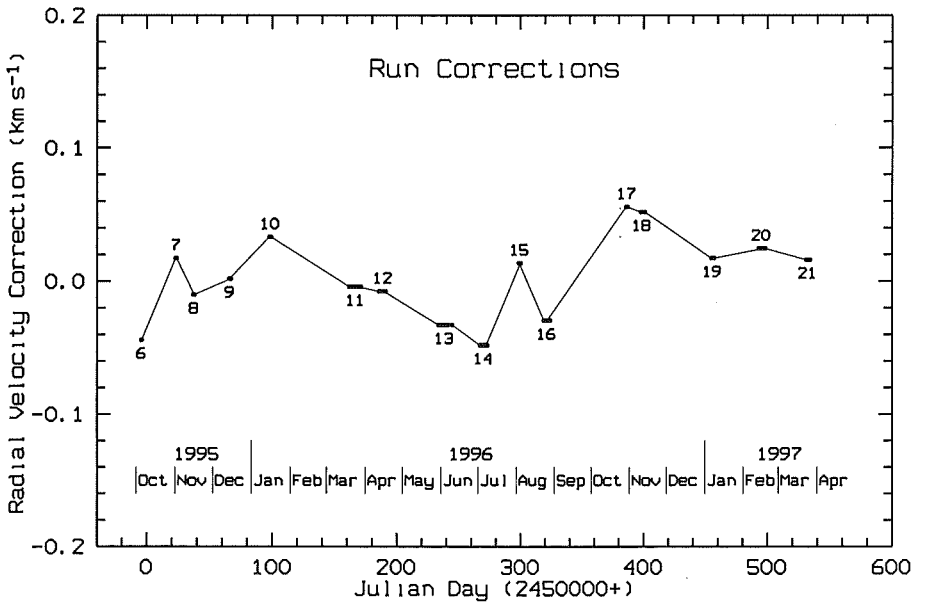

Figure 2.26: *Run corrections derived from the sky velocities.*

stellar image (after the extraction of the échelle orders).

Two examples are presented in Figure 2.24. The sky spectra were all taken on November 10$^{\text{th}}$, 1996, using a set of four different exposure times (30, 60, 120 and 180 seconds). The radial velocity is as high as 1.2 km s^{-1} at the shortest exposures, but only about 0.6 km s^{-1} at the longest ones. However, the data points follow a smooth parabolic line with an extremely low scatter of only $\sigma = 11$ m s^{-1}. A very similar behaviour can be seen in β Leporis, an

IAU standard RV star (spectral type G5II). The spectra were recorded one year earlier, on November 15th and 16th, 1995. The standard deviation of the parabolic fit to the data points is $\sigma = 10$ m s^{-1}, with a similar slope. Both data sets can be shifted vertically relative to each other until they follow the same smooth curve.

As mentioned earlier, the sky observations have been collected so that the stellar velocities can be reduced and possible systematic errors eliminated. However, in the situation when the radial velocities depend on the photon counts, a special procedure has to be developed. For each stellar velocity, a corresponding solar velocity must be available, both velocities taken at the same signal levels. Of course, this does not mean that a real solar image at the required signal level is necessary. One can simply compute the corresponding velocity using a curve like one in Figure 2.24, derived from all sky spectra available.

A total number of 229 solar spectra have been used, all taken with the optical fibre and the PM3000 CCD (FIBCCD configuration, observing runs 6–21). First, they have all been brought to the same thorium intensity, as described in the previous section. Then, a fixed *run correction* has been applied so that all data points follow a common smooth curve. This has been done in several iterations, by adjusting the run corrections each time, until the r.m.s. error reaches its minimum. The result of this procedure is shown in Figure 2.25. A total r.m.s. error of $\sigma = 13$ m s^{-1} has been reached over a period of 18 months. The final run corrections (to be subtracted from the measured velocities) ranging from -48 m s^{-1} to $+56$ m s^{-1} are presented in Figure 2.26. There is a striking similarity between this plot and the distribution of the average thorium intensities (Figure 2.21), suggesting that both effects are probably caused by the same run-to-run changes in the observing equipment (such as the status of the glycerine drop at the fibre input).

A transformation law derived from Figure 2.25 has been used to reduce all stellar radial velocities observed with the PM3000 CCD. For example, if a spectrum of 180 ADU in the continuum is obtained ($\log 180 \approx 2.25$), then a correction of 0.7 km s^{-1} should be subtracted. By doing this, the radial velocity of the Sun is always kept at 0 km s^{-1}. In other words, the stellar velocities are all expressed in a system where the observed velocity of the Sun is zero. Of course, the measured radial velocity does not only reflect the motion of the star as a whole. The measurements are still affected by the *gravitational red shift*, as well as the *convectional blue shift*. Only if these two effects compensate each other will the results represent the true absolute radial velocities.

2.6 Testing the PM3000 CCD camera

An entire observing run at the end of the observing period at Mt John University Observatory was dedicated to a more detailed examination of the problem of correlation between the observed radial velocities and the signal levels, as explained in Section 2.5. Unfortunately, it

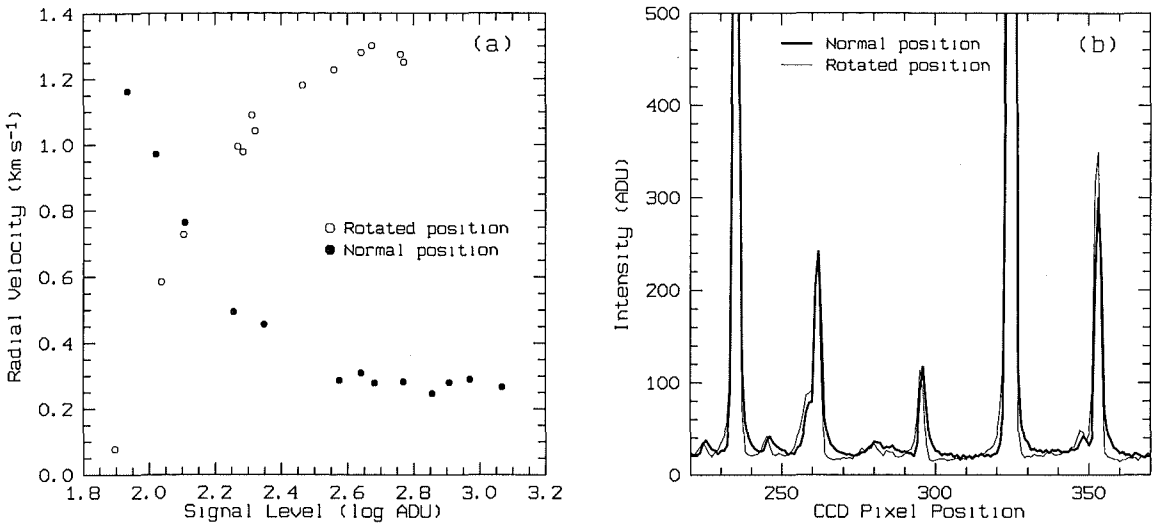

Figure 2.27: *Some effects of the PM3000 CCD camera rotation on (a) the radial velocities, and (b) the line profiles, when the camera is rotated by* 180° *from its normal position.*

was not possible to restore the original FIBCCD configuration, since the focal reducer had already been installed. But, nevertheless, these tests have revealed some interesting details about the PM3000 CCD camera, confirming the assumption that this peculiar behaviour of the radial velocities is entirely caused by the camera and not by the rest of the equipment, or the reduction procedure itself.

The tests basically consisted of a series of observations of the blue sky, using different exposure times to produce different signal levels in the continuum. One half of the observations were made with the CCD camera in its normal position. The camera was then rotated by 180° for the other half of the observations. The results are shown in Figure 2.27. It is obvious that the radial velocities produce a 'mirror image' of their behaviour when the camera is rotated (Figure 2.27a). This means that (in the normal position) the spectra are either blue-shifted at higher signal levels or red-shifted at lower signal levels. A clue to distinguish between these two possibilities is found in Figure 2.27b, where an enlarged portion of the thorium spectrum (around $\lambda = 5258$ Å in order 44) is presented at both camera positions. The thorium spectrum is used here because the lines are more regular than the stellar ones and the effect is more obvious. There is an asymmetry in the line profiles, mainly affecting the very bottom portions of the spectral lines and producing some 'tails' departing from a gaussian shape. The tails are seen only on one side of the profiles (to the right in the normal position and to the left in the rotated position). The additional ADU counts seem to be the *same* for all lines, independent on the central intensity. On a relative scale, the profiles of weaker lines are distorted more than the profiles of stronger lines. Therefore, although the central positions (as determined by the gaussian fitting) will all be shifted to the right (red shift), it is really the weakest lines that will be affected the most. This is in perfect

agreement with the distribution of the dispersion solution residuals seen in Figure 2.11c and can explain the other peculiarities of the FIBCCD radial velocities as well.

The reasons for such a peculiar behaviour of the PM3000 CCD camera are not quite clear. A general appearance of the 'tailed' profiles of spectral lines suggests that the problem should be analysed on a level of the charge transfer efficiency. It is a well known property of every CCD chip, that the charge transfer from one pixel to another during the read-out process is not fully efficient. There is always some charge 'left behind', so that the pixels located further from the read-out gate will be contaminated more. However, one would expect that the amount of charge left behind is proportional to the charge itself, which would produce stronger tails in stronger lines. This is clearly not the case here. The problem might also be located elsewhere in the read-out electronics, but investigating this would go too far from the subject of this thesis. As already explained in Section 2.5, empirical relationship has been determined between the measured velocities and photon counts to account for this effect.

2.7 Other MJUO configurations

A reduction procedure similar to the one presented for the FIBCCD observations in the previous sections, was also applied to the other MJUO configurations (see Tables 2.1, 2.4 and 2.5). The configurations differ in their basic parameters, such as the total number of diffraction orders, spectral ranges and dispersions, but the reduction procedure was designed to be flexible enough to accept these differences. There are several points that should be noted here:

1. A completely new table of Th-Ar calibration lines has been prepared for each configuration, following the same basic steps described in Section 2.4.2. The total number of lines, and their distribution across the CCD image, depend on the particular configuration, but it is always an optimal selection, designed to provide a stable dispersion solution.

2. The ECHCCD spectra are the only ones that allow a full two-dimensional flat-fielding, because the white-lamp diffraction orders can be made wider than the stellar orders, when the optical fibre is not used. This is taken into account during the reduction.

3. In spite of different spectral ranges found in the different configurations, they all include the FIBCCD spectrum as a sub-image. The cross-correlation with synthetic spectra is always done on the same FIBCCD spectral region. One reason for doing this is that the synthetic spectra were originally obtained for the FIBCCD configuration. Although the data would allow a usage of wider wavelength ranges in some spectral orders, this would also introduce some additional systematic differences in radial velocities.

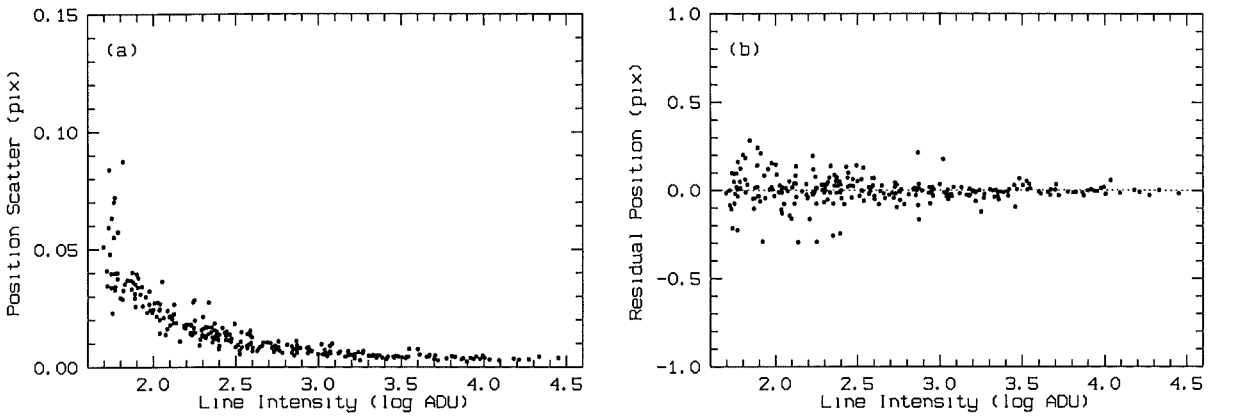

Figure 2.28: *A typical behaviour of the Th-Ar lines in the SITCCD spectra, with (a) the scatter in the pixel position being correlated with the central intensities, and (b) the residuals after the dispersion solution showing an even distribution around the zero line.*

As a single example of various reduction steps in configurations other than FIBCCD, Figure 2.28 demonstrates a typical behaviour of the Th-Ar spectral lines in the SITCCD spectra. This would be interesting to compare with similar FIBCCD plots (Figures 2.11b and c). While the scatter in pixel position remains correlated with the central intensities, the residual positions relative to the dispersion solution fit now seem to be evenly distributed around the zero line, without any detectable slope. This confirms the statement given before, that the correlation of the radial velocities with the CCD photon counts is only a property of the PM3000 CCD system.

The final adjustments of the non-FIBCCD radial velocities (such as removing a possible correlation with the photon counts or applying a run correction) are slightly different from one configuration to another:

- ECHCCD. Since there are not enough observations for a separate detailed analysis in this case without the optical fibre, it was assumed that the same FIBCCD transformation laws for the thorium intensities (Figure 2.23), and the stellar signal levels (Figure 2.25) could be applied. After this, the run corrections were determined using the stars observed in more than one run.

- FOCCCD. Again, the FIBCCD transformation is applied, and then the sky spectra are used to derive the run corrections.

- SITCCD. No adjustments are made for the mean intensities in the thorium or stellar spectra. The run corrections are determined from the sky spectra, so that the total dispersion of observations around a constant mean velocity is as small as possible.

After these additional reduction steps, all MJUO radial velocity measurements are expressed in a common system, where the radial velocity of the Sun is zero. There is only one remaining reduction step to be done in order to bring these measurements to a standard system of radial velocities, as defined by the IAU standard stars, and it will be presented in the following section.

2.8 The IAU standard radial velocity stars

A number of the IAU standard radial velocity stars have been observed at Mt John (24 stars, with 197 measurements in total, when taking into account only the observations involving the optical fibre, i.e. excluding the ECHCCD configuration). These observations are used to determine the zero point of the MJUO system with respect to the IAU system, as well as to check if there are any systematic effects depending on the spectral type or the luminosity

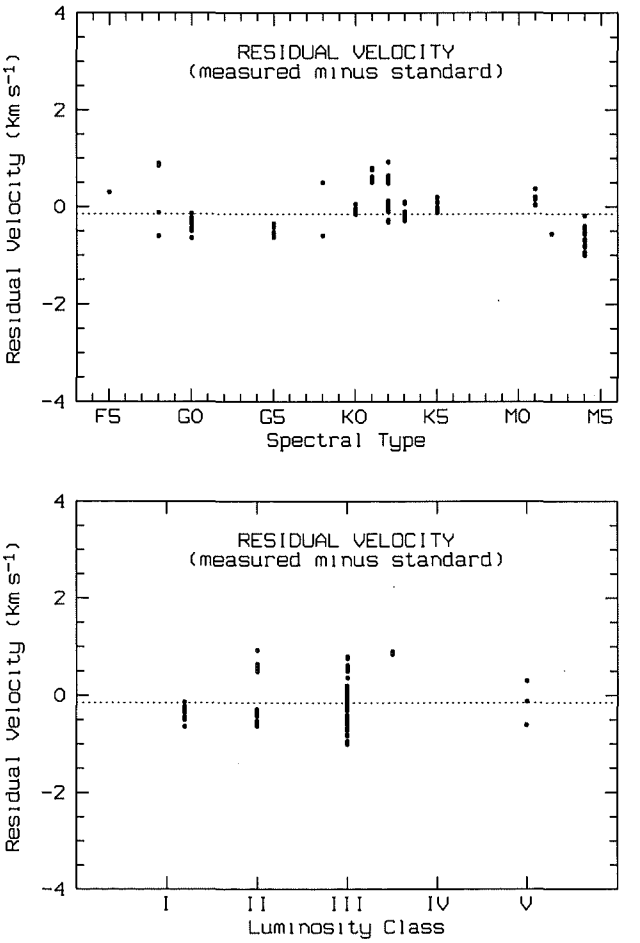

Figure 2.29: *Residual velocities (measured minus standard) for the IAU standard stars, as obtained at Mt John Observatory (ECHCCD excluded). Each dot corresponds to a single observation. The arithmetic mean is represented by a horizontal dashed line.*

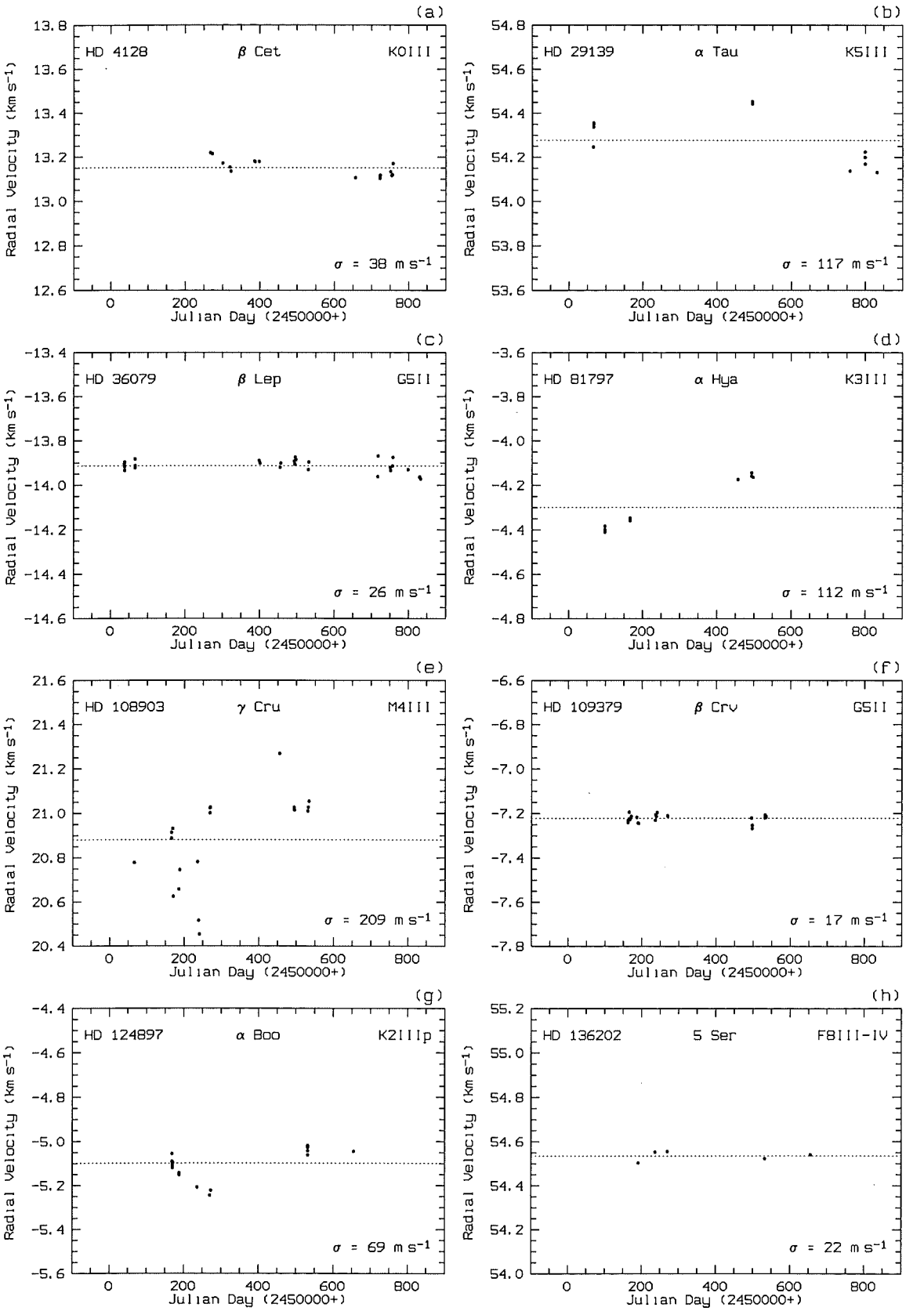

Figure 2.30: *Radial velocities for some IAU standard stars, with corresponding standard deviations (σ), as measured at Mt John Observatory (ECHCCD excluded). A horizontal dashed line is used to represent the mean value.*

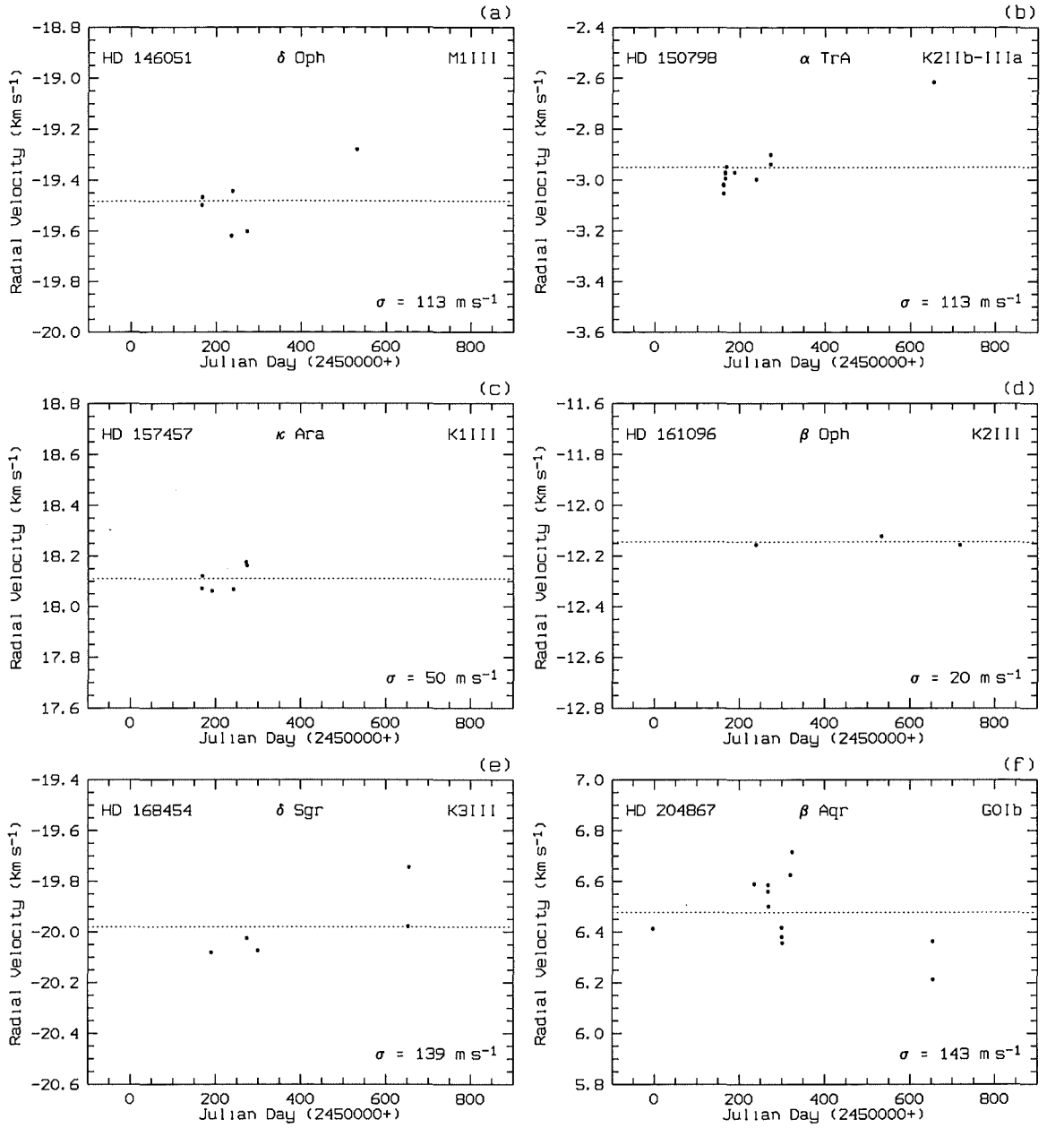

Figure 2.31: *Radial velocities for some IAU standard stars, with corresponding standard deviations (σ), as measured at Mt John Observatory (ECHCCD excluded). A horizontal dashed line is used to represent the mean value.*

class. This is shown in Figure 2.29, where the residual velocity is the difference between the measured and standard values. The two plots demonstrate no detectable correlation between the residual velocities and either the spectral type or the luminosity class. There is a small constant offset of:

$$\mathrm{MJUO} - \mathrm{IAU} = -150 \ \mathrm{m\,s^{-1}} \tag{2.5}$$

and a total standard deviation of:

$$\sigma_{\mathrm{MJUO}-IAU} \approx 400 \ \mathrm{m\,s^{-1}}. \tag{2.6}$$

The offset of $-150\ \mathrm{m\,s^{-1}}$ was then subtracted from all MJUO observations, so that the final velocities are now in the IAU system.

Some of the results (stars observed more than twice) are presented in Figures 2.30 and 2.31. Most of the standard stars exhibit some level of variability, confirming numerous results already published by other authors. However, there are examples of extremely stable velocities, with standard deviations as small as $(20 - 30)\ \mathrm{m\,s^{-1}}$. In particular, this is the case with the two G5II standards, β Leporis and β Corvi (Figures 2.30c and 2.30f).

2.9 The DAO RVS observations

As mentioned earlier, a number of radial velocities have been collected at the Dominion Astrophysical Observatory (see Section 2.2.2 for the instrument description and Section 2.3 for the observing statistics). More than 80 per cent of all observations made at the DAO (Table 2.2) were done using the radial velocity spectrometer (RVS). The data reduction procedure for this detector is completely different from what is normally done with the CCD images. As a matter of fact no additional reduction is necessary, since the radial velocity is produced during the observation by cross-correlating the stellar spectrum with a *standard mask*, directly at the focus of the spectrograph.

Without going deeply into the mechanical details (for more information see Fletcher et al. 1982), but in order to understand the reduction procedure, only the basics of the instrument's operation will be described here. The mask oscillates in the focal plane of the spectrograph (along the dispersion axis) performing many small discrete steps. At each mask position, the resulting light output (stellar spectrum plus the mask) is recorded as a new point on the cross-correlation profile. The minimum is obtained when the mask coincides with the stellar spectrum. The cross-correlation profile is slowly built-up during the observation of a star by averaging many individual scans. In fact, two separate profiles are produced, each of them corresponding to one direction of the mask motion. The two profiles will give two slightly different velocities, which are then combined into one average value.

If the weather conditions are not perfectly stable, the total flux from the star is not constant during a scan, and the cross-correlation profile will get distorted. In order to overcome this problem a separate channel is used to record the total flux at each mask position. The two profiles can be divided later, to make sure that the flux fluctuations are eliminated.

When the exposure is over, the observer has to choose a pair of points to define the central part of the cross-correlation dip, so that a *parabola* can be fitted to the selected points and the central position calculated from the fit. This procedure leads directly to the radial velocity, which is displayed on the screen and also printed. The Earth's motion is automatically subtracted. The only additional reduction that has to be done is a correction

for a possible slow drift, as recorded by frequent 'observations' of a calibration source (an iron-argon lamp).

The fact that the result is produced during the observation does not mean that the observer is forced to accept it. The complete cross-correlation profile of each observation is saved in a computer file, together with all the parameters necessary for the reduction process. Therefore, it is possible to re-reduce the data later, by experimenting with various methods for locating the minimum of the cross-correlation profile. A gaussian fit has been successfully applied in this work, using more data points in the profile wings than with a standard parabolic fit (see Section 2.9.1).

The exact shape of the cross-correlation profile depends on how similar the mask and the actual stellar spectrum are. The mask is normally produced using photography of a real stellar spectrum. Two different masks have been used, designed for observations of different spectral types: the K mask (K96OCT3087), based on the spectrum of Arcturus, and the F mask (F96SEP0187), based on the spectrum of Procyon. Both can be used to measure the radial velocity of a star, but slightly different results will be obtained (see Section 2.9.2).

Out of 306 observations with the RVS in 1997 (observing runs 1 and 2, see Table 2.3), the great majority (86 per cent) were done with the K mask and only 14 per cent with the F mask. However, all 249 observations in 1998 were done with the K mask only.

2.9.1 Data re-reduction

A standard procedure for locating the minimum of a cross-correlation profile is to fit a parabola to its central part. This is normally done immediately after the observation. However, the profile can be successfully approximated by a gaussian function, in which case all the data points (central part plus far wings) can be used to find the minimum. Some examples of the cross-correlation profiles are presented in Figure 2.32. The raw data do not always follow a perfect gaussian shape. This happens because the overall flux can fluctuate during the observation (scintillation noise and transparency fluctuations, as mentioned earlier), especially if the weather conditions are not very good and only a few scans are done. However, if the raw profile is divided by the flux monitor record, such fluctuations disappear and the ratioed profile always has a regular gaussian shape.

It has also been mentioned before that the Earth's motion is automatically eliminated from the measured radial velocity. Nevertheless, the accurate barycentric corrections have been computed independently for all observations, using an algorithm based on the JPL rectangular coordinates of the Sun, Moon and planets (see Appendix F). The difference between the RVS correction (as computed at the DAO) and the true barycentric correction is presented in Figure 2.33. There is an obvious error in the DAO RVS values of up to about 40 $\mathrm{m\,s^{-1}}$, with an evident pattern of periodicity. During each observing night, the difference seems to follow a steady trend (rising or falling), crossing the zero point at some stage, and

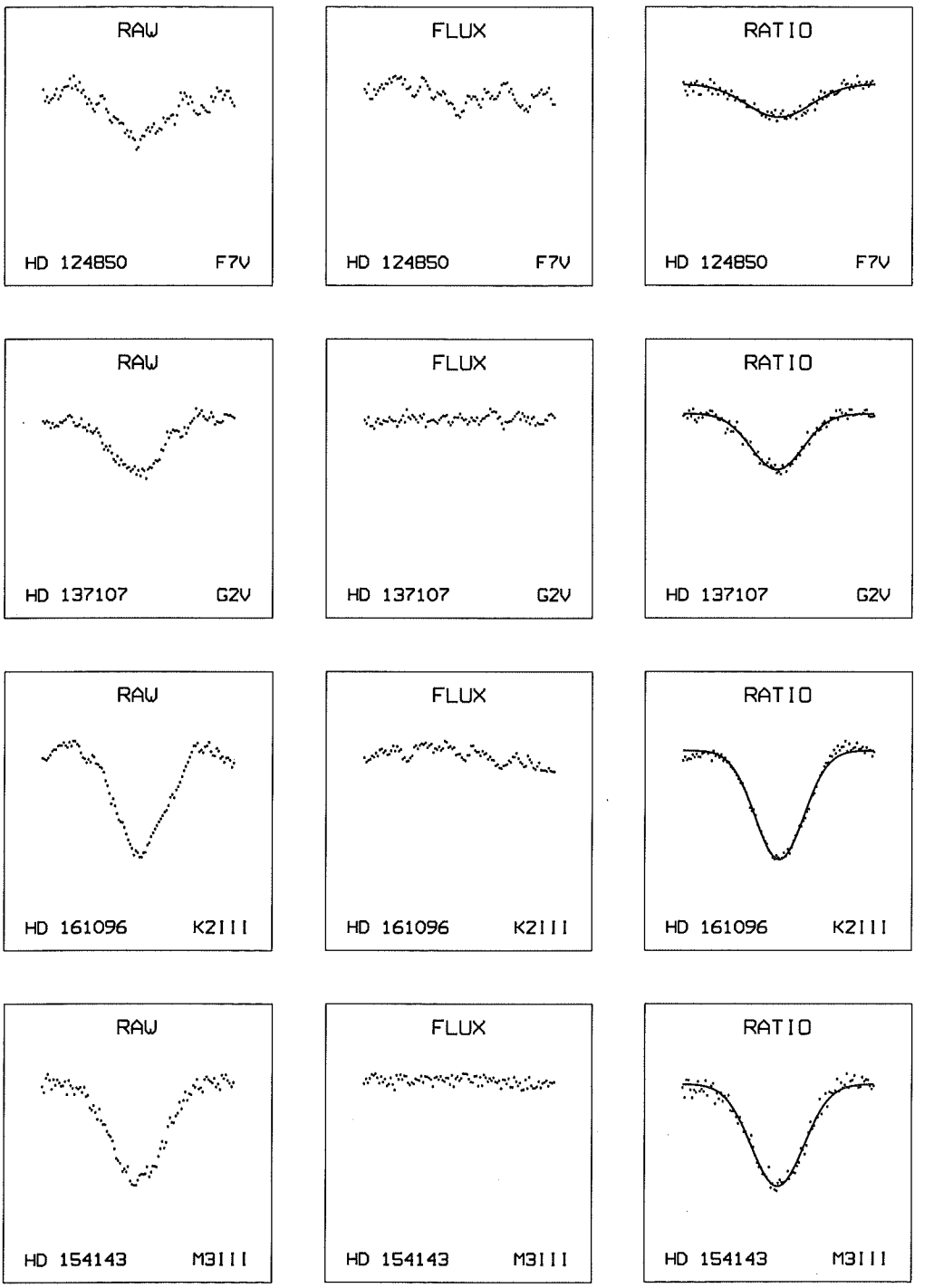

Figure 2.32: *Some cross-correlation dips produced by the RVS using the K mask (June-July 1997). A gaussian function is fitted to the ratio between the raw profile and the flux monitor record.*

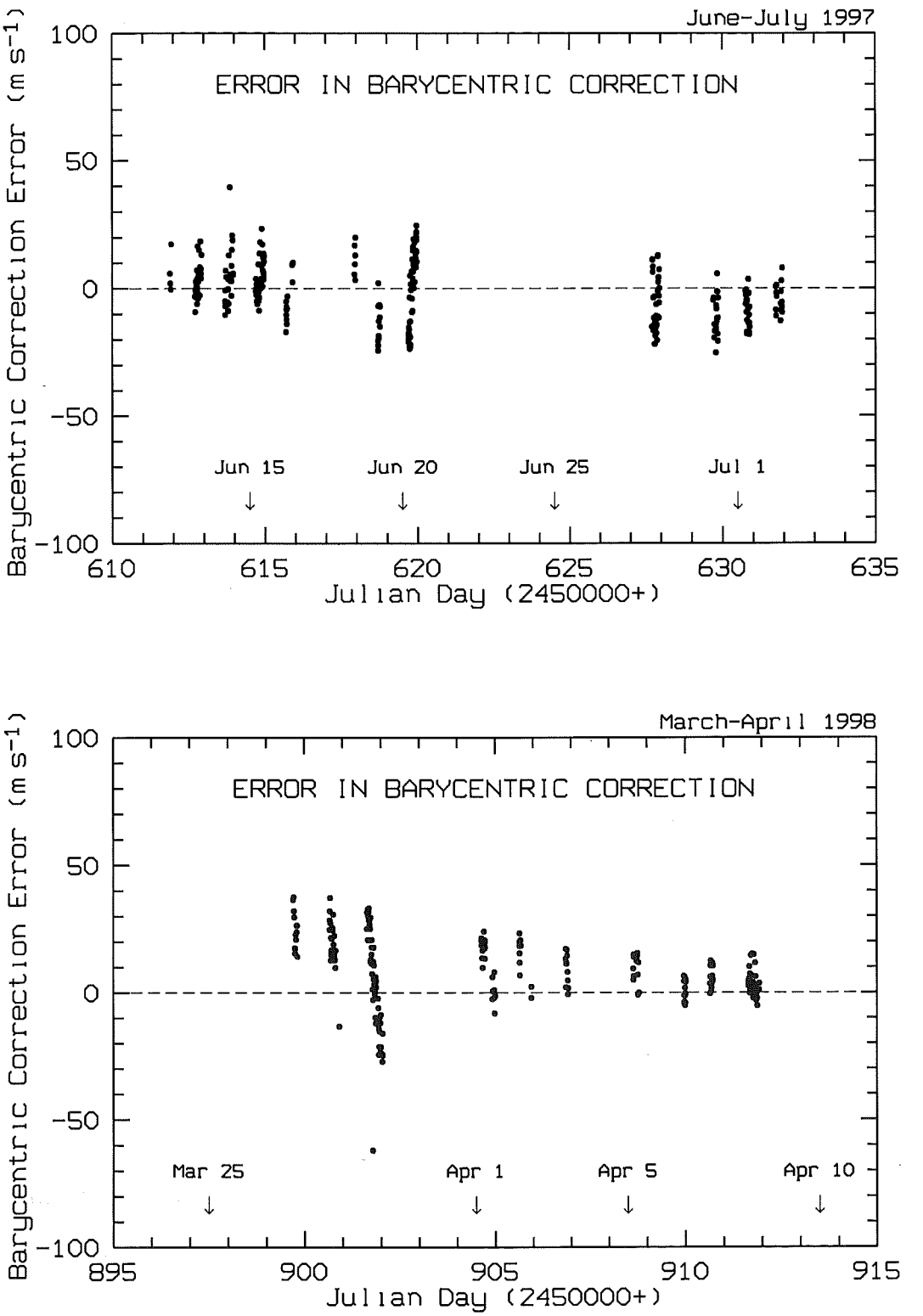

Figure 2.33: *Barycentric correction error (RVS minus JPL).*

then repeating the whole pattern on the following night. Moreover, there is a sort of seasonal modulation, affecting the overall amplitude on a longer time scale. After some investigation, and a series of discussions with M. Fletcher at the DAO, the cause for such a behaviour has finally been revealed. It is simply a result of the two main approximations used in the RVS algorithm:

- using the Sun's centre instead of the solar-system barycentre;
- using the Earth-Moon barycentre instead of the Earth's centre.

For a demonstration on how these approximations affect the radial-velocity corrections, see Appendix F. An additional source of error in the RVS algorithm is also neglecting the stellar *proper motions*, when transforming the coordinates from the catalogue epoch, to the date of observation. The RVS software uses the old 1900.0 coordinates, which makes the calculation even less accurate. Slightly wrong final stellar positions (for stars with large proper motions) can sometimes affect the barycentric correction by a significant amount[9].

2.9.2 Results

All radial velocities have been computed using the ratioed data, with gaussian profiles fitted and barycentric corrections re-computed. The comparison lamp observations have then been used to correct the velocities slightly for a slow drift during an observing night (typically a few hundreds of metres per second).

A number of IAU standard radial velocity stars, as well as the dusk sky, have been observed in order to calibrate the RVS measurements. Using the standard star observations it is possible to find the transformation that will bring all measured velocities to the IAU standard system. This is usually done by computing the *zero point*, assuming that the measured values differ from the standard ones by a common constant offset. But first, the zero-point difference between the two masks has to be computed (Figure 2.34). Only the stars that have their velocities measured with both masks are used. The difference $(\mathrm{F}_{1997} - \mathrm{K}_{1997})$ ranges from 1.3 to 2.3 $\mathrm{km\,s^{-1}}$, which is very different from $\mathrm{F}_{\mathrm{old}} - \mathrm{K}_{\mathrm{old}} = (0.85 \pm 0.05)\ \mathrm{km\,s^{-1}}$, as found by Fletcher et al. (1982). This disagreement is probably due to the fact that the masks used in this thesis differ from those used by Fletcher et al.. The present value, derived

[9]The barycentric correction f_{bar} is the projection of the Earth's velocity $\vec{V}_\oplus$ onto the direction $\vec{e}_*$ towards the star. If the corresponding angle between the two vectors is ψ then f_{bar} and $df_{\mathrm{bar}}/d\psi$ can be calculated as: $f_{\mathrm{bar}} = V_\oplus \cos\psi$ and $df_{\mathrm{bar}}/d\psi = -V_\oplus \sin\psi$, where the derivative is expressed in $\mathrm{km\,s^{-1}}$ per radian. For a star in the pole of the ecliptic ($\psi = 90°$) and with $V_\oplus \approx 30\ \mathrm{km\,s^{-1}}$ the barycentric correction will vary by about 0.5 $\mathrm{km\,s^{-1}}$ per degree. Taking into account a moderately high proper motion of $\mu = 1''$ per year, a total error in the position over a century becomes $\sim 100''$, corresponding to an error of about 14 $\mathrm{m\,s^{-1}}$ in the barycentric correction.

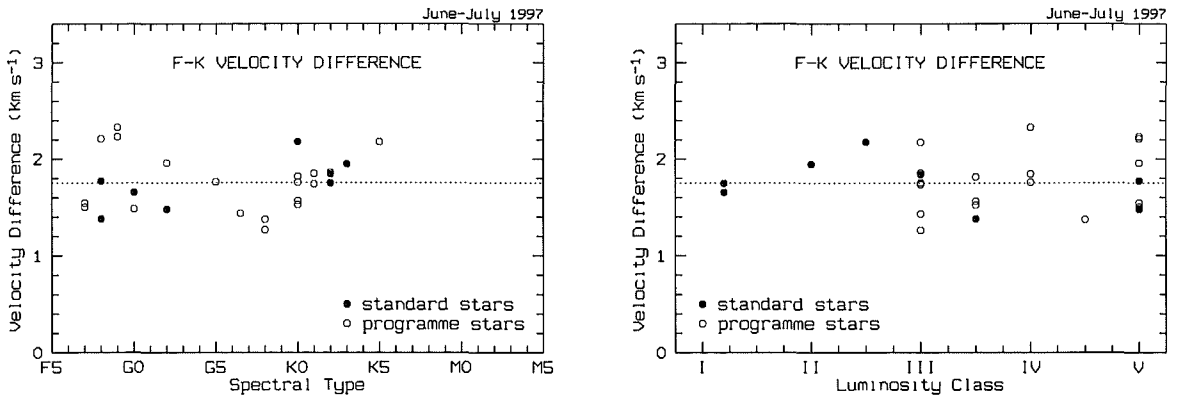

Figure 2.34: *Difference in radial velocities between the F and K masks. Only the stars measured with both masks are shown. Filled dots represent the standard stars, and open circles represent the programme stars. The arithmetic mean is shown as a horizontal dashed line.*

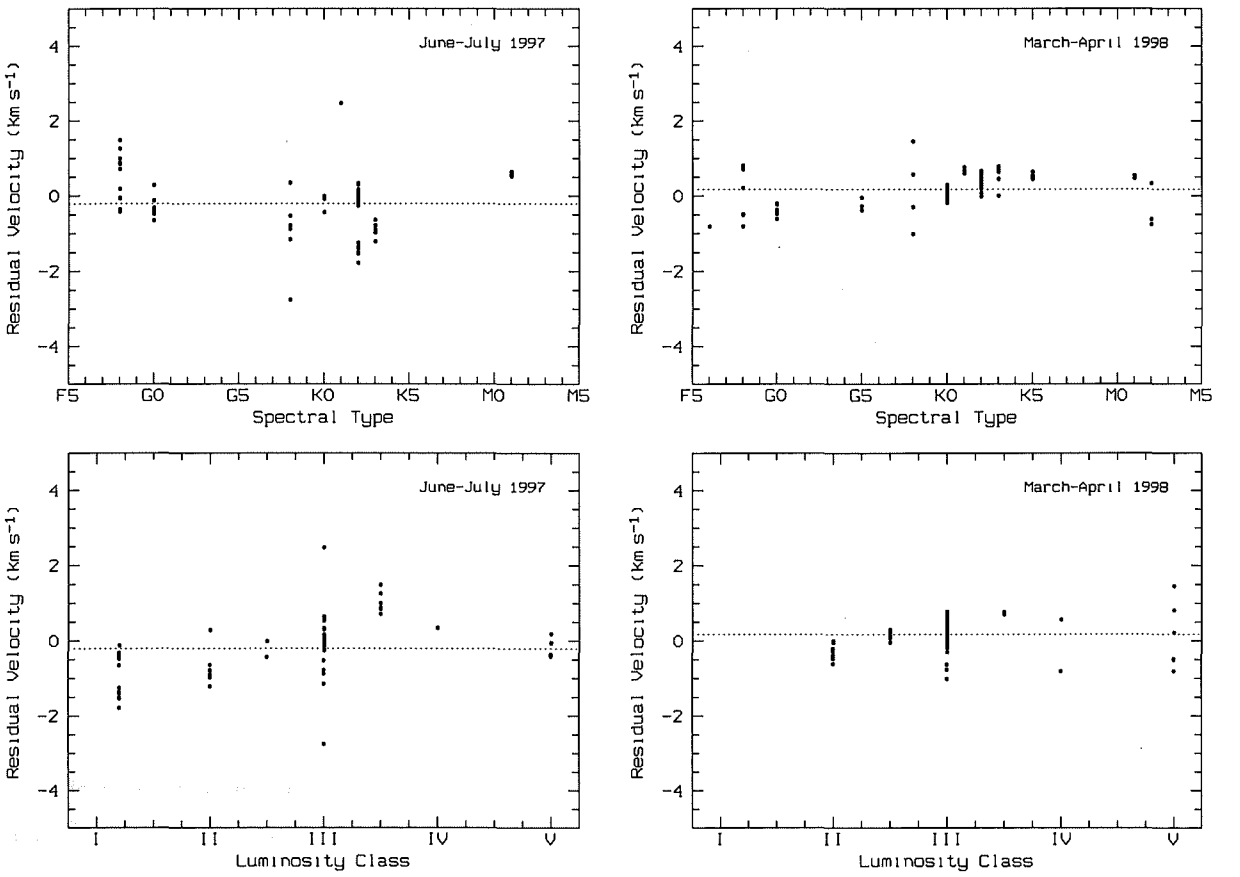

Figure 2.35: *Residual velocities (measured minus standard) for the IAU standard stars, as obtained using the RVS. Each dot corresponds to a single observation. The arithmetic mean is shown as a horizontal dashed line.*

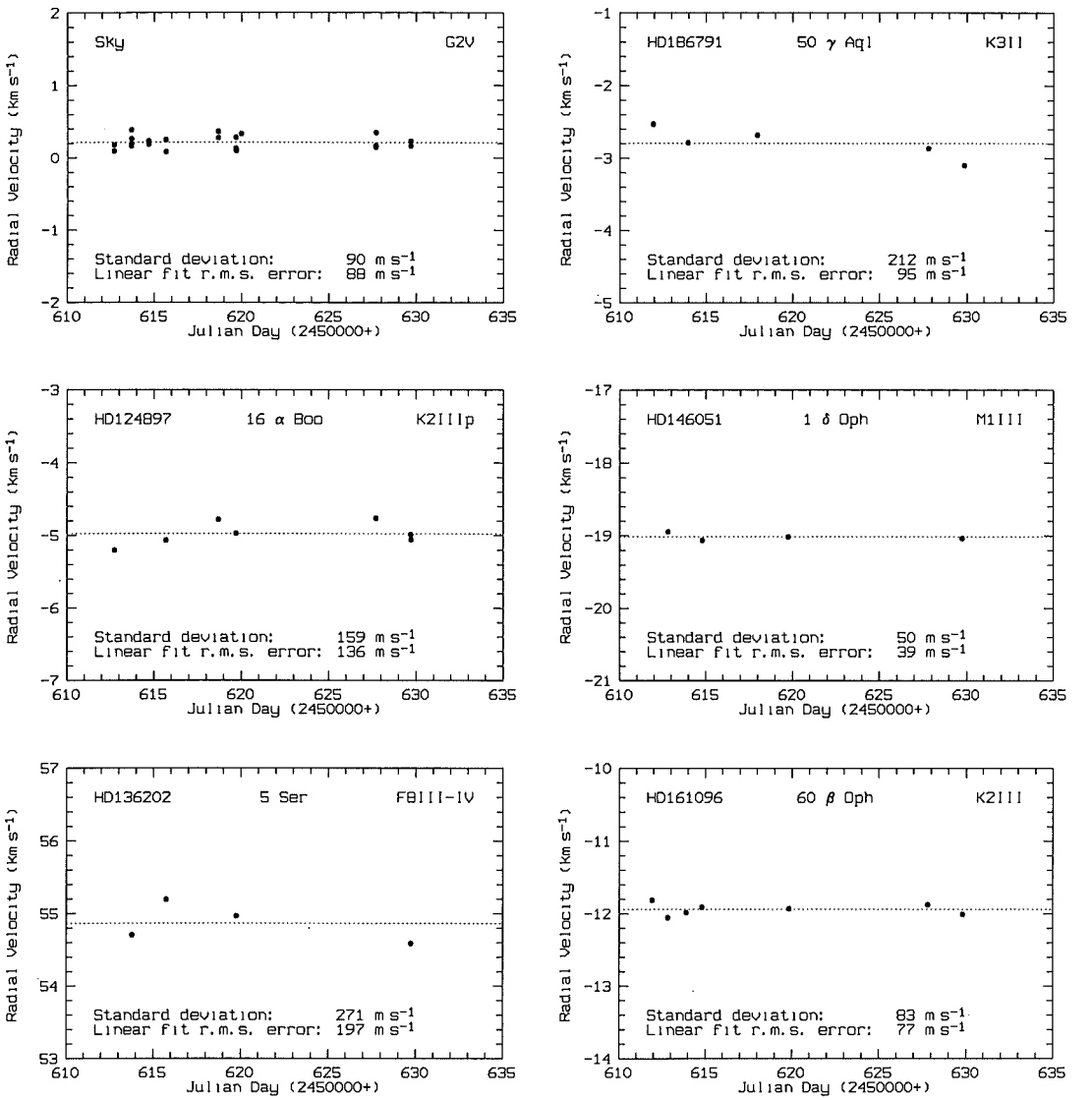

Figure 2.36: *Measured radial velocities for some standard stars (June–July 1997). The mean value is marked by a horizontal dashed line.*

from 27 stars, is $F_{1997} - K_{1997} = (1.75 \pm 0.06)$ km s^{-1}, if the arithmetic mean is simply taken, with a corresponding standard error of the mean $(\sigma/\sqrt{N})$.

The residual velocities between the measured values and standard ones are presented in Figure 2.35. A weak correlation with spectral type and luminosity class seems to exist in the 1997 measurements, but there is not enough data to investigate this peculiarity any further. A constant offset (the arithmetic mean) has been derived from each of the two data sets in Figure 2.35, and it was used to adjust all radial velocities measured with the RVS:

$$\mathrm{RVS}_{1997} - \mathrm{IAU} = -210 \text{ m s}^{-1}, \quad (2.7)$$

$$\mathrm{RVS}_{1998} - \mathrm{IAU} = +170 \text{ m s}^{-1}. \quad (2.8)$$

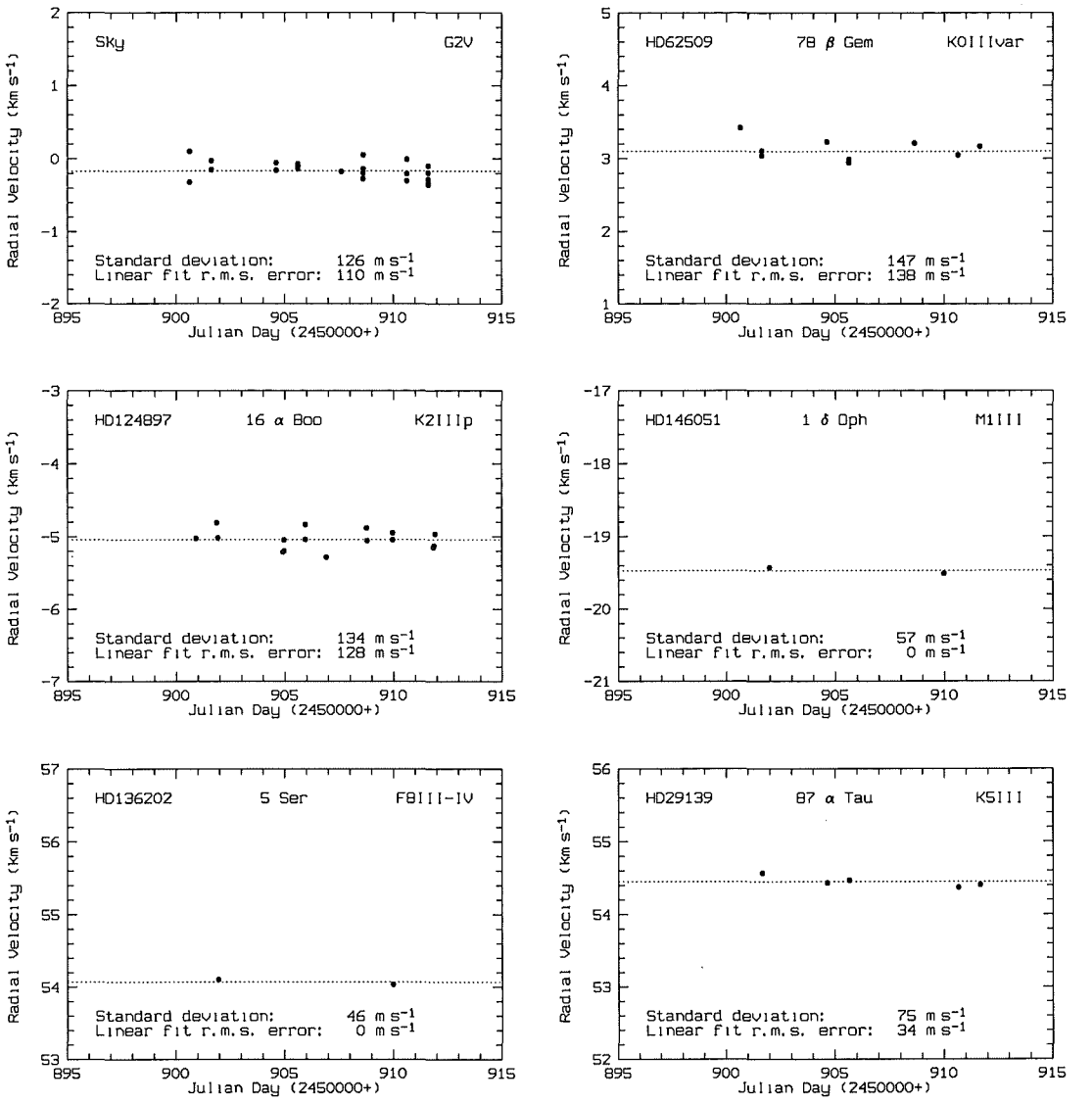

Figure 2.37: *Measured radial velocities for some standard stars (March–April 1998). The mean value is marked by a horizontal dashed line.*

The corresponding standard deviations are:

$$\sigma_{1997} \approx 840 \text{ m s}^{-1}, \tag{2.9}$$

$$\sigma_{1998} \approx 470 \text{ m s}^{-1}. \tag{2.10}$$

The final radial velocities obtained for some of the IAU standard stars are presented in Figures 2.36 and 2.37. Two different measures of the scatter have been computed for each star: the standard deviation for all measured points and the r.m.s. error of a linear fit to the data. The r.m.s. error is usually slightly better than the standard deviation, but in any case a typical uncertainty for the measurements is about 100 m s^{-1}, which is by a factor of two or three better than the usually adopted value for the RVS.

2.10 Comparing the measured and published velocities

After the measured radial velocities have all been brought to the IAU standard system, as described in the previous sections, a final list of observations (including both the MJUO and DAO measurements) has been made, and the measurements have been compared with the published values. As a source of published values for the majority of stars, the Hipparcos Input Catalogue (ESA 1992) has been used. However, in case of the standard RV stars, the current IAU values have been adopted.

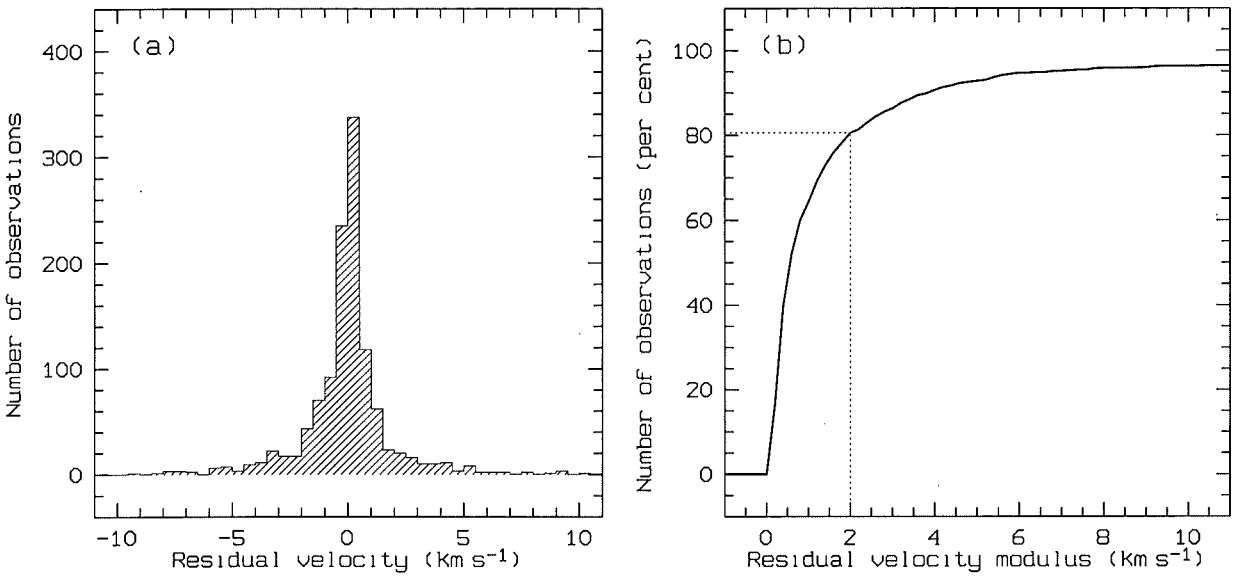

Figure 2.38: *Distribution of the residual velocities (measured minus published) for 1217 radial velocity measurements involved in this project (blue sky excluded), presented (a) as a standard histogram, and (b) as a cumulative distribution, showing a percentage of residuals less than a given value.*

A typical error bar (random uncertainty) of a single radial velocity measurement, as estimated from the standard IAU stars (see Figures 2.30, 2.31, 2.36, and 2.37), is about 20 – 30 $\mathrm{m\,s^{-1}}$ for the MJUO fibre-fed échelle observations and also the DAO CCD observations, while it is about 100 $\mathrm{m\,s^{-1}}$ for the RVS measurements.

The residual velocities (measured minus published) are distributed as presented in Figure 2.38. The distribution was derived from the stellar measurements only (1217 in total), without taking into account the blue sky observations. From the histogram in Figure 2.38a, one can find out that the residuals stay close to zero for the majority of measurements. However, more information can be extracted from the cumulative distribution in Figure 2.38b, presenting the percentage of observations with residuals smaller than a given value, in an absolute amount. For example, over 80 per cent of all observations have their residuals less than 2 $\mathrm{km\,s^{-1}}$. However, not all observations are even within 10 $\mathrm{km\,s^{-1}}$. Those observations

with large residuals most probably correspond to binary stars, although some of them clearly indicate an error in the published value. There are 41 residuals greater than 10 $\mathrm{km\,s^{-1}}$, 17 residuals greater than 20 $\mathrm{km\,s^{-1}}$, and even 4 residuals greater than 100 $\mathrm{km\,s^{-1}}$ (those four residuals belong to the same star, HD 199870, and are a result of an error in the Hipparcos Input Catalogue, as explained below).

A detailed analysis of each star would take too much space and it would be outside the scope of this thesis. However, some of the most interesting examples will be mentioned here:

1. Four observations of HD 199870 (HIP 103519, $m_V = 5\overset{\mathrm{m}}{.}6$, Sp: G8III), all within 20 days, confirm a radial velocity of about -31 $\mathrm{km\,s^{-1}}$, while the published value is -200.7 $\mathrm{km\,s^{-1}}$, apparently taken from Wilson (1953). However, Wilson's actual value is only -20.7 $\mathrm{km\,s^{-1}}$, revealing an obvious error in the Hipparcos Input Catalogue. The remaining difference of about 10 $\mathrm{km\,s^{-1}}$ clearly indicates that the star is a binary. A period of 635 days was determined by Hipparcos.

2. Two observations of HD 204613 (HIP 105969, $m_V = 8\overset{\mathrm{m}}{.}3$, Sp: G0IIIwsp), made ten days apart, give radial velocities of -88.2 $\mathrm{km\,s^{-1}}$ and -88.9 $\mathrm{km\,s^{-1}}$, while the published value is -112.0 $\mathrm{km\,s^{-1}}$. The star is marked as a possible astrometric binary in the Hipparcos Catalogue, although with not enough data for a reliable orbital solution.

3. Two observations of HD 147584 (HIP 80686, ζ TrA, $m_V = 4\overset{\mathrm{m}}{.}9$, Sp: F9V), made 226 days apart, give velocities of $+15.1$ $\mathrm{km\,s^{-1}}$ and $+2.7$ $\mathrm{km\,s^{-1}}$, while the published value is $+8.5$ $\mathrm{km\,s^{-1}}$. The star is not marked as a binary in the Hipparcos Catalogue.

4. Two observations of HD 3919 (HIP 3245, μ Phe, $m_V = 4\overset{\mathrm{m}}{.}6$, Sp: G8III), made 388 days apart, give velocities of $+24.7$ $\mathrm{km\,s^{-1}}$ and $+25.1$ $\mathrm{km\,s^{-1}}$, while the published value is $+18.8$ $\mathrm{km\,s^{-1}}$. The star is not marked as a binary in the Hipparcos Catalogue.

5. Two observations of HD 14728 (HIP 11033, $m_V = 5\overset{\mathrm{m}}{.}9$, Sp: K2III), made 782 days apart, both give a velocity of $+2.3$ $\mathrm{km\,s^{-1}}$, while the published value is -3.0 $\mathrm{km\,s^{-1}}$. The star is not marked as a binary in the Hipparcos Catalogue.

6. Four observations of HD 138852 (HIP 75974, $m_V = 5\overset{\mathrm{m}}{.}8$, Sp: K0III-IV), made within 20 days, give a velocity of about $+4.6$ $\mathrm{km\,s^{-1}}$, while the published value is $+10.1$ $\mathrm{km\,s^{-1}}$. The star is not marked as a binary in the Hipparcos Catalogue.

7. Four observations of HD 144284 (HIP 78527, ϑ Dra, $m_V = 4\overset{\mathrm{m}}{.}0$, Sp: F8IV-V), spread over 282 days, give velocities between -8.9 $\mathrm{km\,s^{-1}}$ and -21.3 $\mathrm{km\,s^{-1}}$, while the published value is -8.5 $\mathrm{km\,s^{-1}}$. The star is not marked as a binary in the Hipparcos Catalogue.

This list of possible new binary stars completes the discussion of the radial velocity measurements presented in this thesis, including the acquisition, reduction and analysis of

the spectroscopic data obtained during the three-year observing period. In the next chapter a study of galactic kinematics will be presented using the Hipparcos parallaxes and proper motions (combined with the radial velocities from this thesis and from other sources) to analyse the stellar space velocities in the solar neighbourhood.

Chapter 3

Analysis of Hipparcos data

3.1 High precision parallaxes and stellar kinematics

A full analysis of stellar kinematics in the solar neighbourhood involves determination of the space velocity vectors for every star under consideration. There are two components of the space velocity vector that are measured directly from the Earth: the *radial velocity* (along the line of sight), normally obtained from the Doppler shift in the stellar spectrum ($V_r = c\,\Delta\lambda/\lambda$), and the *transverse velocity* (in the plane of the sky), derived from the proper motion and parallax ($V_t = 4.74\,\mu/\pi$). While the radial velocity measurements are not affected by the distance towards the star, the transverse velocities are very sensitive to the distance and this is the main source of uncertainties in the total space velocities.

The Hipparcos project (see Chapter 1) has made a significant improvement to a typical precision of stellar transverse velocities, by providing precise parallaxes and proper motions. This has opened a wide range of new possibilities in studying the local stellar kinematics, as will be presented in this chapter.

This analysis of the Hipparcos data will start with a presentation of the programme stars (Eggen's moving groups), and then it will be continued by examining a general sample of stars in the solar neighbourhood. This will provide a necessary frame for studying the reality and nature of moving groups of stars.

Some of the results presented in this chapter have already been published (Skuljan et al. 1997; Skuljan et al. 1999c).

3.2 Eggen's groups

Hipparcos parallaxes and proper motions, together with the radial velocities from other sources, have been used to compute the stellar space velocities for the 880 programme stars, collected from Eggen's papers as possible members of various moving groups (see Chapter 1). The right-handed galactic coordinate system centred at the Sun has been used, with three

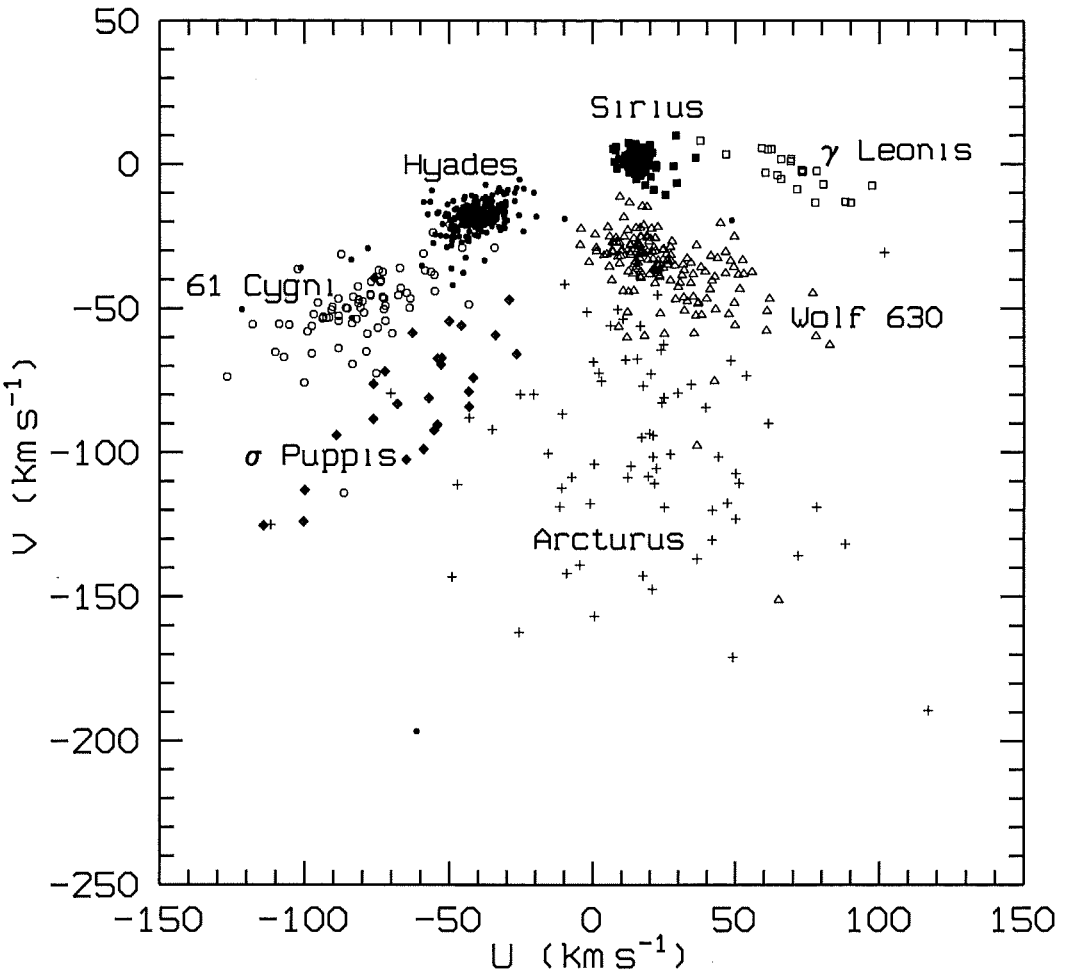

Figure 3.1: *The largest moving groups in the UV plane.*

corresponding velocity components (U, V, W), as defined in Section 1.1. The measured radial velocities (from the observational programme described in Chapter 2) were used for those stars that have been observed, while the Hipparcos Input Catalogue was used as a source of radial velocities for the rest of the stars.

The seven most populated of Eggen's moving groups (Hyades, Wolf 630, Sirius, Arcturus, 61 Cygni, σ Puppis and γ Leonis) are presented in the UV velocity plane in Figure 3.1. The grouping is reasonably clear, at least for the slowest groups ($V \sim 0$). However, these stars have *already been selected* to have similar motions, and one cannot use Figure 3.1 to prove the existence of moving groups, because it is not a random sample of stars. However, the diagram can be used to investigate some other properties of the distribution.

An important result derived from Figure 3.1 is that all the groups have become *more compact* (i.e. better defined) with the Hipparcos measurements. This is shown in Figure 3.2 for the Hyades moving group, comparing the pre-Hipparcos and Hipparcos data (similar diagrams can be obtained for other groups). Many of the stars are clearly moved *into the*

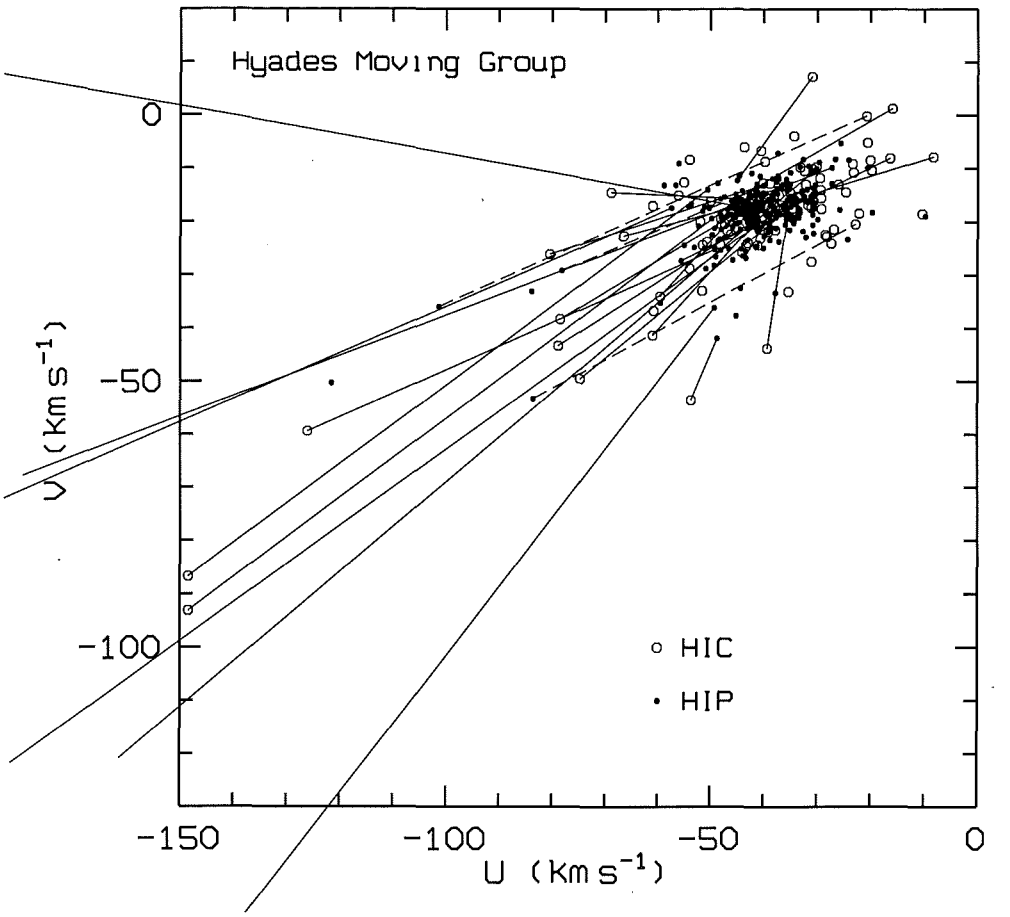

Figure 3.2: *The Hyades moving group in the UV plane. Open circles represent the velocities based on the observations before the Hipparcos mission, as taken from the Hipparcos Input Catalogue (HIC). Some of the points fall outside the bounds of the plot. Filled dots correspond to the Hipparcos data (HIP). Solid lines are used to connect the HIC and HIP positions for some of the stars that are moved into the core of the group when the Hipparcos data are used. Dashed lines indicate when the HIP position pulls a star away from the core.*

core of the group when the Hipparcos data are used. In only a few cases (dashed lines in Figure 3.2) are they moved away from the core, possibly indicating that those stars are not group members. The situation is similar for all of Eggen's groups. For example, the Sirius moving group appears as the most compact concentration of stars in Figure 3.1. That is especially the case for its *nucleus* stars (i.e. the Ursa Major cluster), confirming some predictions published previously (Soderblom & Mayor 1993).

The dispersions in U and V (σ_U, σ_V) are also considerably less when Hipparcos data are used (see Table 3.1). Only the stars with existing HIC data have been used to compute the statistics, with the same sample in all columns. The Arcturus group is the only one with HIP σ_U actually bigger than the HIC value. However, all dispersions in V are at least two times less with Hipparcos data.

These results can be interpreted in two slightly different ways:

- If Eggen's groups are real, and all suggested stars are members, the stars would be expected to appear close to each other in the UV plane, and then the Hipparcos data are indeed much better than the previous astrometric measurements.
- If the Hipparcos parallaxes are considered as the *true values*, so that they are used to test the moving group concept, then a better grouping in the UV-plane means that the moving groups may be real. To really prove this hypothesis, however, additional statistical tests are needed, involving a random sample of stars in the solar neighbourhood.

The truth is probably somewhere in between. At this stage one cannot claim that all the stars are members. But a more concentrated grouping certainly indicates both the high quality of the Hipparcos data and the possible reality of moving groups.

Table 3.1: *Standard deviations for velocity distributions in U and V for some moving groups when pre-Hipparcos (HIC) or Hipparcos (HIP) data are used.*

Group	HIC $\sigma(\mathrm{km\,s^{-1}})$		HIP $\sigma(\mathrm{km\,s^{-1}})$	
Name	σ_U	σ_V	σ_U	σ_V
Hyades	53	43	13	17
Wolf 630	20	29	16	10
Sirius	13	8	4	4
Arcturus	37	86	45	30
61 Cygni	34	25	19	13
σ Puppis	26	36	21	19
γ Leonis	48	36	13	6

It is also interesting to compare the *group* parallaxes (π_{gr}) with the Hipparcos values (π). A group parallax corresponds to such a distance at which a star should be found, in order to have exactly the same V velocity as is adopted for the whole group (Eggen's membership criterion). Figure 3.3 takes into account the stars with previously known trigonometric parallaxes (π_{tr}), so that the distributions $\pi_{\mathrm{gr}} - \pi$ and $\pi_{\mathrm{tr}} - \pi$ can be compared. It is obvious that the group parallaxes are closer to the Hipparcos values. This is especially the case for stars with $\Delta\pi$ within ± 5 mas.

A similar distribution can be found for those stars with previously unknown parallaxes. Their group parallaxes are also very close to the Hipparcos values. It means that the moving group concept can be used to predict the parallax with an uncertainty of about 5–10 mas. Of course, if the parallax itself is of the same order, this cannot be regarded as a good result.

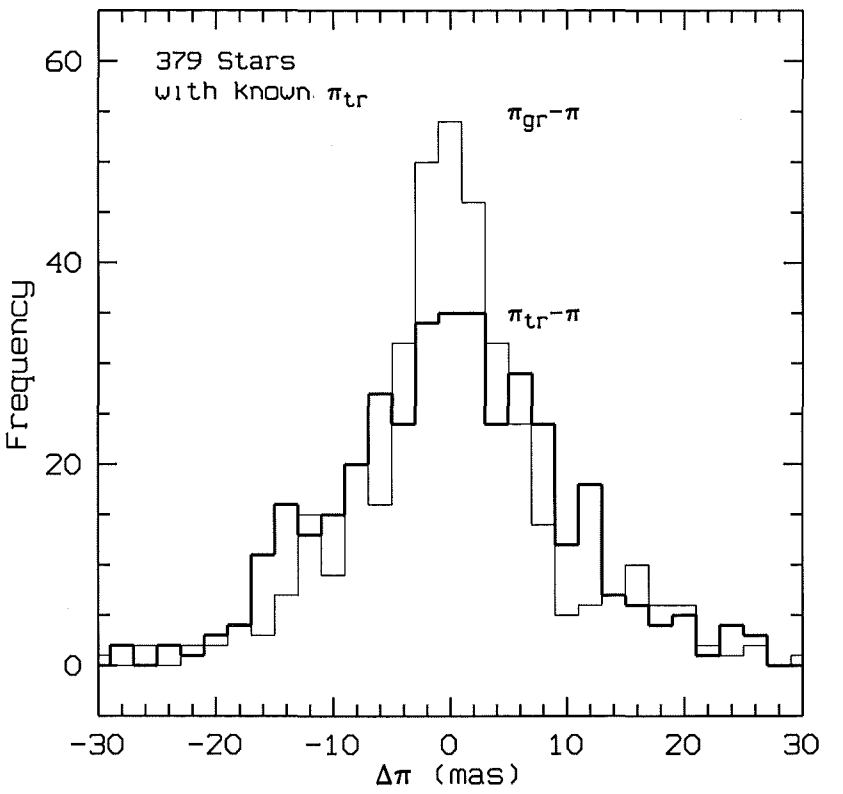

Figure 3.3: *Comparison between the group parallaxes (π_{gr}) and old trigonometric ones (π_{tr}), relative to the Hipparcos values (π). Only the stars with previously known parallaxes are considered.*

There are about 30 per cent of all stars in Eggen's lists with $\pi < 10$ mas, and about 50 per cent with $\pi < 15$ mas.

Another way of comparing π_{gr} with π and π_{tr} is to convert them to absolute magnitudes and display them in an H-R diagram. If all the stars in a moving group were formed together their H-R diagram must be similar to one for a cluster of the same age, with a well defined locus of stars corresponding to an isochrone. If the Hipparcos photometry is used to plot M_V versus $B-V$ for Eggen's groups (Figures 3.4 and 3.5), the diagrams do not confirm the same age for all the stars, as has already been demonstrated by other authors (McDonald & Hearnshaw 1983). The situation is somewhat better in the (M_I,$R-I$) plane, as shown in Figure 3.6 for the Wolf 630 group. The photometric data were taken from Eggen (1969), but they include only about 30 per cent of the Wolf 630 stars. However, the Hipparcos data provide better agreement with the moving group concept than is the case for the old astrometric data.

Returning to Figure 3.1, it is interesting to examine the way in which the moving groups are actually grouped in the UV plane. One would expect that each group appears roughly as a horizontal bar, or a flattened ellipse, if Eggen's criterion of constant V is true. What

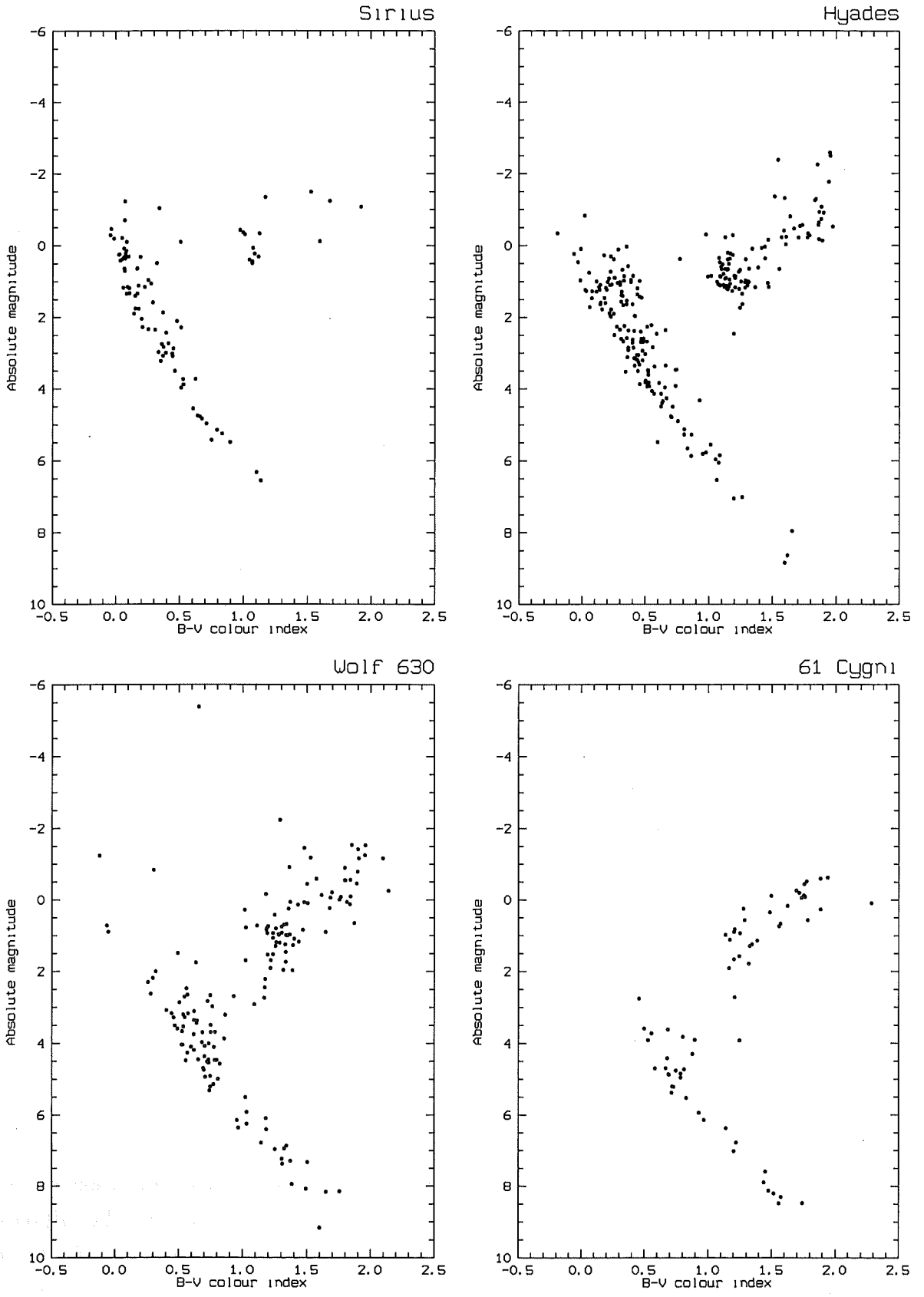

Figure 3.4: *The Hipparcos H-R diagrams for Eggen's moving groups.*

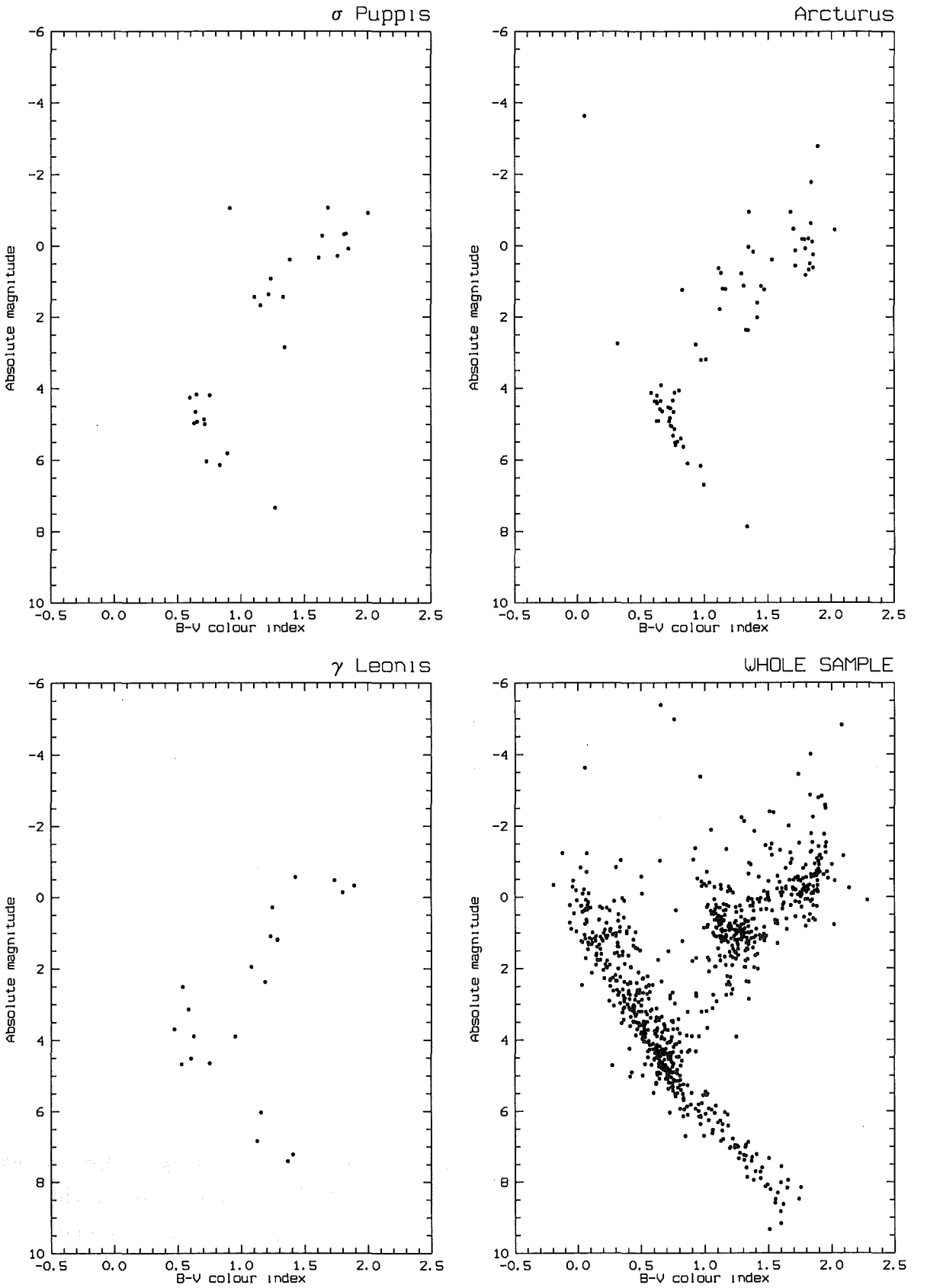

Figure 3.5: *The Hipparcos H-R diagrams for Eggen's moving groups.*

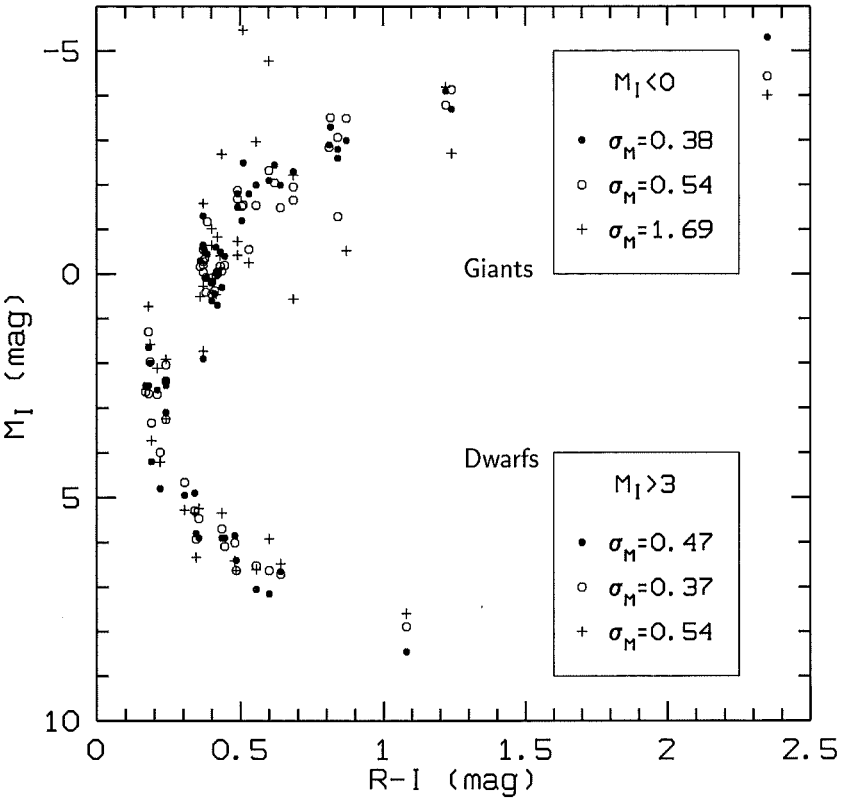

Figure 3.6: *Some Wolf 630 stars in the (M_I,$R-I$) plane, with three different sources of parallaxes used to compute M_I. Filled dots are Eggen's data based on group parallaxes, while circles and crosses correspond to Hipparcos and pre-Hipparcos, respectively. Standard deviations around a mean locus have been computed for dwarfs and giants separately.*

is seen, however, is very different. All the groups show some sort of elliptical concentration, but their major axes are tilted in different directions. The dispersions in V seem to be less than in U, but the plot does not confirm the constant V membership criterion. There is even an indication that those groups with $U < 0$ have positive inclinations and those with $U > 0$ have negative inclinations. All the axes apparently converge to the zero point. The Arcturus group should be excluded from this discussion, since it covers a large portion of the UV plane, and does not look like a moving group at all.

The radial pattern of converging axes described above seems to be more likely caused by the measurement errors, rather than being a real property of moving groups. A closer examination of the Hyades moving group in Figure 3.2, for example, can provide some clue. The corrections from pre-Hipparcos to Hipparcos measurements all go in one general direction and that is the actual major axis of the group. It seems that the group shape is actually caused mainly by the parallax uncertainty itself. This becomes even more obvious in Figure 3.7 (with all moving groups), where each star is presented as a line showing how the U and V components would change if the parallax changed by $\pm\sigma$ (Hipparcos standard

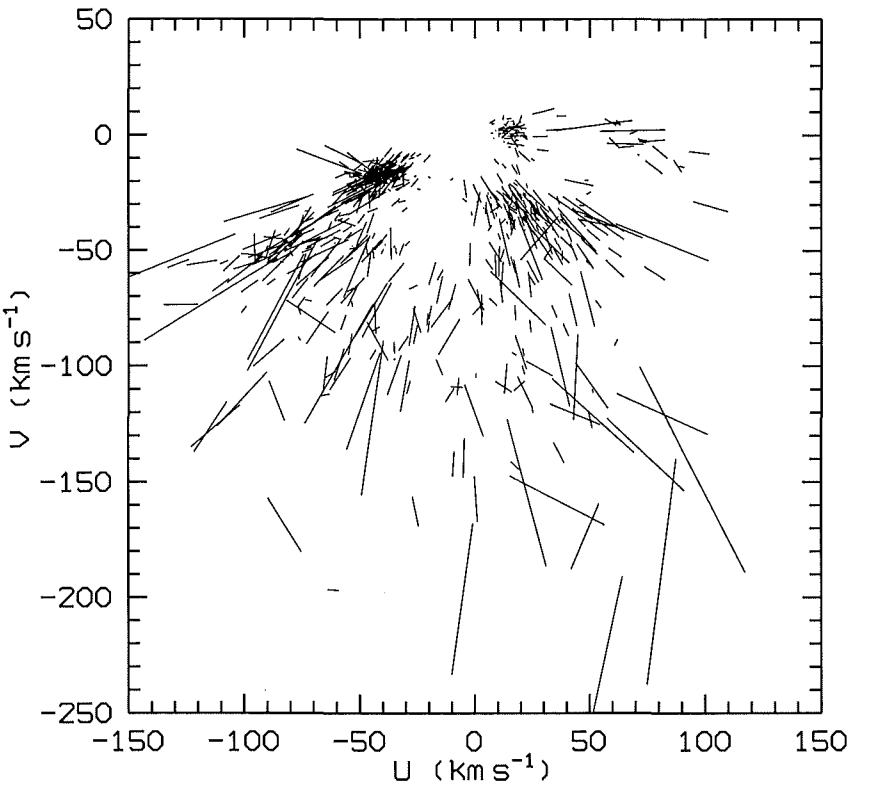

Figure 3.7: *Seven Eggen's moving groups in the UV plane, with each star presented as a straight line, corresponding to a $\pm\sigma$ change in the parallax.*

error). Note that the parallax errors cause a larger scatter in U and V for the higher-velocity old-disk moving groups.

3.3 Stellar velocities in the solar neighbourhood

In the following sections, a general sample of Hipparcos stars in the solar neighbourhood will be considered. The velocity distribution of stars in the solar neighbourhood is an important tool for studying different aspects of galactic kinematics and dynamics. During a long era of ground-based astrometry that preceded the Hipparcos mission, many subtle details in the velocity field have gone undetected due to the smearing caused by large uncertainties in stellar parallaxes. With the Hipparcos measurements it is possible to investigate the structure in more detail, confirming some previous characteristics and discovering some new features.

A typical analysis of the distribution of stars in the UV-plane concentrates on determining the *velocity ellipsoid* and its parameters (dispersions in U, V and W, as well as the orientation of the principal axis, i.e. the longitude of the vertex). More details about this can be found in any textbook on galactic structure and kinematics (e.g. Mihalas & Binney 1981). In addition

to the global properties of the velocity ellipsoid, a variety of different local irregularities (moving groups) are also studied. However, the main attention in the following sections will be focused on some large-scale inhomogeneities, characterized by several *branches* that can be detected in th UV-plane. These new features are probably related to moving groups and can give some additional clues to the problem of star formation and galactic evolution.

3.4 The sample

For this study a sample of 4597 stars has been constructed using the following selection criteria:

1. Parallax (π) greater than 10 mas (stars within 100 pc of the Sun), and $\sigma_\pi/\pi < 0.1$, as taken from the Hipparcos Catalogue (ESA 1997).
2. Survey flag (Hipparcos field H68) set to 'S'.
3. Existing radial velocities in the Hipparcos Input Catalogue (ESA 1992).
4. Existing $B-V$ colours in the Hipparcos Catalogue.

The survey flag has been used so that no stars proposed by various individual projects are included in this analysis, since they could introduce a bias. Stars with parallax uncertainties greater than 10 per cent have been rejected in order to have a reliable error propagation. The Hipparcos $B-V$ colour index is used here as a suitable indicator for dividing the sample into two subsets, as explained in Section 3.8.

There are 12520 'survey' stars (H68 = 'S') with parallaxes greater than 10 mas, out of 118218 entries found in the Hipparcos Catalogue. However, only 11009 of these stars have their parallax uncertainties less than 10 per cent. Finally, for 11007 of them the $B-V$ colours are known. On the other hand, there are 19467 stars with known radial velocities, out of 118209 entries in the Hipparcos Input Catalogue. Only 4597 stars are found in both subsets, if the catalogue running numbers are used as a matching criterion (HIP = HIC).

Before proceeding with the analysis of the velocity distribution, some important points have to be emphasized here concerning the problem of bias. First of all, not all spectral classes are equally represented in the sample. The Hipparcos Catalogue is essentially magnitude limited, which means that there will be a significant deficiency of red dwarfs, compared to the young early-type stars. The situation is illustrated in Figure 3.8. A great majority of stars are concentrated around $B-V = 0.5$, corresponding to the main-sequence F stars. There is also a possible concentration of earlier-type stars around A0, as well as a distinct peak of K giants (red-clump stars on the horizontal branch, to be more precise) around $B-V = 1.0$. This should be kept in mind when drawing any conclusions regarding the stellar ages (see Section 3.8), but it will essentially not affect the final results.

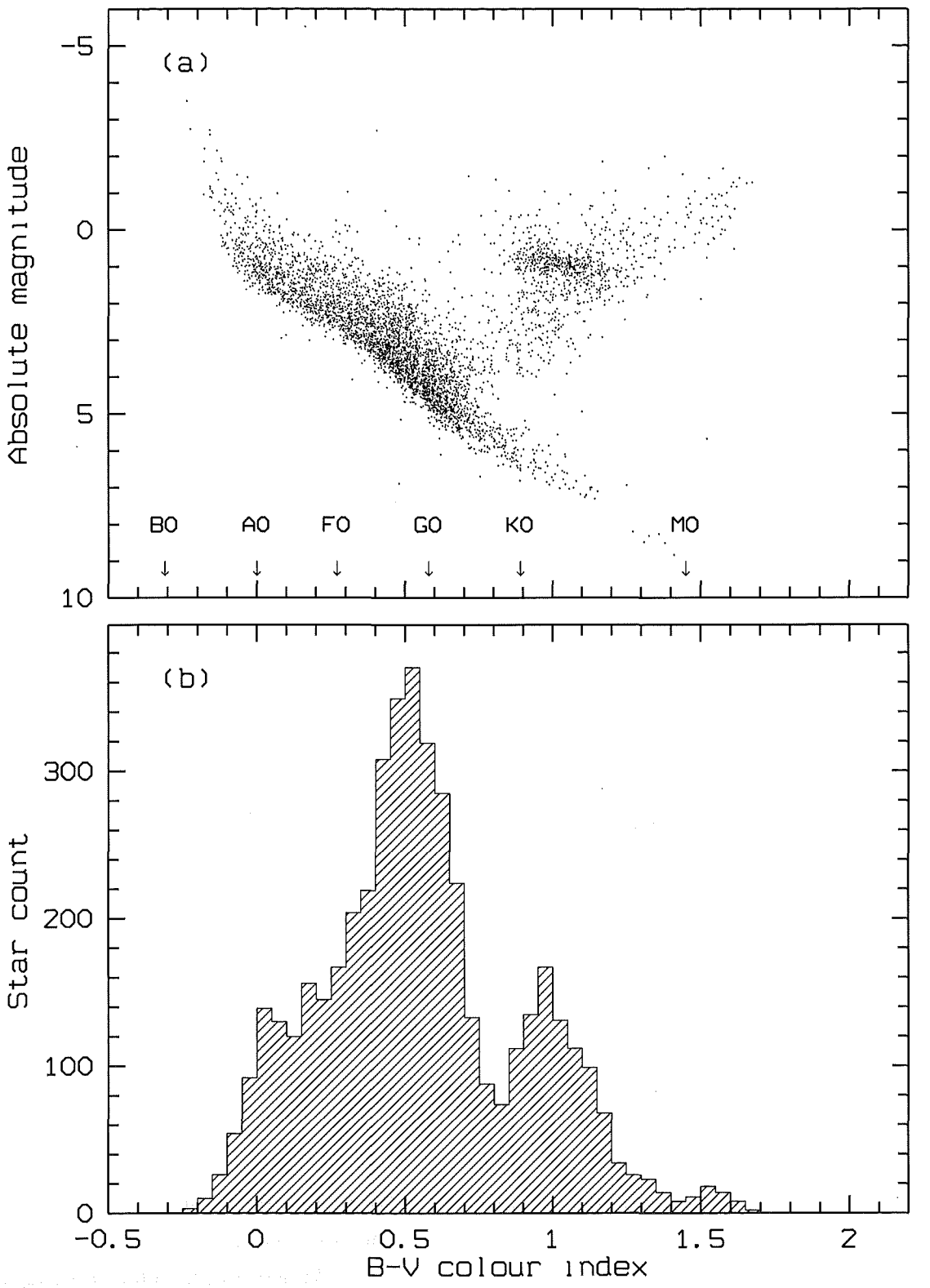

Figure 3.8: *(a) H-R diagram of the 4597 Hipparcos 'survey' stars within 100 pc, with known radial velocities and colours, and (b) the distribution of the $B-V$ colour index. The spectral classes in (a) correspond to the main sequence (Allen 1991).*

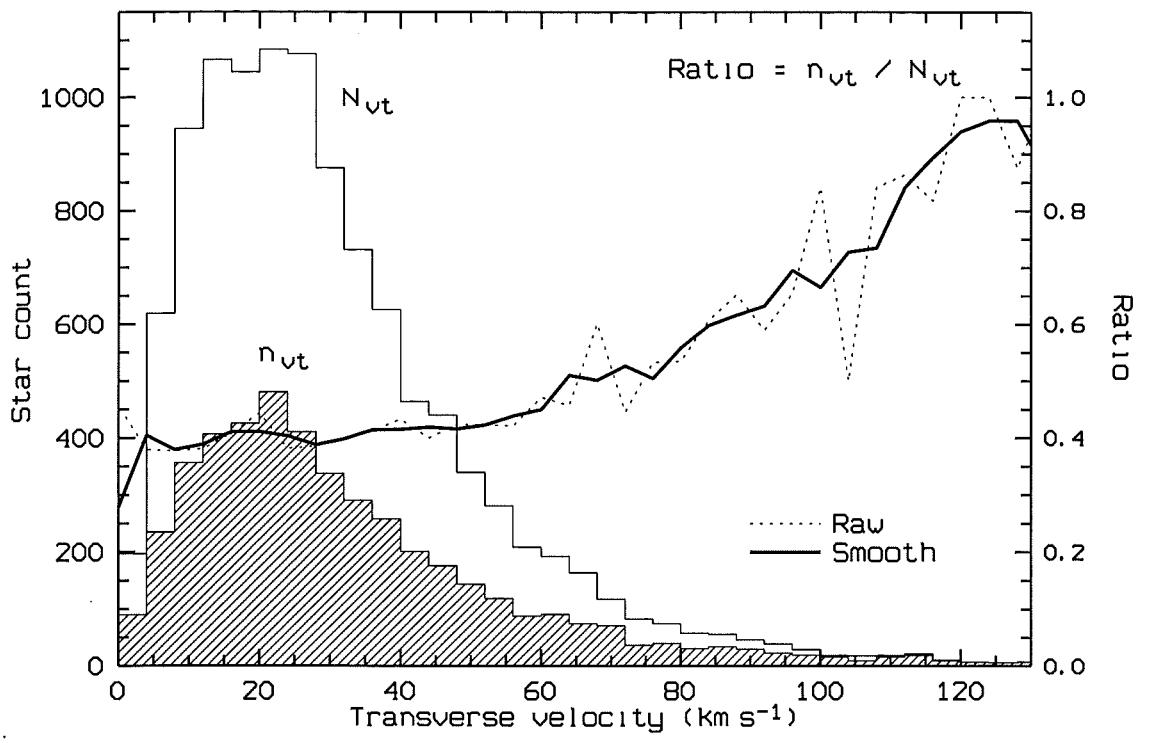

Figure 3.9: *Kinematic bias, presented as a ratio between two distributions: stars with known radial velocities (n_{V_t}) out of the total sample of Hipparcos 'survey' stars within 100 pc (N_{V_t}), where V_t is the transverse velocity. Radial velocities are predominantly known for high-V_t stars, but the effect is important only at $V_t > 70 - 80$ km s^{-1}.*

A possibly more serious problem concerning this stellar sample is a *kinematic bias*. As it has been demonstrated recently (Binney et al. 1997), the radial velocities are predominantly known for high-proper-motion stars. In other words, if only the stars with known radial velocity are used in an analysis, then any velocity distribution derived from such a biased sample might give a false picture, and lead to some wrong conclusions about the local stellar kinematics. That is the reason why many authors today choose not to include the measured radial velocities at all (see also Dehnen & Binney 1998; Dehnen 1998a, 1998b; Crézé et al. 1998; Chereul et al. 1998, 1999).

A check was made for potential kinematic bias in the present stellar sample used in this thesis, and the result is presented in Figure 3.9. Two distributions are shown as functions of the transverse velocity ($V_t = 4.74\,\mu/\pi$), one for the total sample of 11007 'survey' stars within 100 pc (N_{V_t}), and the other only for the stars with known radial velocities (n_{V_t}). The V_t-axis has been divided into 4-km s^{-1} bins and the stars have been counted in each bin. If there was no kinematic bias, then the probability that a star has a radial velocity should be constant from bin to bin, and the ratio n_{V_t}/N_{V_t} would appear as a flat line. It is obvious from Figure 3.9 that this is not the case for this sample. While the radial velocities are known for about 40 per cent of the stars at $V_t = 20$ km s^{-1}, the ratio reaches 80 per cent at

$V_t = 110$ km s^{-1}. However, the effect becomes a real problem only at *higher velocities*, above $70 - 80$ km s^{-1}, as easily seen from the diagram. Below this limit, the ratio stays roughly flat, so that one can expect no significant distortions in the inner parts of the velocity distribution, where the attention will be primarily concentrated. This problem will be addressed again when a comparison is made between the present velocity distribution and those of other authors (see Section 3.5).

3.5 Velocity distribution

A typical error-bar in each velocity component is close to 1 km s^{-1}, with about 80 per cent of stars having their velocity uncertainties less than 2 km s^{-1}, as shown in Figure 3.10. The error propagation has been treated taking into account the full correlation matrix between the Hipparcos astrometric parameters (see Appendix B).

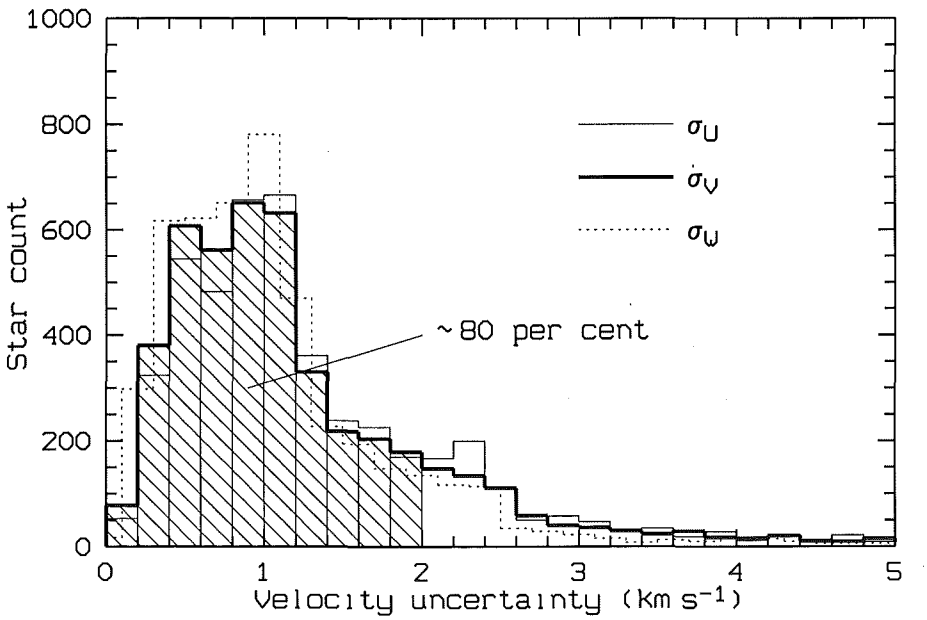

Figure 3.10: *The distribution of the uncertainties in all three velocity components: σ_U (thin line), σ_V (bold line) and σ_W (dotted line). The uncertainties are less than* 2 km s^{-1} *for about 80 per cent of stars (shown as the shaded area under the σ_V histogram).*

In order to estimate the probability density function $f(U, V)$ from the observed data, an *adaptive kernel method* is used in this thesis (for more details see Silverman 1986). The basic idea of this method is to apply a smooth weight function (called the *kernel* function) to estimate the probability density at any given point, using a number of neighbouring data points. The term 'adaptive' here means that the kernel width depends on the actual density, so that, for example, the smoothing is done over a larger area if the density is smaller.

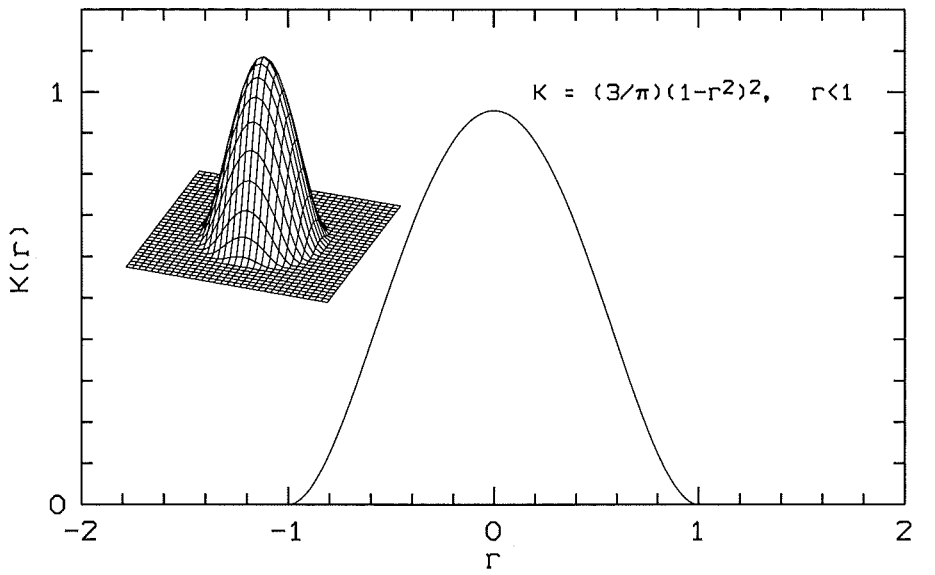

Figure 3.11: *Kernel function $K(r)$ used for the probability density estimation.*

The following definition of the adaptive kernel estimator, $\hat{f}(\vec{\xi})$, is used (see page 101 of Silverman 1986), defined at an arbitrary point $\vec{\xi} = (U, V)$:

$$\hat{f}(\vec{\xi}) = \frac{1}{n} \sum_{i=1}^{n} \frac{1}{h^2 \lambda_i^2} K\left(\frac{\vec{\xi} - \vec{\xi}_i}{h \lambda_i} \right), \tag{3.1}$$

where $K(\vec{r})$ is the kernel function, λ_i represents the local bandwidth factors (dimensionless numbers controlling the overall kernel width at each data point), and h is a general smoothing factor. It is also assumed that there are n data points $\vec{\xi}_i = (U_i, V_i)$. The actual function $K(\vec{r})$ is a 2-D radially symmetric version of the *biweight* kernel (Figure 3.11), and is defined as:

$$K(r) = \begin{cases} \frac{3}{\pi}(1 - r^2)^2, & r < 1, \\ 0, & r \geq 1, \end{cases} \tag{3.2}$$

so that $\int K(\vec{r}) d\vec{r} = 1$ (a condition that any kernel must satisfy in order to produce an estimate $\hat{f}$ as a proper probability density function).

The local bandwidth factors (λ_i), needed for the computation of $\hat{f}(\vec{\xi})$, are defined as:

$$\lambda_i = \left[\frac{\hat{f}(\vec{\xi}_i)}{g} \right]^{-\alpha}, \tag{3.3}$$

where g is the geometric mean of $\hat{f}(\vec{\xi}_i)$:

$$\ln g = \frac{1}{n} \sum_{i=1}^{n} \ln \hat{f}(\vec{\xi}_i) \tag{3.4}$$

and α is a *sensitivity parameter*, which is fixed here at $\alpha = 0.5$ (a typical value for the two-dimensional case). Note that in order to compute λ_i (3.3) one needs the distribution

estimate $\hat{f}(\vec{\xi})$ (3.1), which, in turn, can be computed only when all λ_i are known. This problem, however, can be solved iteratively, by starting with an approximate distribution (a fixed kernel estimate, for example), and then improving the function, as well as the λ_i factors, in a couple of subsequent iterations.

An optimal value for the smoothing parameter h is determined using the least-squares cross-validation method, by minimizing the so-called score function:

$$M_0(h) = \int \hat{f}^2 \; - \; \frac{2}{n} \sum_{i=1}^{n} \hat{f}_{-i}(\vec{\xi}_i). \tag{3.5}$$

The integral $\int \hat{f}^2$ in (3.5) can be computed numerically, while $\hat{f}_{-i}(\vec{\xi}_i)$ is the density estimate at $\vec{\xi}_i$, constructed from all data points *except* $\vec{\xi}_i$. It can be shown that minimizing $M_0(h)$ is *equivalent* (in terms of mathematical expectation) to minimizing the integrated square error $\int (\hat{f} - f)^2$, so that the estimate $\hat{f}$, based on the optimal value for h, is as close as possible to the true distribution f, using the data set available. In the present case (for the whole sample of stars), the minimum of $M_0(h)$ was found at $h = 10.7$ km s^{-1}.

The UV-distribution of stellar velocities with respect to the Sun is shown in Figure 3.12, both as a scatter plot and a smooth contour plot representing the density function $\hat{f}(U, V)$, as computed using the adaptive kernel method described above. The computations have been performed on a grid of square bins having a base of 2 km s^{-1} each. This choice for the bin size has been made taking into account a typical uncertainty in the velocity components, as mentioned earlier (Figure 3.10). The density function has also been rescaled by a multiplication factor nS, where $n = 4597$ is the total number of stars and $S = 4$ km^2 s^{-2} is the area covered by a square bin. The numerical value of the transformed distribution at any given bin is therefore equal to the average number of stars falling in that particular bin (assuming that the current estimate $\hat{f}$ is close to the real distribution f).

The distribution in Figure 3.12 is obviously not uniform, showing some concentrations that have been associated with the Hyades, Pleiades, Sirius and other young moving groups (see e.g. Figueras et al. 1997, Chereul et al. 1997). A closer examination, however, reveals an additional pattern of inhomogeneities on a somewhat larger scale. At least three long *branches* (called here: the Sirius branch, the middle branch and the Pleiades branch, respectively from top to bottom) can be identified by eye. The branches are slightly curved but are almost parallel and are running diagonally across the diagram with a negative slope. The branches have been traced in a preliminary way by following the local maxima (ridge lines) in the UV-distribution, as shown by the dashed lines in Figure 3.12.

It was demonstrated in Section 3.2 that the parallax uncertainty could produce some radially-elongated features in the UV-plane (Skuljan et al. 1997), since the stars tend to move radially relative to the zero point ($U = 0$, $V = 0$) when their parallax is changed. However, this effect would create some branches converging to the zero point, which is clearly not the case in Figure 3.12. A conclusion can be made that the parallax uncertainty

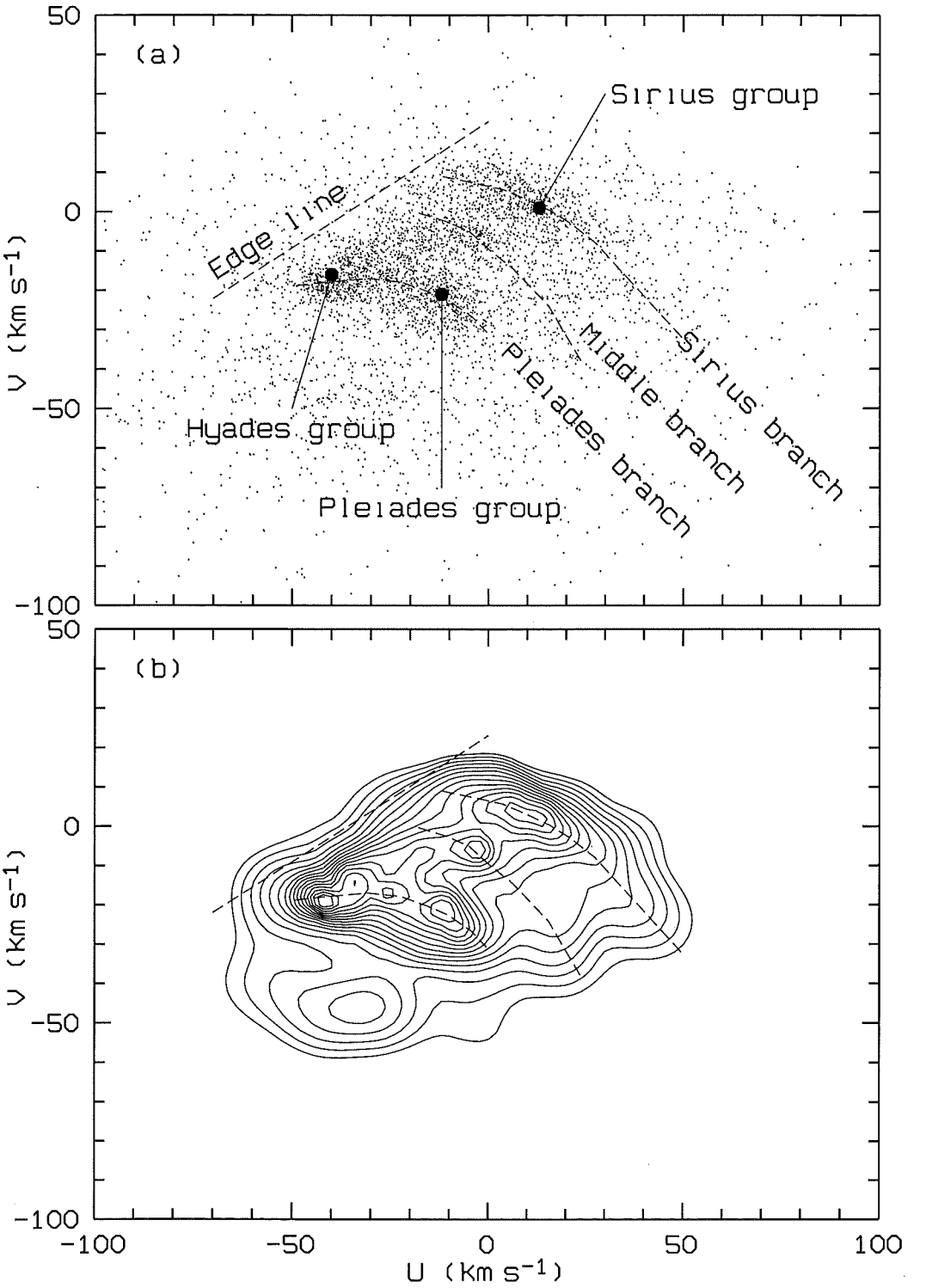

Figure 3.12: *The distribution of stellar velocities in the UV-plane, shown as (a) a scatter plot, and (b) a contour plot of the probability density function on a logarithmic scale. The density function has been obtained using the adaptive kernel method (see text). The three main moving groups are marked as filled circles in (a). The three hypothetical branches and the 'edge line' are shown as dashed lines.*

cannot be responsible for the distribution found.

Besides the three branches described above, there seems to exist a fairly sharp 'edge line' at an angle of about $+30°$ relative to the U-axis, connecting the lower-U extremities of the branches and defining a region above the line where only a few stars can be found. Apparently all the stars seem to occupy the lower part of the UV-plane, bounded by the 'edge line' and the Sirius branch. In such a situation, the traditional velocity-ellipsoid approach does not seem to be appropriate any more.

It would be interesting to compare the distribution from Figure 3.12 to similar diagrams obtained by other authors (Asiain 1998; Asiain et al. 1999a; Chereul et al. 1998, 1999; Dehnen 1998b). In particular, Figure 3 of Dehnen (1998b) demonstrates all basic features that are introduced here, although their distribution was obtained *without* any explicit radial velocities. This clearly suggests that the kinematic bias (Binney et al. 1997) does not affect significantly the inner parts of the UV-distribution, as already mentioned above.

The branch-like velocity distribution, as revealed by analysing the Hipparcos data, is not easy to understand. It may be due to the galactic spiral structure itself, or some other global characteristics of the galactic potential (resonance effects perhaps) combined with the initial velocities at the time of star formation. A possibility also exists that this is a result of a sudden burst of star formation that took place some time ago in several adjacent spiral arms. At this stage, however, no firm conclusions about these speculations can be made. A detailed analysis of stellar orbits in the solar neighbourhood, as well as some more comments on the branch-like velocity distribution introduced here, will be presented in Chapter 4.

3.6 The wavelet transform

In order to determine the precise nature and the statistical significance of the features seen in Figure 3.12, the *wavelet transform* technique has been chosen to analyse the data. There are many examples in the literature demonstrating how this powerful tool can be used in different areas (e.g. Slezak et al. 1990, 1993, 1994; Chereul et al. 1997; Grebenev et al. 1995). Nevertheless, some of the most important properties, relevant to this work, will be pointed out here, concentrating on the two-dimensional case only.

To do a wavelet transform of a function $f(x, y)$, a so-called *analysing wavelet* $\psi(\frac{x}{a}, \frac{y}{a})$ is defined, which is simply another function of a suitable shape (or another family of functions), where a is the *scale* parameter. By fixing the scale parameter, a wavelet of a given particular size is selected out of a family characterized by the same shape ψ. The wavelet transform $w(x, y)$ is then defined as a *correlation* function, so that at any given point (ξ, η) in the XY-plane, one real value for the transform is obtained:

$$w(\xi, \eta) = \int_{-\infty}^{\infty} \int_{-\infty}^{\infty} f(x, y)\, \psi(\frac{x - \xi}{a}, \frac{y - \eta}{a})\, dx\, dy. \tag{3.6}$$

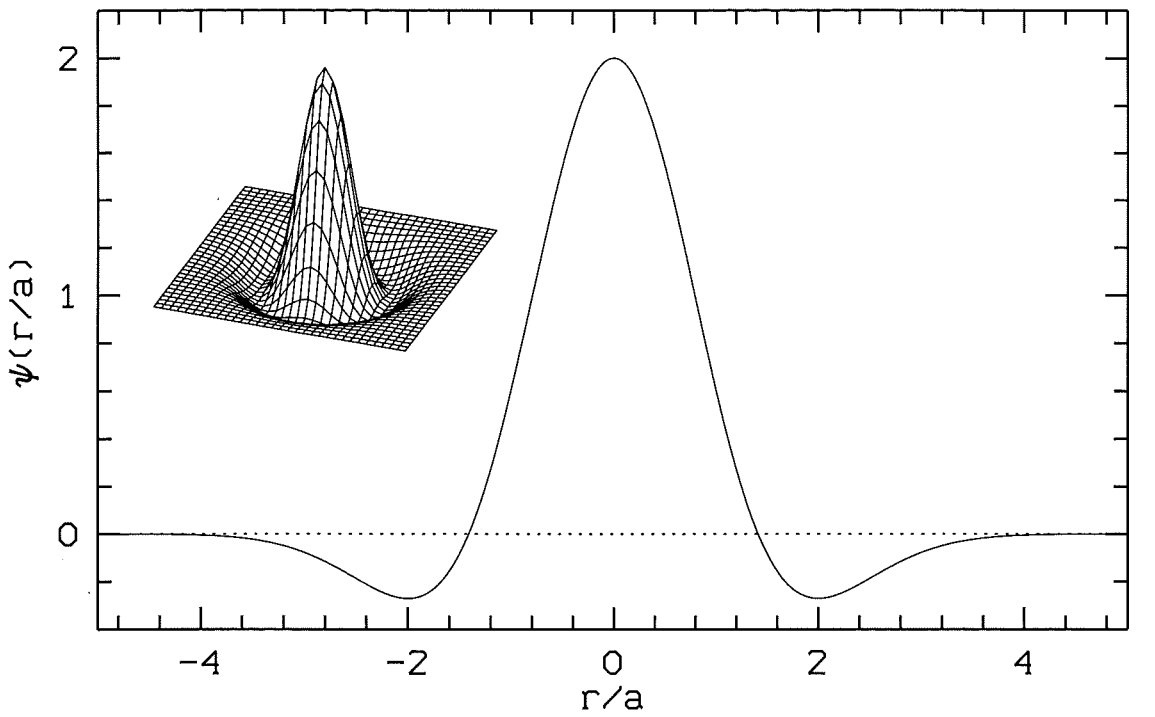

Figure 3.13: *The Mexican hat in two dimensions.*

This quantity $w(\xi, \eta)$ is usually called the *wavelet coefficient* at (ξ, η). Since the analysis is typically made in a discrete case, having a certain finite number of bins in the XY-plane, this means that a finite number of wavelet coefficients will be obtained from (3.6), one value per bin.

The actual choice of the analysing wavelet ψ depends on the particular application. When a given data distribution is searched for certain *groupings* (over-densities) then a so-called *Mexican hat* is most commonly used (e.g. Slezak et al. 1990). A two-dimensional Mexican hat (Figure 3.13) is given by:

$$\psi(r/a) = \left(2 - \frac{r^2}{a^2}\right) e^{-r^2/2a^2}, \tag{3.7}$$

where $r^2 = x^2 + y^2$. The main property of the analysing wavelet ψ is that the total volume must be equal to zero, which is what enables the detection of any over-densities in a given data distribution. The wavelet coefficients will all be zero if the analysed distribution is uniform (the integral of ψ is always zero). But if there is any significant 'bump' somewhere in the distribution, the wavelet transform will give a positive value at that point. Moreover, if the Mexican hat is normalized using a factor a^{-2}, then it is possible to estimate the half-width of the 'bump', by simply varying the scale parameter a. The wavelet coefficient in the centre of the bump will reach its *maximum value* if the scale a is exactly equal to σ, assuming that the 'bump' is a gaussian of a form: $\exp(-\rho^2/2\sigma^2)$, where ρ represents the distance from the centre.

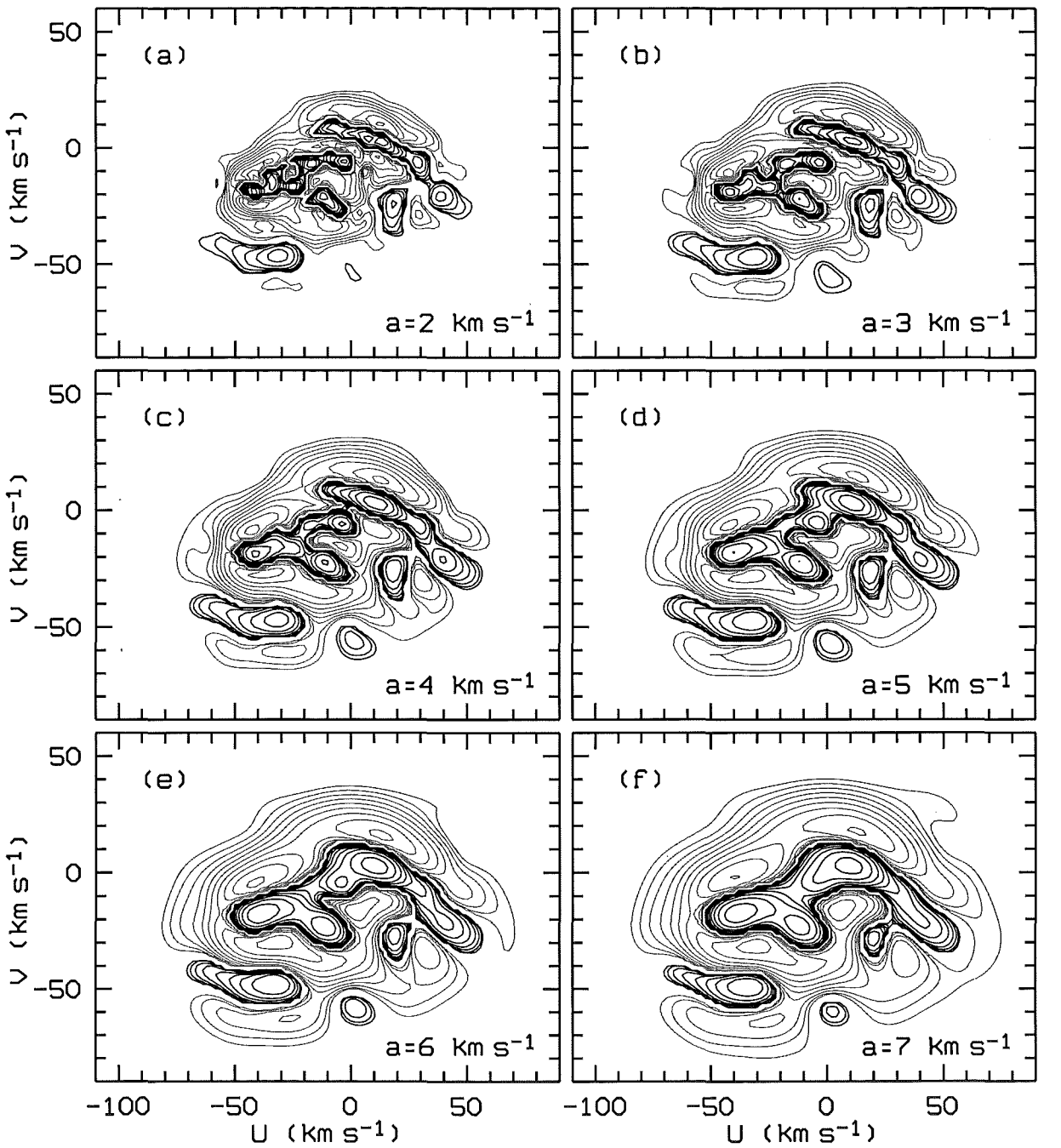

Figure 3.14: *Wavelet transforms of the smooth UV-distribution at several different scales. Solid black lines represent positive contours, while grey lines are used for negative values.*

Many authors choose the scale in such a way that it gives the maximum wavelet transform. This is an attractive option providing straightforward information on the average half-width of the gaussian components in the distribution being analysed. However, there are some situations when somewhat smaller scales would be preferred, in order to separate two close components or to detect some narrow but elongated features.

Several different scales have been applied to the *UV*-distribution from Figure 3.12b, and

the results are shown in Figure 3.14. The positive contours (black lines) describe the regions where there is an over-density of stars (grouping), while the negative contours (grey lines) show the regions with star deficiency (under-density). Attention will be concentrated here only on the positive values. At about $a \sim 4 - 5$ km s^{-1} the normalized wavelet coefficients reach their maxima around the most populated parts of the UV-plane (except the Hyades moving group, where the maximum wavelet transform occurs somewhere below 2 km s^{-1}, i.e. at a scale less than the bin size).

3.7 Confidence levels

An important question at this stage is *how probable* are the features revealed in Figure 3.14, i.e. what are the confidence levels for the contours to be above the random noise? A commonly used procedure to estimate the probabilities in such a case is numerical simulation (sometimes called the Monte Carlo method) based on random number generators (see e.g. Escalera & Mazure 1992).

The distribution in Figure 3.12b will be considered again. By smoothing the probability density function, an average number of stars $\overline{N}_*$ has been found in each bin (to be more precise, an *optimal estimate* of the average value has been found, as close as possible using the data set available). On the other hand, the *observed* number of stars N_* in each bin has a *statistical uncertainty*. This is not only due to the measurement errors. Even if the velocities have no random errors (or extremely small errors, i.e. much less than the bin size) there are still statistical fluctuations related to the finite sample. One can expect that the observed number of stars N_* in each bin will fluctuate following the Poisson distribution, with an average of $\overline{N}_*$. This means that the observed histogram can be regarded as *a single outcome* from an infinite set of possibilities, when the star counts in every bin are allowed to fluctuate according to the Poisson statistics. One can numerically simulate those "other possibilities" and create the distributions (random copies) that "could have happened". If any feature of the distribution is found repeating from one copy to another, then one can be confident that the feature is real, i.e. not generated by noise. In fact, the number of successful appearances divided by the total number of simulations will give the probability of the feature being real.

This idea is used here to find the probabilities that the wavelet coefficients are *positive*, since a positive coefficient is automatically an indicator that there is some grouping in the UV-plane. The process begins with generating a large number ($N = 1000$) of Poisson random copies of the smooth histogram from Figure 3.12b. Then, for each of these copies, a replica of the original data set is derived, by creating N_* stars randomly distributed over each bin (in total, a number of stars close to $n = 4597$ will be obtained for all bins together). Finally, the new data set is treated in the same way as the original: the density function is estimated by

applying the adaptive kernel method[1], and then the wavelet transform of the corresponding smooth histogram is computed. This enables the examination of each coefficient (w) over the whole set of simulations, and the computation of the probability, such that the value is positive. If there are $N_{\rm p}$ simulations with $w > 0$ then a corresponding probability is: $P(w > 0) = N_{\rm p}/N$. This procedure has been repeated for all wavelet transforms that are presented in this thesis. Typically, the features shown have a 90 per cent (or better) probability of being real.

3.8 The data analysis

Although this analysis can be carried on by examining the whole sample of stars, one should be aware of the fact that the stellar kinematic properties may depend on the age. It is reasonable to assume that younger stars have better chances of still keeping the 'memory' of their original velocities that they acquired at formation. If there is any grouping in velocity space, and if the grouping is only a result of cluster evaporation (Eggen's hypothesis), then one would expect to see it most prominently amongst the youngest stars.

In this thesis, the stellar ages are not dealt with explicitly, but the spectral type (more precisely the $B-V$ colour index) is used as an age indicator. The whole sample of stars has been divided into two groups:

1. 1036 early-type stars with $B-V < 0.3$, and
2. 3561 late-type stars with $B-V > 0.3$,

by choosing $B-V = 0.3$ as an arbitrary division point, corresponding approximately to the boundary between the A and F spectral classes. The terms 'early-type' and 'late-type' should be regarded here as suitable names to be used in this thesis only. Note that the present late-type group contains spectral classes F and later, with two distinct clumps (main sequence F stars, plus K giants) as seen in Figure 3.8. Analysing the Hipparcos catalogue, Dehnen & Binney (1998) found Parenago's discontinuity at $B-V = 0.61$, which means that most of the stars blue-ward of that are *younger* than the galactic disk itself. This applies to the F stars in the present sample. A conclusion can be made that the early-type group (spectral classes B–F) contains predominantly young stars, while the late-type group (F–M) is a mixture of older and younger main-sequence stars, rather young red-clump stars, and a few old red giants. The first group should better show the young moving groups and it will allow comparison with the results of other authors. On the other hand, the second group should possibly show the old-disk moving groups (if they exist) that can be compared with Eggen's results.

[1]In order to reduce the computing time, the original smooth distribution is used to compute λ_i directly for every random data set, and the same optimal smoothing factor is assumed.

3.8.1 Early-type stars

The adaptive kernel method has been applied again to derive the probability density function $f(U,V)$ for the 1036 early-type stars. An optimal value for the smoothing parameter in this case is $h = 8.1$ km s^{-1}. The smooth distribution, together with the corresponding wavelet transforms at several different scales, is shown in Figure 3.15. The three branches are well separated and easily detected. Although the 'middle branch' is not sufficiently long for a separate analysis, it will be nevertheless treated as an 'incomplete' branch. The maximum wavelet transform is at about $a = 4$ km s^{-1}, which also corresponds to an average half-width of the branches.

In order to determine the *edge line*, the 5-per-cent level (relative to the maximum) of the smoothed UV-histogram has been used, as indicated in Figure 3.15a. By fitting a straight line to the corresponding portion of the contour, the tilt of $\alpha \approx 32°$ is found ($\tan\alpha \approx 0.62$), and the edge line is estimated to follow the equation $V = 16.4$ km s^{-1} $+ 0.62\,U$.

The tilt of the branches (assuming that they all have the same tilt) has been computed by rotating the wavelet transform (Figure 3.15b) counter-clockwise and examining the distribution along V only (taking a sum of all positive wavelet coefficients at a given V). At an angle of $\beta \approx 25°$ ($\tan\beta \approx 0.47$) the three branches appear as the narrowest (and strongest) gaussians, which means that the tilt of the branches in the UV-plane is $-25°$. The following three equations are found for the branches, which are shown in Figure 3.15:

$$\left.\begin{array}{rcrcll} V_1 &=& 7.6 \text{ km s}^{-1} &-& 0.47\,U & \text{(Sirius branch)},\\ V_2 &=& -8.9 \text{ km s}^{-1} &-& 0.47\,U & \text{(middle branch)},\\ V_3 &=& -26.6 \text{ km s}^{-1} &-& 0.47\,U & \text{(Pleiades branch)}. \end{array}\right\} \qquad (3.8)$$

It should be noted, however, that these three linear relations describe the branches well enough only relatively far from the edge line. The branches seem to curve and follow the edge line at their lower-U extremity. This is especially the case with the Pleiades branch.

Figure 3.16 presents the one-dimensional distribution in the direction perpendicular to the branches ($\beta \approx 25°$) so that each branch appears as a single peak at a fixed position. The zero point of the relative velocity scale has been centred on the middle branch. The three branches are approximately equidistant, with a separation of about 15 km s^{-1}.

3.8.2 Late-type stars

The distribution function in the UV-plane for the 3561 late-type stars has been computed using an optimal smoothing factor of $h = 13.6$ km s^{-1}. The contour diagrams of the distribution and the corresponding wavelet transforms at several different scales, are shown in Figure 3.17. Comparing this with the early-type case in Figure 3.15, a similar pattern is found, although somewhat more complex. Besides the three main branches, there are now some new details, such as a concentration of stars at about $(20, -30)$ km s^{-1} (possibly

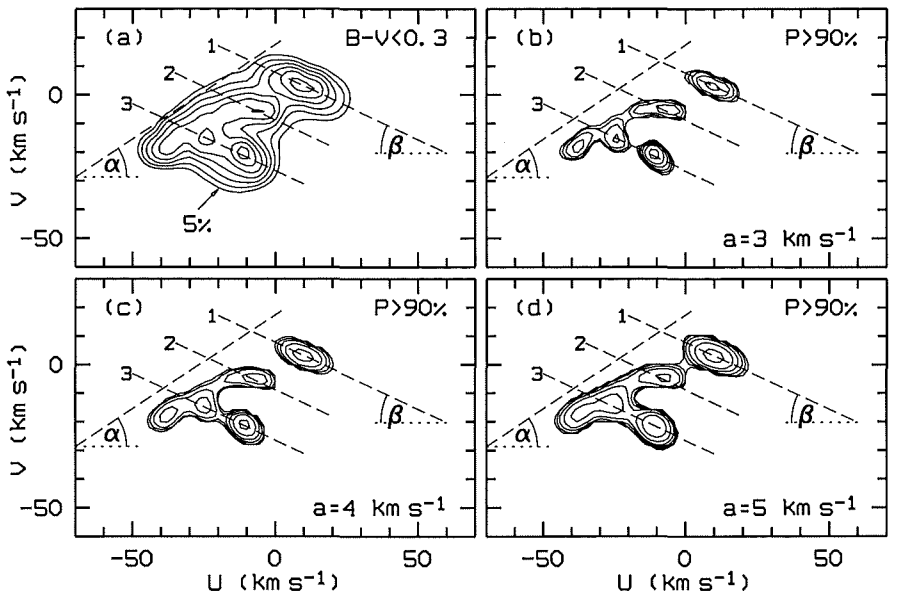

Figure 3.15: *(a) The velocity distribution of early-type stars, together with (b–d) the corresponding wavelet transforms (90 per cent confidence) at several different scales. The dashed lines are used to mark the branches and the edge line (see text for equations of lines).*

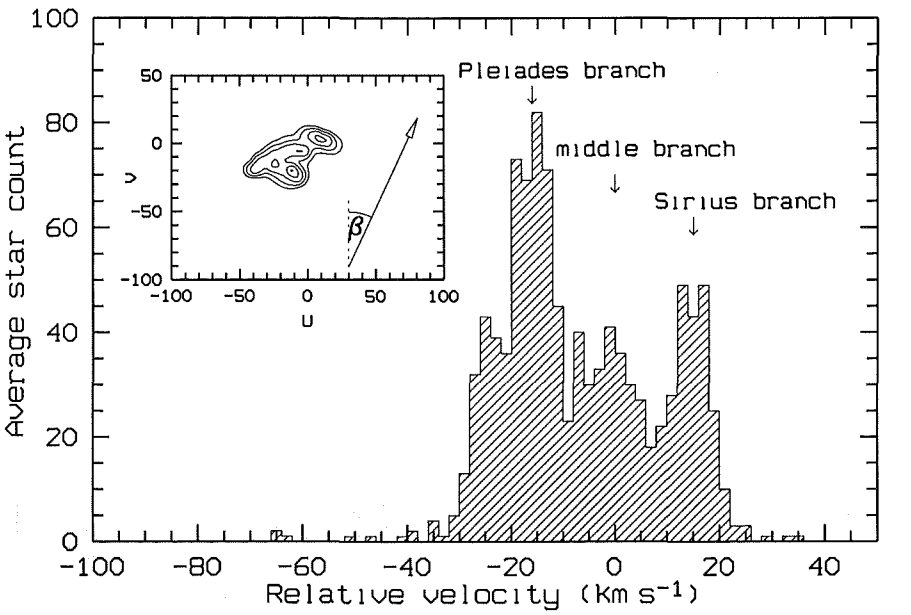

Figure 3.16: *The one-dimensional velocity distribution of early-type stars along an axis perpendicular to the branches (the direction indicated in the inserted image).*

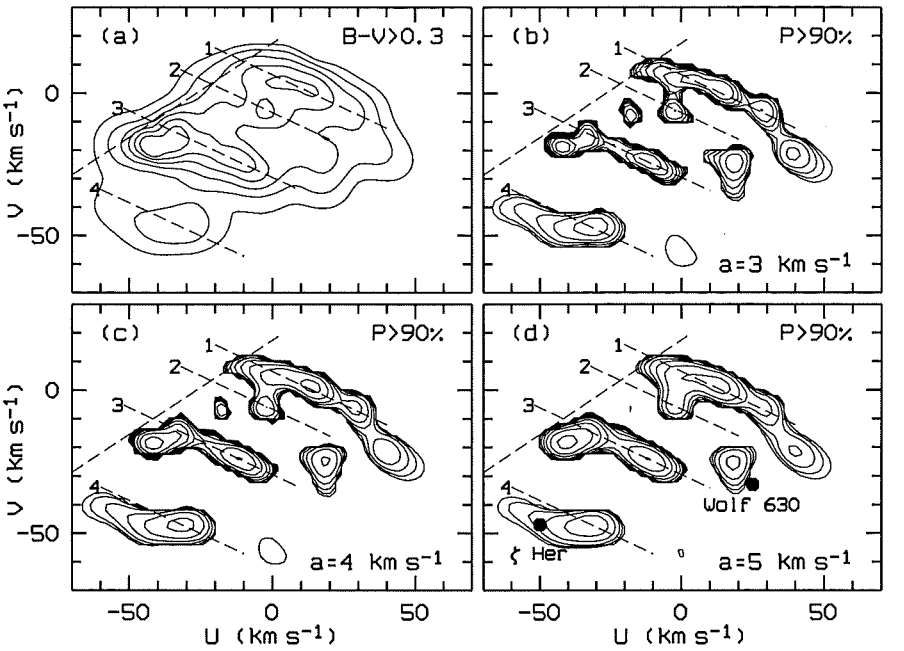

Figure 3.17: *(a) The velocity distribution of late-type stars, and (b-d) the corresponding wavelet transforms (90 per cent confidence) at several different scales. The dashed lines are used to mark the branches and the edge line (see text for equations). Two of Eggen's old-disk moving groups are presented in (d), for reference only.*

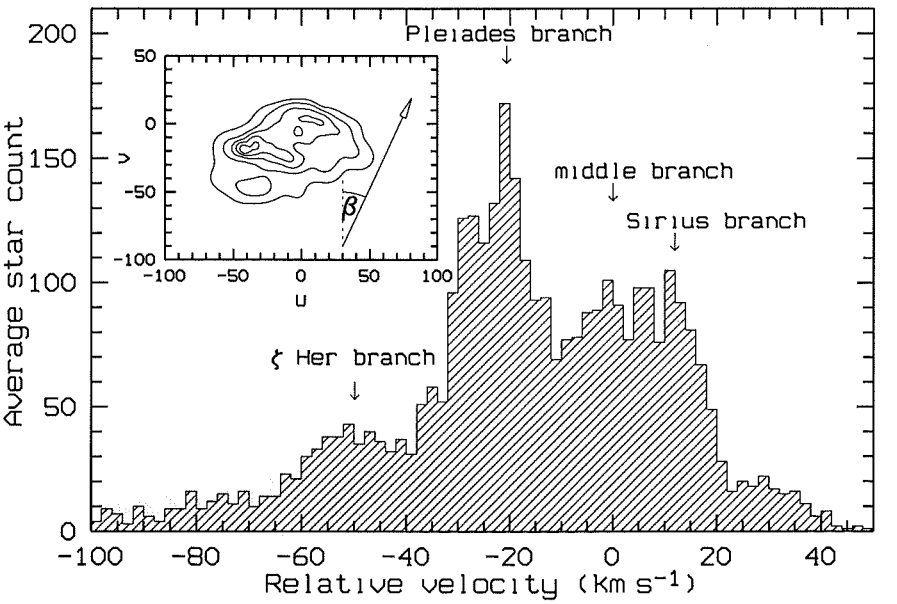

Figure 3.18: *The one-dimensional velocity distribution of late-type stars along an axis perpendicular to the branches (the direction indicated in the inserted image).*

another fragment of the middle branch), as well as a new branch in the bottom part of the diagram, at $(-30, -50)$ km s^{-1}. In order to get the new features named, two of Eggen's old-disk moving groups are introduced here, Wolf 630 and ζ Herculis, also marked in Figure 3.17d. One can simply use the fact that these two Eggen's moving groups (Eggen 1965b; Eggen 1971c) agree well with the features revealed by the wavelet transforms, although the question of the interpretation of such a correlation is still to be answered.

In order to find the positions of the branches in Figure 3.17, one could perhaps proceed as when dealing with the early-type stars. However, the branches now seem longer, and possibly curved (especially the Sirius branch), so that the above procedure for determining the angle β does not seem to be appropriate any more. On the other hand, there is not enough data to do a more sophisticated analysis including the curvature of the detected features. A new approach was to adopt the same inclination angle of $\beta \approx 25°$, as derived from the early-type stars, and then simply find the positions of the branches from the rotated one-dimensional distribution shown in Figure 3.18. The equations for the branches are:

$$\left.\begin{array}{rcrcll} V_1 &=& 6.9 \text{ km s}^{-1} &-& 0.47U & \text{(Sirius branch)}, \\ V_2 &=& -7.0 \text{ km s}^{-1} &-& 0.47U & \text{(middle branch)}, \\ V_3 &=& -29.2 \text{ km s}^{-1} &-& 0.47U & \text{(Pleiades branch)}, \\ V_4 &=& -62.0 \text{ km s}^{-1} &-& 0.47U & (\zeta \text{ Herculis branch}). \end{array}\right\} \quad (3.9)$$

There is also a possible hint of a weak fifth branch (see Figure 3.18) at a relative velocity of about +30 km s^{-1}. An overall impression is that the branches are roughly equidistant, with a separation slightly larger than for the early-type stars. With one additional branch, an average separation is now about 20 km s^{-1}. If this 'periodicity' is real, then a two-dimensional Fourier transform of the distribution will show some peaks in the power spectrum, as will be demonstrated in the following section.

3.9 The Fourier transform

The two-dimensional power spectrum $Q(f_U, f_V)$ of the smooth UV-histogram for the whole sample of stars (square root of the power spectral density) is shown in Figure 3.19. Most of the total power is concentrated within the central bulge (maximum power density of about 4700), corresponding to a roughly gaussian distribution of the stars in the UV-plane. There are also two relatively strong side peaks (maximum power density of about 920) symmetrically arranged around the central bulge at frequencies $(\pm 0.008, \pm 0.031)$ s km^{-1}, as well as two higher harmonics at $(\pm 0.016, \pm 0.054)$ s km^{-1}. The peaks are arranged along a straight line at an angle of $\gamma = 74°$ (the dashed line in Figure 3.19a). Some other features can also be seen at relatively high significance levels, but attention will be concentrated here only on the aligned peaks. They define a planar wave in the velocity plane. Of course, the

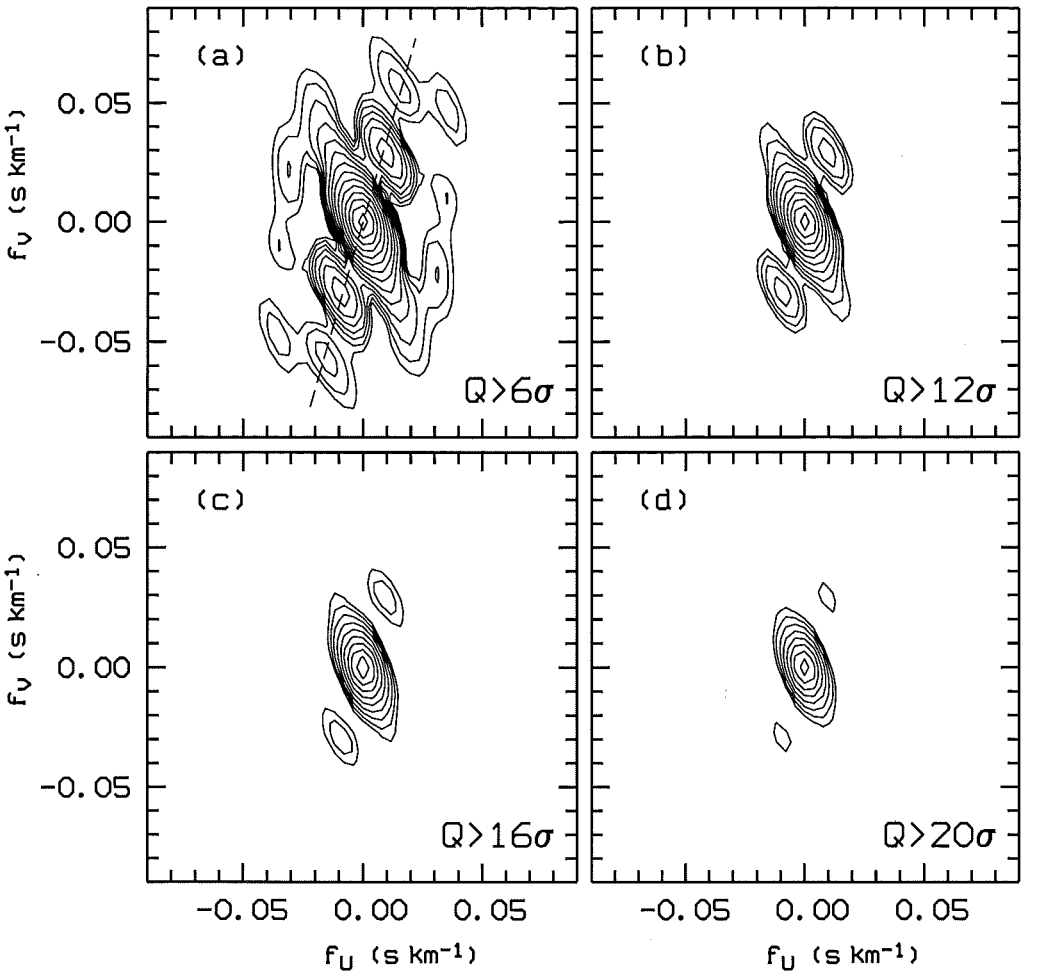

Figure 3.19: *The two-dimensional power spectrum $Q(f_U, f_V)$ of the velocity distribution for the whole sample of stars, at several levels of significance. The strongest peaks are aligned at $\gamma \approx 74°$, as indicated by the dashed line in (a).*

peaks at negative frequencies are simply symmetrical images of the positive ones, without any additional information, so that they can be ignored in this discussion.

In order to estimate the significance of the features in the power spectrum, a numerical simulation procedure was applied, in a similar way as when treating the wavelet transforms. A large number of random copies have been used to see how the power spectral density fluctuates at any given frequency point. The standard deviation σ, has been computed for each bin and the ratio Q/σ has been used as a measure of significance.

Every peak in the power spectrum can be related to a planar wave propagating in a certain direction, with a frequency $f = \sqrt{f_U^2 + f_V^2}$. A period of about 33 km s^{-1} has been found for the stronger side peak (the one closer to the central bulge), and about 17 km s^{-1} for the first harmonic. These values are in good agreement with the wavelet transform analysis: the longer period corresponds to the separation between the two most prominent branches

in the UV-distribution (Sirius and Pleiades), while the second one can be related to the remaining weaker branches. It should be noted, however, that the power spectrum obviously contains much more information than extracted here, and a more detailed analysis is needed.

3.10 Geneva photometry and metal abundances

The problem of the reality of moving groups also involves a study of the chemical compositions of stars. If it is assumed that a moving group consists of stars of the same origin (the moving group hypothesis), then the metal abundances could serve as an additional membership criterion. In principle, one would expect significantly less dispersion in abundances inside a moving group, than in a general sample of stars. It would also be interesting to check if the abundances are dispersed less inside those branches in the velocity plane, in which case a conclusion could be made that the branch-like structure is a result of a certain star formation process in the Galaxy.

The metal abundance in a stellar atmosphere is usually expressed as a ratio between the concentrations of iron (Fe) and hydrogen (H), on a logarithmic scale, and relative to the Sun, which is denoted as [Fe/H]:

$$[\mathrm{Fe/H}] = \log\left(\frac{N_{\mathrm{Fe}}}{N_{\mathrm{H}}}\right)_{*} - \log\left(\frac{N_{\mathrm{Fe}}}{N_{\mathrm{H}}}\right)_{\odot}, \tag{3.10}$$

where N_{Fe} and N_{H} are concentrations of iron and hydrogen (number of atoms per unit volume). A value of [Fe/H] = 0 means that the star has the solar abundance. Positive values correspond to abundances greater than solar, while negative values correspond to abundances less than solar.

The most reliable method for deriving the metal abundance involves the equivalent-width measurements of spectral lines, using high-resolution stellar spectra. There are some catalogues of [Fe/H] determinations, such as that by Cayrel de Strobel et al. (1997), containing 3247 stars. However, the total number of stars having their metal abundances determined in this way is relatively small, so that other methods are needed for more extensive stellar samples in the solar neighbourhood.

A reliable abundance can also be derived from some photometric observations, by comparing the total flux measured in different spectral regions (multi-colour photometry). It has been demonstrated that some combinations of colour indices, such as: $m_1 = (v-b)-(b-y)$ in Strömgren's *uvby* system (see e.g. Crawford 1975; Crawford & Perry 1976), or: $m_2 = (B_1 - B_2) - 0.457\,(B_2 - V_1)$ in the seven-colour Geneva system (see e.g. Golay 1980; Hauck 1978), are sensitive to line-blanketing effects and therefore can be used for estimating the metal abundance.

In this thesis the seven-colour Geneva Observatory photometric system (Rufener 1989; Golay 1980, 1973) has been used to derive the metal abundances for the stars involved in

the moving group study. One of the main reasons for this choice is that the Geneva system represents a homogeneous set of measurements obtained with the same instrument, for a large number of stars ($\sim$ 30 000), including those of late spectral types. The system is based on seven filters, denoted as: U, B_1, B, B_2, V_1, V, G. The response curves are shown in Figure 3.20, using the data from Rufener & Maeder (1971).

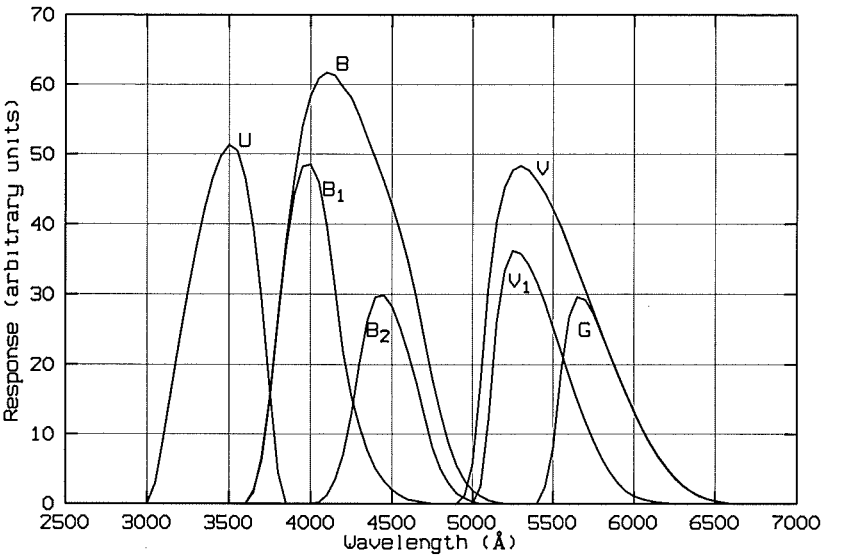

Figure 3.20: *The seven filters used in the Geneva photometric system.*

There are 29397 stars in the fourth edition of the catalogue (a CD-ROM version by the Astronomical Data Center). All stars are presented in Figure 3.21, in a form of a typical colour-colour diagram, similar to Johnson's $U-B$ versus $B-V$ plot. A detailed analysis of this diagram can be found in Golay (1980). The reddening lines are clearly seen in the upper-left portion of the plot, while at least two prominent loci of stars (main-sequence dwarfs and late-type giants) are found well separated in the lower-right section.

Four multicolour parameters are defined in the Geneva photometric system:

$$\left.\begin{aligned} d &= (U-B_1) - 1.430\,(B_1-B_2), \\ \Delta &= (U-B_2) - 0.832\,(B_2-G), \\ g &= (B_1-B_2) - 1.357\,(V_1-G), \\ m_2 &= (B_1-B_2) - 0.457\,(B_2-V_1), \end{aligned}\right\} \tag{3.11}$$

so that they are all reddening free, as can be easily checked by plotting their values versus B_2-V_1. The reddening lines appear horizontal in these plots, as is demonstrated for the parameter m_2 in Figure 3.22. The multicolour parameters (3.11) will not all be analysed in this thesis (for more details see e.g. Golay 1980). Attention will be concentrated here only on m_2, since this parameter has been demonstrated to be sensitive to the metal abundance, as already mentioned above.

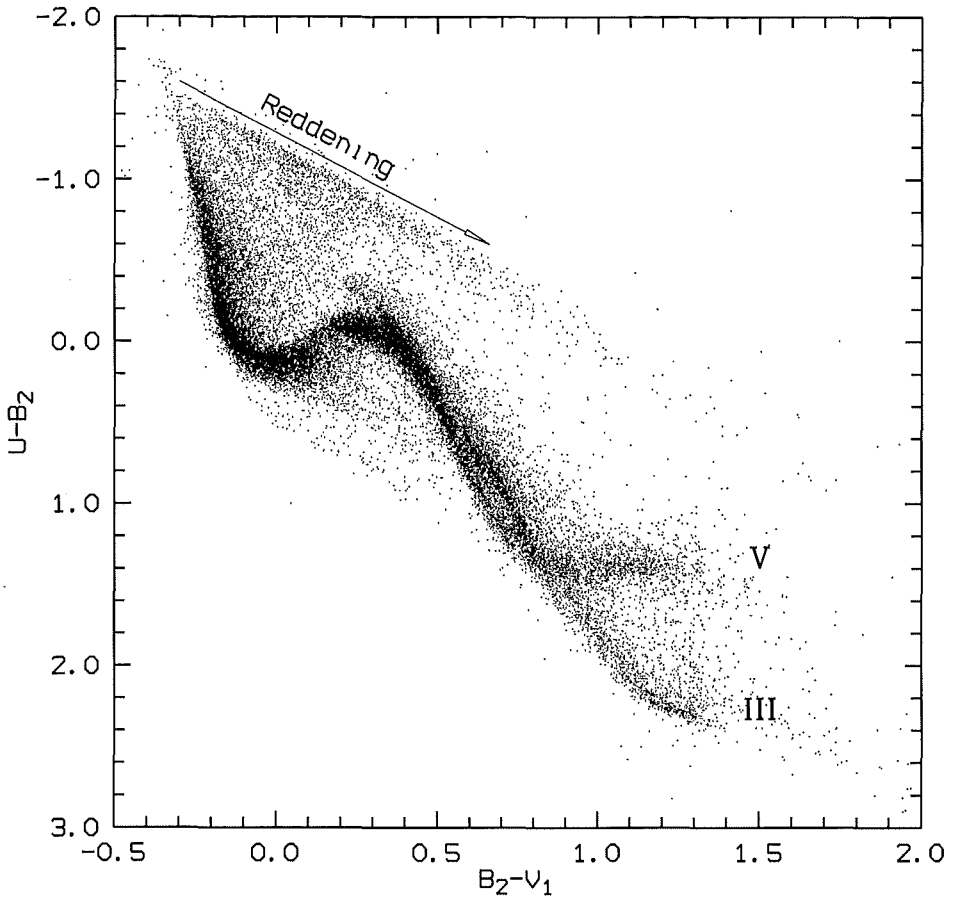

Figure 3.21: *A typical colour-colour diagram for the 29397 stars measured in the Geneva photometric system. The reddening effect is clearly seen, and the luminosity classes V and III appear well separated.*

A standard procedure is to derive a new differential parameter Δm_2 (sometimes called the *blanketing parameter*), defined as:

$$\Delta m_2 = m_2(\text{star}) - m_2(\text{Hyades}), \tag{3.12}$$

where m_2(Hyades) is an average value for the Hyades cluster, taken at the same value of the $B_2 - V_1$ colour index. It can be shown that there exists a linear relation between the parameter Δm_2 and the iron abundance [Fe/H] (Hauck 1973, 1978; Hauck et al. 1985; Hauck 1986). Typically, only the early spectral types A to F (sometimes including G) have been considered at relatively high metallicities, [Fe/H] > -0.6. The metal-deficient stars are normally excluded from these studies. Sometimes a quadratic relation is derived over a wider range of metallicities, including the metal-deficient stars ($-2.13 \leq$ [Fe/H] ≤ 0.5 in Berthet 1990), but restricted again to the spectral types A–F. Some authors combine the Geneva photometry with other photometric systems in order to obtain a more reliable calibration for some classes of stars. For example, Flynn & Morell (1997) used broad-band Cousins *RI* photometry to fit the effective temperatures and then they included Geneva B_1 magnitudes

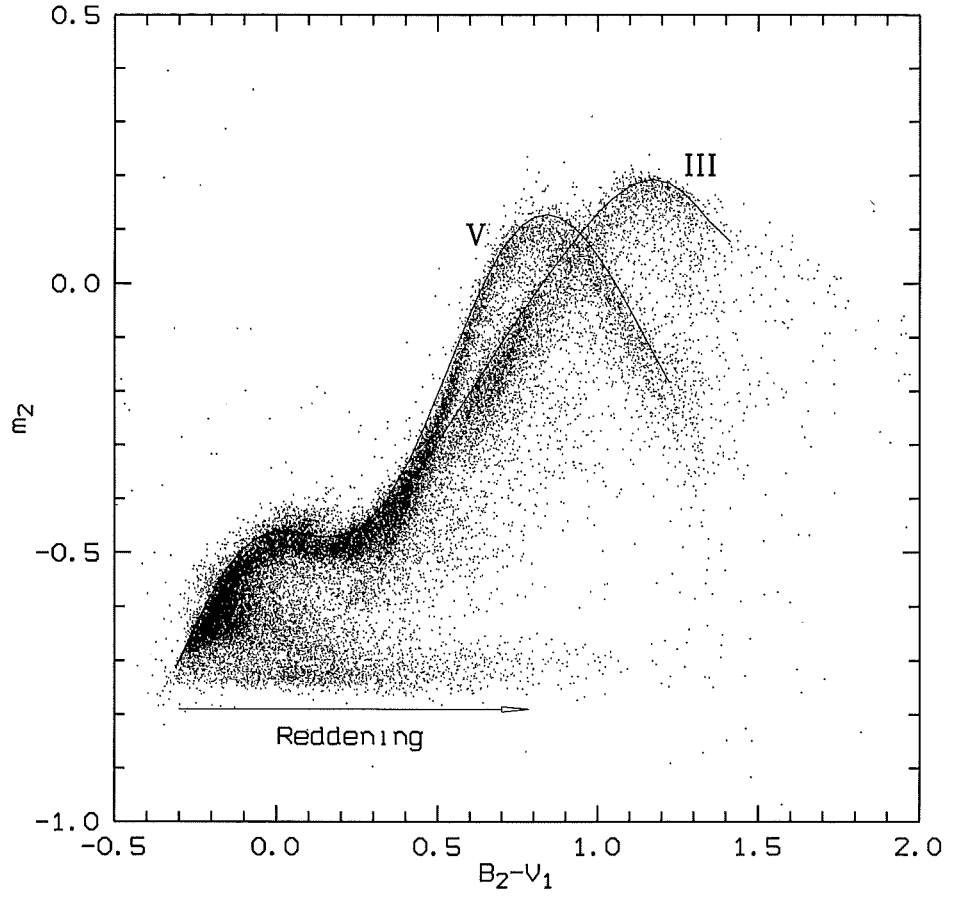

Figure 3.22: *A typical plot of the parameter m_2 (see Equations 3.11) against $B_2 - V_1$. The reddening lines appear horizontal. The reference loci V and III (see Equations 3.13) are shown as solid lines.*

to fit the metal abundances for G and K dwarfs. In fact, no existing calibration has been available for the class III giants, which represent a significant portion of the present sample of stars in the solar neighbourhood (see Figure 3.8).

A new calibration of the blanketing parameter Δm_2 in terms of [Fe/H] has been derived in this thesis. A slightly different definition for Δm_2 (compared to 3.12) has also been adopted, so that the reference locus is not based on the Hyades. A reason for doing this is that the Hyades sequence cannot be used for K giants in the same way as is normally used in the case of main-sequence stars. If the relation (3.12) were directly applied to the K giants, some meaningless values for Δm_2 would be obtained. Having no suitable sequence of giant stars of the same metallicity, one can derive a mean reference locus for the stars marked as III in Figure 3.22. The Δm_2 value derived in this way will be relative to an average value for all K giants in the solar neighbourhood. In fact, the same procedure can also be applied in the case of the main-sequence stars, by defining a mean locus for stars marked as V in Figure 3.22. This will eliminate any systematic differences in the Δm_2 values between the luminosity classes III and V.

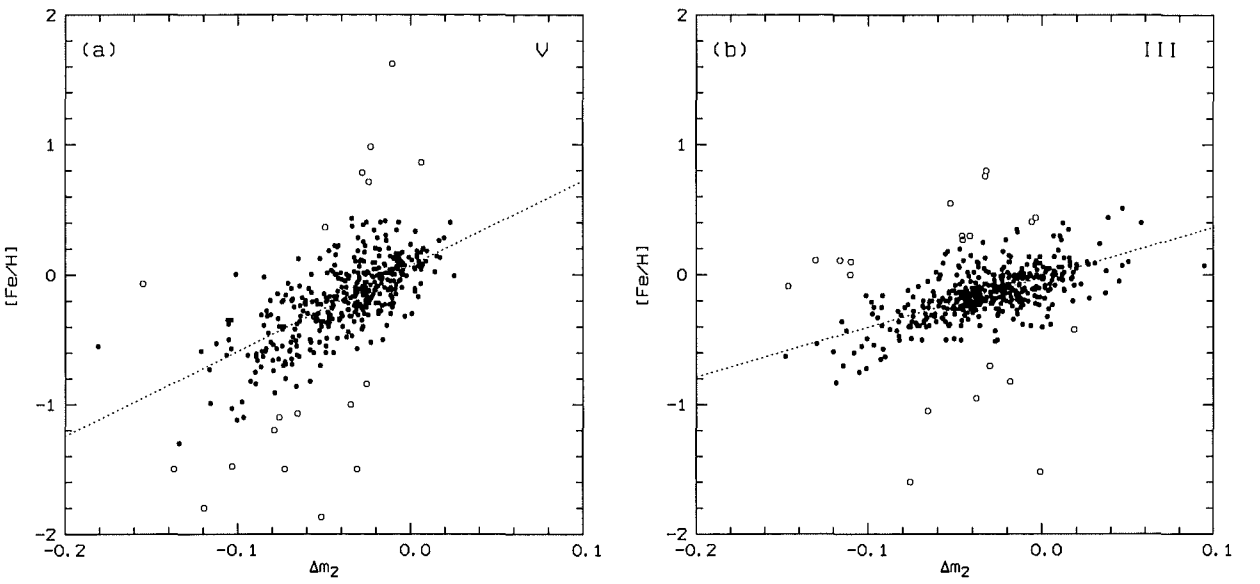

Figure 3.23: . *Calibration of the blanketing parameter Δm_2 in terms of the metal abundances* [Fe/H], *for (a) the main-sequence stars, and (b) the giants of the luminosity class III. The linear least-square fit is indicated by a dashed line (see Equations 3.14). The stars actually used for the fit are represented by the full dots, while the open circles are used for the rejected stars (with the residuals greater than 3σ).*

The new relations for the parameter Δm_2 are:

$$\left.\begin{array}{rcll} \Delta m_2 & = & m_2(\text{star}) - m_2(\text{V}) & (\text{luminosity class V}), \\ \Delta m_2 & = & m_2(\text{star}) - m_2(\text{III}) & (\text{luminosity class III}). \end{array}\right\} \tag{3.13}$$

The reference loci m_2(V) and m_2(III) are defined as shown in Figure 3.22. First, some arbitrary points are set along the upper edge of each sequence[2]. Then a polynomial is fitted to the selected points so that m_2 can be evaluated at any $B_2 - V_1$ colour.

Two stellar samples (for the two luminosity classes, as described above) were constructed for this calibration process, by taking the Hipparcos survey stars of a given luminosity class with known Geneva photometry and metal abundances (using the catalogue by Cayrel de Strobel et al. (1997) as a source of the abundances). There are 416 such stars of luminosity class V, and 441 stars of class III, as presented in Figure 3.23. Some of those stars (about 5 per cent of the total number) had to be rejected, due to the large deviation from the fitted line (open circles in Figure 3.23).

The following relations between Δm_2 and [Fe/H] were derived for the two samples:

$$\left.\begin{array}{rcll} \text{Class V:} \quad [\text{Fe/H}] & = & 6.560\,\Delta m_2 + 0.066 & (N = 395, \sigma = 0.202), \\ \text{Class III:} \quad [\text{Fe/H}] & = & 3.831\,\Delta m_2 - 0.019 & (N = 421, \sigma = 0.143), \end{array}\right\} \tag{3.14}$$

[2]The upper edge is used because it is relatively well defined. This can introduce a systematic offset in the Δm_2 values, but will not affect the final calibration of metal abundances.

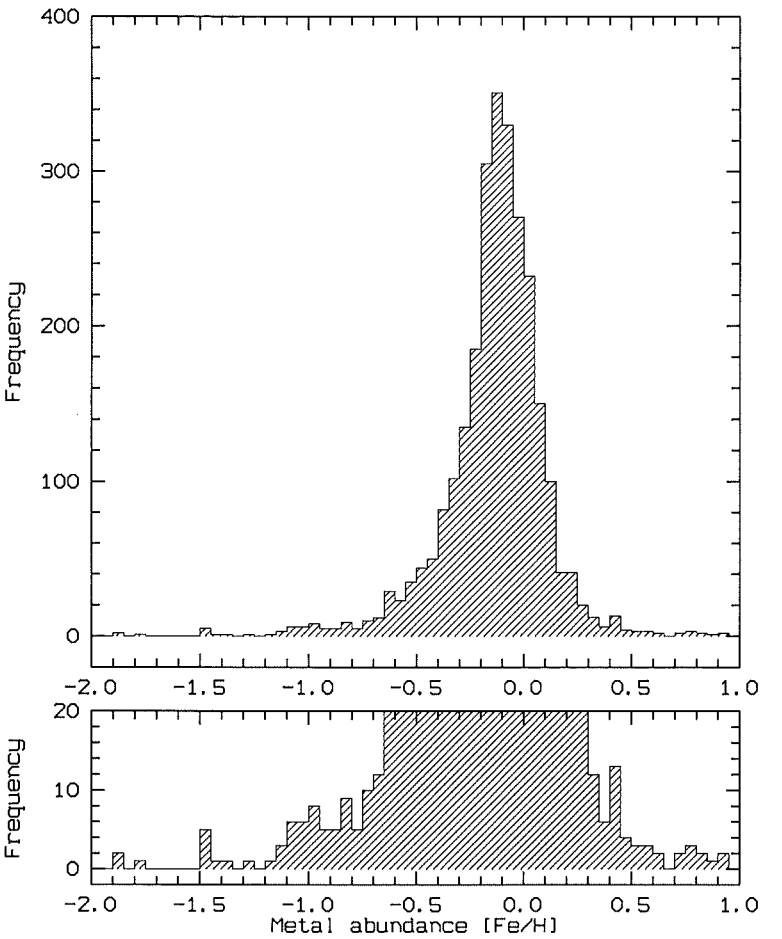

Figure 3.24: *Distribution of metal abundances in the solar neighbourhood as derived from the Geneva photometry of 2666 stars of luminosity classes V and III. The bottom diagram shows an enlarged portion of the histogram including frequencies less than 20.*

where N is the number of stars used (with residuals less than 3σ), and σ is the r.m.s. error of the linear fit. The first relation, with a slope of 6.56, is in good agreement with some published results, ranging roughly between 5 and 7 (e.g. Hauck 1978; Hauck et al. 1985). The second one, with a significantly smaller slope of only 3.83, indicates that the blanketing parameter is less sensitive to the metallicity in the case of the class III giants. Nevertheless, the two relations (3.14) can be successfully used to estimate the metal abundances for a significant number of stars in the solar neighbourhood.

There are 1106 stars with known metal abundances (using the [Fe/H] catalogue by Cayrel de Strobel et al. 1997), out of 4597 Hipparcos stars in the sample introduced in Section 3.4. An additional number of 1158 main-sequence stars, as well as 402 class III giants, with unknown metallicities, but with available Geneva photometry have been extracted. This makes a total number of 2666 stars, which is about 58 per cent of the initial sample. A standard histogram of the metallicities determined in this way is presented in Figure 3.24, with an average value of $\overline{[\mathrm{Fe/H}]} = -0.12$ and a standard deviation of $\sigma = 0.18$ (excluding

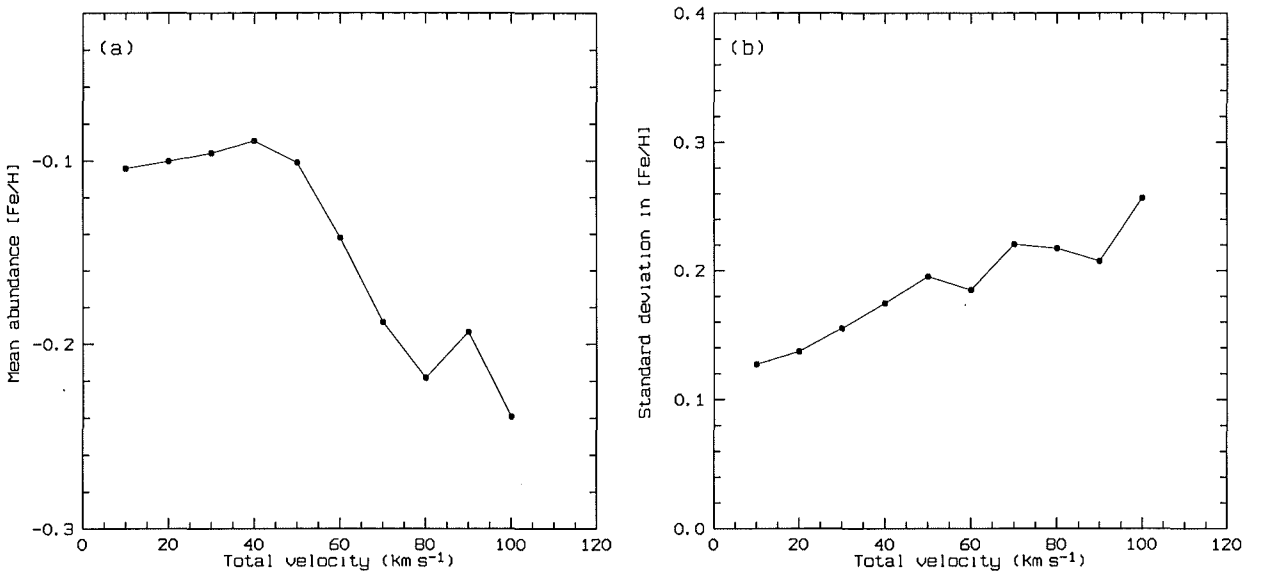

Figure 3.25: *Statistical properties in metal abundances at different velocities. The UV-plane has been divided into circular zones,* 20 km s^{-1} *wide.*

those points with deviations $|[\mathrm{Fe/H}] - \overline{[\mathrm{Fe/H}]}| > 3\sigma$). No obvious features in the distribution can be associated with grouping effects in the velocity plane.

A closer examination reveals a correlation between the statistical properties of the metal abundances and the kinematics. If the velocity plane is divided into circular zones (rings) centred at the zero point (velocity of the Sun), so that each zone corresponds to a single value of the total velocity ($\sqrt{U^2 + V^2}$) in the galactic plane, then the mean metallicity and the corresponding standard deviation will vary from one zone to another, as seen in Figure 3.25. The mean abundances tend to decrease at higher velocities, which is almost certainly a stellar age effect, as a combination of two well known observational facts:

1. A decrease in metal abundance with age (see e.g. Eggen et al. 1962, or Binney & Tremaine 1987, p. 576, Fig. 9-7).

2. An increase in velocity dispersion with age (see e.g. Mihalas & Binney 1981, p. 431, Fig. 7-5).

Due to their larger velocity dispersion, older stars dominate at higher velocities, producing a lower average metal abundance. Apart from this, an additional slow increase in the metallicity *dispersion* at higher velocities is seen in Figure 3.25b. Once again, this is easy to understand, having in mind that high-velocity stars move in eccentric orbits so that any sample of high-velocity stars can include stars of different metal abundances, originating from different regions in the Galaxy[3].

[3]There is a radial gradient of stellar metallicities in the Galaxy so that the abundances decrease when the radius increases. A value of $\partial[\mathrm{Fe/H}]/\partial R = -0.09 \pm 0.02$ dex kpc^{-1} can be found e.g. in Wielen et al. (1996).

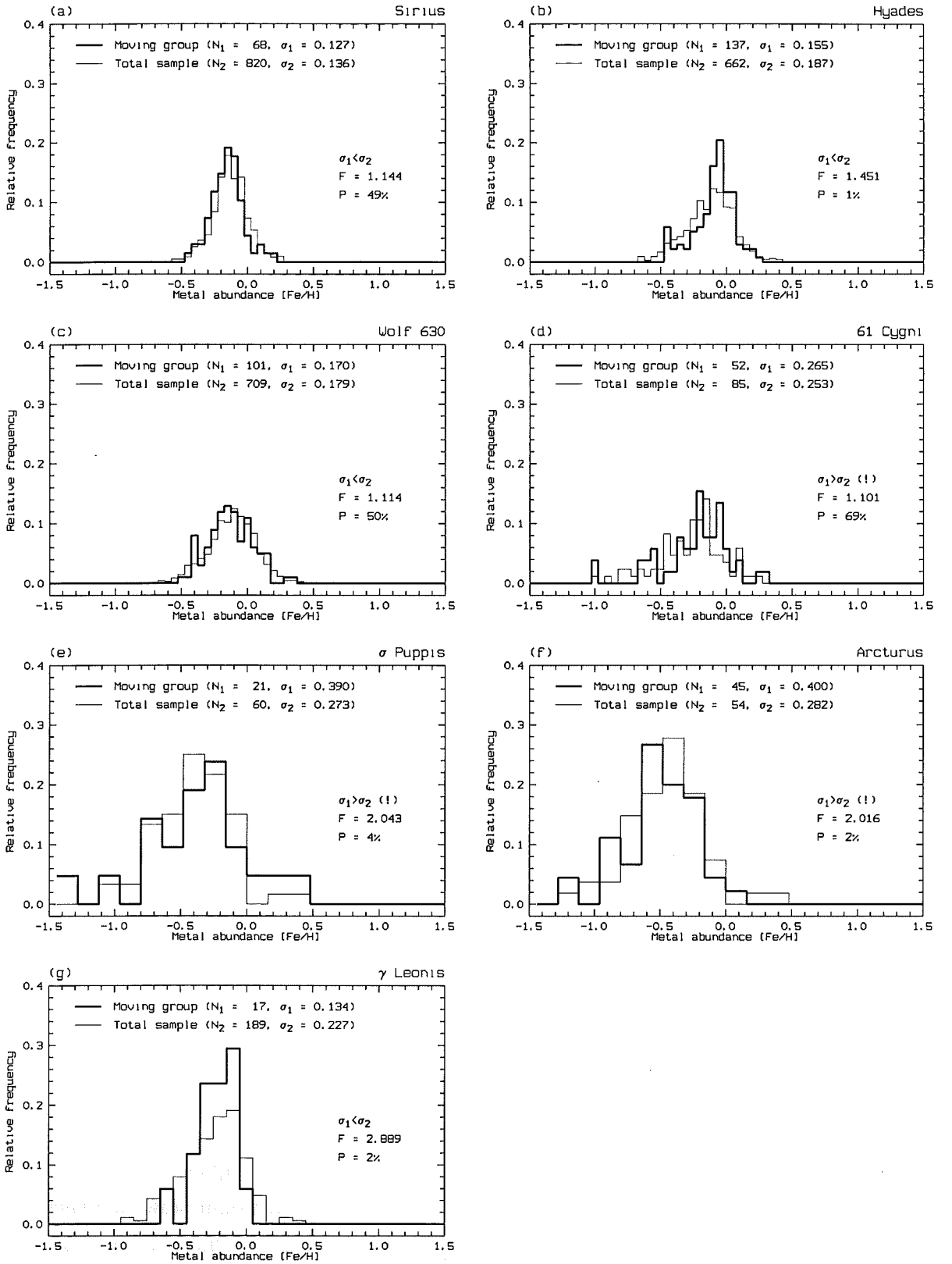

Figure 3.26: *Metallicity distributions for moving groups (bold lines) compared with a total sample of stars at the same value of the space velocity (thin lines). The results of the F-tests are given as explained in the text.*

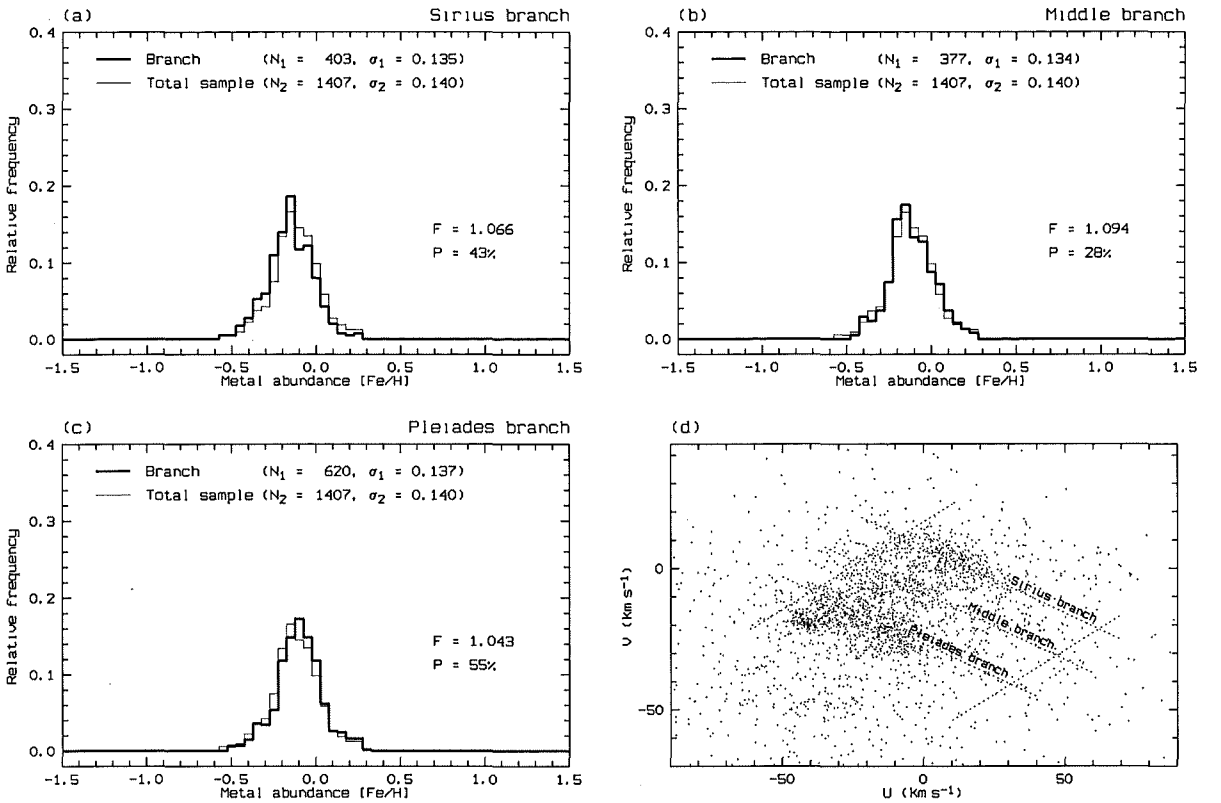

Figure 3.27: *(a–c) Metallicity distributions for the UV-branches (bold lines) compared with the total sample of stars (thin lines). (d) The three main branches in the UV-plane (the dashed lines are explained in the text).*

A series of statistical tests have been performed on the metal abundances in order to check if the values in the moving groups are scattered less than in the total sample of stars. The results of these tests are presented in Figure 3.26. In order to avoid the effect of correlation between the metallicities and stellar velocities (as described above), a separate "total sample" of stars is used with each moving group, depending on the position in the *UV*-plane. For each of the seven largest moving groups introduced in Section 3.2 (see Figure 3.1), the standard deviation (σ_1) has been computed using all stars with known metallicities. In addition, a total sample of stars has been constructed inside a circular zone of a radius equal to the space velocity of each moving group (the same width of 20 km s^{-1} has been used as before, when constructing the zones in Figure 3.25). A corresponding standard deviation (σ_2) for the total sample has been computed as well.

The null hypothesis ($H_0 : \sigma_1 = \sigma_2$) was tested for each moving group by applying the *F-test*, comparing the variances of two normal populations[4]. The statistic F is defined as the ratio of the larger variance to the smaller one, so that a value of F much greater than

[4]Strictly speaking, the F-test can be applied only on two independent normal distributions. No tests have been performed in this thesis in order to check if the distributions are exactly normal. In addition, some of the moving-group stars are also found in the total sample, but this overlapping can be neglected.

one indicates that the null hypothesis should be rejected (i.e. the two populations have significantly different variances). A significance level P has been computed for each case, representing the probability that an error will be made if the null hypothesis is rejected.

As is clearly seen from these plots, in some of the cases (Figures 3.26a, c, d) there are no statistical reasons for rejecting the null hypothesis. A high value for P means that the variances σ_1 and σ_2 are probably the same. Only in the case of the Hyades and γ Leonis groups (Figures 3.26b and g), are there indications that the stars belonging to the group demonstrate significantly less scatter in metallicities than the total sample of stars around the same space velocity. On the other hand, the dispersions in the two remaining groups (Figures 3.26e and f) are even larger than in the total sample.

An additional set of F-tests has been performed on the global branch-like structure in the velocity plane, as introduced in Section 3.5 (see also Figure 3.12). The three main branches have been extracted here using equations (3.8), so that each branch covers a velocity range of ± 8 km s^{-1} above and below the central line (approximately half way between the branches). In addition, only the low-velocity portion of the UV-plane is considered, situated below the 'edge' line, i.e. $V < 16.4$ km s^{-1} $+ 0.62\,U$, and also above an arbitrary lower limit of $V > -60$ km s^{-1} $+ 0.62\,U$, which is simply parallel to the edge line, but shifted towards negative V values (both lines are shown in Figure 3.27d). There are 1407 stars inside these limits, in all three branches together, and the metal abundances have a total standard deviation of $\sigma_2 = 0.140$. However, there are no significant differences between the dispersions in individual branches compared to the total dispersion, as confirmed by the F-tests presented in Figure 3.27.

This examination of stellar metallicities in the solar neighbourhood completes the analysis of the Hipparcos data presented in this thesis. In the next chapter a numerical model of the galactic gravitational potential will be developed and the orbits of moving groups will be studied.

Chapter 4

Galactic orbits

4.1 Coordinates and basic parameters

Numerical modelling of the galactic gravitational potential is a powerful tool for studying the kinematics and dynamics of stellar systems. For a given set of starting stellar positions and velocity vectors, galactic orbits can be computed for these stars by means of numerical integration of the equations of motion. The only requirement is that the galactic gravitational potential is known at any point in space and time. As a result it is possible to examine both the past and future positions and velocities of stars, which provides a simple practical way of studying moving groups.

Before proceeding with a numerical model of the galactic potential, a definition of the coordinate system will be given, as well as definitions of some basic parameters regarding the position and velocity of the Sun.

A galactic system of coordinates was already introduced in Chapter 1, in order to express the space velocity components of stars in the solar neighbourhood. The same reference frame is also used in Appendix A.2. However, this is always a *local* reference frame, centred at the Sun, suitable only for studying the stars in the solar vicinity. When the whole Galaxy is considered, then a *galactocentric* system is defined, with its origin at the centre of the Milky Way. The easiest way to do this is to preserve the existing orientation of axes, and simply translate the heliocentric reference frame to the galactic centre, as shown in Figure 4.1. The lower-case letters are now used for the galactocentric coordinates, with the x-axis pointing away from the Sun, y-axis in the direction of galactic rotation at the Sun, and z-axis towards the north galactic pole. A corresponding set of cylindrical coordinates (R, ϑ, z) is also used, where $R^2 = x^2 + y^2$, and $\tan\vartheta = -y/x$. The angle ϑ is measured *clockwise* from the negative direction of the x-axis, following the galactic rotation, so that $\vartheta = 0°$ corresponds to the direction towards the Sun.

One of the basic assumptions involved with any model of our Galaxy is the exact position and velocity of the Sun. To a first approximation, the Sun can be assumed to be located

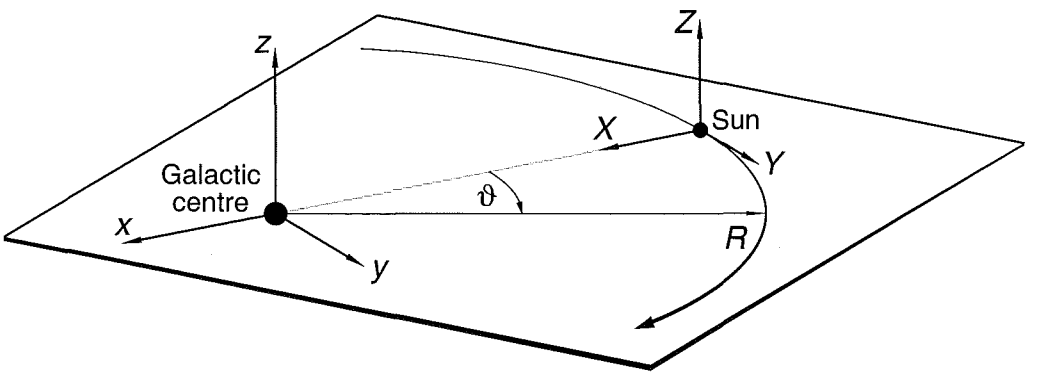

Figure 4.1: *Galactocentric coordinates (xyz), and heliocentric (local) coordinates (XYZ). The two reference frames are translated relative to each other along the x-axis by an amount equal to the Sun's distance from the galactic centre.*

in the galactic plane, so that its position is determined by its distance from the galactic centre or, in other words, by the radius of the corresponding circular orbit, R_0. The velocity of a circular motion at this radius is V_0. An imaginary point moving in a circular orbit at the radius R_0 and with the velocity V_0 is called the Local Standard of Rest (LSR). The Sun's actual orbit deviates from a circle, so that there is an additional component to its total velocity, called the Sun's *peculiar velocity*, which is measured relative to the LSR. Sometimes a term *solar motion* is used to express the same quantity. However, many authors use this term *solar motion* only to describe a velocity derived from various samples of stars in the solar neighbourhood (e.g. Delhaye 1965; Mihalas & Binney 1981). This may be different from the LSR so that the *solar motion*, defined in this way, usually needs some additional reduction to produce the Sun's *peculiar velocity*.

Many different values for the constants mentioned above have been used in the literature. In this thesis, the standard values for the Sun's distance and the circular velocity will be adopted, as recommended by the IAU (Kerr & Lynden-Bell 1986):

$$\left.\begin{aligned} R_0 &= 8.5 \text{ kpc}, \\ V_0 &= 220 \text{ km s}^{-1}. \end{aligned}\right\} \tag{4.1}$$

The Sun's peculiar velocity, as determined by Delhaye (1965), can be expressed in the local galactic coordinates (see Figures 1.1 and 4.1) as:

$$\left.\begin{aligned} U_\odot &= +9 \text{ km s}^{-1}, \\ V_\odot &= +12 \text{ km s}^{-1}, \\ W_\odot &= +7 \text{ km s}^{-1}, \end{aligned}\right\} \tag{4.2}$$

where a positive value for $U_\odot$ is used instead of the original Delhaye's value, in accordance with the present definition of the galactic axes. The solar peculiar motion (4.2) corresponds to a velocity vector of about 16.5 km s^{-1} in the direction $l = 53°$, $b = +25°$.

In addition to these parameters a small height of the Sun above the galactic plane was also adopted (Gilmore et al. 1989, p. 342):

$$z_\odot = 12 \text{ pc}. \tag{4.3}$$

Together with the value for the radius R_0 (4.1), this gives the exact present position of the Sun:

$$\vec{r}_\odot = \begin{pmatrix} x_\odot \\ y_\odot \\ z_\odot \end{pmatrix} = \begin{pmatrix} -8.500 \\ 0.000 \\ 0.012 \end{pmatrix} \text{ kpc}. \tag{4.4}$$

It is now possible to derive an absolute space velocity vector for the Sun, by adding up the peculiar velocity (4.2) to the circular velocity (4.1):

$$\vec{v}_\odot = \begin{pmatrix} v_{x\odot} \\ v_{y\odot} \\ v_{z\odot} \end{pmatrix} = \begin{pmatrix} +9 \\ +232 \\ +7 \end{pmatrix} \text{ km s}^{-1}. \tag{4.5}$$

With the Sun's position and velocity a transformation law between the galactocentric and heliocentric coordinates takes a simple form:

$$\begin{pmatrix} x \\ y \\ z \end{pmatrix} = \begin{pmatrix} X \\ Y \\ Z \end{pmatrix} + \begin{pmatrix} x_\odot \\ y_\odot \\ z_\odot \end{pmatrix}, \qquad \begin{pmatrix} v_x \\ v_y \\ v_z \end{pmatrix} = \begin{pmatrix} U \\ V \\ W \end{pmatrix} + \begin{pmatrix} v_{x\odot} \\ v_{y\odot} \\ v_{z\odot} \end{pmatrix}. \tag{4.6}$$

4.2 A numerical model

A multi-component model of the galactic potential has been constructed, based on a static *axisymmetric* part, and combined with a rotating *spiral* component. The axisymmetric part of the potential has been taken from Flynn et al. (1996) and can be expressed as a sum of three independent components (central component + disk + dark halo):

$$\Psi_{\text{stat}} = \Psi_{\text{cent}} + \Psi_{\text{disk}} + \Psi_{\text{halo}}, \tag{4.7}$$

where each potential is defined per unit mass of the particle moving in the corresponding gravitational field and is expressed in either cylindrical or spherical coordinates[1].

1. The potential of the central component (in spherical coordinates) is given as a sum of two terms ($k = 1, 2$):

$$\Psi_{\text{cent}}(r) = -\sum_{k=1}^{2} \frac{G\mathfrak{M}_{\text{C}_k}}{\sqrt{r^2 + r_{\text{C}_k}^2}}. \tag{4.8}$$

[1]Due to the axial symmetry, these potentials have the simplest representation in cylindrical coordinates (R, ϑ, z), and they depend only on R and z, but not on ϑ. In addition, the central and halo components are spherically symmetric, depending only on the spherical radius ($r^2 = x^2 + y^2 + z^2 = R^2 + z^2$).

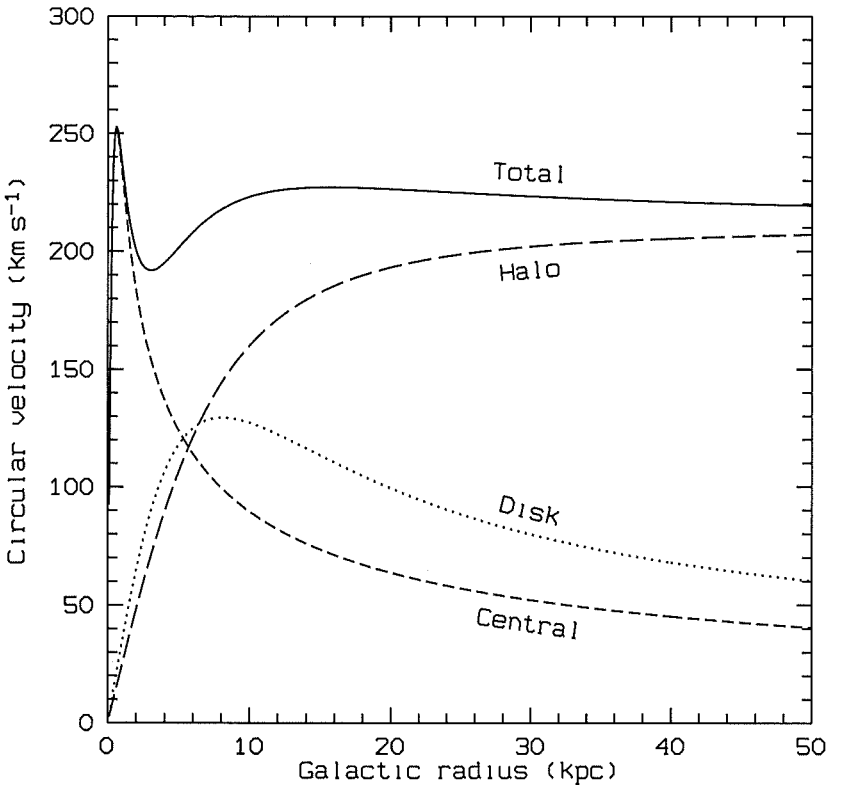

Figure 4.2: *Rotation curves for the galactic potential model by Flynn et al. (1996).*

2. The potential of the disk component (in cylindrical coordinates) is given as a sum of three terms ($k = 1, 2, 3$):

$$\Psi_{\rm disk}(R,z) = -\sum_{k=1}^{3} \frac{G\,\mathfrak{M}_{{\rm D}_k}}{\sqrt{R^2 + (a_k + \sqrt{z^2+b^2})^2}}. \tag{4.9}$$

3. The potential of the dark halo (in spherical coordinates) is represented by:

$$\Psi_{\rm halo}(r) = \frac{1}{2}\,V_{\rm H}^2\,\ln(r^2 + r_0^2). \tag{4.10}$$

In these equations, G is the gravitational constant, while all the other parameters, describing the galactic model itself, are given by Flynn et al. (1996) in their Table 1. The only minor adjustment to these parameters (made in this thesis) concerns the parameter $V_{\rm H}$ in the dark halo component (4.10), which is set to $V_{\rm H} = 210\ {\rm km\,s^{-1}}$, instead of $V_{\rm H} = 220\ {\rm km\,s^{-1}}$ as given by these authors. Actually, the present value was originally provided by the first author (Flynn 1996), before the model was published.

As a numerical test of the gravitational potential model, the *circular velocities* at different galactic radii have been computed, as shown in Figure 4.2. For a given gravitational potential Ψ, the centripetal acceleration, $V_{\rm c}^2/R$, of a circular motion at a radius R, must be equal to the *gradient* of the potential itself:

$$\frac{\partial\Psi}{\partial R} = \frac{V_{\rm c}^2}{R}, \tag{4.11}$$

which gives the circular velocity as:

$$V_c = \sqrt{R\frac{\partial \Psi}{\partial R}}. \tag{4.12}$$

The rotation curves presented in Figure 4.2 are identical to the corresponding curves of Flynn et al. (1996), suggesting that the value of $V_H = 210$ km s^{-1} was also used by those authors. The total rotation curve is approximately flat around the solar radius and beyond ($R \geq 8.5$ kpc) at a value of about 220 km s^{-1}.

In addition to the axisymmetric potential described above, a rotating spiral component was also introduced, to represent the *spiral density wave* propagating through the Galaxy, in accordance with the theory by Lin & Shu (1964) and also Lin et al. (1969). The spiral component is limited to the galactic disk only and it will be assumed that it does not depend on z. In this case the total galactic potential can be expressed as the sum of the static axisymmetric part, $\Psi_{stat}(R, z)$, and a time-dependent spiral component, $\Psi_{spir}(R, \vartheta, t)$:

$$\Psi_{tot} = \Psi_{stat} + \Psi_{spir}. \tag{4.13}$$

A two-arm spiral pattern will be assumed, as proposed by Yuan (1969a, 1969b). The same model has been used by other authors to search for places of formation of various samples of stars (e.g. Wielen 1973; Palouš et al. 1977; Asiain et al. 1999b). The model is based on the assumption that the galactic spiral arms can be approximated by a pair of *logarithmic spirals* (Figure 4.3b), rotating uniformly, as a rigid body, with a *pattern (angular) speed* of:

$$\Omega_p = 13.5 \text{ km s}^{-1} \text{ kpc}^{-1} \tag{4.14}$$

clockwise when seen from the north galactic pole. The Galaxy itself (i.e. the galactic material content) rotates in the same direction, but the rotation is *differential* (depending on the radius). Under the assumption that the rotation curve is exactly flat at $V_c = 220$ km s^{-1} (see Figure 4.2), the angular speed of the galactic rotation is $\Omega_{Gal} = 220/R$ km s^{-1} kpc^{-1}, which is about 26 km s^{-1} kpc^{-1} at the Sun ($R_\odot = 8.5$ kpc). Therefore, the galactic matter in the solar neighbourhood rotates almost twice as fast as the spiral pattern, periodically crossing the spiral arms and the inter-arm regions.

A single logarithmic spiral (Figure 4.3a) can be expressed in polar coordinates (R, ϑ) as:

$$\vartheta - \vartheta_s = -\cot i \, \ln \frac{R}{R_s}, \tag{4.15}$$

where (R_s, ϑ_s) is a suitable reference point on the spiral and i is the *pitch angle* (i.e. the angle between the spiral and a circle at any point[2]). All angles in Figure 4.3 are measured *clockwise* (i.e. opposite from the usual way in mathematics), because this is the direction of the galactic rotation when seen from the north galactic pole. As a consequence of this choice,

[2]This angle is the same at every point along the spiral.

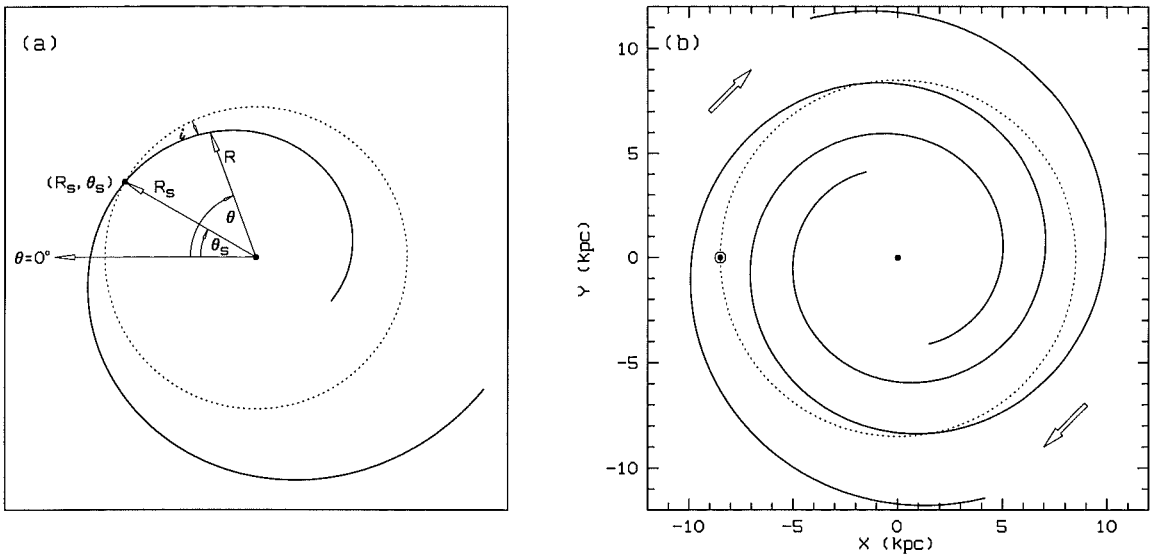

Figure 4.3: *(a) A logarithmic spiral, defined by an arbitrary reference point* (R_s, ϑ_s) *and the pitch angle* i *relative to a circle at any point. (b) A two-arm galactic spiral pattern at* $t = 0$*. The Sun is located in between the arms. The arrows indicate the direction of galactic rotation.*

the pitch angle is *positive* if R decreases as ϑ increases (i.e. if $dR/d\vartheta < 0$), as is the case in Figure 4.3. Otherwise, if $dR/d\vartheta > 0$, the pitch angle would be negative. In our Galaxy the pitch angle is positive, with a value of $i = 6°.2$ (Yuan 1969b).

It should be pointed out that the galactic spiral pattern with the parameters described above has not been generally accepted. Some authors have suggested considerably different values for both the pattern speed and the pitch angle. For example, a pattern speed of $\Omega_p = 23\ \mathrm{km\,s^{-1}\,kpc^{-1}}$ and a pitch angle of $8° - 10°$ (depending on the adopted value for R_0) can be found in Marochnik & Suchkov (1996). An even higher value for the pattern speed of $\Omega_p = 28\ \mathrm{km\,s^{-1}\,kpc^{-1}}$ has been proposed by Mishurov et al. (1997). In their attempt to interpret the mean properties of the velocity field of young stars in the solar neighbourhood, Crézé & Mennessier (1973) have derived a value of $\Omega_p = 20\ \mathrm{km\,s^{-1}\,kpc^{-1}}$ with an indication that the pitch angle might be of the opposite sign! However, those parameters suggested by Yuan (1969b) tend to be in use more often.

It is possible now to construct a gravitational potential Ψ_{spir} in the galactic plane, having logarithmic spirals as equipotential lines, with a cosine-type variation in the perpendicular direction. This potential can be defined as:

$$\Psi_{spir} = -A \cos 2\varphi, \tag{4.16}$$

where A is the amplitude of the potential wave and the phase angle φ has a form:

$$\varphi = \vartheta - \Omega_p t - \vartheta_s + \cot i \ln \frac{R}{R_s}. \tag{4.17}$$

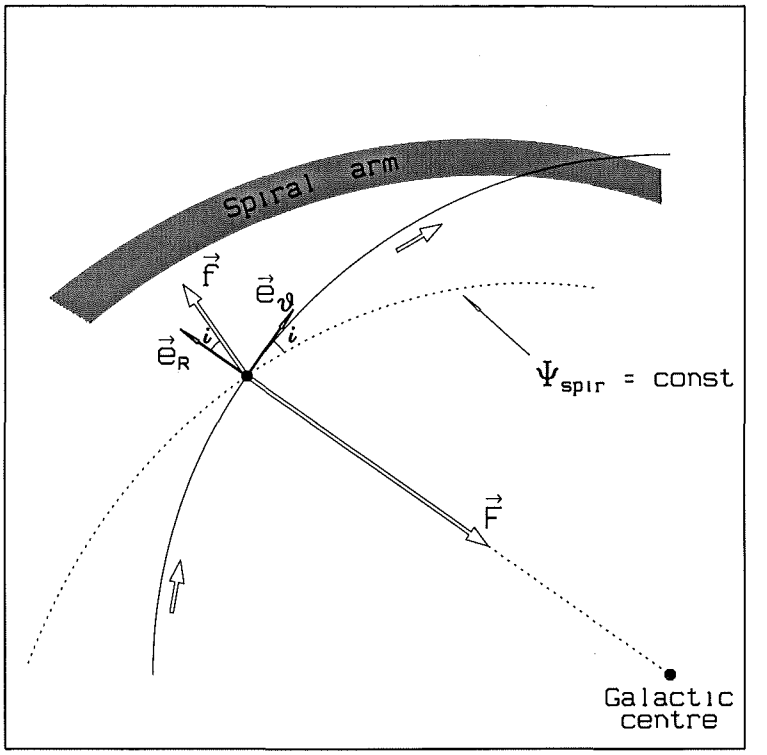

Figure 4.4: *Gravitational forces $\vec{F}$ and $\vec{f}$ due to the axisymmetric and spiral potentials.*

At any given moment of time (t) the actual spiral pattern will appear rotated, but the phase angle φ will always be zero at the spiral arms (see Equation 4.15). This means that the gravitational potential Ψ_{spir} will have its minimum along a spiral arm and its maximum in between the arms. The multiplication factor 2 in (4.16) makes sure that there are two spiral arms, separated by 180°, as shown in Figure 4.3b.

At $t = 0$ (present time), the Sun is located in between the arms, so that the reference point is at $\vartheta_s = 0°$, $R_s = 7.02$ kpc (Yuan 1969b)[3].

To complete the expression for the potential (4.16), it is necessary to define the amplitude (A) of the spiral wave. This is usually derived from an assumption about the magnitude of the gravitational force due to the spiral field. According to Yuan, the *maximum ratio* between the *radial forces* due to the spiral and axisymmetric fields at any given point is $\alpha = 0.05$. In order to see how this factor α is related to the amplitude A, it will be necessary to evaluate the corresponding forces, using the geometry presented in Figure 4.4. The axisymmetric field generates a radial force $\vec{F}$ (per unit mass), which can be expressed as:

$$\vec{F} = -\frac{V_c^2}{R}\,\vec{e}_R, \tag{4.18}$$

where the centripetal acceleration is used, as introduced when discussing Equation (4.12).

[3]Yuan's value for R_s is actually 8.26 kpc, but in his model the Sun is located at 10 kpc from the galactic centre. It was necessary to reduce his value by a factor of 0.85, to move the Sun to a radius of $R_\odot = 8.5$ kpc.

On the other hand, the spiral gravitational field generates an additional force $\vec{f}$, which is always perpendicular to a logarithmic spiral at the point under consideration, but its magnitude oscillates depending on the actual position of the spiral arms. The force is always directed towards the nearest spiral arm where a minimum potential is found. In Figure 4.4 for example, the force is pointing outwards, but this particular choice will not affect the final result. An explicit expression for the force $\vec{f}$ can be derived from the potential Ψ_{spir} in the following way:

$$\vec{f} = -\nabla\Psi_{\text{spir}} = -\left(\frac{\partial\Psi_{\text{spir}}}{\partial R}\,\vec{e}_R + \frac{1}{R}\,\frac{\partial\Psi_{\text{spir}}}{\partial\vartheta}\,\vec{e}_\vartheta\right), \tag{4.19}$$

where the gradient has been expressed in cylindrical coordinates and noting that the potential does not depend on z. After evaluating the partial derivatives using (4.16) and (4.17) one obtains:

$$\vec{f} = -2\,\frac{A}{R}\,(\vec{e}_R\,\cot i + \vec{e}_\vartheta)\,\sin 2\varphi. \tag{4.20}$$

The maximum magnitude of this vector (at $\sin 2\varphi = 1$) is:

$$f_{\max} = 2\,\frac{A}{R}\,\sqrt{1+\cot^2 i} = 2\,\frac{A}{R\,\sin i}. \tag{4.21}$$

Having now evaluated both forces, one can finally calculate the α-ratio, as introduced above, by dividing the radial components of the two forces:

$$\alpha = \frac{f_{\max}\,\cos i}{F}, \tag{4.22}$$

which gives:

$$\alpha = 2\,\frac{A}{V_c^2}\,\cot i, \tag{4.23}$$

so that the expression for the amplitude A can be derived as:

$$A = \frac{1}{2}\,\alpha\,V_c^2\,\tan i, \tag{4.24}$$

in accordance with the value used by other authors (e.g. Palouš et al. 1977). Relation (4.24) completes the set of equations needed for the computation of the spiral gravitational potential.

Using both the axisymmetric potential (4.7, 4.8, 4.9, 4.10), and the spiral component (4.16, 4.17, 4.24), the model of the galactic potential can be computed at any given point in space and time and a suitable numerical integration method can be applied in order to derive the orbits. An improved Runge-Kutta algorithm, as described by Press et al. (1994), is used in this thesis. The computations are done in cylindrical coordinates, by simultaneously

integrating the following set of six linear differential equations[4]:

$$\left.\begin{aligned}
\frac{dR}{dt} &= V_R, \\
\frac{d\vartheta}{dt} &= V_\vartheta, \\
\frac{dz}{dt} &= V_z, \\
\frac{dV_R}{dt} &= R V_\vartheta^2 - \frac{\partial \Psi}{\partial R}, \\
\frac{dV_\vartheta}{dt} &= -2\frac{V_R V_\vartheta}{R} - \frac{1}{R^2}\frac{\partial \Psi}{\partial \vartheta}, \\
\frac{dV_z}{dt} &= -\frac{\partial \Psi}{\partial z}.
\end{aligned}\right\} \tag{4.25}$$

After the integration, the cylindrical coordinates are transformed back into rectangular ones for further analysis, so that in practice one ends up with a set of six scalar quantities describing the position $(x,\ y,\ z)$ and velocity $(v_x,\ v_y,\ v_z)$ of a star. The initial position and velocity vectors are computed from the local position and velocity relative to the Sun by applying the translation formulae (4.6).

4.3 The Sun's orbit

As an example of the numerical model described in the previous section the orbit of the Sun has been computed and is presented in Figure 4.5. Actually two orbits have been computed, one (4.5a) using the total gravitational potential (including the spiral component), and the other (4.5b) with the axisymmetric potential only. This can provide an idea of how the galactic spiral arms affect the stellar orbits.

Both orbits have been computed over a period of 1 Gyr, starting from now, and covering about four full cycles (one cycle takes about 250 Myr). Only the first two cycles are presented in Figures 4.5a and 4.5b, since the remaining portions overlap those already shown, especially in the case when the spiral potential is not taken into account. The two orbits are very similar. At any moment in time the true Sun's position stays close to the position computed when only the axisymmetric component of the potential is taken into account. This is illustrated in the bottom two plots (Figures 4.5c and 4.5d) as the differences in cylindrical coordinates R and ϑ. For a reference, an interval in longitude of 1° corresponds to a distance of about 0.15 kpc along the circular orbit. The total difference in the Sun's position at any time is never much larger than 1 kpc or so.

[4]These equations can be derived easily from $\vec{a} = -\nabla\Psi$, where the acceleration $\vec{a}$ in cylindrical coordinates has the form: $\vec{a} = (\ddot{R} - R\dot{\vartheta}^2)\,\vec{e}_R + (2\dot{R}\dot{\vartheta} + R\ddot{\vartheta})\,\vec{e}_\vartheta + \ddot{z}\,\vec{e}_z$ and also: $\nabla = \vec{e}_R\frac{\partial}{\partial R} + \vec{e}_\vartheta\frac{1}{R}\frac{\partial}{\partial \vartheta} + \vec{e}_z\frac{\partial}{\partial z}$.

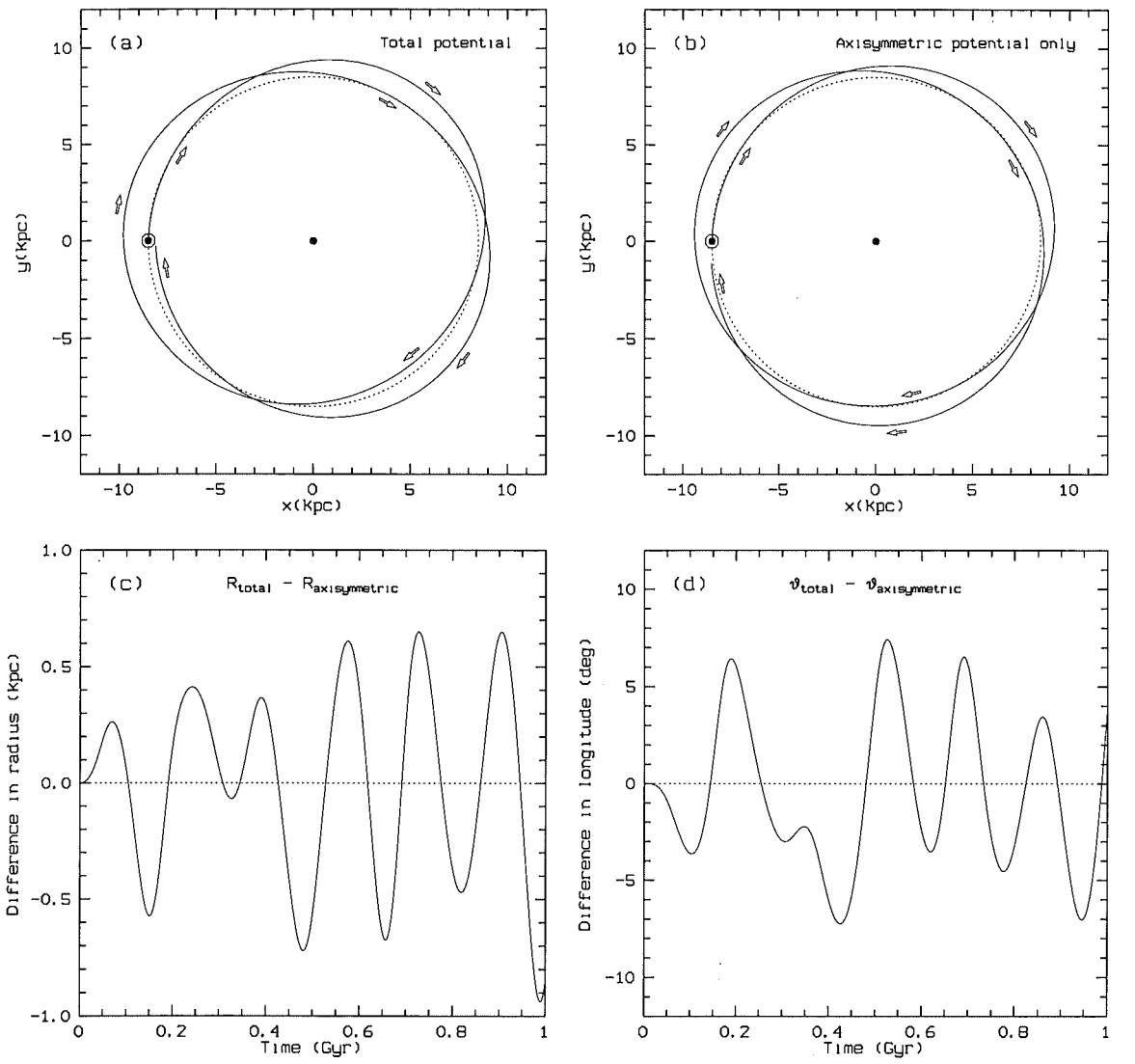

Figure 4.5: *(Top) The Sun's orbit about the galactic centre, as integrated using (a) the total potential (axisymmetric plus spiral) and (b) the axisymmetric potential only (with no spiral component). A circular orbit at* $R = 8.5$ kpc *is shown as a dotted line. (Bottom) The difference between the two orbits (a) and (b) as a function of time, shown as (c) the difference in radius and (d) difference in longitude.*

4.4 Orbits of stars in the solar neighbourhood

Using the numerical model of the galactic potential described in Section 4.2, it was possible to compute the orbits of stars in the solar neighbourhood and to examine the positions and velocities of these stars in the galactic plane at different times in the past. A reason for doing this is that past positions of stars might give a clue to understanding the present velocity distribution. This was mentioned when analysing the Hipparcos data for nearby stars (see Section 3.5).

The same sample of 4597 stars in the solar neighbourhood, as introduced in Section 3.4, will now be discussed again. For all these stars the positions and velocities at $t_0 = 0$ are already known, so that the orbits can be integrated backwards in time with intermediate results at say, $t_1 = -10$ Myr, $t_2 = -20$ Myr, $t_3 = -30$ Myr and so on. At each of these moments a two-dimensional histogram of stellar positions in the galactic plane is computed, using a bin size of 0.1 kpc.

The result is presented in Figures 4.6 and 4.7. Each of the twelve plots corresponds to a single moment of time. Different colours are used to represent the number density of stars, from the lowest (blue) to the highest (yellow). The spiral pattern corresponding to the same moment of time is shown in red. The green circle is a circular orbit at the solar radius and the present position of the Sun is marked at $x = -8.5$ kpc, $y = 0$ in all plots.

The branch-like structure of the velocity distribution in the UV-plane (see e.g. Figure 3.12) turns out to be reflected in the galactic XY-plane, including the three main branches and other weaker features. This is especially well illustrated for the relatively recent past positions (up to about $t = -100$ Myr). Moreover, somewhere between $t = -50$ Myr and $t = -70$ Myr, the separation between the branches, as well as their general tilt, is found to match the galactic spiral structure itself. If this is not a coincidence it might mean that there was a sudden burst of star formation some 50–70 Myr ago, affecting several adjacent spiral arms. What is now seen in the solar neighbourhood is a selection of stars from these arms, with velocities such that they arrive in the same place after the same period of time, although travelling different distances. The burst itself could have affected even a larger portion of the Galaxy, but not all the stars could have arrived in the solar neighbourhood by now and also many of them have already left this space.

However, this is only speculation that will need additional and more detailed analysis to be proved. It also involves several other problems that do not fit very well. First, a burst of star formation like this implies that most of the stars in the solar vicinity should be extraordinarily young and of the same age. However, it is known that many of the stars in those UV-branches are significantly older, which is the case even with the youngest stellar groups (the Sirius group, for example). Moreover, the moving groups definitely have different ages and there are even some groups apparently consisting of stars with a wide range of different ages, such as the Pleiades moving group (Eggen 1992; Asiain et al. 1999a, 1999b).

A sudden burst of star formation would also need an appropriate triggering event in the near past, such as a close passage of a massive object (another galaxy perhaps). An event like this could have also produced a perturbation in stellar orbits, that might have resulted in a branch-like velocity distribution today. This is also a speculation, especially when there have been no other indications of a recent close encounter with a massive object like this. It might be a pure coincidence that the Magellanic Clouds actually passed their perigalacticon (i.e. the point in their orbits closest to the Milky Way) some 50 Myr ago (Murai & Fujimoto

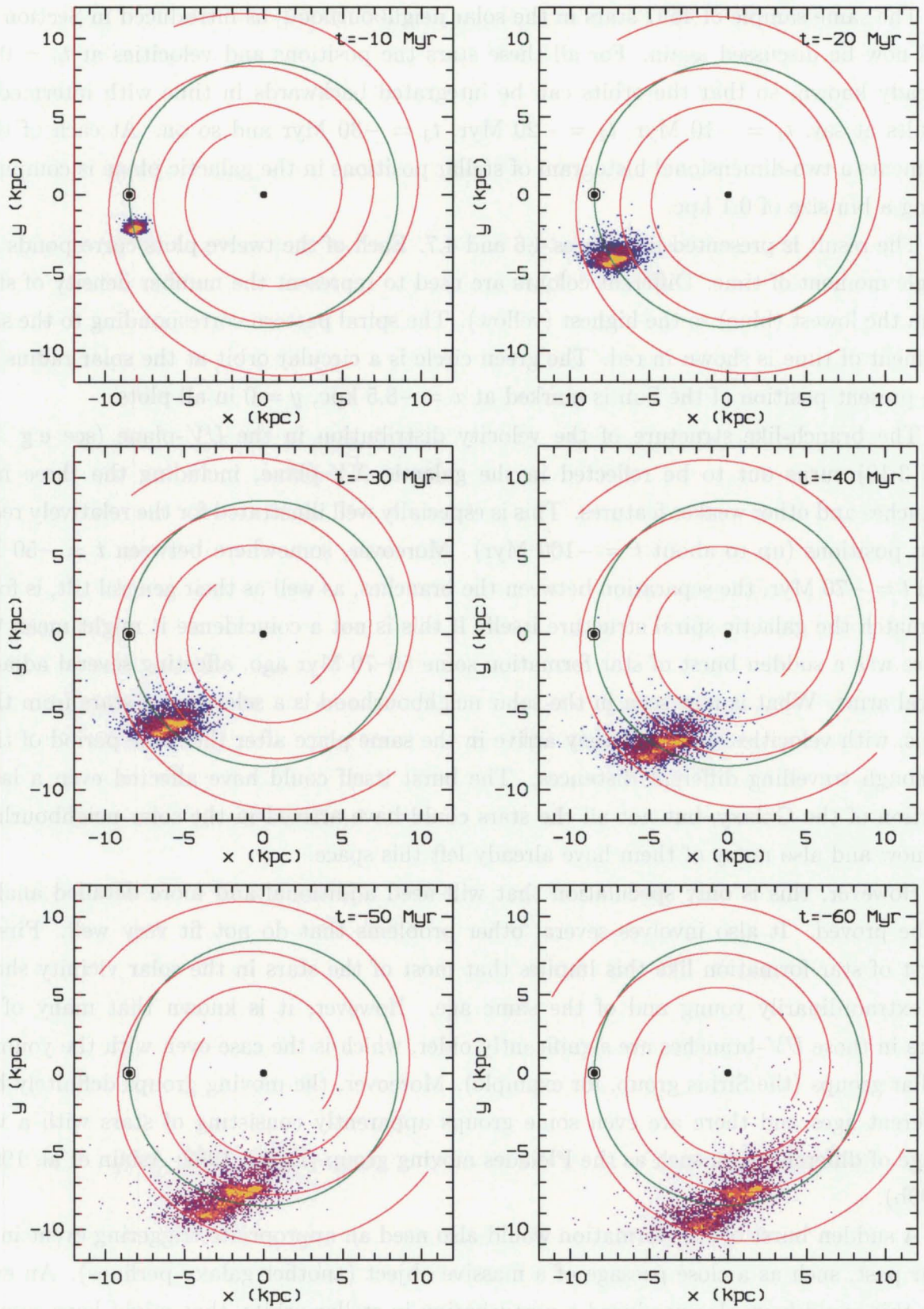

Figure 4.6: *Stars from the solar neighbourhood as they were distributed in the galactic plane in the past (part I).*

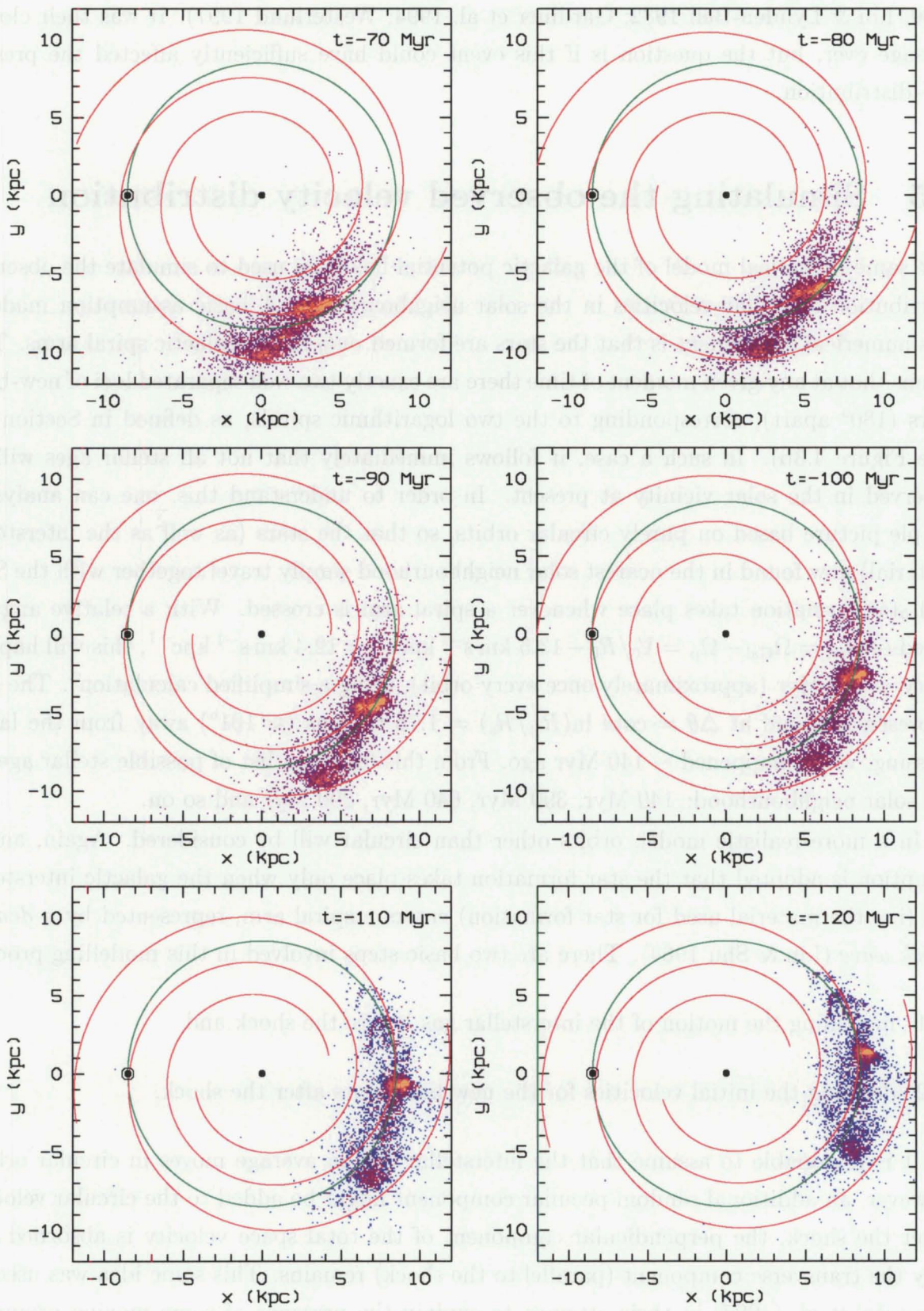

Figure 4.7: *Stars from the solar neighbourhood, as they were distributed in the galactic plane in the past (part II).*

1980; Lin & Lynden-Bell 1982; Gardiner et al. 1994; Westerlund 1997). It was their closest passage ever, but the question is if this event could have sufficiently affected the present UV-distribution.

4.5 Simulating the observed velocity distribution

The same numerical model of the galactic potential has been used to simulate the observed distribution of stellar velocities in the solar neighbourhood. A basic assumption made in this numerical experiment is that the stars are formed *only* in the galactic spiral arms. This means that at any given moment of time there are exactly two well separated loci of new-born stars (180° apart), corresponding to the two logarithmic spirals, as defined in Section 4.2 (see Figure 4.3b). In such a case, it follows immediately that not all stellar ages will be observed in the solar vicinity at present. In order to understand this, one can analyse a simple picture based on purely circular orbits, so that the stars (as well as the interstellar material) now found in the nearest solar neighbourhood simply travel together with the Sun, and star formation takes place whenever a spiral arm is crossed. With a relative angular speed of $\Omega_{\rm rel} = \Omega_{\rm Gal} - \Omega_{\rm p} = V_0/R_0 - 13.5\ {\rm km\,s^{-1}\,kpc^{-1}} = 12.4\ {\rm km\,s^{-1}\,kpc^{-1}}$, this will happen every ~ 250 Myr (approximately once every orbit), using a simplified calculation[5]. The Sun is presently found at $\Delta\theta = \cot i\, \ln(R_\odot/R_{\rm s}) = 1.76$ radians ($\approx 101°$) away from the latest crossing, which happened ~ 140 Myr ago. From this follows a list of possible stellar ages in the solar neighbourhood: 140 Myr, 390 Myr, 640 Myr, 890 Myr and so on.

In a more realistic model, orbits other than circular will be considered. Again, an assumption is adopted that the star formation takes place only when the galactic interstellar gas (i.e. the material used for star formation) enters a spiral arm, represented by a *density shock wave* (Lin & Shu 1964). There are two basic steps involved in this modelling process:

1. modelling the motion of the interstellar gas before the shock and

2. deriving the initial velocities for the new-born stars after the shock.

It is reasonable to assume that the interstellar gas on average moves in circular orbits. However, an additional random peculiar component might be added to the circular velocity. After the shock, the perpendicular component of the total space velocity is absorbed and only the transverse component (parallel to the shock) remains. This same idea was used by Comerón et al. (1997) in their attempt to explain the presence of some moving groups in the solar neighbourhood. The basic geometry is shown in Figure 4.8. If the interstellar gas

[5] An angular speed of 1 ${\rm km\,s^{-1}\,kpc^{-1}}$ is very nearly equal to one radian per Gyr, since there are 3.156×10^{16} seconds in a Gyr, and 3.086×10^{16} km in a kpc. The time interval between two consecutive spiral arm crossings is Δt [Gyr] $= \pi/\Omega_{\rm rel}$.

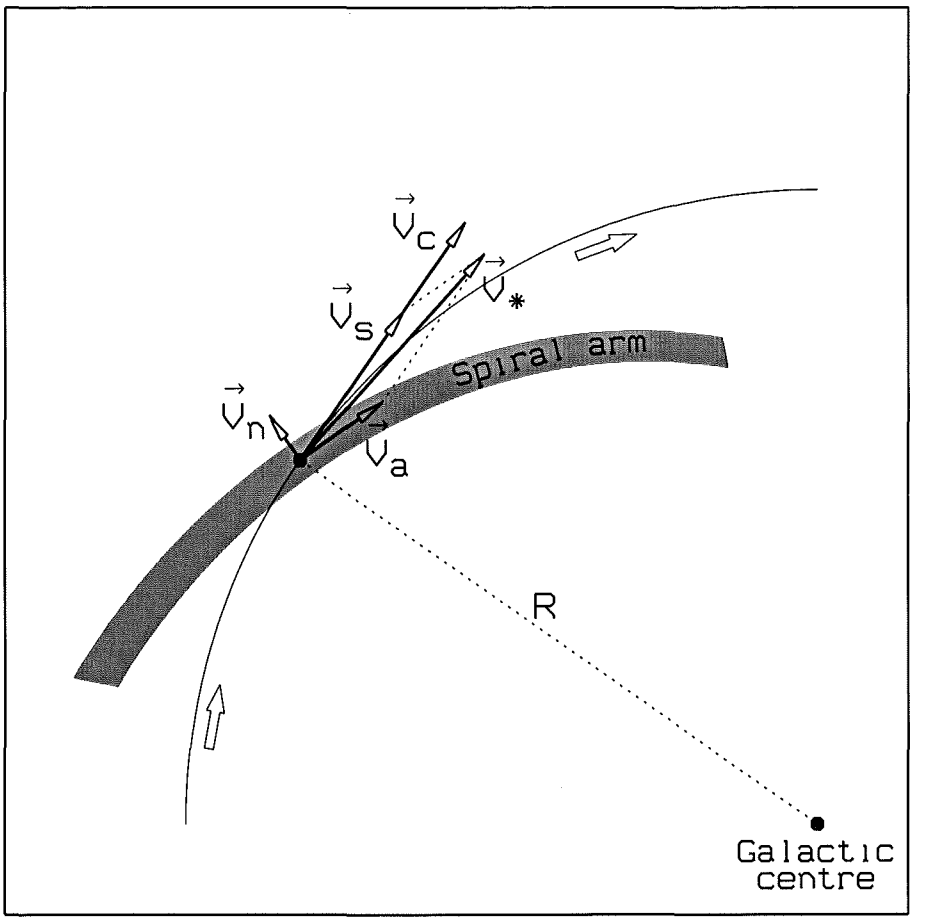

Figure 4.8: *Deriving the initial space velocity $\vec{V}_*$ of a star that has just been formed from the interstellar gas inside a spiral arm.*

moves with a circular velocity $\vec{V}_c$ at a radius R, then it will enter the spiral shock with a relative velocity:

$$\vec{V}_{rel} = \vec{V}_c - \vec{V}_s, \tag{4.26}$$

where $\vec{V}_s$ is the circular velocity of the spiral pattern:

$$\vec{V}_s = \Omega_p R \vec{e}_\vartheta. \tag{4.27}$$

The vector $\vec{V}_{rel}$ can be expressed in terms of two components relative to the shock: a perpendicular component ($\vec{V}_n$) and a transverse component ($\vec{V}_a$). After the shock, only the transverse component remains, so that the total space velocity becomes:

$$\vec{V}_* = \vec{V}_a + \vec{V}_s. \tag{4.28}$$

In order to account for the peculiar motion of the interstellar gas a random gaussian fluctuation is applied to the magnitude of the transverse velocity vector $\vec{V}_a$ before it is added to the circular motion of the spiral arm using (4.28). A standard deviation of $\sigma = 10$ km s^{-1}

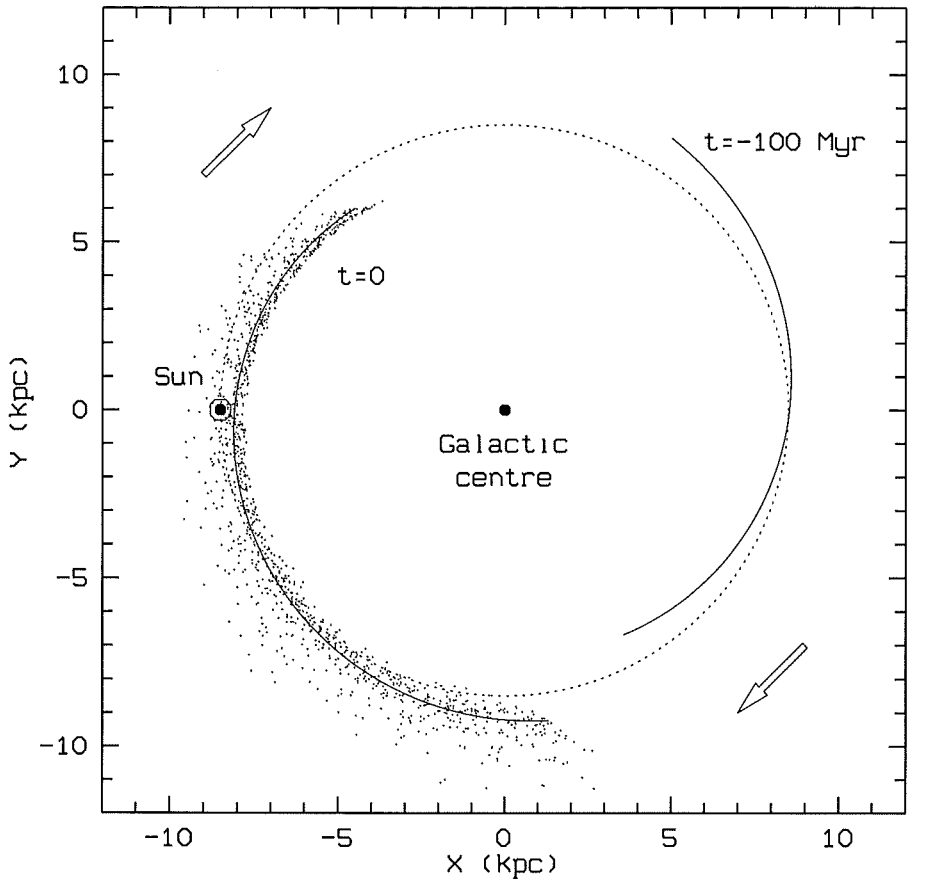

Figure 4.9: *Stars formed in a spiral arm* 100 Myr *ago (solid line at* $t = -100$ Myr*) with an initial velocity dispersion of* $\sigma = 10$ km s^{-1} *will appear scattered around the mean locus at* $t = 0$.

is used, in accordance with a typical velocity dispersion found in some of Eggen's moving groups (e.g. Eggen 1969; Eggen et al. 1973).

A number of stars can be 'created' in this way along a given spiral arm and their orbits can be integrated over time as explained previously (Section 4.2). An example is shown in Figure 4.9, where a number of stars have been created along a portion of a spiral arm ($\pm 60°$ around the intersection with the solar circle) at $t = -100$ Myr. A corresponding locus of stars with no initial velocity dispersion is represented as a solid line at $t = 0$. Taking into account a velocity dispersion of $\sigma = 10$ km s^{-1} the stars appear scattered around the mean locus at $t = 0$ and some of them fall in the solar neighbourhood.

In order to create a numerical model of the velocity distribution of stars now observed in the solar neighbourhood a large number of stellar orbits ($\sim 2 \times 10^6$) have been integrated in this way. For every stellar age[6] between 10 Myr and 1000 Myr, with a step of 10 Myr, 12 000 stars have been created along a 120° arc of a single spiral arm (two arms per age), centred

[6]A constant star-formation rate has been assumed over the past 10^9 years.

at the node (i.e. the intersection with the solar circle). The corresponding longitudinal 'density' is one hundred stars per degree, which is about one star per 1.5 pc at the solar radius. This density is a compromise between the total amount of computing time needed for the integration and the total number of stars found in the solar neighbourhood as a result. No attempt has been made in this thesis to model the real density at star formation.

The model distribution of stellar velocities in the galactic plane at present ($t = 0$) is shown in Figure 4.10. There are 2634 stars (out of 2 400 000 stars created over the past 1000 Myr as explained above) that are now found inside a sphere of a radius $r = 200$ pc centred at the Sun. For all these stars the local galactic components (U and V) of the space velocity vector have been computed and a two-dimensional histogram has been constructed in a similar way to that already discussed in Chapter 3 when analysing the Hipparcos data. A bin size of 0.5 $\mathrm{km\,s^{-1}}$ has now been used.

The model distribution is not identical (perhaps not even similar) to the observed one (see Figure 3.12), but the disagreement can probably be expected from a simple model like this. The distribution in Figure 4.10 covers a relatively small portion of the UV-plane, with neither U nor V velocities exceeding -40 $\mathrm{km\,s^{-1}}$ on the negative side and about 0 $\mathrm{km\,s^{-1}}$ on the positive side. There are some details in the histogram confirming that the galactic spiral structure can affect the local distribution of stellar velocities. The distribution is not symmetrical and some weak tails ('branches') can be detected. There is a strong central concentration of stars around $(-10, -15)$ $\mathrm{km\,s^{-1}}$, probably reflecting the fact that the initial circular velocity of the interstellar gas was changed after the spiral shock. A closer examination of the central part of the distribution (best seen in Figure 4.10a) reveals a pair of very close elongated features parallel to each other ($\sim$ 10 $\mathrm{km\,s^{-1}}$ long and $\sim$ 2 $\mathrm{km\,s^{-1}}$ apart). Each of these two features corresponds to stars that were formed in a different spiral arm.

The distribution of stellar ages in the same sample of stars is presented in Figure 4.11. Four well defined peaks (marked as A, B, P and Q) are found coinciding with the possible ages already derived at the beginning of this section. Each peak corresponds to a single spiral arm. The peaks are produced alternately by the two spiral arms, so that the first one (A) and the third one (B) are generated by the inner arm[7], while the remaining two peaks (P and Q) are produced by the outer arm. A comparison with the observed stellar ages in the solar neighbourhood has also been made using a recent result by Asiain et al. (1999a). A list of 16 moving groups younger than about 700 Myr were suggested by these authors and they are presented as black dots in Figure 4.11. Apart from the two moving groups at ages close to 500 Myr (apparently falling in a region where no stars should be found according to the model), all the other ages agree well with the model. However, a more detailed analysis including the field stars is necessary in order to draw any firm conclusions

[7]The terms 'inner' and 'outer' are used in this thesis to refer to the two spiral arms as they appear around the Sun at present ($t = 0$). Looking from the Sun the inner arm is seen towards the galactic centre, while the outer arm is in the opposite direction.

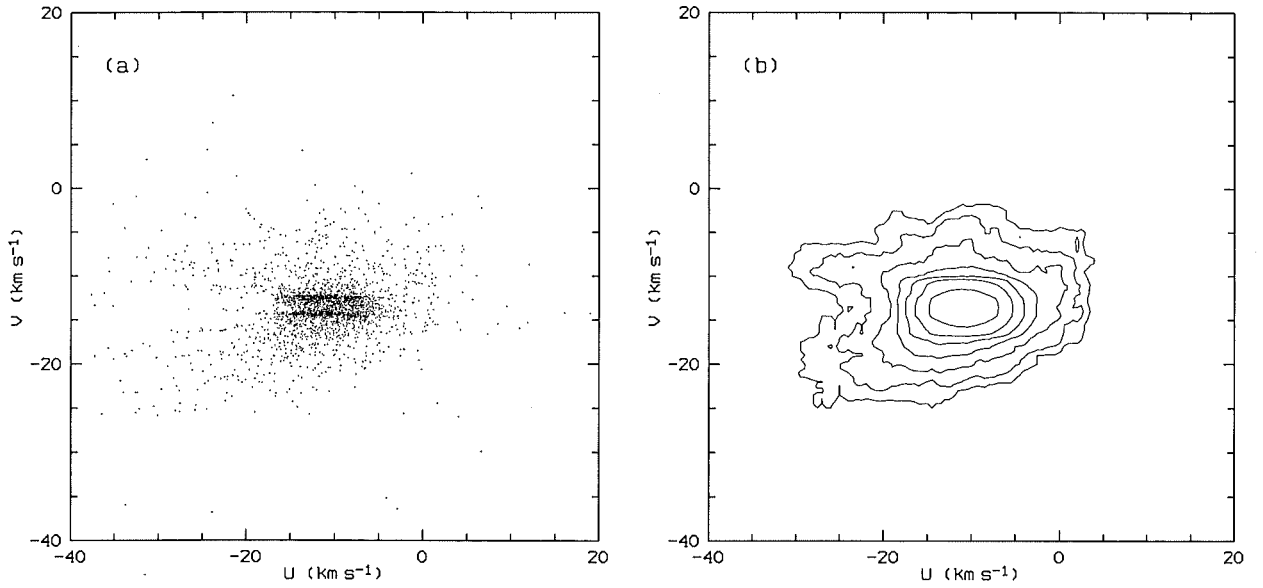

Figure 4.10: *The model distribution of stellar velocities in the solar neighbourhood (within 200 pc of the Sun) presented as (a) a scatter plot and (b) a contour plot, assuming that stars are formed only in spiral arms, with initial velocities given by Equation 4.28.*

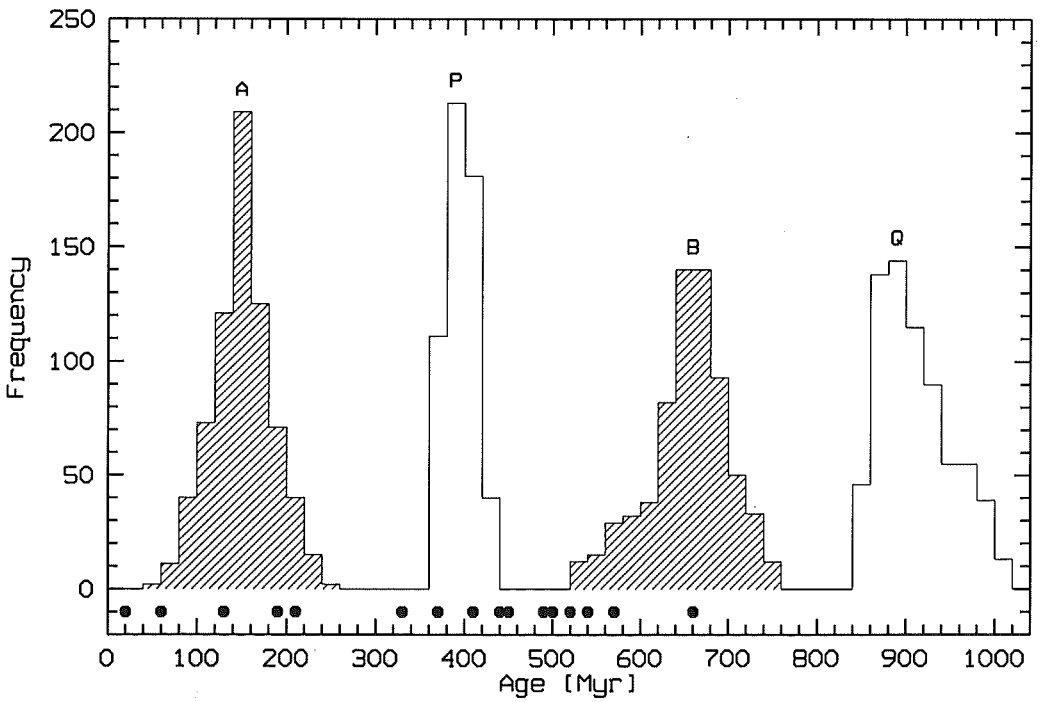

Figure 4.11: *The model distribution of stellar ages in the solar neighbourhood, using the same model as in Figure 4.10. Shaded peaks (marked as A and B) correspond to the inner arm. The remaining two peaks (P and Q) correspond to the outer arm. Black dots represent the ages of 16 moving groups found by Asiain et al. (1999a) in a sample of early-type stars.*

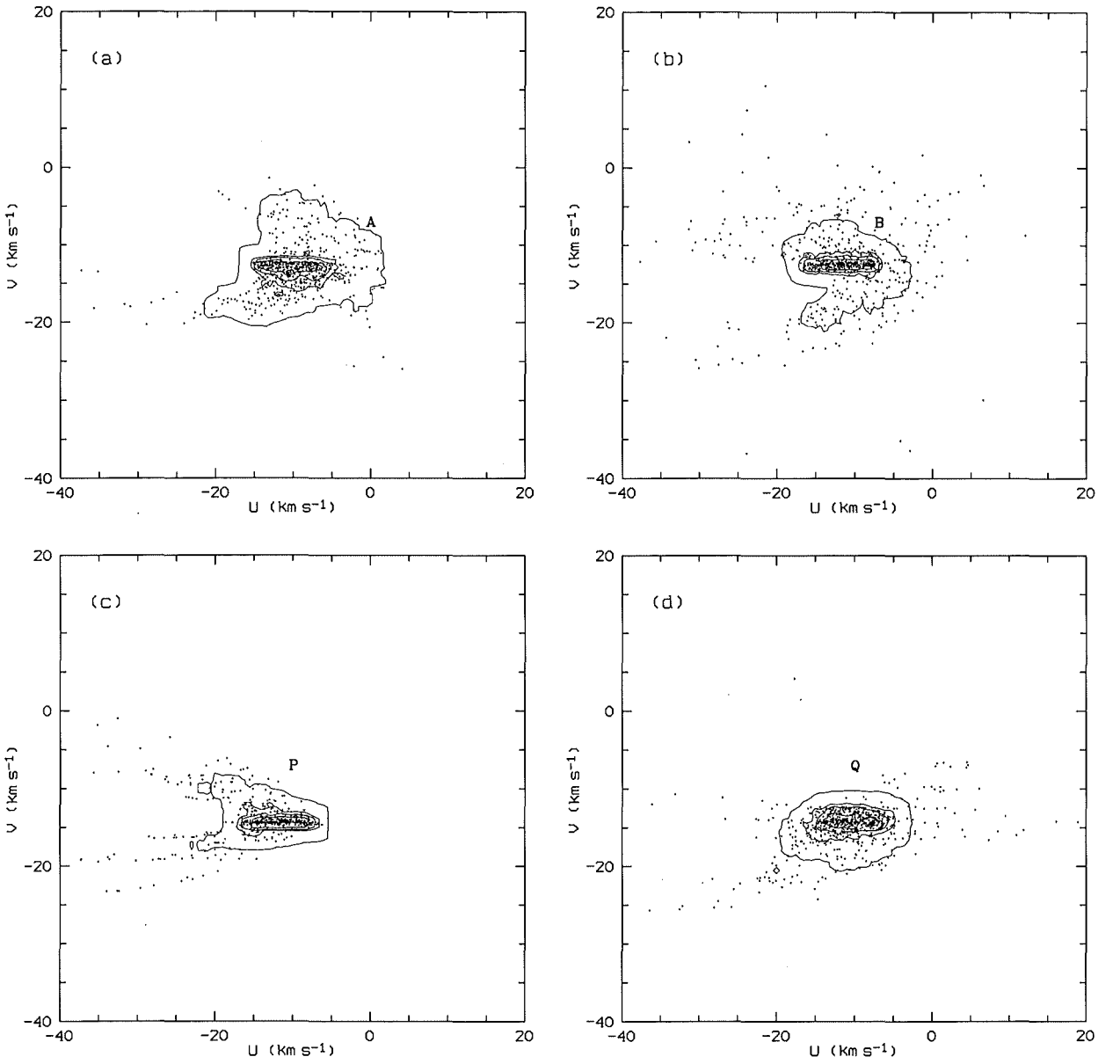

Figure 4.12: *The model distributions of stars of different ages corresponding to individual peaks (A, B, P and Q) in the age histogram (Figure 4.11).*

from this comparison.

In order to see how the stellar ages produced by this model are distributed in the UV-plane, four separate plots are presented in Figure 4.12. Each plot corresponds to a certain age range and a given spiral arm, represented by a single peak in the age histogram. As already mentioned, the central concentrations A and B (inner arm) both appear slightly higher (i.e. with the V component closer to zero) than P and Q (outer arm). However, apart from this small displacement in V of about 2 km s^{-1}, the age separation in the velocity plane is generally not clear. There are some differences between the weak peripheral parts of the four distributions, but they will not be analysed.

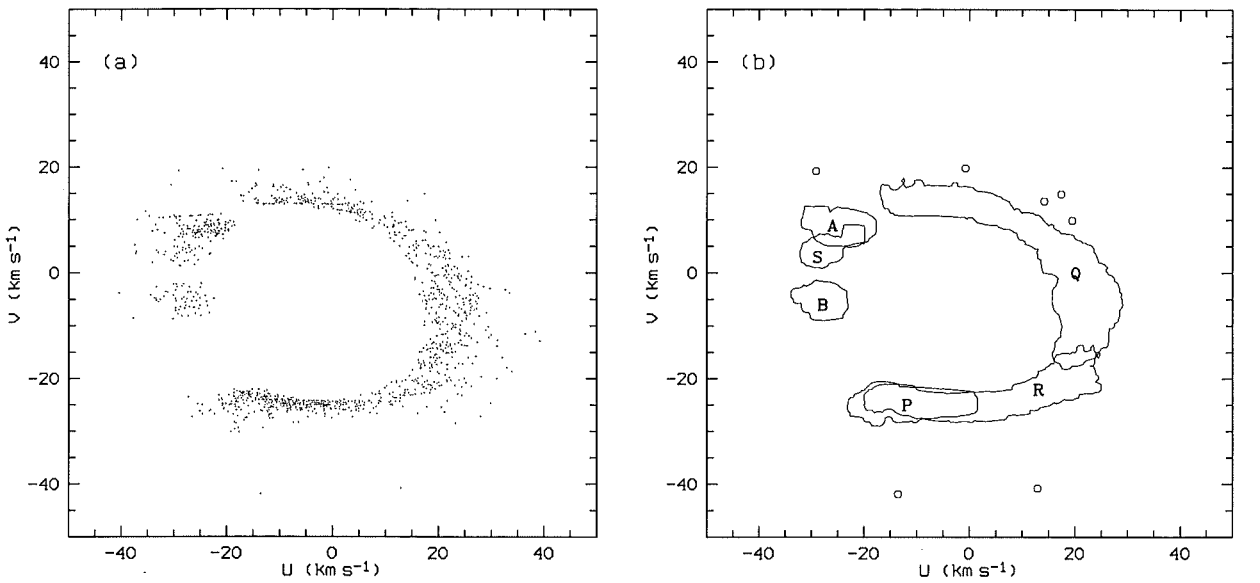

Figure 4.13: *An alternative model distribution of stellar velocities in the solar neighbourhood assuming a larger pitch angle of* $i = 20°$*: (a) a scatter plot, (b) regions covered by stars of different ages and from different spiral arms, as defined in Figure 4.14. Open circles represent the stars corresponding to the inner arm at about* 800 Myr *(peak C).*

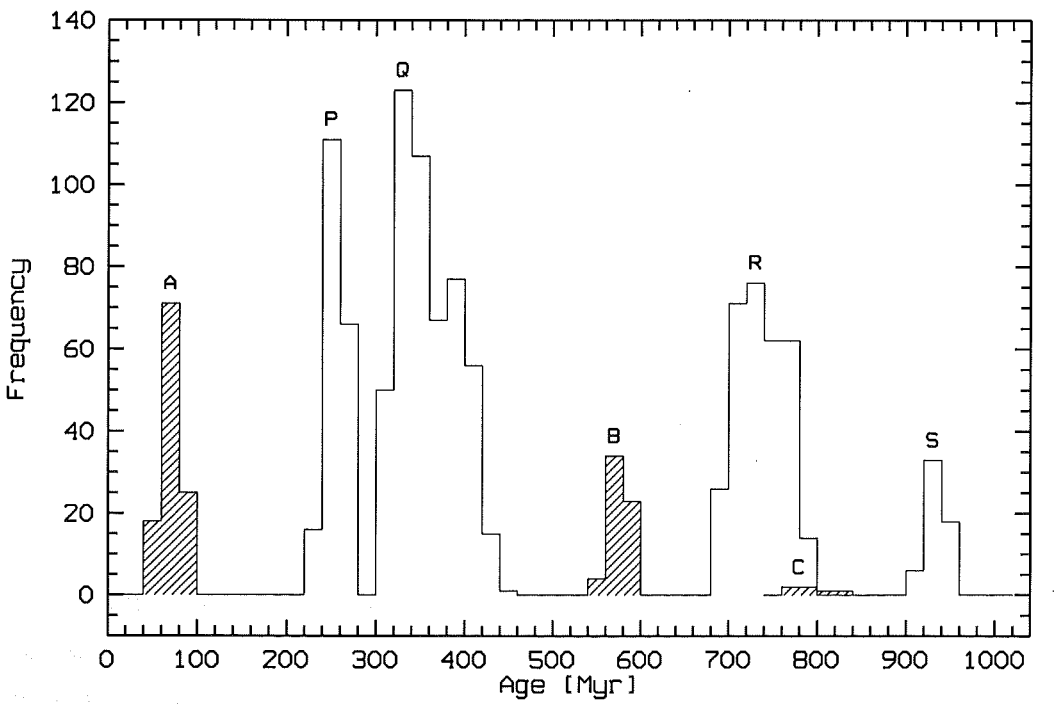

Figure 4.14: *The age distribution of stars in the solar neighbourhood for the model presented in Figure 4.13. Shaded peaks (marked as A, B and C) correspond to the inner arm, while the remaining peaks (P, Q, R and S) correspond to the outer arm.*

The fact that the observed velocity distribution contains many more features than revealed in the model described above might mean that the real galactic spiral structure is more complicated. A pair of perfect logarithmic spirals at a low pitch angle of $i = 6°.2$ is probably only a rough approximation to the real structure. It is a well known observational fact that the local galactic structure is characterized by a significantly higher pitch angle of about $i_{\text{local}} \approx 20°$, as derived from various spiral arm tracers within several kiloparsecs of the Sun (Morgan et al. 1952; Morgan et al. 1953; Becker & Fenkart 1970; Courtès et al. 1970; Weaver 1970). One can assume that such local deviations from the global pitch angle can be found all over the Galaxy. Another possibility is that several spiral patterns may coexist (Crézé & Mennessier 1973). As a result, the initial velocities at star formation will differ from one region to another and a different pattern of grouping in the velocity plane will be detected around the Sun at present.

An experiment has been made in order to test how a different pitch angle would affect the stellar velocities. The same computation process as described above has been repeated, but with a new pitch angle of $i = 20°$. This is probably not a realistic value for the global pitch angle in our Galaxy, but in the absence of a more sophisticated numerical model that would allow some isolated local distortions of the spiral pattern, this inconvenience must be tolerated. The resulting distribution of stars in the velocity plane is presented in Figure 4.13 and the distribution of stellar ages is given in Figure 4.14. The youngest possible age is now found at about 70 Myr since the inner arm's node is only about 30° away from the Sun. The age separation in the UV plane is evident and several groups of stars can be detected. While almost all the stars created in the inner arm (regions A and B in Figure 4.13b) appear as two well separated 'moving groups', the outer arm generates a more complicated structure in the velocity plane, including some longer branches (regions Q and R). Some of the groups of different age have similar velocities so that they appear overlapped in the UV-plane (regions A and S, and P and R).

There are also other possibilities that can be taken into account when modelling the observed velocity distribution. One such possibility is that our Galaxy might have a *bar*, which would break the axial symmetry of the static potential. This option is not considered in this thesis, but there are examples in the literature demonstrating how a galactic bar can produce some of the observed features in the velocity distribution (e.g. Dehnen 1998a).

4.6 Evolution of a moving group

In this section a numerical model of a moving group will be presented based on Eggen's hypothesis, i.e. that moving groups are composed of stars evaporated from star clusters. The basic idea in this modelling process is to 'create' such a cluster (a large number of stars inside a small volume or at a single point somewhere in the Galaxy), assuming a certain velocity

dispersion around a given space velocity, and then to follow the stellar orbits as they evolve in time. For the sake of simplicity, the gravitational interaction between the stars inside the cluster will be ignored. In other words, the 'evaporation' starts immediately after the creation (with all stars leaving the cluster simultaneously) and each star is considered as a free particle moving in the galactic gravitational potential.

The Hyades moving group has been chosen as an example for this experiment, assuming that the group itself is a result of the dissipation of the Hyades cluster. The experiment can be divided into two stages. In the first stage, the present position, velocity and age of the Hyades cluster are taken and the galactic orbit is integrated backwards in time. As a result, the position and velocity at star formation can be computed. In the second stage, a hypothetical cluster is created with the initial parameters as derived above, but allowing a slightly higher velocity dispersion, more suitable for a moving group than for a cluster. The orbits are then integrated forwards in time and the positions and velocities are examined around the current position of the Sun. In fact, the same examination can also be done at many other moments of time, and many different points in space along the orbit, so that a better picture is obtained of various distributions found by an observer inside the moving group.

Some of the results found in this section were also presented at the ESA Symposium 'Hipparcos – Venice '97' (Skuljan et al. 1997), although using only the axisymmetric part of the galactic gravitational potential and adopting slightly different initial values for the Hyades cluster position, velocity and age. As a source of the present data for the Hyades cluster a recent paper by Perryman et al. (1998) was used. The heliocentric[8] position and velocity of the centre of mass derived from 134 stars within $r = 10$ pc of the cluster centre are:

$$\begin{pmatrix} X \\ Y \\ Z \end{pmatrix} = \begin{pmatrix} -43.08 \\ +0.33 \\ -17.09 \end{pmatrix} \pm \begin{pmatrix} 0.25 \\ 0.06 \\ 0.11 \end{pmatrix} \text{ pc}, \tag{4.29}$$

$$\begin{pmatrix} U \\ V \\ W \end{pmatrix} = \begin{pmatrix} -41.70 \\ -19.23 \\ -1.08 \end{pmatrix} \pm \begin{pmatrix} 0.16 \\ 0.11 \\ 0.11 \end{pmatrix} \text{ km s}^{-1}. \tag{4.30}$$

The age of the cluster, also given by Perryman et al. and determined by theoretical isochrone fitting to the observed H-R diagram, is 625 ± 50 Myr. Using the transformation (4.6) the galactocentric coordinates can be derived as:

$$\begin{pmatrix} x \\ y \\ z \end{pmatrix} = \begin{pmatrix} -8.54308 \\ +0.00033 \\ -0.00509 \end{pmatrix} \text{ kpc}, \qquad \begin{pmatrix} v_x \\ v_y \\ v_z \end{pmatrix} = \begin{pmatrix} -32.70 \\ +212.77 \\ +5.92 \end{pmatrix} \text{ km s}^{-1}. \tag{4.31}$$

[8]In fact, the *barycentric* position and velocity are given by Perryman et al. (1998). However, the difference between the barycentric and heliocentric vectors in this example can be ignored.

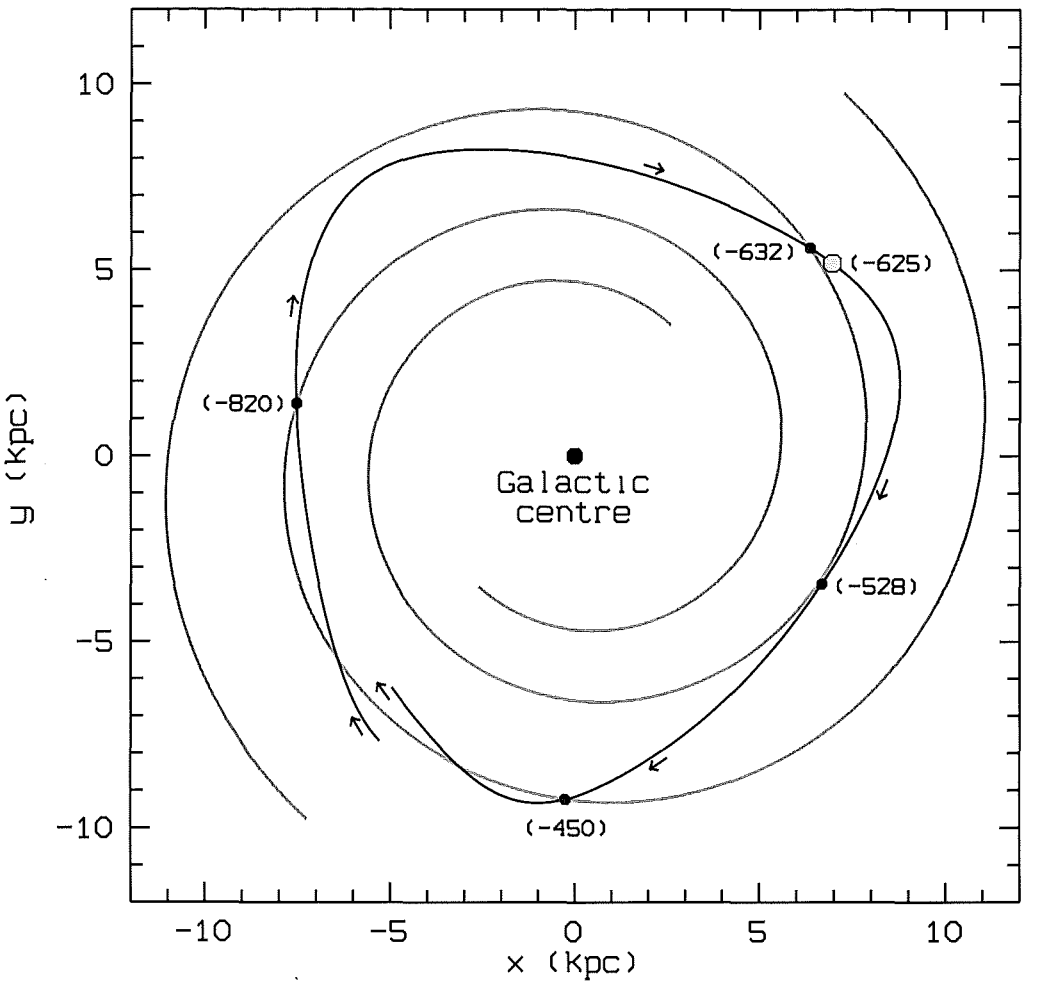

Figure 4.15: *The place of formation of the Hyades cluster (open circle) in the galactic plane at* $t = -625$ Myr. *The spiral pattern at the same moment is shown in grey. A portion of the orbit of the cluster before and after the creation is given in a reference frame rotating with the spiral pattern. Numbers in brackets are times in* Myr *relative to the present time.*

When these initial parameters are used to integrate the orbit backwards in time, the following position and velocity are obtained at $t = -625$ Myr:

$$\begin{pmatrix} x \\ y \\ z \end{pmatrix}_0 = \begin{pmatrix} +6.95344 \\ +5.18500 \\ +0.08718 \end{pmatrix} \text{ kpc}, \qquad \begin{pmatrix} v_x \\ v_y \\ v_z \end{pmatrix}_0 = \begin{pmatrix} +150.134 \\ -153.303 \\ -1.385 \end{pmatrix} \text{ km s}^{-1}, \tag{4.32}$$

where zero in the index corresponds to the time of star formation.

Figure 4.15 shows the position of the Hyades cluster in the galactic plane at formation ($t = -625$ Myr). The spiral pattern at the same moment is also presented, as well as a portion of the orbit of the cluster in a reference frame *rotating with the spiral pattern.* The positions are also plotted earlier than $t = -625$ Myr in order to examine other possible places of formation at different ages. According to the model, the Hyades cluster was formed very

close to a spiral arm. If one assumes a slightly different age of $t = -632$ Myr, the position will fall exactly on the spiral arm. This is an important result demonstrating that the numerical model of the galactic spiral structure is in good agreement with the stellar ages (assuming that star formation takes place in spiral arms). It can be seen from Figure 4.15 that the two other nearest spiral arm crossings correspond to the ages of -450 Myr and -820 Myr, with an additional passage close to a spiral arm at -528 Myr. However, all these values are outside the 50 Myr error bar given by Perryman et al. (1998).

With the initial position and velocity (4.32), a model cluster has been created containing 10 000 stars[9] with a velocity dispersion of $\sigma = 10$ km s^{-1} in all three directions. This choice for the velocity dispersion is based on the dispersions found in Eggen's moving groups, as explained in the previous section. Due to the different initial velocities, the stars move in different orbits and the original cluster 'evaporates', changing its shape. The evolution of the cluster can be seen in Figure 4.16. The orbit of the centre of mass (represented by the solid line) shows a characteristic pattern consisting of two loops, similar to the orbit of the Sun (see Figure 4.5). All cluster stars move close to this orbit, crossing it periodically. As a result, the cluster evolves into an elongated *supercluster*, as already explained in Chapter 1. The system can be found in slightly different positions with respect to the orbit. Its width is not uniform and some extremely narrow sections (called *nodes* in this thesis) can be detected.

After 625 Myr the original centre of mass (i.e. the Hyades cluster) will reach its present position close to the Sun, while all the other stars will appear scattered in the solar neighbourhood. With the initial values derived above, the Sun falls relatively close to one of the narrowest parts (nodes) of the supercluster, but this is only a result of the particular age of 625 Myr used to compute the initial position and velocity of the cluster. Simulations show that the age is a critical parameter. If a slightly different age is assumed, a different current distribution of stars around the Sun will be obtained. The Sun can be found in a narrow or in a broad section of the supercluster, depending on the age, as seen in Figure 4.17. Moreover, the distribution of stars in the velocity plane (bottom row of plots in Figure 4.17) has a very similar shape. When the core cluster is found in a broad part of the supercluster in the galactic plane, it is also found in a broad section of the velocity distribution (e.g. for an age of 590 Myr). The same applies to the narrow sections of the two distributions (e.g. for an age of 630 Myr).

An enlarged portion of the galactic plane around the present position of the Sun ($x = -8.5$ kpc, $y = 0$) is presented in Figure 4.18, where each of the seventeen plots corresponds to a single age between 585 Myr and 665 Myr (± 40 Myr around the adopted age of 625 Myr). In order to extract only the stars in the solar neighbourhood, a circle of a given radius is constructed centred at the position of the Sun. Two such circles are shown in Figure 4.18, the smaller one with a radius of 200 pc and the bigger one with a radius of 300 pc. With

[9]It has been found by experimentation that with 10 000 stars at star formation, a few hundred will be found in the solar neighbourhood at present, as is the case with the real Hyades moving group.

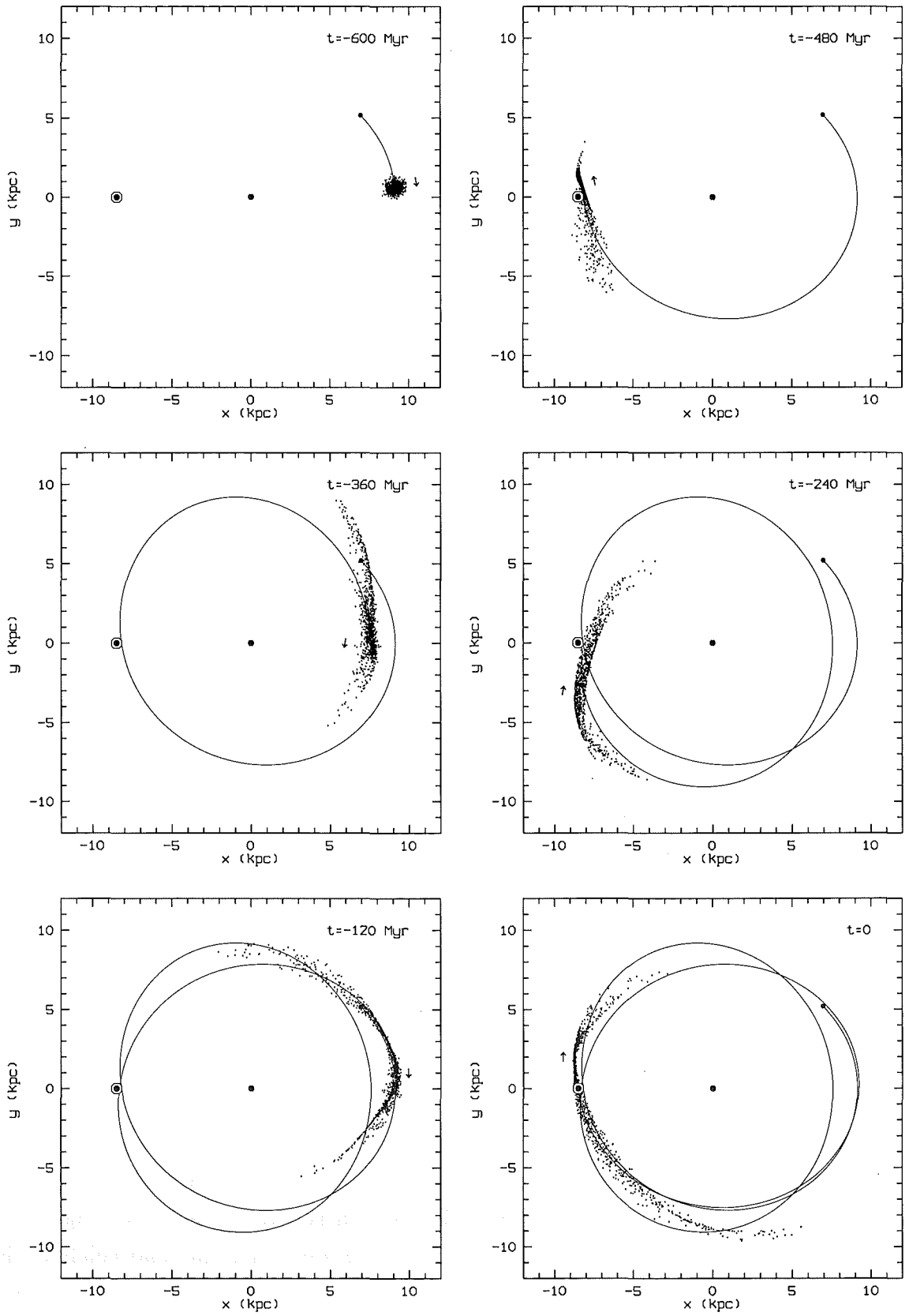

Figure 4.16: *A hypothetical Hyades supercluster evolving in time as it orbits around the galactic centre.*

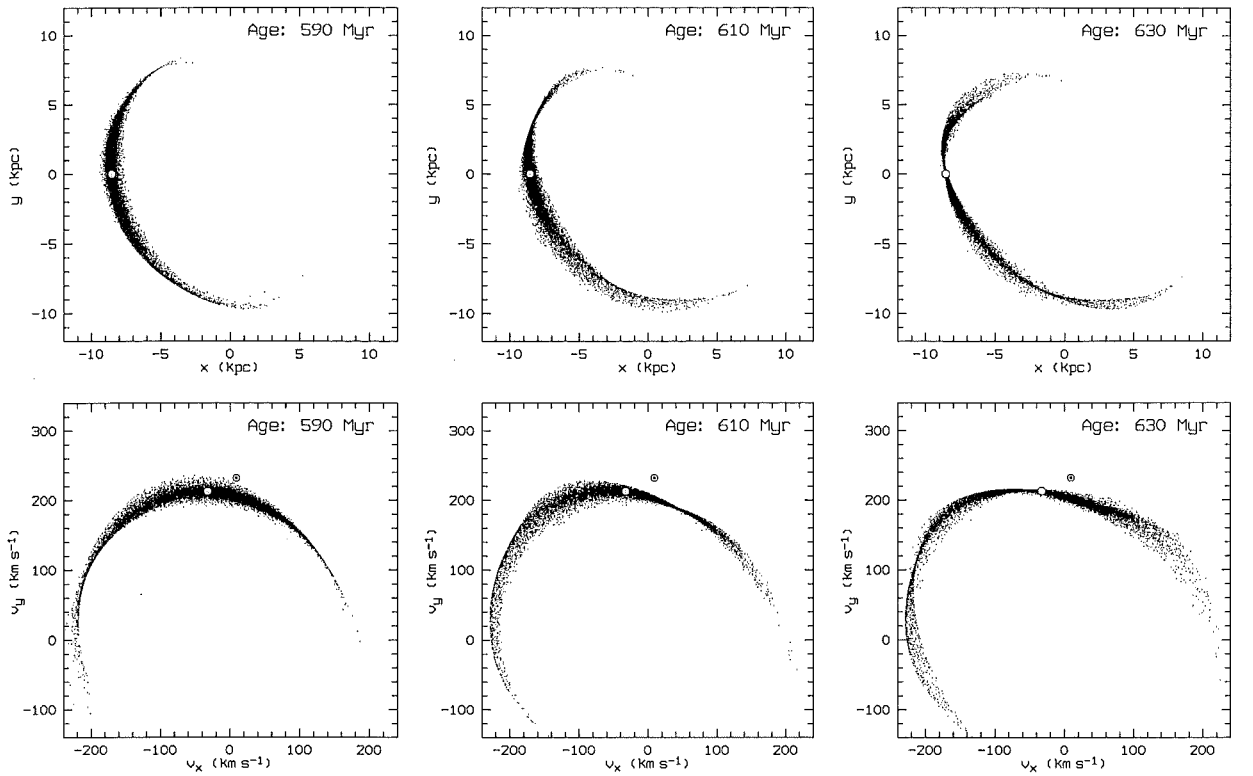

Figure 4.17: *(Top) The model Hyades supercluster as it appears in the galactic plane at present, when three different ages are used to compute the initial position and velocity. (Bottom) The supercluster in the velocity plane for the same three ages. The Hyades cluster is marked in each plot as a small circle. The velocity of the Sun is also marked as a circled dot in the bottom plots.*

an initial number of 10 000 stars at creation only about 100–300 stars are currently found within 200 pc and 250–450 within 300 pc, depending on the actual age. For most of the ages the supercluster appears broad enough around the Sun so that the stars inside the solar neighbourhood are almost uniformly distributed over the area of the circle. This uniformity is broken only when the Sun is found close to a node of the supercluster (ages around 635 Myr).

The velocity distributions for the same stars found in the solar neighbourhood are presented in Figures 4.19 and 4.20, each figure corresponding to a single value for the radius (200 pc and 300 pc respectively). A general impression is that at each given age the two distributions have the same shape, but a larger area is covered when the solar neighbourhood is larger (Figure 4.20). For example, at an age of 590 Myr both distributions look symmetric, almost uniformly filling a circular area in the UV-plane. However the radius of the circle is about 5 km s^{-1} at $r = 200$ pc and 7 km s^{-1} at $r = 300$ pc, almost exactly in proportion with the radius of the solar neighbourhood. The same result can be obtained for the elliptical distributions at other ages.

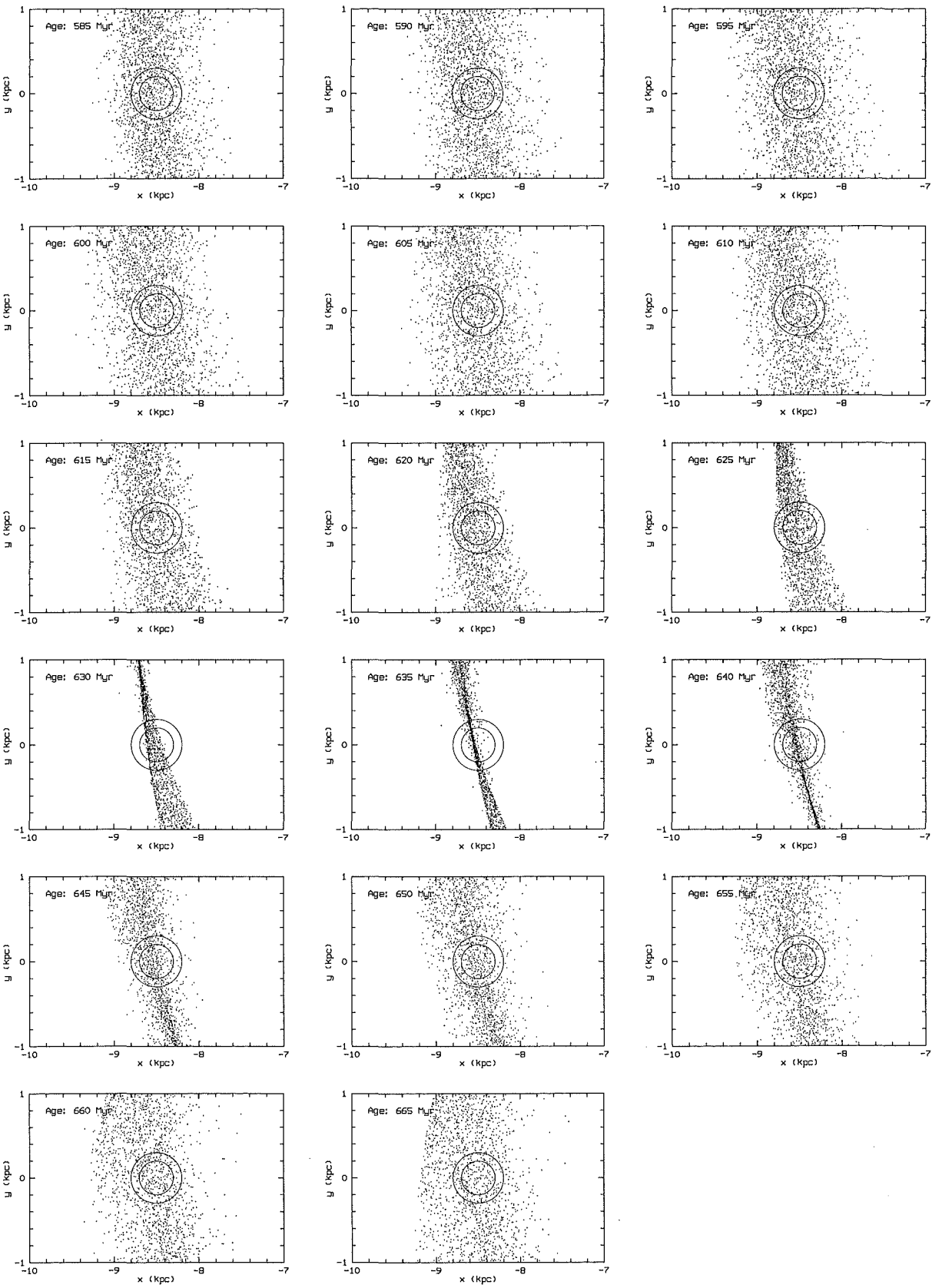

Figure 4.18: *The model Hyades supercluster in the XY-plane for various ages. The solar neighbourhood is represented by two different circles ($r_1 = 200$ pc and $r_2 = 300$ pc).*

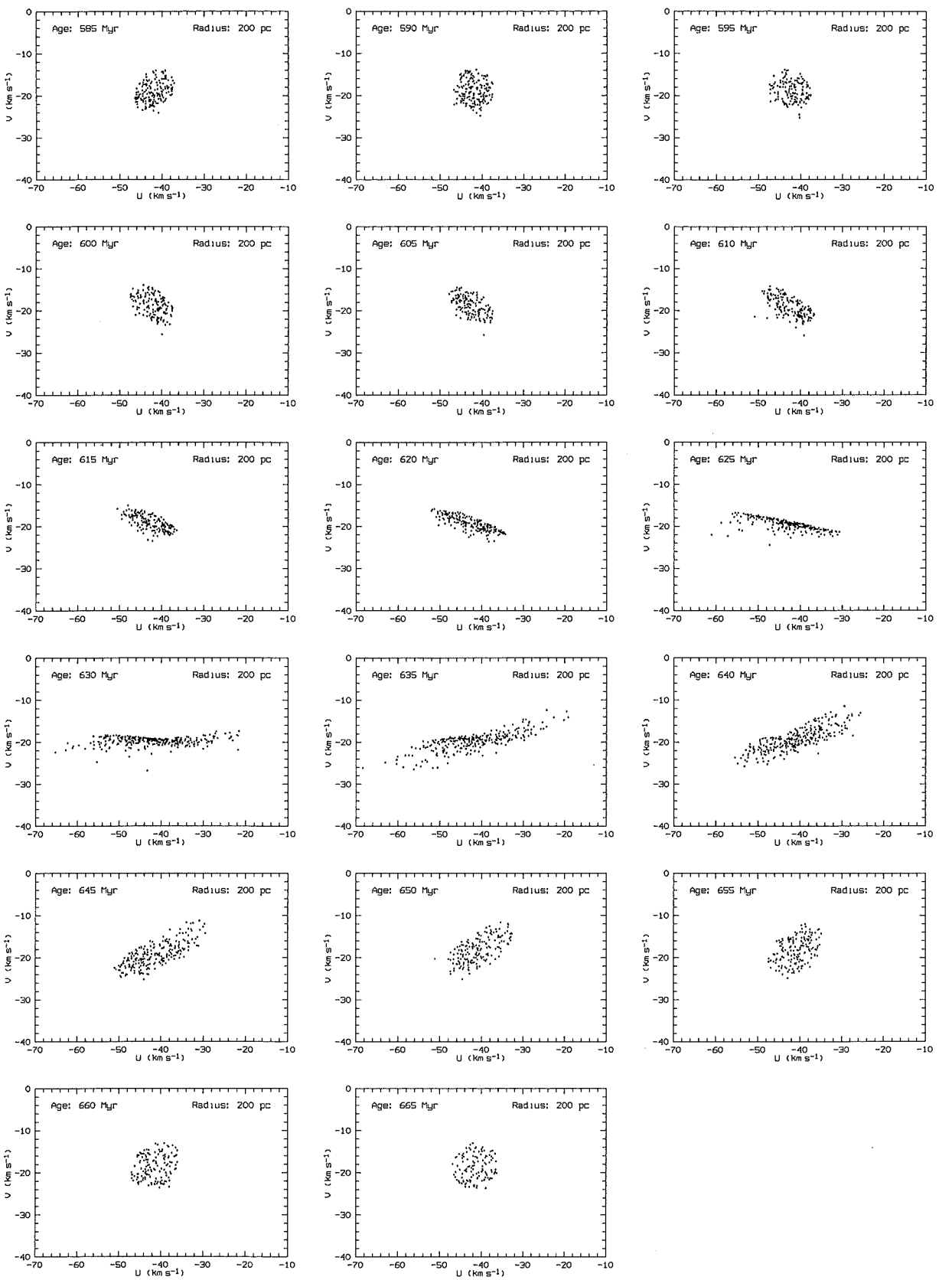

Figure 4.19: *The model Hyades moving group in the UV-plane for various ages, assuming a solar neighbourhood radius of* 200 pc.

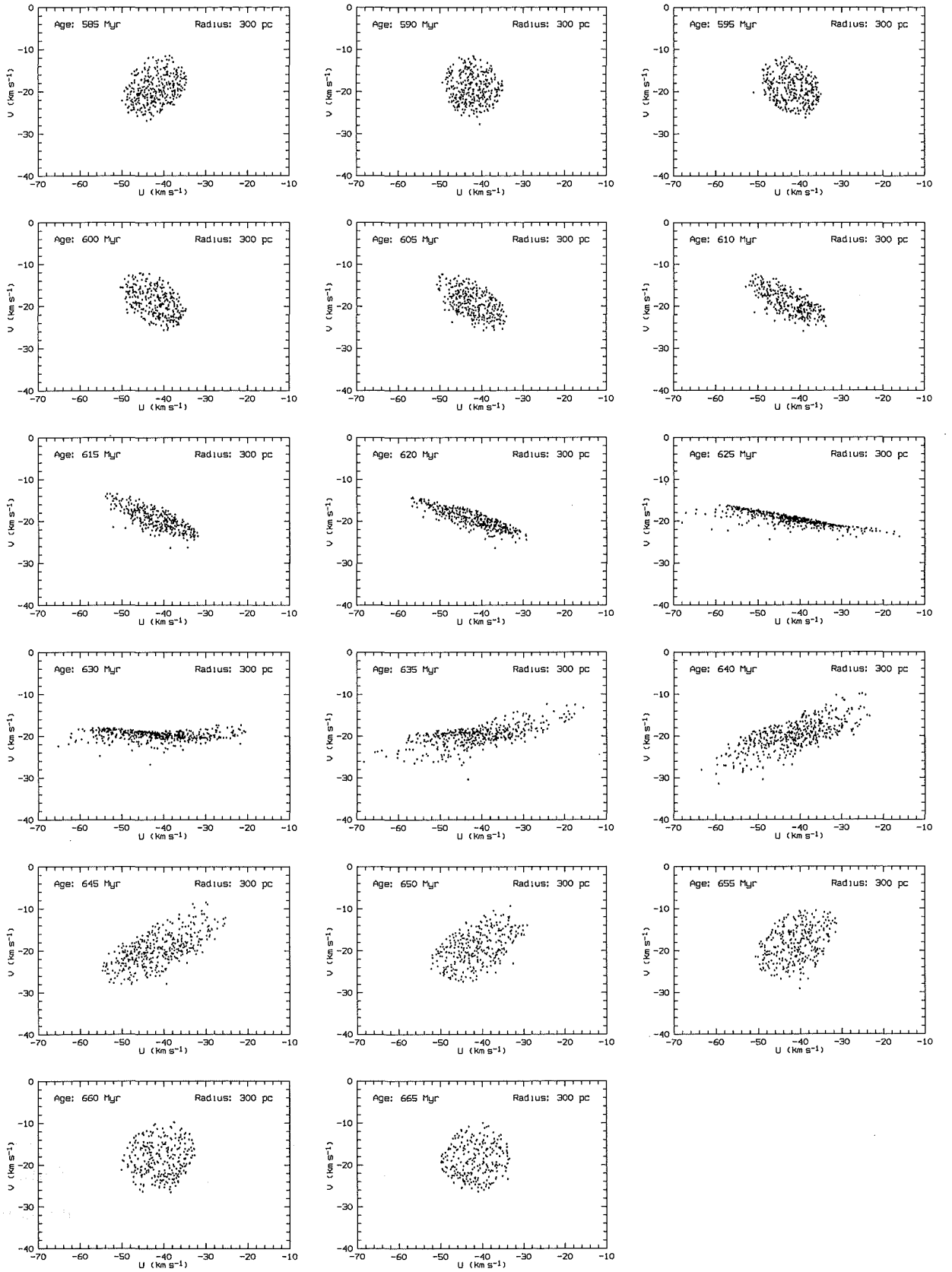

Figure 4.20: *The model Hyades moving group in the UV-plane for various ages, assuming a solar neighbourhood radius of* 300 pc.

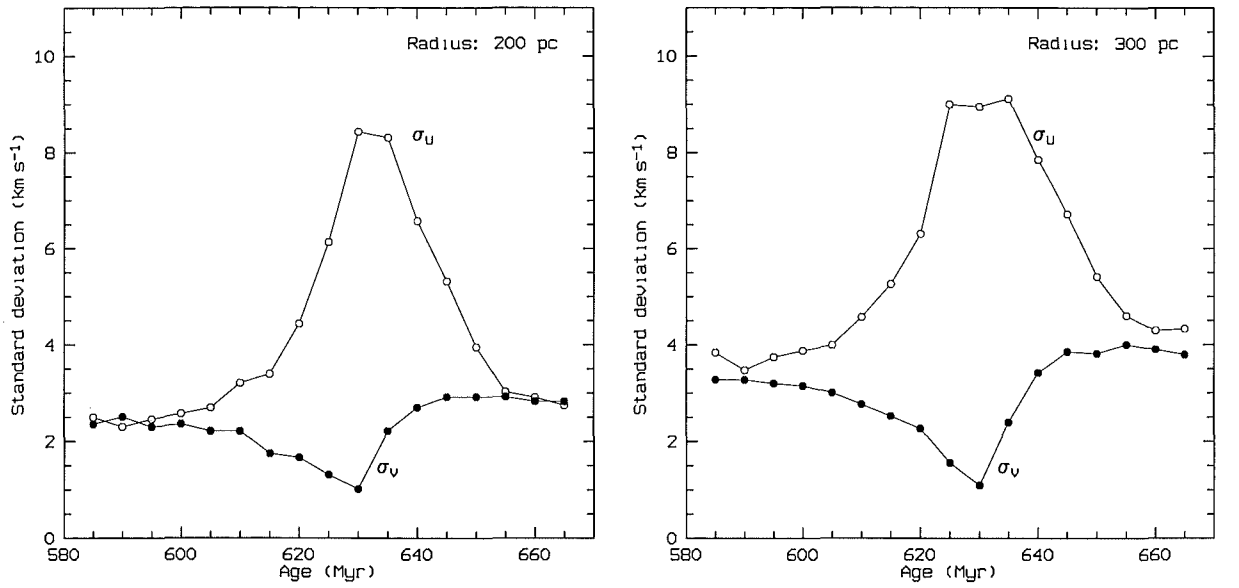

Figure 4.21: *Velocity dispersions for the model Hyades moving group at various ages and for two different solar neighbourhoods ($r_1 = 200$ pc, $r_2 = 300$ pc). Open circles (σ_U) represent the standard deviation in U and filled dots (σ_V) represent the standard deviation in V.*

The shape of the distribution changes rapidly with age. During the 80 Myr interval covered by Figures 4.19 and 4.20, a full cycle is completed between a circular shape, at an age of 590 Myr, and through various elliptical stages of different eccentricity and tilt back to the circular shape again at an age of 665 Myr. The major axis of the distribution rotates counter-clockwise during this transformation process. The circular shapes correspond to the broadest parts of the supercluster, while the elliptical shapes are found in narrower sections. The distribution becomes almost linear close to a node of the supercluster.

Due to the variable shape and apparent rotation of the velocity distribution, the dispersions (i.e. standard deviations σ_U and σ_V) in the U and V velocity components both depend on the age. This is presented in Figure 4.21. However, there is a difference in behaviour of the two standard deviations. The variations in σ_V are relatively slow, staying within 1 km s^{-1} at almost every age except when approaching the node. This is not difficult to understand from Figures 4.19 and 4.20, where the apparent height of the distribution in the V-direction does not change much from one plot to another (except close to the node), while the distribution itself changes both its tilt and its length. The minimum value of about 1 km s^{-1} is reached at an age of 630 Myr (slightly off the node) and this value is the same for both radii of the solar neighbourhood. At other ages the values stay around $2-3$ km s^{-1}, for $r = 200$ pc, and around $3-4$ km s^{-1}, for $r = 300$ pc. On the other hand, the standard deviation σ_U shows more variation as a direct result of the rotation of the distribution in the UV-plane. Sufficiently far from the node the values stay close to σ_V (as long as the shape of the distribution is nearly circular). Closer to the node, however, the values increase steeply

up to a maximum of about 9 $\mathrm{km\,s^{-1}}$, when the distribution appears as a horizontal bar in the UV-plane.

In a situation like this it is very difficult (if at all possible) to find a connection between the dispersions in the galactic velocity components of an observed moving group in the solar neighbourhood, and the initial dispersions acquired at star formation. Only if the moving group is observed at one of the narrowest sections of the supercluster, does the dispersion in U become close to the original velocity dispersion. However, this can hardly be of any practical significance, so long as our observations stay within a few hundred parsecs of the Sun, where it is almost impossible to tell what section of the supercluster is being observed.

To conclude this section it has to be pointed out that any modelling of the galactic rotation in a way presented in this chapter is always uncertain to some level due to various effects that might influence the stellar orbits in the complex galactic gravitational filed. For some of these effects see e.g. Wielen et al. (1996), where it was demonstrated that the Sun has actually migrated from the inner part of the Galaxy to the present radius during its lifetime of about 4.5 Gyr. The same authors estimated that the Sun was formed at a galactic radius of only about 6.6 kpc. However, one can assume that these effects can be neglected over the relatively short periods of time (several hundred Myr) that are used in this thesis.

Chapter 5

Conclusions

5.1 Aim of this thesis

This thesis presents the results of a research project undertaken at the University of Canterbury in order to test the reality of *moving groups* of stars in our Galaxy. Moving groups have been suggested by Olin Eggen (in a series of papers spanning several decades) to be former clusters that have evaporated to become field stars with similar galactic orbits. A hypothesis has also been proposed (Eggen's membership criterion) that all stars belonging to a moving group should have the same velocity component in the direction of galactic rotation (i.e. V = [constant]), while the other two components (towards the galactic centre and towards the north galactic pole, i.e. U and W) are distributed with some dispersion that is possibly related to the original velocity dispersion at star formation. In the absence of reliable stellar trigonometric parallaxes, Eggen has introduced the concept of *group parallaxes*. The group parallax for a star belonging to a moving group corresponds to such a distance at which the V component of the space velocity takes the same value as for the rest of the group.

In 1982 J. Hearnshaw and P. Cottrell (Department of Physics and Astronomy, University of Canterbury) made a successful proposal (Hipparcos Scientific Proposal No. 61) to the European Space Agency (ESA) for over 800 moving group stars found in Eggen's papers to be observed by the Hipparcos satellite. As a result, precise positions, parallaxes and proper motions have been obtained for these stars (as part of the Hipparcos Catalogue) with a typical uncertainty (median precision) of about 1 mas in positions and parallaxes and 1 mas yr^{-1} in proper motions. These astrometric data, when combined with the radial velocities from other sources, can be used to compute stellar space velocities so that the orbits of stars in the solar neighbourhood can be studied.

Three major research areas have been involved in this project, as presented in various chapters in this thesis:

1. High-precision radial-velocity measurements of the programme stars (Chapter 2).

2. Analysis of the Hipparcos data, mainly concentrated on the velocity distribution in the galactic plane (Chapter 3).

3. Modelling of stellar orbits using a numerical model of the galactic gravitational potential (Chapter 4).

The main results obtained in each of these areas are summarized in the following sections of this chapter.

5.2 Radial-velocity measurements

The absolute stellar radial velocities have been obtained for more than 400 programme stars (1536 radial-velocity observations in total) during the three-year observing period. Most of the observing time was spent at Mt John University Observatory (MJUO), Lake Tekapo, New Zealand, using the fibre-fed échelle spectrograph and a CCD detector on the one-metre McLellan telescope. In addition, a significant number of radial-velocity measurements were made at the Dominion Astrophysical Observatory (DAO), Victoria, B.C., Canada, using the coudé spectrograph and either a CCD or the radial velocity spectrometer (RVS) on the 1.2-m telescope. The radial velocities for all observations using a CCD detector have been obtained by cross-correlation with synthetic spectra computed especially for this project by R. Kurucz, at the Harvard-Smithsonian Center for Astrophysics. A precision of $20-30\ \mathrm{m\,s^{-1}}$ has been achieved in this way for stars with intrinsically constant radial velocities. On the other hand, a precision of about $100\ \mathrm{m\,s^{-1}}$ has been obtained for the RVS observations. All radial velocities have been brought to the IAU system using the observations of the IAU radial-velocity standard stars. By comparing the measured and published radial velocities (or by comparing more individual measurements for a single star) several possible candidates for new binary stars have also been discovered.

5.3 Hipparcos data

Using the Hipparcos parallaxes and proper motions combined with the radial velocities from the observational programme of this thesis (or with the published velocities from the Hipparcos Input Catalogue), the space velocities have been analysed for various samples of stars in the solar neighbourhood. First, the most populated of Eggen's moving groups (i.e. the Hyades, Wolf 630, Sirius, Arcturus, 61 Cygni, σ Puppis and γ Leonis groups) have been analysed as part of the Hipparcos Scientific Proposal No. 61. It follows from the velocity distribution of these stars in the galactic UV-plane that the grouping is better with the Hipparcos data than in the case when the ground-based measurements are used. The dispersions in both U and V velocity components become significantly less for most of the

groups when the Hipparcos data are used. This indicates both the high quality of Hipparcos data and a possible reality of moving groups. However, further analysis demonstrates that better grouping (i.e. less velocity dispersion) might be only a result of improved parallaxes, since all stars in the UV-plane tend to be pulled closer to the zero point. Another result is that Eggen's group parallaxes are significantly closer to Hipparcos values than is the case with the previous ground-based measurements. This might be interpreted as the validity of the moving group concept. However, the parallax itself is relatively small for most of the stars, so that this comparison is not convincing. The H-R diagrams for Eggen's moving groups using the Hipparcos data do not confirm the same origin of all stars belonging to the same group. This means that either many of the stars are not members, or the concept is not valid.

A separate analysis was made using a general sample of 4597 stars in the solar neighbourhood, including all 'survey' stars from the Hipparcos Catalogue with existing radial velocities in the Hipparcos Input Catalogue and with parallaxes greater than 10 mas and parallax errors less than 10 per cent. The velocity distribution was estimated using the adaptive kernel method and it was analysed using the wavelet transform technique. The distribution was found to exhibit a branch-like structure. At least three main branches were detected. They are slightly curved but are almost parallel and run diagonally across the UV-diagram at a negative slope. The branches create a quasi-periodic structure in the UV-plane which can be detected using the two-dimensional Fourier transform as well. Moving groups are also seen in the velocity distribution as certain concentrations along the branches.

Stellar metal abundances have been derived from the Geneva Observatory seven-colour photometry. The calibrations have been done separately for two luminosity classes (V and III). A series of statistical tests has been performed in order to check if stellar metallicities are less scattered in moving groups (or in those velocity branches) than in the total sample of stars. These tests do not confirm the hypothesis that moving groups are composed of stars having the same origin.

5.4 Galactic orbits

A numerical model of the galactic gravitational potential has been developed including both the static axisymmetric part (central bulge + galactic disk + dark halo) and the time-dependent spiral component. This model has been used to examine the orbits of stars and to study the evolution of moving groups. Simulations show that some grouping in the velocity plane (including those branches detected in the sample of Hipparcos stars) can be a result of galactic spiral structure. Stars formed in different spiral arms sometimes appear in the same region in the velocity plane (i.e. as a moving group), although they have different origins.

Numerical tests involving creation and evolution of a single stellar cluster that evapo-

rates gradually to become a moving group in the solar neighbourhood demonstrate that the membership criterion of constant V can only serve as a first approximation. The actual distribution of stars in the UV-plane can have different shapes depending on the age, and both velocity components have to be taken into account. On the other hand, the dispersions in U and V can hardly be related to the original velocity dispersion acquired at star formation.

5.5 Eggen's moving groups: fact or fiction?

The title of this section is in fact the title of the Hipparcos Scientific Proposal No. 61, which includes the programme stars as presented, observed and studied in this thesis. Although it seemed at first that a firm answer to this question would be possible as the final result of this project, such an answer in fact was not obtained.

There are two main restraining factors in a study of moving groups of stars. First, there are still no systematic astrometric observations that would cover a significantly larger portion of the galactic disk around the Sun (several kiloparsecs at least) in a form similar to the Hipparcos Catalogue. Second, there are no numerical models of the galactic potential that would produce confident stellar orbits on a longer time scale. Only future development in both of these areas will provide additional information needed for a better understanding of moving groups.

There have been various proposals during the past decade for some future astrometric space missions that would exceed the performance of Hipparcos. These include the GAIA (Global Astrometric Interferometer for Astrophysics), DIVA (Deutsches Interferometer für Vielkanalphotometrie und Astrometrie) and SIM (Space Interferometry Mission) projects. They are all based on interferometry and offer more stars observed with a better precision than Hipparcos. For example, the GAIA project (see e.g. Perryman et al. 1997) has been designed to measure positions, proper motions and parallaxes for at least 40–50 million objects down to a visual magnitude of about 15^{m}, with a precision of 10 microarcsec, and possibly some 350 million objects to 18^{m} with a lower precision. This would provide direct distances up to 10 kpc with a precision better than 10 per cent.

One can probably not expect that better parallaxes will significantly improve the velocity distribution of stars already observed by Hipparcos within $\sim$ 100 pc. However, collecting additional observations at larger distances would allow identifying some longer fragments of hypothetical superclusters and possibly reveal the origin of moving groups. At the same time, these observations would help develop a better theoretical model that would provide answers to the question of the nature of moving groups.

The research presented in this thesis has demonstrated that moving groups are indeed an observational fact. The velocity distribution in the solar neighbourhood is highly non-uniform and fragmented into various concentrations, i.e. groups of stars that share common

space motions. Some of those concentrations are clearly a result of cluster evaporation (e.g. the Hyades moving group), confirming the moving group hypothesis for the young-disk groups. Other concentrations seem to represent clumps of stars with similar motions but different origins and ages (e.g. the Pleiades moving group). Finally, some sort of a branch-like structure can be detected, indicating that moving groups are aligned in a certain way and not simply scattered across the velocity plane. Some of these features can be a result of galactic spiral structure, or some other global properties of the galactic gravitational potential.

The reality probably involves all these possibilities. Moving groups in the solar neighbourhood can be produced by various mechanisms and only improved observations and theoretical models in the future will be able to answer the question of the nature of moving groups with more confidence.

Appendix A

Coordinate systems

A.1 Equatorial and local coordinates

A common way of expressing the positions of stars in astronomy is to provide the three spherical equatorial coordinates: right ascension (α), declination (δ) and distance (b), as shown in Figure A.1. The fundamental plane of this reference system is parallel to the Earth's equator, while the zero point in α coincides with the *vernal equinox* for a given moment of time. The mean equator and equinox J2000 is used in this thesis (the epoch of the FK5 system), which corresponds to JD 245 1545.0 (2000 January 1, 12^{h}).

Instead of using the spherical coordinates (α, δ, b), a rectangular equatorial system xyz

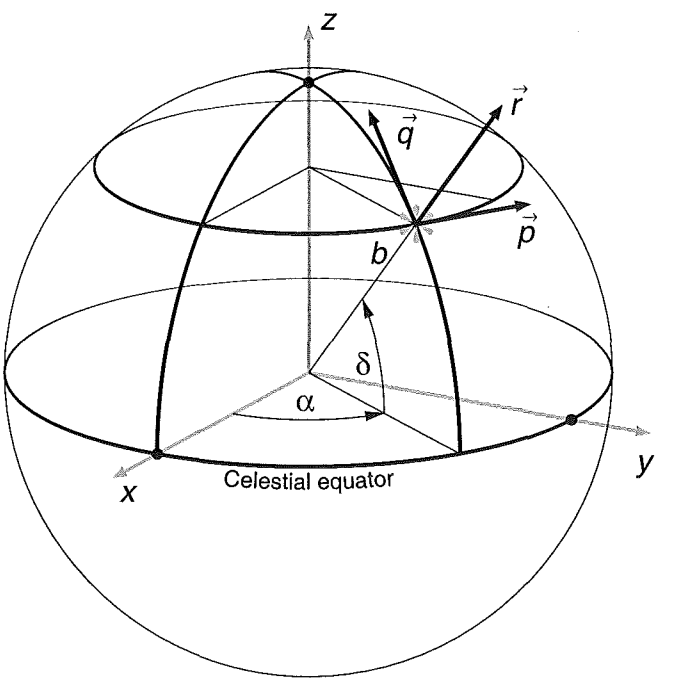

Figure A.1: *Equatorial coordinate system, with local vectors $\vec{p}$, $\vec{q}$, $\vec{r}$ for a star at (α, δ).*

can be defined, with the x-axis pointing to the vernal equinox (zero point in α) and the z-axis towards the north celestial pole (both x and y axes belong to the equatorial plane).

Due to the complicated motion (precession and nutation) of the Earth's equator, the coordinate system described above can be defined only with a limited accuracy. There is a new (improved) definition, based on the positions of many extragalactic sources, and known as the *International Celestial Reference System* (ICRS). In practice, the ICRS coincides with the FK5 (mean equator and equinox J2000) within an uncertainty of 50–80 mas, so that the difference can be ignored here.

The transformation between the spherical and rectangular equatorial coordinates has a form:

$$\left.\begin{aligned} x &= b\,\cos\delta\,\cos\alpha, \\ y &= b\,\cos\delta\,\sin\alpha, \\ z &= b\,\sin\delta. \end{aligned}\right\} \tag{A.1}$$

Sometimes the actual distance towards the star (b) is not relevant, and only the angles α and δ are considered. In such a case one can put $b = 1$, and simply omit the distance parameter from transformation A.1.

For a given point (α, δ) on the celestial sphere, a *local* coordinate system (pqr) can also be constructed, as shown in Figure A.1, where $\vec{p}$, $\vec{q}$ and $\vec{r}$ are unit vectors. The pq-plane is tangential to the celestial sphere, with the vectors $\vec{p}$ and $\vec{q}$ pointing in the directions of increasing α and δ respectively. The direction of the third vector ($\vec{r}$) is always away from the centre.

The components of the vectors $\vec{p}$, $\vec{q}$ and $\vec{r}$, in terms of the equatorial coordinates α and δ are:

$$\vec{p} = \begin{pmatrix} -\sin\alpha \\ \cos\alpha \\ 0 \end{pmatrix}, \qquad \vec{q} = \begin{pmatrix} -\sin\delta\,\cos\alpha \\ -\sin\delta\,\sin\alpha \\ \cos\delta \end{pmatrix}, \qquad \vec{r} = \begin{pmatrix} \cos\delta\,\cos\alpha \\ \cos\delta\,\sin\alpha \\ \sin\delta \end{pmatrix}. \tag{A.2}$$

It is simple to express the position and velocity vectors $(\vec{b}, \vec{v})$ of a star in local coordinates:

$$\begin{pmatrix} b_p \\ b_q \\ b_r \end{pmatrix} = \begin{pmatrix} 0 \\ 0 \\ A_\mathrm{p}/\pi \end{pmatrix}, \qquad \begin{pmatrix} v_p \\ v_q \\ v_r \end{pmatrix} = \begin{pmatrix} A_\mathrm{v}\mu_{\alpha*}/\pi \\ A_\mathrm{v}\mu_\delta/\pi \\ V_\mathrm{r} \end{pmatrix}, \tag{A.3}$$

where π is the parallax, $\mu_\alpha*$ and μ_δ are the proper motions ($\mu_\alpha* = \mu_\alpha\,\cos\delta$) and V_r is the radial velocity. The two constants A_p and A_v are chosen in such a way that the components of $\vec{b}$ and $\vec{v}$ are expressed in pc and $\mathrm{km\,s^{-1}}$ respectively, when parallax, proper motion and radial velocity are measured in mas, $\mathrm{mas\,yr^{-1}}$ and $\mathrm{km\,s^{-1}}$, respectively. Hence:

$$\left.\begin{aligned} A_\mathrm{p} &= 1000\ \mathrm{mas\,pc}, \\ A_\mathrm{v} &= 4.74047\ \mathrm{km\,s^{-1}yr}, \end{aligned}\right\} \tag{A.4}$$

where:

$$A_{\rm v} = \frac{1 \text{ astronomical unit [km]}}{1 \text{ year [s yr}^{-1}]} = \frac{149\,597\,870 \text{ [km]}}{31\,557\,600 \text{ [s yr}^{-1}]}. \tag{A.5}$$

The three local vectors $(\vec{p}, \vec{q}, \vec{r})$ also define the *rotation matrix* R that converts the local coordinates into the equatorial ones:

$$R = \begin{pmatrix} p_x & q_x & r_x \\ p_y & q_y & r_y \\ p_z & q_z & r_z \end{pmatrix} = \begin{pmatrix} -\sin\alpha & -\sin\delta\cos\alpha & \cos\delta\cos\alpha \\ \cos\alpha & -\sin\delta\sin\alpha & \cos\delta\sin\alpha \\ 0 & \cos\delta & \sin\delta \end{pmatrix}. \tag{A.6}$$

By using this matrix, the equatorial position and velocity can be computed as:

$$\begin{pmatrix} b_x \\ b_y \\ b_z \end{pmatrix} = R \begin{pmatrix} b_p \\ b_q \\ b_r \end{pmatrix}, \qquad \begin{pmatrix} v_x \\ v_y \\ v_z \end{pmatrix} = R \begin{pmatrix} v_p \\ v_q \\ v_r \end{pmatrix}. \tag{A.7}$$

A.2 Galactic coordinates

When studying the structure and kinematics of the Milky Way galaxy, then the galactic coordinate system is used. It is a rectangular system centred at the Sun, with the X-axis pointing to the galactic centre, Y-axis in the direction of galactic rotation (in the galactic plane, clockwise when seen from the north galactic pole), and Z-axis towards the north galactic pole (Figure A.2). The same capital letters (X, Y, Z) are used to denote the galactic coordinates of a star (i.e. its position in parsecs), while U, V and W are used for the corresponding galactic components of the space velocity vector[1]:

$$U = \frac{dX}{dt}, \quad V = \frac{dY}{dt}, \quad W = \frac{dZ}{dt}. \tag{A.8}$$

The galactic system is defined by the equatorial position of the north galactic pole ($\alpha_{\rm G}$, $\delta_{\rm G}$) and the longitude of the ascending node (l_Ω). In this thesis the values given in the Hipparcos Catalogue will be used, with respect to the ICRS (ESA 1997, Vol. 1, p. 91):

$$\left.\begin{aligned} \alpha_{\rm G} &= 192\overset{\circ}{.}859\,48, \\ \delta_{\rm G} &= +27\overset{\circ}{.}128\,25, \\ l_\Omega &= 32\overset{\circ}{.}931\,92. \end{aligned}\right\} \tag{A.9}$$

In order to transform the equatorial rectangular coordinates into galactic ones, the galactic rotation matrix G is used:

$$\begin{pmatrix} X \\ Y \\ Z \end{pmatrix} = G \begin{pmatrix} b_x \\ b_y \\ b_z \end{pmatrix}, \qquad \begin{pmatrix} U \\ V \\ W \end{pmatrix} = G \begin{pmatrix} v_x \\ v_y \\ v_z \end{pmatrix}. \tag{A.10}$$

[1]The U component of the space velocity is positive towards the galactic centre and negative in the opposite direction, due to the definition of the X-axis. Some authors, however, define U to be positive for a motion away from the centre (this is particularly the case in Eggen's papers).

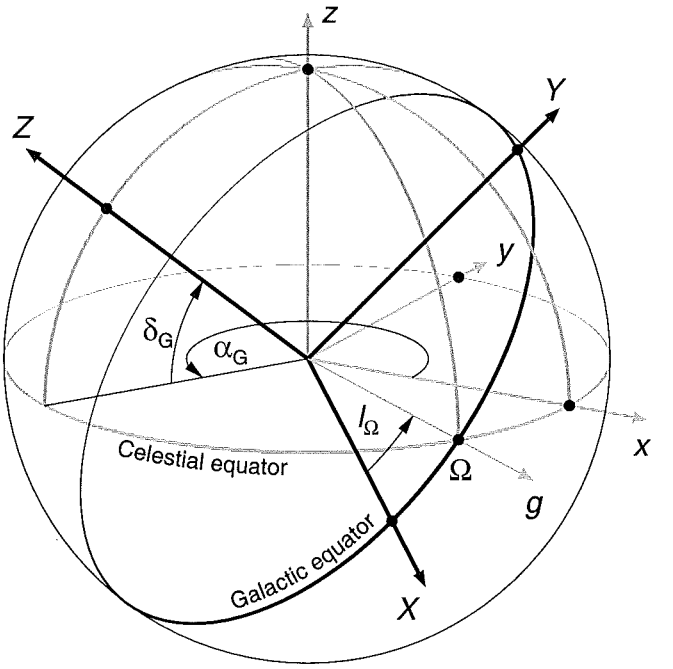

Figure A.2: *Galactic coordinate system.*

The rotation matrix G can be expressed as a product of three successive elementary rotations (see Appendix E for more details on elementary rotations):

- First, a rotation of $90° + \alpha_G$ about the equatorial z-axis (x goes to g).
- Next, a rotation of $90° - \delta_G$ about the new g-axis (z goes to Z).
- Finally, a rotation of $-l_\Omega$ about the galactic Z-axis (g goes to X).

To compute the matrix G, the elementary rotations are multiplied:

$$G = R_Z(-l_\Omega)\, R_X(90° - \delta_G)\, R_Z(90° + \alpha_G). \tag{A.11}$$

In an expanded form, this can be written as:

$$G = \begin{pmatrix} -\sin\alpha_G \cos l_\Omega + \cos\alpha_G \sin l_\Omega \sin\delta_G & \cos\alpha_G \cos l_\Omega + \sin\alpha_G \sin l_\Omega \sin\delta_G & -\sin l_\Omega \cos\delta_G \\ -\sin\alpha_G \sin l_\Omega - \cos\alpha_G \cos l_\Omega \sin\delta_G & \cos\alpha_G \sin l_\Omega - \sin\alpha_G \cos l_\Omega \sin\delta_G & \cos l_\Omega \cos\delta_G \\ \cos\alpha_G \cos\delta_G & \sin\alpha_G \cos\delta_G & \sin\delta_G \end{pmatrix}, \tag{A.12}$$

which, together with the numerical values (A.9), gives:

$$G = \begin{pmatrix} -0.054\,875\,560 & -0.873\,437\,090 & -0.483\,835\,016 \\ 0.494\,109\,428 & -0.444\,829\,630 & 0.746\,982\,244 \\ -0.867\,666\,149 & -0.198\,076\,373 & 0.455\,983\,776 \end{pmatrix}. \tag{A.13}$$

A direct transformation from the local coordinates to the galactic ones can be done by using the matrix product GR:

$$\begin{pmatrix} X \\ Y \\ Z \end{pmatrix} = GR \begin{pmatrix} b_p \\ b_q \\ b_r \end{pmatrix}, \qquad \begin{pmatrix} U \\ V \\ W \end{pmatrix} = GR \begin{pmatrix} v_p \\ v_q \\ v_r \end{pmatrix}. \tag{A.14}$$

Appendix B

Error propagation

B.1 Univariate and multivariate statistics

In the simplest (*univariate*) case, the result of an experiment is a single random variable, a. Everything that is known about such a variable (in statistical terms) is its *mean* and its *variance*, defined in the following way:

$$\left.\begin{aligned} \mu &= \frac{\sum_{k=1}^{n} a_k}{n}, && \text{(mean)} \\ \sigma^2 &= \frac{\sum_{k=1}^{n} (a_k - \mu)^2}{n-1}, && \text{(variance)} \end{aligned}\right\} \tag{B.1}$$

where the *sample mean* and *sample variance* are actually used, assuming that there are n estimates for the variable: a_1, a_2, $\ldots a_n$. The variance is usually expressed as σ^2, where σ is the *standard deviation.*

Another experiment (*multivariate case*) can also be considered, resulting in a set of m different quantities: a_1, a_2, a_3, $\ldots a_m$. This can be a real measurement process, but it can also be a purely numerical process, such as the lest-square fit to some data points, generating a set of parameters. In this multivariate case, a_i is not an i-th estimate of the same variable, but it is rather an *element* of a set of quantities (or a *component* of a vector). Sometimes the vector notation $\vec{a}$ is used to represent the whole set. If the experiment is repeated, another estimate for the vector $\vec{a}$ will be obtained (all m values together). In some sense, each element a_i can be regarded as a separate univariate variable, having its own mean and variance, but the situation can be more complicated. In general, the values a_i can be correlated to each other, so that estimation of one of them is dependent on the estimations of all the others. A typical example can be a polynomial least-square fit: the coefficients of the fit are always strongly correlated. The means and variances alone cannot describe such multivariate data completely. One has to use *covariances* in addition, so that a complete list

of statistical parameters for a set of multivariate data becomes:

$$\left.\begin{aligned} \mu_i &= \frac{\sum_{k=1}^{n} a_{ik}}{n}, && \text{(means)} \\ \sigma_i^2 = \sigma_{ii} &= \frac{\sum_{k=1}^{n} (a_{ik} - \mu_i)^2}{n-1}, && \text{(variances)} \\ \sigma_{ij} &= \frac{\sum_{k=1}^{n} (a_{ik} - \mu_i)(a_{jk} - \mu_j)}{n-1}. && \text{(covariances)} \end{aligned}\right\} \tag{B.2}$$

Here σ_{ii} is used as an alternative way to express the variance σ_i^2 of the i-th variable. It is also possible to regard the variance σ_{ii} as the *covariance* of a_i with itself. Actually, the definition of covariance includes the definition of variance (for $i = j$), as can be easily seen from (B.2).

While the means and variances are m-dimensional vectors (like the original set of variables), the covariances can be arranged into an $m \times m$ matrix:

$$\Sigma = \begin{pmatrix} \sigma_{11} & \sigma_{12} & \dots & \sigma_{1m} \\ \sigma_{21} & \sigma_{22} & \dots & \sigma_{2m} \\ . & . & \dots & . \\ . & . & \dots & . \\ . & . & \dots & . \\ \sigma_{m1} & \sigma_{m2} & \dots & \sigma_{mm} \end{pmatrix}. \tag{B.3}$$

Instead of covariances, the *correlation coefficients* are often used, given by:

$$\rho_{ij} = \frac{\sigma_{ij}}{\sigma_i \sigma_j}, \quad (\rho_{ii} \equiv 1), \tag{B.4}$$

so that all $m \times m$ coefficients can also be arranged in a matrix:

$$\mathrm{P} = \begin{pmatrix} \rho_{11} & \rho_{12} & \dots & \rho_{1m} \\ \rho_{21} & \rho_{22} & \dots & \rho_{2m} \\ . & . & \dots & . \\ . & . & \dots & . \\ . & . & \dots & . \\ \rho_{m1} & \rho_{m2} & \dots & \rho_{mm} \end{pmatrix} = \begin{pmatrix} 1 & \rho_{12} & \dots & \rho_{1m} \\ \rho_{21} & 1 & \dots & \rho_{2m} \\ . & . & \dots & . \\ . & . & \dots & . \\ . & . & \dots & . \\ \rho_{m1} & \rho_{m2} & \dots & 1 \end{pmatrix}. \tag{B.5}$$

There is a simple matrix relation between Σ and P, based on (B.4). However, for this purpose, the standard deviations σ_i have to be arranged in a diagonal matrix:

$$\Delta = \begin{pmatrix} \sigma_1 & 0 & \dots & 0 \\ 0 & \sigma_2 & \dots & 0 \\ . & . & \dots & . \\ . & . & \dots & . \\ . & . & \dots & . \\ 0 & 0 & \dots & \sigma_m \end{pmatrix}, \tag{B.6}$$

where, obviously, the standard deviation matrix Δ contains only the square roots of the diagonal elements of Σ. The transformation between Σ and P (e.g. Chatfield & Collins 1980, p. 26) has a form:

$$\left.\begin{aligned} \Sigma &= \Delta\,\mathrm{P}\,\Delta, \\ \mathrm{P} &= \Delta^{-1}\,\Sigma\,\Delta^{-1}, \end{aligned}\right\} \tag{B.7}$$

where Δ^{-1} means matrix inversion.

B.2 General error propagation

If an initial set of m parameters $a_1, a_2, \ldots a_m$ is given (as introduced in the previous section), together with their corresponding covariance matrix Σ, and then an arbitrary transformation (a set of functions) is applied to get another (*transformed*) set of parameters $(c_1, c_2, \ldots c_m)$:

$$\vec{c} = f(\vec{a}), \tag{B.8}$$

then a new covariance matrix will be necessary to describe the derived values:

$$S = \begin{pmatrix} s_{11} & s_{12} & \ldots & s_{1m} \\ s_{21} & s_{22} & \ldots & s_{2m} \\ . & . & \ldots & . \\ . & . & \ldots & . \\ . & . & \ldots & . \\ s_{m1} & s_{m2} & \ldots & s_{mm} \end{pmatrix}. \tag{B.9}$$

Here s_{ij} has the same meaning for the two quantities c_i and c_j as σ_{ij} has for a_i and a_j, using the definitions analogue to (B.2). In order to find a relation between the matrices Σ and S, one has to know the exact form of the transformation (B.8). In general, there are m functions of m variables:

$$\left.\begin{aligned} c_1 &= f_1(a_1, a_2, \ldots a_m), \\ c_2 &= f_2(a_1, a_2, \ldots a_m), \\ &. \\ &. \\ &. \\ c_m &= f_m(a_1, a_2, \ldots a_m), \end{aligned}\right\} \tag{B.10}$$

with a Jacobian matrix:

$$J = \begin{pmatrix} \partial f_1/\partial a_1 & \partial f_1/\partial a_2 & \ldots & \partial f_1/\partial a_m \\ \partial f_2/\partial a_1 & \partial f_2/\partial a_2 & \ldots & \partial f_2/\partial a_m \\ . & . & \ldots & . \\ . & . & \ldots & . \\ . & . & \ldots & . \\ \partial f_m/\partial a_1 & \partial f_m/\partial a_2 & \ldots & \partial f_m/\partial a_m \end{pmatrix}. \tag{B.11}$$

Then, to the first order in the covariances (The Hipparcos Catalogue, ESA 1997, Volume 1, p. 90), the relation between Σ and S can be expressed in a form:

$$S = J\,\Sigma\,J^{\mathrm{T}}, \tag{B.12}$$

where T denotes the transposition. Once the covariance matrix S has been computed, then it is easy to extract the standard deviations s_i as the square roots of the diagonal elements[1]. A diagonal matrix (B.6) can also be constructed, and the new correlation matrix computed using (B.7).

B.3 Errors in galactic positions and velocities

The general error propagation described in the previous section will be applied here to the problem of the uncertainties (standard errors) in galactic position and velocity components for a given star, as computed from the six *spherical* equatorial parameters: α, δ, π, $\mu_{\alpha*}$, μ_δ, V_{r}. First, a 6×6 covariance matrix has to be constructed, by taking into account:

- Standard errors in the five Hipparcos astrometric parameters: $\sigma_{\alpha*}$, σ_δ, σ_π, $\sigma_{\mu_{\alpha*}}$, σ_{μ_δ}, expressed in mas and mas yr^{-1} (Hipparcos fields H14–H18).
- Standard error in radial velocity ($\sigma_{V_{\mathrm{r}}}$), expressed in km s^{-1} (from an independent source, e.g. Hipparcos Input Catalogue).
- Correlation coefficients (dimensionless) between the astrometric parameters: $\rho^{\delta}_{\alpha*}$, $\rho^{\pi}_{\alpha*}$, ρ^{π}_{δ}, $\rho^{\mu_{\alpha*}}_{\alpha*}$, $\rho^{\mu_{\alpha*}}_{\delta}$, $\rho^{\mu_{\alpha*}}_{\pi}$, $\rho^{\mu_\delta}_{\alpha*}$, $\rho^{\mu_\delta}_{\delta}$, $\rho^{\mu_\delta}_{\pi}$, $\rho^{\mu_\delta}_{\mu_{\alpha*}}$ (H19–H28).

Since the radial velocity is not correlated with the five astrometric parameters, the matrices (B.5) and (B.6) can be constructed as:

$$\mathrm{P} = \begin{pmatrix} 1 & \rho^{\delta}_{\alpha*} & \rho^{\pi}_{\alpha*} & \rho^{\mu_{\alpha*}}_{\alpha*} & \rho^{\mu_\delta}_{\alpha*} & 0 \\ \rho^{\delta}_{\alpha*} & 1 & \rho^{\pi}_{\delta} & \rho^{\mu_{\alpha*}}_{\delta} & \rho^{\mu_\delta}_{\delta} & 0 \\ \rho^{\pi}_{\alpha*} & \rho^{\pi}_{\delta} & 1 & \rho^{\mu_{\alpha*}}_{\pi} & \rho^{\mu_\delta}_{\pi} & 0 \\ \rho^{\mu_{\alpha*}}_{\alpha*} & \rho^{\mu_{\alpha*}}_{\delta} & \rho^{\mu_{\alpha*}}_{\pi} & 1 & \rho^{\mu_\delta}_{\mu_{\alpha*}} & 0 \\ \rho^{\mu_\delta}_{\alpha*} & \rho^{\mu_\delta}_{\delta} & \rho^{\mu_\delta}_{\pi} & \rho^{\mu_\delta}_{\mu_{\alpha*}} & 1 & 0 \\ 0 & 0 & 0 & 0 & 0 & 1 \end{pmatrix}, \quad \Delta = \begin{pmatrix} \sigma_{\alpha*} & 0 & 0 & 0 & 0 & 0 \\ 0 & \sigma_\delta & 0 & 0 & 0 & 0 \\ 0 & 0 & \sigma_\pi & 0 & 0 & 0 \\ 0 & 0 & 0 & \sigma_{\mu_{\alpha*}} & 0 & 0 \\ 0 & 0 & 0 & 0 & \sigma_{\mu_\delta} & 0 \\ 0 & 0 & 0 & 0 & 0 & \sigma_{V_{\mathrm{r}}} \end{pmatrix} \tag{B.13}$$

and then the covariance matrix (B.7) is:

$$\Sigma = \Delta\,\mathrm{P}\,\Delta. \tag{B.14}$$

Now the coordinate transformations can be considered. The process starts from the local coordinates (A.3) and then a rotation is performed to the equatorial system (A.7). This can

[1] In order to have non-negative diagonal elements s_{ii} for any given Jacobian J, the original covariance matrix Σ must be *positive definite*. This is always the case if the matrix is computed from (B.2).

be regarded as a six-dimensional transformation from the initial set of six spherical elements to the final set of six equatorial rectangular parameters:

$$\begin{pmatrix} \alpha* \\ \delta \\ \pi \\ \mu_{\alpha*} \\ \mu_\delta \\ V_\mathrm{r} \end{pmatrix} \longrightarrow \begin{pmatrix} b_x \\ b_y \\ b_z \\ v_x \\ v_y \\ v_z \end{pmatrix}, \tag{B.15}$$

where $\alpha* = \alpha\cos\delta$ is used, rather than α, in order to maintain the homogeneity with the standard error in right ascension (it is $\sigma_{\alpha*}$ and not σ_α that is tabulated).

The transformation can be expressed explicitly as a set of six functions:

$$\left.\begin{aligned}
b_x &= \frac{A_\mathrm{p}}{\pi} r_x, \\
b_y &= \frac{A_\mathrm{p}}{\pi} r_y, \\
b_z &= \frac{A_\mathrm{p}}{\pi} r_z, \\
v_x &= \frac{A_\mathrm{v}}{\pi}\mu_{\alpha*} p_x + \frac{A_\mathrm{v}}{\pi}\mu_\delta q_x + V_\mathrm{r} r_x, \\
v_y &= \frac{A_\mathrm{v}}{\pi}\mu_{\alpha*} p_y + \frac{A_\mathrm{v}}{\pi}\mu_\delta q_y + V_\mathrm{r} r_y, \\
v_z &= \frac{A_\mathrm{v}}{\pi}\mu_{\alpha*} p_z + \frac{A_\mathrm{v}}{\pi}\mu_\delta q_z + V_\mathrm{r} r_z.
\end{aligned}\right\} \tag{B.16}$$

The Jacobian of the transformation can be computed directly as:

$$J = \begin{pmatrix}
\kappa\frac{\partial b_x}{\partial\alpha}\sec\delta & \kappa\frac{\partial b_x}{\partial\delta} & \frac{\partial b_x}{\partial\pi} & \frac{\partial b_x}{\partial\mu_{\alpha*}} & \frac{\partial b_x}{\partial\mu_\delta} & \frac{\partial b_x}{\partial V_\mathrm{r}} \\
\kappa\frac{\partial b_y}{\partial\alpha}\sec\delta & \kappa\frac{\partial b_y}{\partial\delta} & \frac{\partial b_y}{\partial\pi} & \frac{\partial b_y}{\partial\mu_{\alpha*}} & \frac{\partial b_y}{\partial\mu_\delta} & \frac{\partial b_y}{\partial V_\mathrm{r}} \\
\kappa\frac{\partial b_z}{\partial\alpha}\sec\delta & \kappa\frac{\partial b_z}{\partial\delta} & \frac{\partial b_z}{\partial\pi} & \frac{\partial b_z}{\partial\mu_{\alpha*}} & \frac{\partial b_z}{\partial\mu_\delta} & \frac{\partial b_z}{\partial V_\mathrm{r}} \\
\kappa\frac{\partial v_x}{\partial\alpha}\sec\delta & \kappa\frac{\partial v_x}{\partial\delta} & \frac{\partial v_x}{\partial\pi} & \frac{\partial v_x}{\partial\mu_{\alpha*}} & \frac{\partial v_x}{\partial\mu_\delta} & \frac{\partial v_x}{\partial V_\mathrm{r}} \\
\kappa\frac{\partial v_y}{\partial\alpha}\sec\delta & \kappa\frac{\partial v_y}{\partial\delta} & \frac{\partial v_y}{\partial\pi} & \frac{\partial v_y}{\partial\mu_{\alpha*}} & \frac{\partial v_y}{\partial\mu_\delta} & \frac{\partial v_y}{\partial V_\mathrm{r}} \\
\kappa\frac{\partial v_z}{\partial\alpha}\sec\delta & \kappa\frac{\partial v_z}{\partial\delta} & \frac{\partial v_z}{\partial\pi} & \frac{\partial v_z}{\partial\mu_{\alpha*}} & \frac{\partial v_z}{\partial\mu_\delta} & \frac{\partial v_z}{\partial V_\mathrm{r}}
\end{pmatrix}, \tag{B.17}$$

where $(\partial/\partial\alpha)\sec\delta = \partial/\partial\alpha*$ and $\kappa = 206\,264\,806^{-1}$ rad mas^{-1}. This factor κ is necessary since the operators $\partial/\partial\alpha$ and $\partial/\partial\delta$ are normally expressed in rad^{-1}, while mas^{-1} are needed here (the uncertainties in the Hipparcos catalogue are given in mas).

In order to evaluate the derivatives $\partial/\partial\alpha$ and $\partial/\partial\delta$, the following relations will be used for the rotation matrix R (A.6):

$$\left.\begin{aligned}
\frac{\partial R}{\partial \alpha} &= \begin{pmatrix} -p_y & -q_y & -r_y \\ p_x & q_x & r_x \\ 0 & 0 & 0 \end{pmatrix}, \\
\frac{\partial R}{\partial \alpha *} &= \begin{pmatrix} -p_y \sec\delta & -q_y \sec\delta & p_x \\ p_x \sec\delta & q_x \sec\delta & p_y \\ 0 & 0 & 0 \end{pmatrix}, \\
\frac{\partial R}{\partial \delta} &= \begin{pmatrix} 0 & -r_x & q_x \\ 0 & -r_y & q_y \\ 0 & -r_z & q_z \end{pmatrix}.
\end{aligned}\right\} \tag{B.18}$$

After computing and substituting all the partial derivatives, the Jacobian matrix becomes:

$$J = \begin{pmatrix}
\kappa\frac{A_\mathrm{p}}{\pi}p_x & \kappa\frac{A_\mathrm{p}}{\pi}q_x & -\frac{A_\mathrm{p}}{\pi^2}r_x & 0 & 0 & 0 \\
\kappa\frac{A_\mathrm{p}}{\pi}p_y & \kappa\frac{A_\mathrm{p}}{\pi}q_y & -\frac{A_\mathrm{p}}{\pi^2}r_y & 0 & 0 & 0 \\
\kappa\frac{A_\mathrm{p}}{\pi}p_z & \kappa\frac{A_\mathrm{p}}{\pi}q_z & -\frac{A_\mathrm{p}}{\pi^2}r_z & 0 & 0 & 0 \\
-\kappa v_y \sec\delta & \kappa(V_\mathrm{r}q_x - \frac{A_\mathrm{v}}{\pi}\mu_\delta r_x) & -\frac{A_\mathrm{v}}{\pi^2}(\mu_{\alpha*}p_x + \mu_\delta q_x) & \frac{A_\mathrm{v}}{\pi}p_x & \frac{A_\mathrm{v}}{\pi}q_x & r_x \\
\kappa v_x \sec\delta & \kappa(V_\mathrm{r}q_y - \frac{A_\mathrm{v}}{\pi}\mu_\delta r_y) & -\frac{A_\mathrm{v}}{\pi^2}(\mu_{\alpha*}p_y + \mu_\delta q_y) & \frac{A_\mathrm{v}}{\pi}p_y & \frac{A_\mathrm{v}}{\pi}q_y & r_y \\
0 & \kappa(V_\mathrm{r}q_z - \frac{A_\mathrm{v}}{\pi}\mu_\delta r_z) & -\frac{A_\mathrm{v}}{\pi^2}(\mu_{\alpha*}p_z + \mu_\delta q_z) & \frac{A_\mathrm{v}}{\pi}p_z & \frac{A_\mathrm{v}}{\pi}q_z & r_z
\end{pmatrix}. \tag{B.19}$$

An additional rotation is necessary to get the galactic components. Using the 3×3 matrix G (A.13), and bearing in mind the transformation (A.10), one can easily construct a 6×6 matrix that will transform the six equatorial parameters into galactic ones:

$$\begin{pmatrix} X \\ Y \\ Z \\ U \\ V \\ W \end{pmatrix} = Q \begin{pmatrix} b_x \\ b_y \\ b_z \\ v_x \\ v_y \\ v_z \end{pmatrix}, \qquad Q = \begin{pmatrix} G & O \\ O & G \end{pmatrix}, \tag{B.20}$$

where O is a 3×3 zero-matrix. The Jacobian of this transformation is also Q, so that the total *local-to-galactic* Jacobian is QJ.

Using (B.12), the covariance matrix S for the galactic components of the position and velocity vectors can now be written in a form:

$$S = QJ \ \Sigma \ J^\mathrm{T}Q^\mathrm{T}, \tag{B.21}$$

where $(QJ)^{\mathrm{T}} = J^{\mathrm{T}}Q^{\mathrm{T}}$.

The square roots of the diagonal elements s_{11}, s_{22}, ... s_{66} will give the standard errors in X, Y, Z, U, V and W respectively.

Appendix C

An example: position and velocity of Arcturus

It will be illustrated here how the coordinate transformation and error propagation procedures, introduced in Appendices A and B, work on a real star. As a suitable example, Arcturus (α Bootis) is taken, as one of the brightest programme stars. It is also a standard radial velocity star, as adopted by the IAU. The basic astrometric parameters for Arcturus, taken from the Hipparcos Catalogue (ESA 1997), are presented in Table C.1. The radial velocity and its uncertainty were taken from the IAU list of standard radial velocity stars (e.g. the Astronomical Almanac for the year 2000).

Table C.1: *(First row) Spherical parameters for Arcturus (HIP 69673), as taken from the Hipparcos Catalogue. (Second row) Standard errors for the spherical parameters. (Third row) Correlation coefficients between the astrometric parameters.*

α	δ	π	$\mu_{\alpha*}$	μ_δ	V_r
$^\circ$	$^\circ$	mas	mas yr^{-1}	mas yr^{-1}	km s^{-1}
213.91811403	+19.18726997	88.85	−1093.45	−1999.40	−5.3
$\sigma_{\alpha*}$	σ_δ	σ_π	$\sigma_{\mu_{\alpha*}}$	σ_{μ_δ}	σ_{V_r}
mas	mas	mas	mas yr^{-1}	mas yr^{-1}	km s^{-1}
0.92	0.42	0.74	0.60	0.52	0.1

$\rho^\delta_{\alpha*}$	$\rho^\pi_{\alpha*}$	ρ^π_δ	$\rho^{\mu_{\alpha*}}_{\alpha*}$	$\rho^{\mu_{\alpha*}}_\delta$	$\rho^{\mu_{\alpha*}}_\pi$	$\rho^{\mu_\delta}_{\alpha*}$	$\rho^{\mu_\delta}_\delta$	$\rho^{\mu_\delta}_\pi$	$\rho^{\mu_\delta}_{\mu_{\alpha*}}$
−0.52	0.16	−0.13	−0.07	0.05	−0.01	0.03	−0.12	−0.03	−0.31

C.1 Galactic position and velocity

First, the local position and velocity (A.3) are computed:

$$\begin{pmatrix} b_p \\ b_q \\ b_r \end{pmatrix} = \begin{pmatrix} 0.000 & \mathrm{pc} \\ 0.000 & \mathrm{pc} \\ 11.255 & \mathrm{pc} \end{pmatrix}, \qquad \begin{pmatrix} v_p \\ v_q \\ v_r \end{pmatrix} = \begin{pmatrix} -58.340 & \mathrm{km\,s^{-1}} \\ -106.675 & \mathrm{km\,s^{-1}} \\ -5.300 & \mathrm{km\,s^{-1}} \end{pmatrix}. \tag{C.1}$$

Next, the equatorial rotation matrix R (A.6) is computed:

$$R = \begin{pmatrix} 0.558007489 & 0.272731229 & -0.783738042 \\ -0.829835913 & 0.183392965 & -0.527009846 \\ 0.000000000 & 0.944449415 & 0.328656816 \end{pmatrix}. \tag{C.2}$$

The galactic position and velocity follow from (A.14):

$$\begin{pmatrix} X \\ Y \\ Z \end{pmatrix} = \begin{pmatrix} 3.875 & \mathrm{pc} \\ 1.043 & \mathrm{pc} \\ 10.515 & \mathrm{pc} \end{pmatrix}, \qquad \begin{pmatrix} U \\ V \\ W \end{pmatrix} = \begin{pmatrix} 25.107 & \mathrm{km\,s^{-1}} \\ -119.043 & \mathrm{km\,s^{-1}} \\ -3.116 & \mathrm{km\,s^{-1}} \end{pmatrix}. \tag{C.3}$$

C.2 Standard errors

The 6×6 correlation and standard deviation matrices (B.13) can be constructed using the values from Table C.1:

$$\left.\begin{aligned} \mathrm{P} &= \begin{pmatrix} 1.00 & -0.52 & 0.16 & -0.07 & 0.03 & 0.00 \\ -0.52 & 1.00 & -0.13 & 0.05 & -0.12 & 0.00 \\ 0.16 & -0.13 & 1.00 & -0.01 & -0.03 & 0.00 \\ -0.07 & 0.05 & -0.01 & 1.00 & -0.31 & 0.00 \\ 0.03 & -0.12 & -0.03 & -0.31 & 1.00 & 0.00 \\ 0.00 & 0.00 & 0.00 & 0.00 & 0.00 & 1.00 \end{pmatrix}, \\ \Delta &= \begin{pmatrix} 0.92 & 0.00 & 0.00 & 0.00 & 0.00 & 0.00 \\ 0.00 & 0.42 & 0.00 & 0.00 & 0.00 & 0.00 \\ 0.00 & 0.00 & 0.74 & 0.00 & 0.00 & 0.00 \\ 0.00 & 0.00 & 0.00 & 0.60 & 0.00 & 0.00 \\ 0.00 & 0.00 & 0.00 & 0.00 & 0.52 & 0.00 \\ 0.00 & 0.00 & 0.00 & 0.00 & 0.00 & 0.10 \end{pmatrix}. \end{aligned}\right\} \tag{C.4}$$

Using (B.14) the full covariance matrix is computed:

$$\Sigma = \begin{pmatrix} 0.846400 & -0.200928 & 0.108928 & -0.038640 & 0.014352 & 0.000000 \\ -0.200928 & 0.176400 & -0.040404 & 0.012600 & -0.026208 & 0.000000 \\ 0.108928 & -0.040404 & 0.547600 & -0.004440 & -0.011544 & 0.000000 \\ -0.038640 & 0.012600 & -0.004440 & 0.360000 & -0.096720 & 0.000000 \\ 0.014352 & -0.026208 & -0.011544 & -0.096720 & 0.270400 & 0.000000 \\ 0.000000 & 0.000000 & 0.000000 & 0.000000 & 0.000000 & 0.010000 \end{pmatrix}. \tag{C.5}$$

Next, the Jacobian (B.19) is evaluated:

$$J = \begin{pmatrix} 3.045\,10^{-8} & 1.488\,10^{-8} & 9.928\,10^{-2} & 0 & 0 & 0 \\ -4.528\,10^{-8} & 1.001\,10^{-8} & 6.676\,10^{-2} & 0 & 0 & 0 \\ 0 & 5.153\,10^{-8} & -4.163\,10^{-2} & 0 & 0 & 0 \\ -1.624\,10^{-7} & -4.123\,10^{-7} & 6.938\,10^{-1} & 2.977\,10^{-2} & 1.455\,10^{-2} & -7.837\,10^{-1} \\ -2.951\,10^{-7} & -2.773\,10^{-7} & -3.247\,10^{-1} & -4.427\,10^{-2} & 9.785\,10^{-3} & -5.270\,10^{-1} \\ 0 & 1.457\,10^{-7} & 1.134 & 0 & 5.039\,10^{-2} & 3.287\,10^{-1} \end{pmatrix} \tag{C.6}$$

and also the six-dimensional galactic matrix Q, as defined in (B.20):

$$Q = \begin{pmatrix} -0.054876 & -0.873437 & -0.483835 & 0 & 0 & 0 \\ 0.494109 & -0.444830 & 0.746982 & 0 & 0 & 0 \\ -0.867666 & -0.198076 & 0.455984 & 0 & 0 & 0 \\ 0 & 0 & 0 & -0.054876 & -0.873437 & -0.483835 \\ 0 & 0 & 0 & 0.494109 & -0.444830 & 0.746982 \\ 0 & 0 & 0 & -0.867666 & -0.198076 & 0.455984 \end{pmatrix}. \tag{C.7}$$

The covariance matrix for the galactic coordinates can be computed using relation (B.21):

$$S = \begin{pmatrix} \boxed{0.001042} & 0.000280 & 0.002826 & 0.007229 & -0.031840 & 0.000494 \\ 0.000280 & \boxed{0.000075} & 0.000761 & 0.001946 & -0.008570 & 0.000133 \\ 0.002826 & 0.000761 & \boxed{0.007670} & 0.019617 & -0.086398 & 0.001341 \\ 0.007229 & 0.001946 & 0.019617 & \boxed{0.052404} & -0.220606 & 0.006257 \\ -0.031840 & -0.008570 & -0.086398 & -0.220606 & \boxed{0.973936} & -0.014322 \\ 0.000494 & 0.000133 & 0.001341 & 0.006257 & -0.014322 & \boxed{0.009115} \end{pmatrix}, \tag{C.8}$$

where the diagonal elements are actually the variances: σ_X^2, σ_Y^2, σ_Z^2, σ_U^2, σ_V^2 and σ_W^2, respectively. By taking the square roots of the variances, the standard errors in all six galactic parameters are found:

$$\begin{pmatrix} \sigma_X \\ \sigma_Y \\ \sigma_Z \end{pmatrix} = \begin{pmatrix} 0.032 & \text{pc} \\ 0.009 & \text{pc} \\ 0.088 & \text{pc} \end{pmatrix}, \qquad \begin{pmatrix} \sigma_U \\ \sigma_V \\ \sigma_W \end{pmatrix} = \begin{pmatrix} 0.229 & \text{km s}^{-1} \\ 0.987 & \text{km s}^{-1} \\ 0.095 & \text{km s}^{-1} \end{pmatrix}. \tag{C.9}$$

Appendix D

Reduction of celestial coordinates

D.1 Precession

Both the Earth's equator and the plane of the ecliptic are in motion. This means that the equatorial reference frame (as defined in Appendix A) is not fixed in space, and a coordinate transformation has to be applied in order to change from one epoch to another. The motion of the ecliptic is called the *planetary precession*, causing a slow drift of the equinox, as well as a decrease in the obliquity. On the other hand, the Earth's equator is involved in an even more prominent motion (*lunisolar precession*), which is basically a rotation of the celestial pole around the pole of the ecliptic. Planetary and lunisolar precession, when combined together, give the *general precession*, which can be regarded as a rotation of the equatorial coordinate frame (Figure D.1).

The precession from $x_0y_0z_0$ to xyz can be divided into three elementary rotations, involving three *accumulated precession angles* (ζ_A, z_A, ϑ_A) that can be computed for any given moment of time, as will be explained later. The elementary rotations (Figure D.1) are:

- First, a rotation of $-\zeta_A$ about the original z_0-axis. This moves the y_0-axis to η and x_0 to ξ.
- Next, a rotation of $+\vartheta_A$ about the η-axis (new y-axis from the previous rotation). This moves the z_0-axis to z and also ξ to μ.
- Finally, a rotation of $-z_A$ about the new z-axis (η goes to y and μ goes to x).

The reduction for precession is a relatively straightforward task in rectangular coordinates (Hohenkerk et al. 1992). To transform the position vector $\vec{r}_0$ referred to the fixed epoch J2000.0, to the position vector $\vec{r}$ referred to the epoch of date, the rotation matrix P is simply applied:

$$\vec{r} = P\,\vec{r}_0. \tag{D.1}$$

In order to compute the precession matrix P, the following steps are performed:

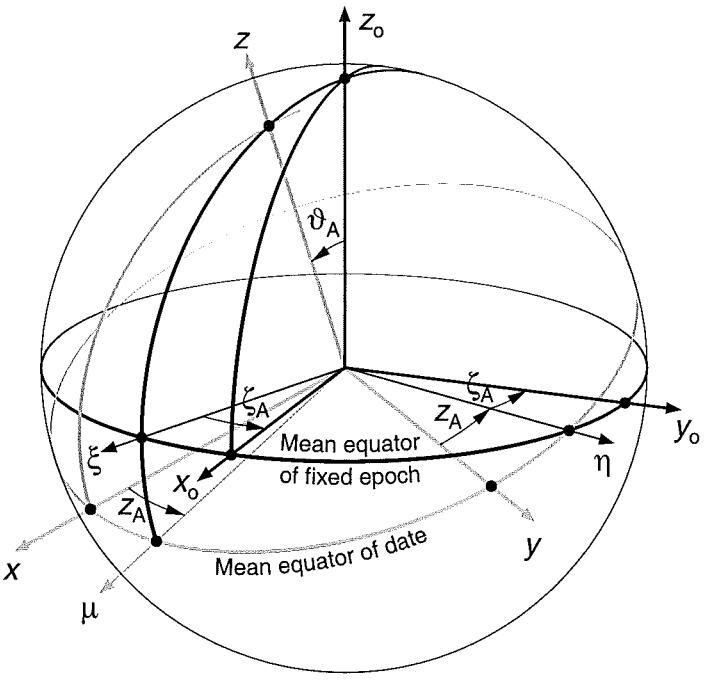

Figure D.1: *Precession from the mean equator of fixed epoch to the mean equator of date.*

1. The period of time is expressed in *Julian centuries*:

$$T = \frac{\mathrm{JD} - \mathrm{JD}_0}{36525}, \tag{D.2}$$

where JD corresponds to the date, and $\mathrm{JD}_0 = 245\,1545$. The scale of TDT[1] should be used.

2. The precession angles (ζ_A, z_A, ϑ_A) are computed:

$$\left.\begin{aligned} \zeta_A &= 2306''.2181\,T + 0''.30188\,T^2 + 0''.017998\,T^3, \\ z_A &= 2306''.2181\,T + 1''.09468\,T^2 + 0''.018203\,T^3, \\ \vartheta_A &= 2004''.3109\,T - 0''.42665\,T^2 - 0''.041833\,T^3. \end{aligned}\right\} \tag{D.3}$$

3. The three elementary rotations are multiplied (in the reverse order, as explained in Appendix E):

$$P = R_Z(-z_A)\,R_Y(\vartheta_A)\,R_Z(-\zeta_A). \tag{D.4}$$

[1]Terrestrial Dynamical Time. Until 1984, *ephemeris time* (ET) was used to describe a uniform time scale argument of the fundamental ephemerides of the Sun, Moon, and planets. Two other time scales are used today: *Terrestrial Dynamical Time* (TDT) and *Barycentric Dynamical Time* (TDB), both acting as a replacement for ET. The first is used in a reference frame centred in the Earth, while the second is used in a frame centred at the solar system barycentre. The difference between TDT and TDB is very small and can be ignored. The difference between TDT and UT is called *ephemeris correction* (ΔT = TDT − UT). At present (1999) the correction is about $+64^s$, slowly increasing by about one second per year.

In an expanded form, the precession matrix is:

$$P = \begin{pmatrix} \cos z_A \cos\vartheta_A \cos\zeta_A - \sin z_A \sin\zeta_A & -\cos z_A \cos\vartheta_A \sin\zeta_A - \sin z_A \cos\zeta_A & -\cos z_A \sin\vartheta_A \\ \sin z_A \cos\vartheta_A \cos\zeta_A + \cos z_A \sin\zeta_A & -\sin z_A \cos\vartheta_A \sin\zeta_A + \cos z_A \cos\zeta_A & -\sin z_A \sin\vartheta_A \\ \sin\vartheta_A \cos\zeta_A & -\sin\vartheta_A \sin\zeta_A & \cos\vartheta_A \end{pmatrix}. \tag{D.5}$$

D.2 Nutation

The term *nutation* is used to describe oscillations of the Earth's rotation axis about the mean precessional motion. The oscillations are complicated, including a number of different periods, but at any given moment of time, the total effect of the nutation is a simple rotation of the equatorial reference frame relative to its mean position. This transformation can also be represented as a sequence of three elementary rotations, as shown in Figure D.2, where the total nutation is resolved into two components: nutation in longitude ($\Delta\psi$) and nutation in obliquity ($\Delta\varepsilon$), while the mean obliquity of the ecliptic is ε_0 and the true obliquity is $\varepsilon = \varepsilon_0 + \Delta\varepsilon$. Using these angles, the three elementary rotations from xyz to $x'y'z'$ are:

- First, a rotation of $+\varepsilon_0$ about the x-axis, which moves the z-axis to ζ. This is, in fact, a transformation from the mean equator of date to the mean ecliptic of date.
- Next, a rotation of $-\Delta\psi$ about the new ζ-axis. This moves the equinox along the ecliptic so that x goes to x'.

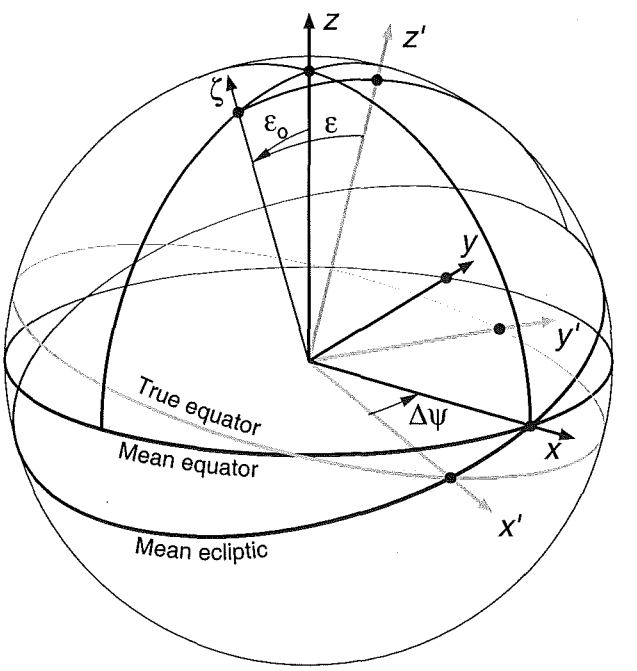

Figure D.2: *Nutation from the mean equator of date to the true equator of date.*

- Finally, a rotation of $-\varepsilon$ about the new x'-axis, so that ζ goes to z'.

A product of these elementary rotations will give the total nutation matrix N that can be used to transform the position vector $\vec{r}$ referred to the mean equator of date, to the position vector $\vec{r}'$ referred to the true equator of date:

$$\vec{r}' = N\vec{r}. \tag{D.6}$$

The 1980 IAU Theory of Nutation will be used here, as described e.g. in Hohenkerk et al. (1992). The basis of this theory is a table of 106 periodic terms (Table D.1), which, when combined together, give the two basic nutation angles ($\Delta\psi$ and $\Delta\varepsilon$). In order to compute the nutation matrix N, the following steps will be performed:

1. For the given Julian date JD, the time is expressed in Julian centuries T, as defined in (D.2).

2. The five *fundamental arguments* (l, l', F, D, Ω), describing the basic geometry between the Earth, Moon and Sun, are computed:

$$\left.\begin{array}{rcrrrrrrrr}
l &=& 134^\circ 57' 46\overset{''}{.}733 &+& (1325^{\mathrm{r}} + 198^\circ 52' 02\overset{''}{.}633)\,T &+& 31\overset{''}{.}310\,T^2 &+& 0\overset{''}{.}064\,T^3, \\
l' &=& 357^\circ 31' 39\overset{''}{.}804 &+& (99^{\mathrm{r}} + 359^\circ 03' 01\overset{''}{.}224)\,T &-& 0\overset{''}{.}577\,T^2 &-& 0\overset{''}{.}012\,T^3, \\
F &=& 93^\circ 16' 18\overset{''}{.}877 &+& (1342^{\mathrm{r}} + 82^\circ 01' 03\overset{''}{.}137)\,T &-& 13\overset{''}{.}257\,T^2 &+& 0\overset{''}{.}011\,T^3, \\
D &=& 297^\circ 51' 01\overset{''}{.}307 &+& (1236^{\mathrm{r}} + 307^\circ 06' 41\overset{''}{.}328)\,T &-& 6\overset{''}{.}891\,T^2 &+& 0\overset{''}{.}019\,T^3, \\
\Omega &=& 135^\circ 02' 40\overset{''}{.}280 &-& (5^{\mathrm{r}} + 134^\circ 08' 10\overset{''}{.}539)\,T &+& 7\overset{''}{.}455\,T^2 &+& 0\overset{''}{.}008\,T^3,
\end{array}\right\} \tag{D.7}$$

   where 1^{r} means a full circle (360°).

3. The mean obliquity of the ecliptic is computed:

$$\varepsilon_0 = 23^\circ 26' 21\overset{''}{.}448 - 46\overset{''}{.}8150\,T - 0\overset{''}{.}00059\,T^2 + 0\overset{''}{.}001813\,T^3. \tag{D.8}$$

4. The nutation in longitude ($\Delta\psi$) and obliquity ($\Delta\varepsilon$) are computed, using Table D.1:

$$\Delta\psi = \sum_{i=1}^{106} S_i \sin A_i, \qquad \Delta\varepsilon = \sum_{i=1}^{106} C_i \cos A_i, \tag{D.9}$$

   where the coefficients S_i and C_i are tabulated, and A_i is a combination of the five fundamental arguments in the form:

$$A_i = a_i l + b_i l' + c_i F + d_i D + e_i \Omega, \tag{D.10}$$

   using the multipliers a_i, b_i, c_i, d_i, e_i from Table D.1 as well. Note that the coefficients S_i and C_i are given as *linear functions* of time: there are two values per each coefficient, so that the second value should be multiplied by T and then added to the first one (e.g. $S_1 = -17\overset{''}{.}1996 - 0\overset{''}{.}01742\,T$).

Table D.1: *Nutation in longitude and obliquity (periodic terms 1–53).*

Sequence Number	Fundamental Arguments					Nutation in Longitude $\Delta\psi$		Nutation in Obliquity $\Delta\varepsilon$	
	l	l'	F	D	Ω				
i	a_i	b_i	c_i	d_i	e_i	S_i [0″.0001]		C_i [0″.0001]	
1	0	0	0	0	1	−171996	−174.2 T	92025	+8.9 T
2	0	0	0	0	2	2062	+0.2 T	−895	+0.5 T
3	−2	0	2	0	1	46	+0.0 T	−24	+0.0 T
4	2	0	−2	0	0	11	+0.0 T	0	+0.0 T
5	−2	0	2	0	2	−3	+0.0 T	1	+0.0 T
6	1	−1	0	−1	0	−3	+0.0 T	0	+0.0 T
7	0	−2	2	−2	1	−2	+0.0 T	1	+0.0 T
8	2	0	−2	0	1	1	+0.0 T	0	+0.0 T
9	0	0	2	−2	2	−13187	−1.6 T	5736	−3.1 T
10	0	1	0	0	0	1426	−3.4 T	54	−0.1 T
11	0	1	2	−2	2	−517	+1.2 T	224	−0.6 T
12	0	−1	2	−2	2	217	−0.5 T	−95	+0.3 T
13	0	0	2	−2	1	129	+0.1 T	−70	+0.0 T
14	2	0	0	−2	0	48	+0.0 T	1	+0.0 T
15	0	0	2	−2	0	−22	+0.0 T	0	+0.0 T
16	0	2	0	0	0	17	−0.1 T	0	+0.0 T
17	0	1	0	0	1	−15	+0.0 T	9	+0.0 T
18	0	2	2	−2	2	−16	+0.1 T	7	+0.0 T
19	0	−1	0	0	1	−12	+0.0 T	6	+0.0 T
20	−2	0	0	2	1	−6	+0.0 T	3	+0.0 T
21	0	−1	2	−2	1	−5	+0.0 T	3	+0.0 T
22	2	0	0	−2	1	4	+0.0 T	−2	+0.0 T
23	0	1	2	−2	1	4	+0.0 T	−2	+0.0 T
24	1	0	0	−1	0	−4	+0.0 T	0	+0.0 T
25	2	1	0	−2	0	1	+0.0 T	0	+0.0 T
26	0	0	−2	2	1	1	+0.0 T	0	+0.0 T
27	0	1	−2	2	0	−1	+0.0 T	0	+0.0 T
28	0	1	0	0	2	1	+0.0 T	0	+0.0 T
29	−1	0	0	1	1	1	+0.0 T	0	+0.0 T
30	0	1	2	−2	0	−1	+0.0 T	0	+0.0 T
31	0	0	2	0	2	−2274	−0.2 T	977	−0.5 T
32	1	0	0	0	0	712	+0.1 T	−7	+0.0 T
33	0	0	2	0	1	−386	−0.4 T	200	+0.0 T
34	1	0	2	0	2	−301	+0.0 T	129	−0.1 T
35	1	0	0	−2	0	−158	+0.0 T	−1	+0.0 T
36	−1	0	2	0	2	123	+0.0 T	−53	+0.0 T
37	0	0	0	2	0	63	+0.0 T	−2	+0.0 T
38	1	0	0	0	1	63	+0.1 T	−33	+0.0 T
39	−1	0	0	0	1	−58	−0.1 T	32	+0.0 T
40	−1	0	2	2	2	−59	+0.0 T	26	+0.0 T
41	1	0	2	0	1	−51	+0.0 T	27	+0.0 T
42	0	0	2	2	2	−38	+0.0 T	16	+0.0 T
43	2	0	0	0	0	29	+0.0 T	−1	+0.0 T
44	1	0	2	−2	2	29	+0.0 T	−12	+0.0 T
45	2	0	2	0	2	−31	+0.0 T	13	+0.0 T
46	0	0	2	0	0	26	+0.0 T	−1	+0.0 T
47	−1	0	2	0	1	21	+0.0 T	−10	+0.0 T
48	−1	0	0	2	1	16	+0.0 T	−8	+0.0 T
49	1	0	0	−2	1	−13	+0.0 T	7	+0.0 T
50	−1	0	2	2	1	−10	+0.0 T	5	+0.0 T
51	1	1	0	−2	0	−7	+0.0 T	0	+0.0 T
52	0	1	2	0	2	7	+0.0 T	−3	+0.0 T
53	0	−1	2	0	2	−7	+0.0 T	3	+0.0 T

Table D.1: *Nutation in longitude and obliquity (periodic terms 54–106).*

Sequence Number	Fundamental Arguments					Nutation in Longitude $\Delta\psi$		Nutation in Obliquity $\Delta\varepsilon$	
	l	l'	F	D	Ω				
i	a_i	b_i	c_i	d_i	e_i	S_i [0″.0001]		C_i [0″.0001]	
54	1	0	2	2	2	−8	+0.0 T	3	+0.0 T
55	1	0	0	2	0	6	+0.0 T	0	+0.0 T
56	2	0	2	−2	2	6	+0.0 T	−3	+0.0 T
57	0	0	0	2	1	−6	+0.0 T	3	+0.0 T
58	0	0	2	2	1	−7	+0.0 T	3	+0.0 T
59	1	0	2	−2	1	6	+0.0 T	−3	+0.0 T
60	0	0	0	−2	1	−5	+0.0 T	3	+0.0 T
61	1	−1	0	0	0	5	+0.0 T	0	+0.0 T
62	2	0	2	0	1	−5	+0.0 T	3	+0.0 T
63	0	1	0	−2	0	−4	+0.0 T	0	+0.0 T
64	1	0	−2	0	0	4	+0.0 T	0	+0.0 T
65	0	0	0	1	0	−4	+0.0 T	0	+0.0 T
66	1	1	0	0	0	−3	+0.0 T	0	+0.0 T
67	1	0	2	0	0	3	+0.0 T	0	+0.0 T
68	1	−1	2	0	2	−3	+0.0 T	1	+0.0 T
69	−1	−1	2	2	2	−3	+0.0 T	1	+0.0 T
70	−2	0	0	0	1	−2	+0.0 T	1	+0.0 T
71	3	0	2	0	2	−3	+0.0 T	1	+0.0 T
72	0	−1	2	2	2	−3	+0.0 T	1	+0.0 T
73	1	1	2	0	2	2	+0.0 T	−1	+0.0 T
74	−1	0	2	−2	1	−2	+0.0 T	1	+0.0 T
75	2	0	0	0	1	2	+0.0 T	−1	+0.0 T
76	1	0	0	0	2	−2	+0.0 T	1	+0.0 T
77	3	0	0	0	0	2	+0.0 T	0	+0.0 T
78	0	0	2	1	2	2	+0.0 T	−1	+0.0 T
79	−1	0	0	0	2	1	+0.0 T	−1	+0.0 T
80	1	0	0	−4	0	−1	+0.0 T	0	+0.0 T
81	−2	0	2	2	2	1	+0.0 T	−1	+0.0 T
82	−1	0	2	4	2	−2	+0.0 T	1	+0.0 T
83	2	0	0	−4	0	−1	+0.0 T	0	+0.0 T
84	1	1	2	−2	2	1	+0.0 T	−1	+0.0 T
85	1	0	2	2	1	−1	+0.0 T	1	+0.0 T
86	−2	0	2	4	2	−1	+0.0 T	1	+0.0 T
87	−1	0	4	0	2	1	+0.0 T	0	+0.0 T
88	1	−1	0	−2	0	1	+0.0 T	0	+0.0 T
89	2	0	2	−2	1	1	+0.0 T	−1	+0.0 T
90	2	0	2	2	2	−1	+0.0 T	0	+0.0 T
91	1	0	0	2	1	−1	+0.0 T	0	+0.0 T
92	0	0	4	−2	2	1	+0.0 T	0	+0.0 T
93	3	0	2	−2	2	1	+0.0 T	0	+0.0 T
94	1	0	2	−2	0	−1	+0.0 T	0	+0.0 T
95	0	1	2	0	1	1	+0.0 T	0	+0.0 T
96	−1	−1	0	2	1	1	+0.0 T	0	+0.0 T
97	0	0	−2	0	1	−1	+0.0 T	0	+0.0 T
98	0	0	2	−1	2	−1	+0.0 T	0	+0.0 T
99	0	1	0	2	0	−1	+0.0 T	0	+0.0 T
100	1	0	−2	−2	0	−1	+0.0 T	0	+0.0 T
101	0	−1	2	0	1	−1	+0.0 T	0	+0.0 T
102	1	1	0	−2	1	−1	+0.0 T	0	+0.0 T
103	1	0	−2	2	0	−1	+0.0 T	0	+0.0 T
104	2	0	0	2	0	1	+0.0 T	0	+0.0 T
105	0	0	2	4	2	−1	+0.0 T	0	+0.0 T
106	0	1	0	1	0	1	+0.0 T	0	+0.0 T

5. The true obliquity of the ecliptic is found:

$$\varepsilon = \varepsilon_0 + \Delta\varepsilon. \tag{D.11}$$

6. The three elementary rotations are multiplied:

$$N = R_{\mathrm{x}}(-\varepsilon)\, R_{\mathrm{z}}(-\Delta\psi)\, R_{\mathrm{x}}(\varepsilon_0). \tag{D.12}$$

In an expanded form, the nutation matrix is:

$$N = \begin{pmatrix} \cos\Delta\psi & -\sin\Delta\psi\cos\varepsilon_0 & -\sin\Delta\psi\sin\varepsilon_0 \\ \sin\Delta\psi\cos\varepsilon & \cos\Delta\psi\cos\varepsilon\cos\varepsilon_0 + \sin\varepsilon\sin\varepsilon_0 & \cos\Delta\psi\cos\varepsilon\sin\varepsilon_0 - \sin\varepsilon\cos\varepsilon_0 \\ \sin\Delta\psi\sin\varepsilon & \cos\Delta\psi\sin\varepsilon\cos\varepsilon_0 - \cos\varepsilon\sin\varepsilon_0 & \cos\Delta\psi\sin\varepsilon\sin\varepsilon_0 + \cos\varepsilon\cos\varepsilon_0 \end{pmatrix}. \tag{D.13}$$

D.3 Positions of stars

The coordinates of stars are usually taken from a catalogue for a fixed epoch (e.g. J2000.0), and then the new coordinates are computed for the epoch of observation. However, in order to get the coordinates of a star for a moment of time different from the catalogue epoch, it is not enough to simply rotate the coordinate axes by applying the precession and nutation matrices. The star itself is moving, and its position is changing in time even if the coordinate system is fixed.

Therefore, one should use *two independent epochs* to describe the position of a star:

- The epoch of the reference frame (i.e. the epoch of the equator and equinox)
- The epoch of the stellar position in that particular reference frame (i.e. the moment of time when the coordinates are taken).

These two epochs can be different. For example, the Hipparcos Catalogue gives the positions in the ICRS reference frame (equator and equinox J2000.0), but the measurements themselves (on average) correspond to a mean epoch of J1991.25. When the Hipparcos Catalogue is used to get the positions for a new epoch, then the precession and nutation from J2000 to the epoch have to be applied, and also the stellar motion effect from J1991.25 to the new epoch.

In general, a transformation of stellar coordinates from one epoch to another has to be done in two steps:

1. In the original reference frame, the new position of the star is found, due to the space motion.
2. The rotation of the reference frame is applied.

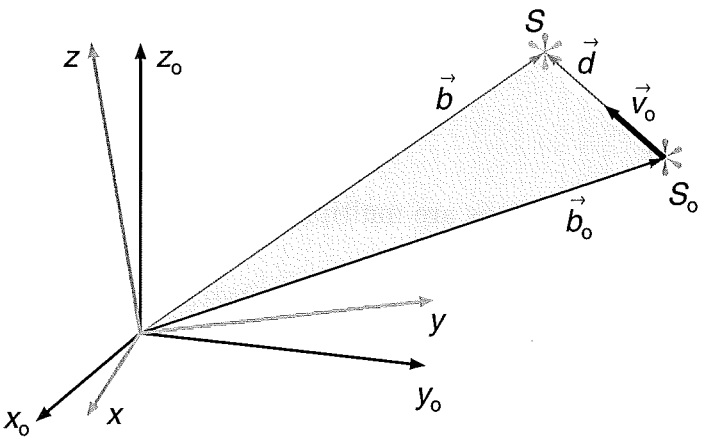

Figure D.3: *Transformation of stellar positions from one epoch to another.*

This is illustrated in Figure D.3, where a star S_0, with a position vector $\vec{b}_0$ and a velocity $\vec{v}_0$ in a reference frame $x_0y_0z_0$, is transformed into S, with a new position $\vec{b}$ in the new reference frame xyz. If the time period between the two epochs is $\Delta t = t - t_0$, then:

$$\left.\begin{aligned} \vec{b}' &= \vec{b}_0 + \vec{v}_0 \Delta t, \\ \vec{b} &= NP\,\vec{b}', \end{aligned}\right\} \tag{D.14}$$

where $\vec{b}'$ is the position vector of the star at the new moment t, but still expressed in the old reference frame $x_0y_0z_0$, and P and N are the precession and nutation matrices.

D.4 Sidereal time

Greenwich Mean Sidereal Time (GMST) is the Greenwich hour angle of the mean equinox of date, and can be computed for any given moment of *universal time* (UT):

$$\mathrm{GMST} = \mathrm{GMST_o} + \mu\,\mathrm{UT}, \tag{D.15}$$

where $\mathrm{GMST_o}$ corresponds to 0^{h} UT, and μ is a conversion factor between the sidereal and mean solar time scales ($\mu \approx 1.002737909$). At 0^{h} UT on a given day JD, the following relation is valid:

$$\mathrm{GMST_o} = 24\,110^{\mathrm{s}}\!.548\,41 + 8\,640\,184^{\mathrm{s}}\!.812\,866\,T_{\mathrm{U}} + 0^{\mathrm{s}}\!.093\,104\,T_{\mathrm{U}}^2 - 0^{\mathrm{s}}\!.000\,006\,2\,T_{\mathrm{U}}^3, \tag{D.16}$$

where T_{U} is expressed in Julian centuries, similar as (D.2), but in terms of universal time:

$$T_{\mathrm{U}} = \frac{\mathrm{JD_{UT}} - 245\,1545.0}{36525}. \tag{D.17}$$

Greenwich Apparent Sidereal Time (GAST) is the Greenwich hour angle of the true equinox of date and is given by:

$$\mathrm{GAST} = \mathrm{GMST} + \frac{1}{15}\Delta\psi\,\cos\varepsilon, \tag{D.18}$$

where $\Delta\psi$ is the nutation in longitude (D.9), and ε is the true obliquity of the ecliptic (D.11).

At any meridian other than Greenwich, the **Local Mean Sidereal Time** (LMST) and **Local Apparent Sidereal Time** (LAST) are computed, simply by adding the longitude λ to the corresponding Greenwich times:

$$\left.\begin{array}{rcl} \text{LMST} &=& \text{GMST} + \lambda, \\ \text{LAST} &=& \text{GAST} + \lambda. \end{array}\right\} \tag{D.19}$$

D.5 Earth's shape and rotation

All astronomical observations are normally done from the surface of the Earth, so that the observed positions and radial velocities are not the same as if they were taken from the Earth's centre. The terms *topocentre* and *geocentre* will be used to describe the observer and the Earth's centre, respectively. At one stage during the reduction procedure, the observations have to be transformed from the topocentric reference frame to the geocentric one, and for this to be done the *geocentric position* and *velocity* of the observer have to be known.

It will be assumed that the Earth has a shape of a rotating ellipsoid, with the equatorial radius a, polar radius b, and the angular velocity ω, as shown in Figure D.4. The *flattening* (f) of the ellipsoid and its *eccentricity* (e) are given by:

$$f = \frac{a-b}{a}, \qquad e = \frac{\sqrt{a^2-b^2}}{a}. \tag{D.20}$$

In practice, however, it is usually the pair (a, f) or $(a, 1/f)$ that is given, in which case the polar axis and the eccentricity can be calculated as:

$$b = a(1-f), \qquad e = \sqrt{2f-f^2}. \tag{D.21}$$

A so-called WGS 84 geodetic reference spheroid will be adopted here (see e.g. Archinal 1992), with the following parameters:

$$a = 6\,378\,137 \text{ m}, \qquad 1/f = 298.257\,223\,563, \qquad \omega = 7.292\,115 \times 10^{-5} \text{rad s}^{-1}. \tag{D.22}$$

An observer P in Figure D.4 is defined by its geocentric position $\vec{\rho}$. The equatorial rectangular reference frame $\xi\eta\zeta$ rotates with the Earth, so that the position of the observer is fixed in time. The $\xi\zeta$-plane is defined by the Greenwich meridian. The position vector $\vec{\rho}$ can be expressed as:

$$\vec{\rho} = \begin{pmatrix} \xi \\ \eta \\ \zeta \end{pmatrix} = \begin{pmatrix} \rho \cos\varphi' \cos\lambda \\ \rho \cos\varphi' \sin\lambda \\ \rho \sin\varphi' \end{pmatrix}, \tag{D.23}$$

where λ, φ' and ρ are geocentric longitude, latitude and radius, respectively.

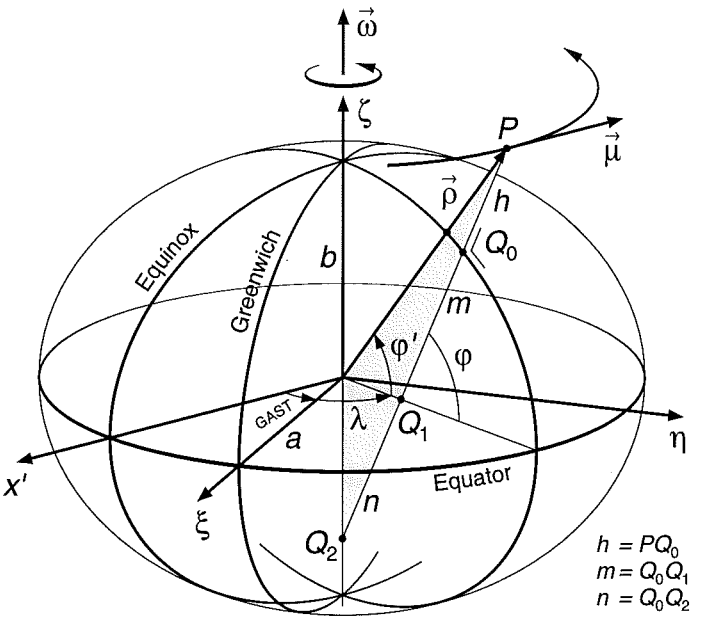

Figure D.4: *The Earth's ellipsoid rotating with an angular velocity ω around the polar axis ζ. An observer P at the geocentric position $\vec{\rho}$ rotates with a velocity vector $\vec{\mu}$.*

In practice, however, the position of a point on the Earth is described using a slightly different set of parameters – *geodetic* longitude, latitude and height above the sea level (λ, φ, h). The longitude λ is the same, but the latitude φ is different. It is now defined as an angle between the *normal* to the Earth's surface and the equatorial plane. The normal to the surface is shown in Figure D.4 as a straight line from P to Q_0 (the sea level), and then to Q_1 (equatorial plane) and Q_2 (ζ-axis). A quantity m is defined as the distance from Q_0 to Q_1, and also a quantity n as the distance from Q_0 all the way to Q_2. It follows from the geometrical properties of the ellipse that:

$$n = \frac{a}{\sqrt{1 - e^2 \sin^2 \varphi}}, \qquad m = (1 - e^2)n. \tag{D.24}$$

In terms of the geodetic coordinates, the position vector $\vec{\rho}$ can be expressed as:

$$\vec{\rho} = \begin{pmatrix} \xi \\ \eta \\ \zeta \end{pmatrix} = \begin{pmatrix} (n+h)\cos\varphi\cos\lambda \\ (n+h)\cos\varphi\sin\lambda \\ (m+h)\sin\varphi \end{pmatrix}. \tag{D.25}$$

It is also possible to construct a non-rotating coordinate system, by choosing not the Greenwich meridian, but a meridian passing through the *vernal equinox* as a fixed zero plane. In this way, a coordinate system referred to the *true equator and equinox* of date is defined, coinciding exactly with the $x'y'z'$ system introduced in Figure D.2 (reduction for nutation). The angle between ξ and x' is the *Greenwich apparent sidereal time* (GAST) corresponding to the moment of the observation. In the new reference frame, similarly to

(D.25), the position vector has a form:

$$\vec{\rho} = \begin{pmatrix} x' \\ y' \\ z' \end{pmatrix} = \begin{pmatrix} (n+h)\cos\varphi\cos(\text{LAST}) \\ (n+h)\cos\varphi\sin(\text{LAST}) \\ (m+h)\sin\varphi \end{pmatrix}, \tag{D.26}$$

where (D.19) has been used in order to convert between the *Greenwich* and *local* sidereal times.

Due to the Earth's rotation, the observer P performs a circular motion with a velocity vector $\vec{\mu}$ that can be expressed as:

$$\vec{\mu} = \vec{\omega} \times \vec{\rho} = \begin{pmatrix} 0 \\ 0 \\ \omega \end{pmatrix} \times \begin{pmatrix} x' \\ y' \\ z' \end{pmatrix}. \tag{D.27}$$

Relations (D.26) and (D.27) can be used to compute the geocentric equatorial position and velocity of the observer, with respect to the true equator and equinox of date.

Appendix E

Rotation of axes using matrices

E.1 Rotation matrix

Let $\vec{r}$ be an arbitrary position vector in a reference frame xyz. If the coordinate system is rotated, a new set of coordinate axes: x', y', z' will be obtained, and the components of $\vec{r}$ will also change. A new notation, $\vec{r}\,'$, will be used for the new vector. Any rotation of coordinates can be expressed in a matrix form:

$$\vec{r}\,' = R\,\vec{r} \quad \Longleftrightarrow \quad \begin{pmatrix} x' \\ y' \\ z' \end{pmatrix} = \begin{pmatrix} r_{11} & r_{12} & r_{13} \\ r_{21} & r_{22} & r_{23} \\ r_{31} & r_{32} & r_{33} \end{pmatrix} \begin{pmatrix} x \\ y \\ z \end{pmatrix}, \tag{E.1}$$

where R is the *rotation matrix*, and it is assumed that the vectors are represented as *columns*.

E.2 Elementary rotations

By *elementary rotations*, the rotations about the coordinate axes are assumed. For a given rotation angle φ, there are three elementary rotations, about the x, y and z axes respectively:

$$\left.\begin{aligned} R_{\mathrm{X}}(\varphi) &= \begin{pmatrix} 1 & 0 & 0 \\ 0 & \cos\varphi & \sin\varphi \\ 0 & -\sin\varphi & \cos\varphi \end{pmatrix}, \\ R_{\mathrm{Y}}(\varphi) &= \begin{pmatrix} \cos\varphi & 0 & -\sin\varphi \\ 0 & 1 & 0 \\ \sin\varphi & 0 & \cos\varphi \end{pmatrix}, \\ R_{\mathrm{Z}}(\varphi) &= \begin{pmatrix} \cos\varphi & \sin\varphi & 0 \\ -\sin\varphi & \cos\varphi & 0 \\ 0 & 0 & 1 \end{pmatrix}. \end{aligned}\right\} \tag{E.2}$$

E.3 Successive rotations

If a rotation can be performed in two steps: R_1 and R_2, then the total rotation matrix R is found from:

$$\vec{r}' = R_2\,(R_1\,\vec{r}) = (R_2\,R_1)\vec{r} = R\,\vec{r}, \tag{E.3}$$

where it is obvious how the two original matrices are multiplied in a reverse order. Any given sequence of n successive rotations: R_1, R_2, $\ldots R_n$ can be represented by a single matrix R being a product of original rotation matrices, but performed in a reverse order:

$$R = R_n \ldots R_3\,R_2\,R_1. \tag{E.4}$$

Appendix F

Radial velocity correction

F.1 Measured radial velocities

Whenever a radial velocity is measured in astronomy, one is aware of the fact that the *total Doppler shift* in the observed spectrum is caused not only by the motion of the source, but also by the motion of the observer (with respect to a common inertial reference frame). This motion of the observer has to be computed and then eliminated from the observed radial velocity, in a procedure called the *radial velocity correction.* Depending on the actual choice of the reference frame in which the procedure is done, two radial velocity corrections are usually found:

- *barycentric* correction, when the stellar velocity is reduced to the solar-system barycentre, and
- *heliocentric* correction, when the stellar velocity is reduced to the centre of the Sun (i.e. the *heliocentre*).

The difference between these two corrections is very small (9–16 $\mathrm{m\,s^{-1}}$ at maximum, as will be demonstrated later), and it is often neglected. However, for highest-precision measurements this difference becomes significant.

The observer's motion can be regarded as the sum of two independent components:

- the Earth's rotation around its polar axis, and
- the Earth's revolution around the solar-system barycentre (or around the Sun).

The Earth's rotation is a highly regular motion that can be predicted with extreme accuracy, as described in Appendix D.5. On the other hand, the Earth's revolution is more complicated, due to the influence of all the other bodies in the solar system, mainly the Moon and the big planets.

F.2 JPL planetary and lunar ephemerides

A very accurate orbit of the Earth (and other planets as well) has become available during the past decade in a form of pre-computed positions and velocities, distributed by the *Jet Propulsion Laboratory* (JPL). The ephemerides have been calculated by a simultaneous numerical integration of equations of motion, taking into account all available observations. There are several types of ephemerides to choose from, depending on the time period covered and their complexity. In this thesis, the DE200 ephemeris is used[1], which has also been the basis of the Astronomical Almanac since 1984.

The ephemeris package in electronic form can be obtained over Internet, from the anonymous FTP server *navigator.jpl.nasa.gov*. The data, together with some software tools (also found at the Internet site), can easily be used to generate positions and velocities for a chosen solar-system body, relative to any other body, over a given period of time.

There are six rectangular equatorial parameters (referred to the mean equator and equinox J2000.0) that can be computed: the three space coordinates (x, y, z, in astronomical units), as well as the three velocity components ($\dot{x}$, $\dot{y}$, $\dot{z}$, in astronomical units per day). Using these values, it is a straightforward task then to eliminate the Earth's motion from an observed radial velocity, as will be demonstrated in the following sections.

In order to make the discussion clearer, a *notation convention* will be adopted here for the position and velocity vectors, as summarized in Table F.1. Different letters are used to denote the vectors depending on the actual centre of coordinates. For example, the heliocentric position of the Earth will be denoted as $\vec{s}_\oplus$, while the barycentric position of the Earth will be denoted as $\vec{b}_\oplus$.

F.3 Barycentric correction

Let a star be observed from the Earth in a direction $\vec{e}_*$ (unit vector), as shown in Figure F.1. The observer is involved both in the Earth's rotation (vector $\vec{\mu}$) and revolution (vector $\vec{v}_\oplus$). These vectors, when projected onto the direction towards the star, make a combined contribution to the observed radial velocity, which is called the *barycentric correction* ($f_{\rm tot} = f_{\rm rev} + f_{\rm rot}$). When defined in this way, the correction has to be *added* to the observed radial velocity in order to get the true radial velocity. The 'true' velocity here means a velocity that would be found by an observer at rest with respect to the solar system barycentre[2].

In order to eliminate the observer's motion, the position and velocity vectors will be

[1]There are other ways of computing the Earth's velocity with high accuracy, such as a self-consistent Fortran program by Stumpff (1980).

[2]This is, in principle, not the same velocity as what would be found by an observer *placed at* the solar system barycentre, since the directions towards the star are different. However, this small effect can be ignored.

Table F.1: *Notation convention for the position and velocity vectors.*

Centre	*Definition*	*Position vector*	*Velocity vector*
Heliocentre	Centre of the Sun	$\vec{s}$	$\vec{u}$
Barycentre	Solar system barycentre	$\vec{b}$	$\vec{v}$
–	Earth-Moon barycentre	$\vec{g}$	$\vec{w}$
Geocentre	Centre of the Earth	$\vec{\rho}$	$\vec{\mu}$
Topocentre	Observer	$\vec{\sigma}$	$\vec{\tau}$

expressed in a common equatorial coordinate system. A convenient choice, of course, is the *true equator and equinox of date*, in which the celestial and terrestrial coordinates can be easily connected (see Appendix D).

The radial velocity V_r of the star is the projection of the space velocity vector $\vec{v}_*$ on the direction towards the star:

$$V_r = \vec{v}_* \cdot \vec{e}_*. \tag{F.1}$$

The barycentric correction procedure can be described in the following steps:

1. For a given moment of UT, the *terrestrial dynamical time* is computed, using the time correction ΔT found in the Astronomical Almanac:

$$\mathrm{TDT} = \mathrm{UT} + \Delta\mathrm{T}. \tag{F.2}$$

2. The rotation matrices P and N, due to the precession and nutation, are computed, as given by (D.5) and (D.13). This is a transformation from the mean equator and equinox J2000.0 to the true equator and equinox of date.

3. The equatorial position and velocity[3] of the star (A.7) are computed, and then the position is transformed to the true equator and equinox of date (D.14).

4. The geocentric position and velocity of the observer are computed, using (D.26) and (D.27).

5. The barycentric position and velocity of the Earth are computed for the equator and equinox J2000 ($\vec{b}_0$, $\vec{v}_0$), using the JPL ephemerides, and then transformed to the true equator and equinox of date: $\vec{b}_\oplus = NP\,\vec{b}_0$ and $\vec{v}_\oplus = NP\,\vec{v}_0$.

6. The topocentric direction towards the star is:

$$\vec{\sigma}_* = \vec{b}_* - \vec{b}_\oplus - \vec{\rho}, \qquad \vec{e}_* = \frac{\vec{\sigma}_*}{|\vec{\sigma}_*|}. \tag{F.3}$$

[3]If the true radial velocity is not known at this stage, it can be set to zero, but the whole procedure should be repeated once the radial velocity has been determined.

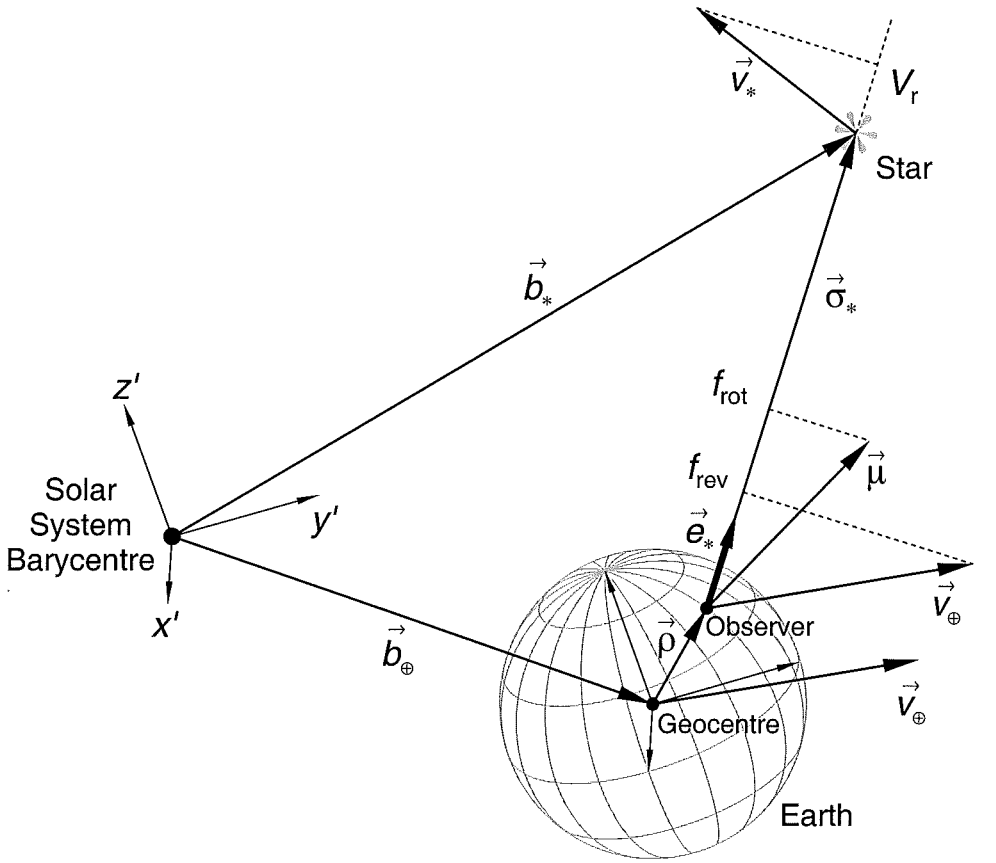

Figure F.1: *Barycentric correction. A star is observed from the Earth, in a direction* $\vec{e}_*$. *All vectors are referred to the true equator and equinox of date* $(x'y'z')$.

7. The observer's motion vectors $\vec{v}_\oplus$ and $\vec{\mu}$ are projected onto the direction towards the star:

$$\left.\begin{aligned} f_{\rm rot} &= \vec{\mu}\cdot\vec{e}_*, \\ f_{\rm rev} &= \vec{v}_\oplus\cdot\vec{e}_*, \\ f_{\rm tot} &= f_{\rm rot}+f_{\rm rev}. \end{aligned}\right\} \qquad \text{(F.4)}$$

8. Finally, the true radial velocity is derived:

$$V_{\rm r} = V'_{\rm r} + f_{\rm tot}, \qquad \text{(F.5)}$$

where $V'_{\rm r}$ is the measured radial velocity.

The barycentric correction procedure, as described above, can be modified in order to give the *heliocentric* correction instead. For this purpose, the heliocentric (not barycentric) position and velocity of the Earth have to be computed in step 5, using also the JPL ephemerides. The difference between the barycentric and heliocentric corrections will be discussed in more detail later, in Section F.5.

F.4 The radial velocity of the Sun

A special case of the heliocentric correction is the radial velocity of the Sun, where the heliocentre is not only the reference point, but also an object being observed. The radial velocity of the Sun is used as a suitable zero point, in order to calibrate the stellar radial velocities. In practice, the telescope is directed not towards the Sun itself, but towards the much less bright *blue sky* (morning or afternoon), so that only the scattered light is measured. It is easy to show that the radial velocity of the "sky" is in fact the same as the radial velocity of the Sun, so that both terms are often used to describe the same quantity.

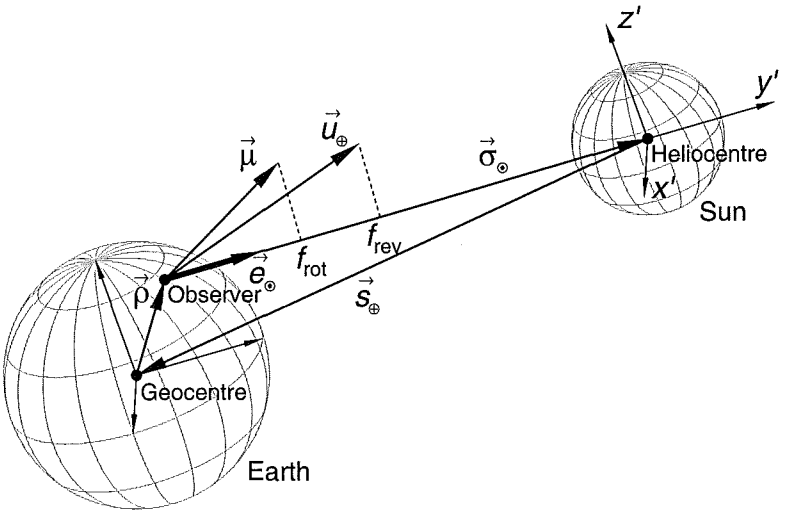

Figure F.2: *The Sun is observed from the Earth, in a direction* $\vec{e}_\odot$. *All vectors are referred to the true equator and equinox of date* $(x'y'z')$.

The basic geometry involved in this case is shown in Figure F.2. The correction procedure can be performed in the following steps:

1. The terrestrial dynamical time (F.2) is computed.
2. The rotation matrices P (D.5) and N (D.13) are computed.
3. The geocentric position and velocity of the observer are computed, using (D.26) and (D.27).
4. The heliocentric position and velocity of the Earth for the equator and equinox J2000 ($\vec{s}_0$, $\vec{u}_0$) are computed, using the JPL ephemerides, and then transformed to the true equator and equinox of date: $\vec{s}_\oplus = NP\,\vec{s}_0$ and $\vec{u}_\oplus = NP\,\vec{u}_0$.
5. The topocentric direction towards the Sun is:

$$\vec{\sigma}_\odot = -(\vec{s}_\oplus + \vec{\rho}), \qquad \vec{e}_\odot = \frac{\vec{\sigma}_\odot}{|\vec{\sigma}_\odot|}. \tag{F.6}$$

6. The observer's motion vectors $\vec{u}_\oplus$ and $\vec{\mu}$ are projected onto the direction towards the Sun:

$$\left.\begin{aligned} f_{\rm rot} &= \vec{\mu}\cdot\vec{e}_\odot, \\ f_{\rm rev} &= \vec{u}_\oplus\cdot\vec{e}_\odot, \\ f_{\rm tot} &= f_{\rm rot}+f_{\rm rev}. \end{aligned}\right\} \tag{F.7}$$

7. For a measured radial velocity $V_{\rm r}'$, the true radial velocity is derived:

$$V_{\rm r} = V_{\rm r}' + f_{\rm tot}. \tag{F.8}$$

F.5 Approximate corrections and the problem of residuals

The barycentric correction procedure, as described in section F.3, should be the only standard way of reducing the stellar radial velocities, since the solar system barycentre is the closest approximation to an inertial reference frame. However, many software packages today use other algorithms and simplifications leading to somewhat different results. It will be demonstrated in this section how these approximate procedures differ from the true barycentric correction.

The most frequent simplifications are:

- The heliocentre used instead of the solar system barycentre (i.e. the heliocentric correction instead of the barycentric one).
- The Earth-Moon barycentre used instead of the geocentre (i.e. ignoring the Moon's influence on the Earth's orbit).

Both these effects are small, but should be taken into account when the highest precision measurements are performed. They affect only the *annual* term of the radial velocity correction (i.e. the term generated by the Earth's orbital motion), while the *diurnal* term (the Earth's rotation) remains the same, and it can be simply ignored for this discussion, assuming that it is always zero, and the observer is at the Earth's centre.

In order to evaluate these effects quantitatively, the Earth's orbital motion relative to the solar system barycentre will be decomposed into three components (Figure F.3):

1. The Earth's motion around the Earth-Moon barycentre, represented by a velocity vector $\vec{w}_\oplus$.
2. An orbital motion of the Earth-Moon barycentre around the Sun (vector $\vec{u}_\otimes$).
3. The Sun's orbital motion around the solar system barycentre (vector $\vec{v}_\odot$).

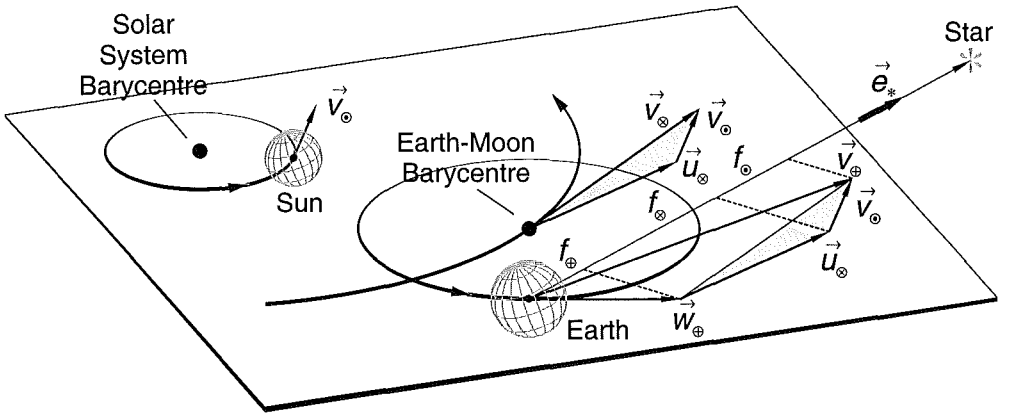

Figure F.3: *The barycentric correction as a sum of three components:* $f_\oplus$, $f_\otimes$, *and* $f_\odot$.

From Figure F.3 one finds:

$$\vec{v}_\otimes = \vec{u}_\otimes + \vec{v}_\odot, \qquad \vec{v}_\oplus = \vec{w}_\oplus + \vec{v}_\otimes = \vec{w}_\oplus + \vec{u}_\otimes + \vec{v}_\odot, \tag{F.9}$$

so that the total barycentric correction ($f_{\rm bar}$) can be computed as a sum of the corresponding projections on the direction towards the star:

$$f_{\rm bar} = \vec{v}_\oplus \cdot \vec{e}_* = \vec{w}_\oplus \cdot \vec{e}_* + \vec{u}_\otimes \cdot \vec{e}_* + \vec{v}_\odot \cdot \vec{e}_* = f_\oplus + f_\otimes + f_\odot, \tag{F.10}$$

where $\vec{e}_*$ is a unit vector, and $f_\otimes$ is the approximate radial velocity correction (the heliocentric correction for an observer at the Earth-Moon barycentre).

Finally, an expression is obtained for the *residual correction*, i.e. the difference between the approximate correction and the actual barycentric correction:

$$\Delta f = f_\otimes - f_{\rm bar} = -(f_\oplus + f_\odot) = -(\vec{w}_\oplus + \vec{v}_\odot) \cdot \vec{e}_*. \tag{F.11}$$

The residual correction is, obviously, not constant. It depends on the direction towards the star, but even for one single direction, it also depends on the orbital velocity vectors $\vec{w}_\oplus$ and $\vec{v}_\odot$, taking its maximum when the two vectors are parallel, and its minimum when they are anti-parallel.

The two orbital vectors $\vec{w}_\oplus$ and $\vec{v}_\odot$ can be computed using the JPL ephemerides. Both the Sun's orbit around the solar system barycentre and the Earth's orbit around the Earth-Moon barycentre are complex, and the velocity vectors change, as shown in Figures F.4 and F.5.

As an example, the residual correction Δf will be computed for a hypothetical observer at an arbitrary longitude, continuously observing stars all over the sky during an observing run. Assuming a typical observing programme containing a number of objects at different right ascensions, one can suppose that at any moment of time the telescope stays close to the meridional plane. For the sake of simplicity, it will be assumed that the observations

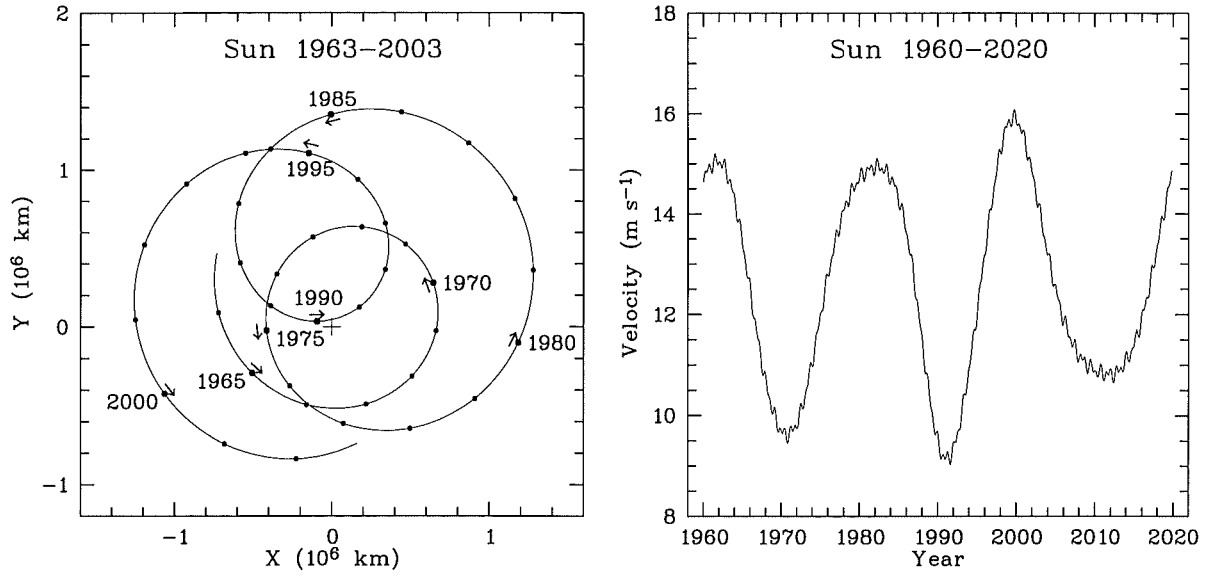

Figure F.4: *The Sun's orbit around the solar system barycentre projected onto the plane of the ecliptic (left) and the magnitude of the Sun's velocity vector (right).*

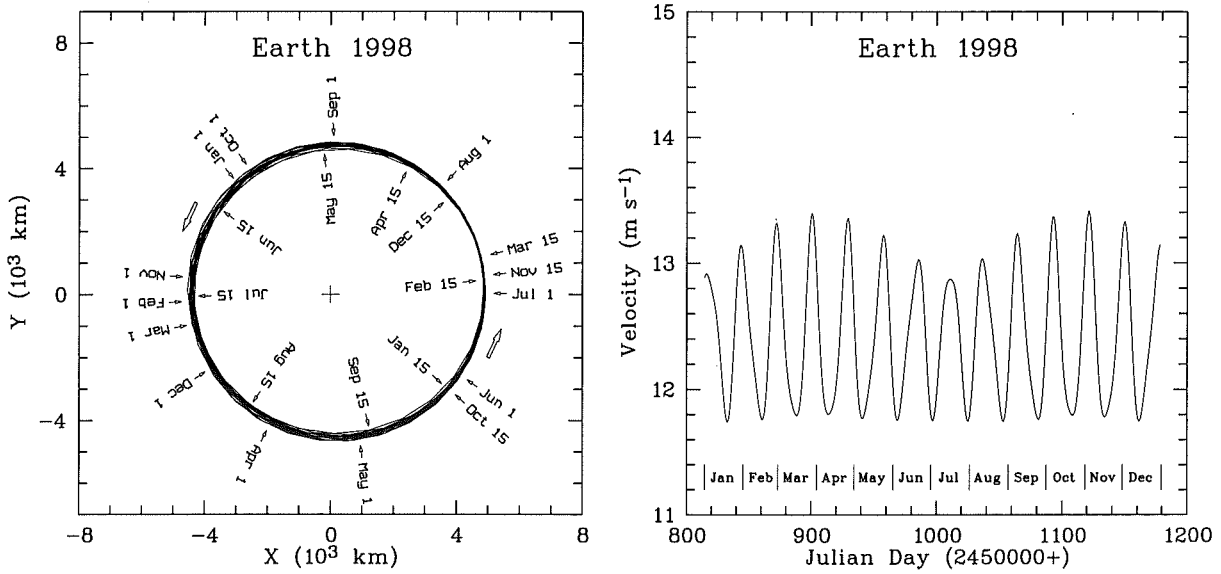

Figure F.5: *The Earth's orbit around the Earth-Moon barycentre projected onto the plane of the ecliptic (left) and the magnitude of the Earth's velocity vector (right).*

are made every hour and only the equatorial stars ($\delta = 0°$) are observed when passing the meridian (α = LAST). This means that the direction towards the star rotates in space synchronously with the Earth's rotation. One expects the residual correction Δf to change from one observation to another. For a particular choice of $\lambda = 0^{\mathrm{h}}$ (Greenwich meridian) and a three-week observing run from 1998 March 20$^{\mathrm{th}}$ till April 10$^{\mathrm{th}}$, the result is shown in Figure F.6. The period of about one day (due to the Earth's rotation) is easily seen, as

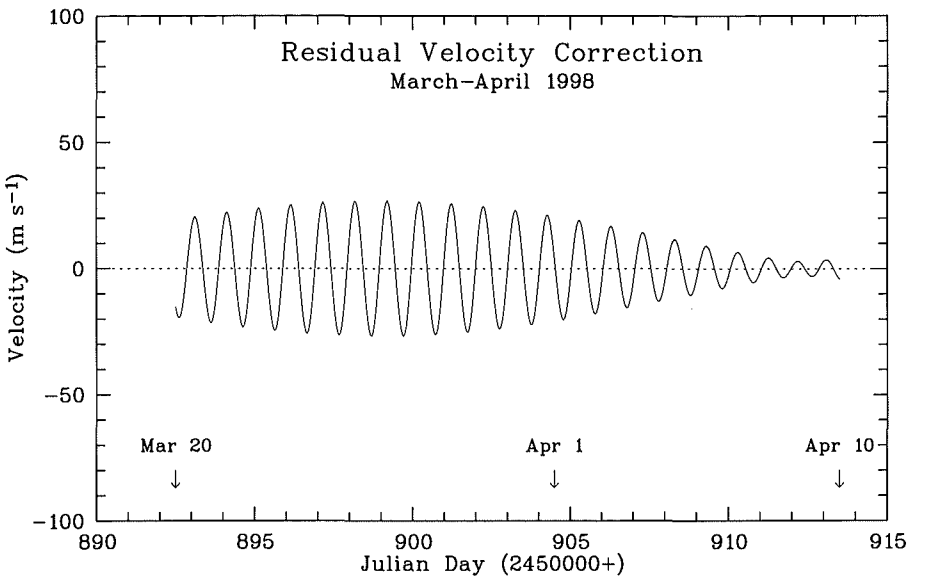

Figure F.6: *Residual radial velocity correction when both the Sun's orbit around the solar-system barycentre and the Earth's orbit around the Earth-Moon barycentre are ignored.*

well as the slow modulation of the amplitude on a monthly basis (due to the Earth's motion around the Earth-Moon barycentre). The maximum residual correction of about 30 m s^{-1} is found around March 26$^{\text{th}}$, when the Earth's and Sun's motions are almost parallel, while the minimum occurs around April 9$^{\text{th}}$, when these two vectors are almost anti-parallel.

Acknowledgements

While working on my PhD project at the University of Canterbury I have met many people who have contributed to this thesis in one way or another.

First, I would like to thank my supervisor, Prof. John Hearnshaw, for everything he has done for me since the very first day of my arrival in New Zealand (this includes even some basic furniture and appliances that Ljiljana and I needed very much in the beginning). During my work on this moving group project John was always there for help and guidance, and at every meeting with him I learnt something new about astronomy. John has always had some nice words to describe my work and that has been a great stimulus to me.

I enjoy this rare privilege of having not one, but two supervisors. So, I would like to thank my associate supervisor, Assoc. Prof. Peter Cottrell, for his continual support and help during my work, and especially at those times when John was away. Peter has always been a rich source of optimism and numerous fresh new ideas, new directions in which I could go, new things that I should do. Not that I have always tried all those new things, though.

I have spent many observing nights at Mt John University Observatory in Lake Tekapo. This has been an important experience for my development as an astronomer. John Baker and Stephen Barlow were always there to make sure that everything was going smoothly with the equipment, and Pam Kilmartin and Alan Gilmore were there for some additional help during the night, or simply to keep me company and invite me for a wonderful dinner, when the weather was not useful for observations.

I would also like to thank the complete staff of the Dominion Astrophysical Observatory, especially Dr Jim Hesser, who made my observing time at their observatory possible. Numerous e-mails exchanged with Murray Fletcher helped me to better understand the RVS reduction procedure.

The staff and students in the Department of Physics and Astronomy also deserve my acknowledgement, especially the astronomy students: Irene, Ljiljana, Lyndon, Orlon, Stuart and others, for providing a nice and pleasant atmosphere in the department over all this time.

And I have to mention here Prof. Per Olof Lindblad from Stockholm Observatory, who helped me with a short, but very useful conversation about stellar orbits, while he and

Gunilla and Jenny were here, travelling around New Zealand.

I have received various grants providing financial support during this PhD work, including a University of Canterbury Doctoral Scholarship, the Royal Society's R. H. T. Bates Scholarship and a Marsden Fund studentship. My overseas trips were supported by the Marsden Fund and the Frank Bradshaw & Elizabeth Pepper Wood Fund, as well as some additional funding from the Department of Physics and Astronomy.

Finally, I want to thank Ljiljana, because she has always been with me. And my parents and my family back in Yugoslavia, who have always understood and supported my wish to become an astronomer. And my dear teacher, colleague and friend, Prof. Mirjana Vukićević-Karabin from Belgrade University, who encouraged me to come to New Zealand.

References

Agekyan T. A., Belozerova M. A., 1979, 'The evaporation of stars from clusters, with the development of coronas and moving clusters', Soviet Astr. 23, 4 (also: Astron. Zh. 56, 9)

Agekyan T. A., Orlov V. V., 1984, 'Moving-cluster membership of solar neighborhood stars', Soviet Astr. 28, 36 (also: Astron. Zh. 61, 60)

Allen C. W., 1991, 'Astrophysical quantities', 3rd edition, The Athlone Press, London

Archinal B. A., 1992, 'Terrestrial coordinates and the rotation of the Earth', in Explanatory supplement to the Astronomical Almanac, Seidelmann P. K. (ed.), University Science Books, Mill Valley, California, p. 199

Asiain R., 1998, 'Moving groups among early type stars: detection and evolution', PhD thesis, University of Barcelona

Asiain R., Figueras F., Torra J., Chen B., 1999a, 'Detection of moving groups among early type stars', A&A 341, 427

Asiain R., Figueras F., Torra J., 1999b, 'On the evolution of moving groups: an application to the Pleiades moving group', A&A, in press

Becker W., Fenkart R., 1970, 'Galactic clusters and HII regions', Proceedings of the IAU Symposium No. 38: 'The spiral structure of our Galaxy', Becker W., Contopoulos G. (eds.), D. Reidel Publishing Company, Dordrecht, Holland, p. 205

Berthet S., 1990, 'New calibrations of blanketing parameters Δm_2 and δm_1 in terms of [Fe/H]', A&A 236, 440

Binney J. J., Tremaine S., 1987, 'Galactic dynamics', Princeton University Press, Princeton, New Jersey

Binney J. J., Dehnen W., Houk N., Murray C. A., Penston M. J., 1997, 'The kinematics of main-sequence stars from Hipparcos data', Proceedings of the ESA Symposium 'Hipparcos – Venice '97', ESA SP-402, p. 473

Boss L., 1908, 'Convergent of a moving cluster in Taurus', AJ 26, 31

Brault J. W., White O. R., 1971, 'The analysis and restoration of astronomical data via the fast Fourier transform', A&A 13, 169

Bubeniček J., Palouš J., Piskunov A. E., 1985, 'Hyades moving group: new members, kinematics and age', Astron. Zh. 62, 1073 (in Russian)

Cayrel de Strobel G., Soubiran C., Friel E. D., Ralite N., François P., 1997, 'A catalogue of [Fe/H] determinations: 1996 edition', A&A Suppl. Ser. 124, 299

Chatfield C., Collins A. J., 1980, 'Introduction to multivariate analysis', Chapman and Hall, New York

Chen B., Asiain R., Figueras F., Torra J., 1997, 'Identification of moving groups from a sample of B, A and F type stars', A&A 318, 29

Chereul E., Crézé M., Bienaymé O., 1997, 'The distribution of nearby stars in phase space mapped by Hipparcos, II. Wavelet analysis of 3D-density and 2D-velocity distributions', Proceedings of the ESA Symposium 'Hipparcos – Venice '97', ESA SP-402, p. 545

Chereul E., Crézé M., Bienaymé O., 1998, 'The distribution of nearby stars in phase space mapped by Hipparcos, II. Inhomogeneities among A-F type stars', A&A 340, 384

Chereul E., Crézé M., Bienaymé O., 1999, 'The distribution of nearby stars in phase space mapped by Hipparcos, III. Clustering and streaming among A-F type stars', A&A Suppl. Ser. 135, 5

Comerón F., Torra J., Figueras F., 1997, 'Understanding some moving groups in terms of a global spiral shock', A&A 325, 149

Courtès G., Georgelin Y. P., Georgelin Y. M., Monnet G., 1970, 'A new interpretation of the Galactic structure from HII regions', Proceedings of the IAU Symposium No. 38: 'The spiral structure of our Galaxy', Becker W., Contopoulos G. (eds.), D. Reidel Publishing Company, Dordrecht, Holland, p. 209

Crawford D. L., 1975, 'Empirical calibrations of the *uvby*, β systems. I. The F-type stars', AJ 80, 955

Crawford D. L., Perry C. L., 1976, 'The relation between the blanketing parameter $\delta m_1(\beta)$ and [Fe/H] abundances', PASP 88, 454

Crézé M., Mennessier M. O., 1973, 'An attempt to interpret the mean properties of the velocity field of young stars in terms of Lin's theory of spiral waves', A&A 27, 281

Crézé M., Chereul E., Bienaymé O., Pichon C., 1998, 'The distribution of nearby stars in phase space mapped by Hipparcos, I. The potential well and local dynamical mass', A&A 329, 920

Cummings I. N., 1998, 'High precision radial-velocity measurements of late-type evolved stars', PhD thesis, University of Canterbury

de Bruijne J. H. J., 1999, 'A refurbished convergent point method for finding moving groups in the Hipparcos Catalogue', MNRAS 306, 381

de Bruijne J. H. J., Hoogerwerf R., Brown A. G. A., Aguilar L. A., de Zeeuw P. T., 1997, 'Improved methods for identifying moving groups', Proceedings of the ESA Symposium 'Hipparcos – Venice '97', ESA SP-402, p. 575

De Cuyper J.-P., Hensberge H., 1998, 'Wavelength calibration at moderately high resolution', A&A Suppl. Ser. 128, 409

Dehnen W., 1998a, 'The distribution of nearby stars in velocity space', Proceedings of the 'Galaxy Dynamics' conference, ASP Conference Series, Merritt D. R., Valluri M., Sellwood J. A. (eds.), in press (also: astro-ph/9810320)

Dehnen W., 1998b, 'The distribution of nearby stars in velocity space inferred from Hipparcos data', AJ 115, 2384

Dehnen W., Binney J. J., 1998, 'Local stellar kinematics from Hipparcos data', MNRAS 298, 387

Delhaye J., 1965, 'Solar motion and velocity distribution of common stars', in Galactic structure, Blaauw A., Schmidt M. (eds.), The University of Chicago Press, Chicago, p. 61

Eggen O. J., 1957, 'The Taurus group', Obs. 77, 229

Eggen O. J., 1959a, 'The gamma Leonis group of high velocity stars', Obs. 79, 88

Eggen O. J., 1959b, 'White dwarf members of the 61 Cygni group', Obs. 79, 135

Eggen O. J., 1960, 'Stellar groups, VIII. The structure of the Sirius group', MNRAS 120, 563

Eggen O. J., 1964a, 'Ages and kinematics of clusters', Proceedings of the IAU-URSI Symposium No. 20: 'The Galaxy and the Magellanic Clouds', Kerr F. J., Rodgers A. W. (eds.), Australian Academy of Science, Canberra, Australia, p. 10

Eggen O. J., 1964b, 'Colors, luminosities, and motions of the nearer G-type stars', AJ 69, 570

Eggen O. J., 1965a, 'Moving groups of stars', in Galactic structure, Blaauw A., Schmidt M. (eds.), The University of Chicago Press, Chicago, p. 111

Eggen O. J., 1965b, 'The Wolf 630 group', Obs. 85, 191

Eggen O. J., 1969, 'Stellar groups in the old disk population', PASP 81, 553

Eggen O. J., 1970, 'Stellar kinematics and evolution', in Vistas in Astronomy, Beer A. (ed.), Vol. 12, p. 367

Eggen O. J., 1971a, 'Luminosities, temperatures, and kinematics of K-type dwarfs', ApJ Suppl. Ser. 22, 389

Eggen O. J., 1971b, 'Narrow- and broad-band photometry of red stars, VI. Luminosities and temperatures for old disk-population red stars of high luminosity', ApJ 165, 317

Eggen O. J., 1971c, 'The ζ Herculis, σ Puppis, ε Indi, and η Cephei groups of old disk population stars', PASP 83, 251

Eggen O. J., 1971d, 'The Arcturus group', PASP 83, 271

Eggen O. J., 1971e, 'Some red giants of the old disk population', PASP 83, 423

Eggen O. J., 1971f, 'Luminosities and motions of the F-type stars, I. Luminosity and metal abundance indices for disk population stars', PASP 83, 741

Eggen O. J., 1972a, 'The red giants in the Hyades group', PASP 84, 406

Eggen O. J., 1972b, 'Luminosities and motions of the F-type stars, II. Metal deficient stars', ApJ 175, 787

Eggen O. J., 1973, 'Luminosity and velocity distribution of high-luminosity red stars, III. Old-disk-population giants', PASP 85, 542

Eggen O. J., 1974a, 'Luminosity and velocity distribution of high-luminosity red stars, IV. The G-type giants', PASP 86, 129

Eggen O. J., 1974b, 'The oldest disk stars', PASP 86, 162

Eggen O. J., 1976, 'A sample of old-disk-population stars', PASP 88, 426

Eggen O. J., 1977a, 'Intermediate band photometry of late-type stars, II. Some stellar groups', ApJ 215, 812

Eggen O. J., 1977b, 'Intermediate-band photometry of late-type stars, III. The Geneva Observatory (GO) photometric system', PASP 89, 706

Eggen O. J., 1978, 'Intermediate-band photometry of late-type stars, V. Calibration of indices', ApJ 221, 881

Eggen O. J., 1979, 'Intermediate-band photometry of late-type stars, VIII. Nonvariable stars in the halo population near the Sun', ApJ 229, 158

Eggen O. J., 1983a, 'Concentrations in the Local Association – I. The southern concentrations NGC 2516, IC 2602, Centaurus-Lupus and Upper Scorpius', MNRAS 204, 377

Eggen O. J., 1983b, 'Concentrations in the Local Association – II. The northern concentrations including the α Persei, Pleiades, M34 and δ Lyrae clusters', MNRAS 204, 391

Eggen O. J., 1983c, 'Concentrations in the Local Association – III. Late-type bright giants, ages and abundances', MNRAS 204, 405

Eggen O. J., 1992, 'The Pleiades supercluster in FK 5', AJ 103 (4), 1302

Eggen O. J., 1994, 'Stellar clusters, superclusters and groups', in Galactic and Solar System optical astrometry, Morrison L. V., Gilmore G. F. (eds.), Cambridge University Press, p. 191

Eggen O. J., Lynden-Bell D., Sandage A. R., 1962, 'Evidence from the motions of old stars that the Galaxy collapsed', ApJ 136, 748

Eggen O. J., Freeman K. C., Rodgers A. W., 1973, 'Structure of the Galaxy', in Reports on Progress in Physics, Vol. 36, No. 6, p. 625

ESA, 1985, 'Ad Astra Hipparcos', ESA BR-24

ESA, 1989, 'The Hipparcos Mission', ESA SP-1111

ESA, 1992, 'The Hipparcos Input Catalogue', ESA SP-1136

ESA, 1997, 'The Hipparcos Catalogue', ESA SP-1200

Escalera E., Mazure A., 1992, 'Wavelet analysis of subclustering: an illustration, Abell 754', ApJ 388, 23

Figueras F., Gómez A. E., Asiain R., Chen B., Comerón F., Grenier S., Lebreton Y., Moreno M., Sabas V., Torra J., 1997, 'Identification of moving groups in a sample of early-type main-sequence stars', Proceedings of the ESA Symposium 'Hipparcos – Venice '97', ESA SP-402, p. 519

Fletcher J. M., Harris H. C., McClure R. D., Scarfe C. D., 1982, 'A photoelectric radial-velocity spectrometer on the 1.2-m telescope of the Dominion Astrophysical Observatory', PASP 94, 1017

Flynn C., 1996, 'An axisymmetric model of the galactic potential', private communication

Flynn C., Morell O., 1997, 'Metallicities and kinematics of G and K dwarfs', MNRAS 286, 617

Flynn C., Sommer-Larsen J., Christensen P. R., 1996, 'Kinematics of the outer stellar halo', MNRAS 281, 1027

Gardiner L. T., Sawa T., Fujimoto M., 1994, 'Numerical simulations of the Magellanic system – I. Orbits of the Magellanic Clouds and the global gas distribution', MNRAS 266, 567

Gilmore G., King I. R., van der Kruit P. C., 1989, 'The Milky Way as a galaxy', 19th advanced course of the Swiss Society of Astrophysics and Astronomy, Geneva Observatory

Golay M., 1973, 'Applications of the $UB_1B_2V_1G$ photometric system', Proceedings of the IAU Symposium No. 50: 'Spectral classification and multicolour photometry', Fehrenbach Ch., Westerlund B. E. (eds.), D. Reidel Publishing Company, Boston, p. 145

Golay M., 1980, 'The Geneva seven-colour photometric system', in Vistas in Astronomy, Beer A., Pounds K., Beer P. (eds.), Vol. 24, p. 141

Grebenev S. A., Forman W., Jones C., Murray S., 1995, 'Wavelet transform analysis of the small-scale X-ray structure of the cluster Abell 1367', ApJ 445, 607

Hauck B., 1973, 'Three-dimensional representation of A0 – G5 stars', Proceedings of the IAU Symposium No. 54: 'Problems of calibration of absolute magnitudes and temperature of stars', Hauck B., Westerlund B. E. (eds.), D. Reidel Publishing Company, Boston, p. 117 (in French)

Hauck B., 1978, 'The relation between the blanketing parameter Δm_2 and [Fe/H] abundances', A&A 63, 273

Hauck B., 1986, 'Metallicism among A and F giant stars', A&A 155, 371

Hauck B., Foy R., Proust D., 1985, 'Detailed analysis of the δ Del star HD 115604 = 20 CVn', A&A 149, 167

Hearnshaw J. B., 1977, 'The Cassegrain échelle spectrograph at Mt John Observatory', Proc. Astron. Soc. Australia 3 (2), 102

Hertzsprung E., 1909, 'On new members of the system of the stars β, γ, δ, ε, ζ, Ursae Majoris', ApJ 30, 135

Hohenkerk C. Y., Yallop B. D., Smith C. A., Sinclair A. T., 1992, 'Celestial reference systems', in Explanatory supplement to the Astronomical Almanac, Seidelmann P. K. (ed.), University Science Books, Mill Valley, California, p. 95

Hoogerwerf R., Aguilar L. A., 1999, 'Identification of moving groups and member selection using Hipparcos data', MNRAS 306, 394

Kerr F. J., Lynden-Bell D., 1986, 'Review of Galactic constants', MNRAS 221, 1023

Kershaw G. M., Hearnshaw J. B., 1989, 'High precision radial velocities using an optical fibre feed', Southern Stars 33 (3), 89

Kurucz R. L., 1996, 'Seven synthetic stellar spectra between 5000 Å and 5651 Å', private communication

Lin C. C., Shu F. H., 1964, 'On the spiral structure of disk galaxies', ApJ 140, 646

Lin C. C., Yuan C., Shu F. H., 1969, 'On the spiral structure of disk galaxies, III. Comparison with observations', ApJ 155, 721

Lin D. N. C., Lynden-Bell D., 1982, 'On the proper motion of the Magellanic Clouds and the halo mass of our Galaxy', MNRAS 198, 707

Marochnik L. S., Suchkov A. A., 1996, 'The Milky Way Galaxy', Gordon and Breach Publishers, Luxembourg

McClure R. D., Fletcher J. M., Grundman W. A., Richardson E. H., 1985, 'The DAO radial velocity spectrometer and recent results', Proceedings of the IAU Colloquium No. 88: 'Stellar radial velocities', Van Vleck Observatory Contribution No. 3, Philip A. G. D., Latham D. W. (eds.), L. Davis Press, Inc., Schenectady, New York, p. 49

McDonald A. R. E., Hearnshaw J. B., 1983, 'The Wolf 630 moving group of stars', MNRAS 204, 841

Mihalas D., Binney J. J., 1981, 'Galactic astronomy: structure and kinematics', W. H. Freeman and Company, San Francisco

Mishurov Yu. N., Zenina I. A., Dambis A. K., Mel'nik A. M., Rastorguev A. S., 1997, 'Is the Sun located near the corotation circle?', A&A 323, 775

Morgan W. W., Sharpless S., Osterbrock D., 1952, 'Some features of Galactic structure in the neighbourhood of the Sun', AJ 57, 3

Morgan W. W., Whitford A. E., Code A. D., 1953, 'Studies in Galactic structure I. A preliminary determination of the space distribution of the blue giants', ApJ 118, 318

Mülläri A. A., Nechitailov Yu. V., Ninković S., Orlov V. V., 1994, 'The orbits of moving clusters in the Galactic dynamical models', Ap&SS 218, 1

Murai T., Fujimoto M., 1980, 'The Magellanic Stream and the Galaxy with a massive halo', Proc. Astron. Soc. Japan 32, 581

Murdoch K., Hearnshaw J. B., 1991a, 'The precision of radial-velocity determinations of solar-type stars by cross-correlation', Ap&SS 186, 137

Murdoch K., Hearnshaw J. B., 1991b, 'High precision radial velocities of southern solar-type stars by cross correlation', Ap&SS 186, 169

Palmer B. A., Engleman R. Jr., 1983, 'Atlas of the thorium spectrum', Los Alamos National Laboratory, LA-9615

Palouš J., Hauck B., 1986, 'The Sirius supercluster', A&A 162, 54

Palouš J., Ruprecht J., Dluzhnevskaya O. B., Piskunov T., 1977, 'Places of formation of 24 open clusters', A&A 61, 27

Perryman M. A. C., Lindegren L., Turon C., 1997, 'The scientific goals of the GAIA mission', Proceedings of the ESA Symposium 'Hipparcos – Venice '97', ESA SP-402, p. 743

Perryman M. A. C., Brown A. G. A., Lebreton Y., Gómez A., Turon C., Cayrel de Strobel G., Mermilliod J. C., Robichon N., Kovalevsky J., Crifo F., 1998, 'The Hyades: distance, structure, dynamics, and age', A&A 331, 81

Popović G. M., Ninković S., Pavlović R., 1995, 'An analysis of nine moving clusters', Bull. Astron. Belgrade 152, 59

Press W. H., Teukolsky S. A., Vetterling W. T., Flannery B. P., 1994, 'Numerical recipes in C – the art of scientific computing', 2nd edition, Cambridge University Press

Proctor R. A., 1869, 'Preliminary paper on certain drifting motions of the stars', Proc. Royal Soc. London 18, 169

Reader J., Corliss C. H., 1980, 'Wavelengths and transition probabilities for atoms and atomic ions, Part I. Wavelengths', NSRDS – National Standard Reference Data System

Rufener F., 1989, 'Catalogue of stars measured in the Geneva Observatory photometric system (fourth edition)', A&A Suppl. Ser. 78, 469

Rufener F., Maeder A., 1971, 'A note concerning the determination of the Geneva Observatory photometric system's pass-bands', A&A Suppl. Ser. 4, 43

Silverman B. W., 1986, 'Density estimation for statistics and data analysis', Chapman and Hall, New York

Simkin S. M., 1974, 'Measurements of velocity dispersions and Doppler shifts from digitized spectra', A&A 31, 129

Skuljan J., Cottrell P. L., Hearnshaw J. B., 1997, 'Eggen's moving groups: fact or fiction?', Proceedings of the ESA Symposium 'Hipparcos – Venice '97', ESA SP-402, p. 525

Skuljan J., Hearnshaw J. B., Cottrell P. L., 1999a, 'Absolute radial velocities by cross-correlation with synthetic spectra', Proceedings of the IAU Colloquium No. 170: 'Precise stellar radial velocities', ASP Conference Series, Hearnshaw J. B., Scarfe C. D. (eds.), p. 91

Skuljan J., Hearnshaw J. B., Cottrell P. L., 1999b, 'Using the radial velocity spectrometer at the Dominion Astrophysical Observatory', Proceedings of the IAU Colloquium No. 170: 'Precise stellar radial velocities', ASP Conference Series, Hearnshaw J. B., Scarfe C. D. (eds.), p. 98

Skuljan J., Hearnshaw J. B., Cottrell P. L., 1999c, 'Velocity distribution of stars in the solar neighbourhood', MNRAS 308, 731

Slezak E., Bijaoui A., Mars G., 1990, 'Identification of structures from galaxy counts: use of the wavelet transform', A&A 227, 301

Slezak E., de Lapparent V., Bijaoui A., 1993, 'Objective detection of voids and high-density structures in the first CfA redshift survey slice', ApJ 409, 517

Slezak E., Durret F., Gerbal D., 1994, 'A wavelet analysis search for substructures in eleven X-ray clusters of galaxies', AJ 108 (6), 1996

Soderblom D. R., Mayor M., 1993, 'Stellar kinematic groups, I. The Ursa Major group', AJ 105 (1), 226

Stumpff P., 1980, 'Two self-consistent Fortran subroutines for the computation of the Earth's motion', A&A Suppl. Ser. 41, 1

Tobin W., 1992, 'Gain, noise and related characteristics of the Mt John Photometrics CCD system', Southern Stars 34 (8), 421

Weaver H., 1970, 'Spiral structure of the Galaxy derived from the Hat Creek survey of neutral hydrogen', Proceedings of the IAU Symposium No. 38: 'The spiral structure of our Galaxy', Becker W., Contopoulos G. (eds.), D. Reidel Publishing Company, Dordrecht, Holland, p. 126

Westerlund B. E., 1997, 'The Magellanic Clouds', Cambridge University Press

Wielen R., 1973, 'Places of formation of nearby classical cepheids', A&A 25, 285

Wielen R., Fuchs B., Dettbarn C., 1996, 'On the birth-place of the Sun and the places of formation of other nearby stars', A&A 314, 438

Wilson R. E., 1953, 'General catalogue of stellar radial velocities', Carnegie Institution of Washington Publ. 601 (a CD-ROM version)

Yuan C., 1969a, 'Application of the density-wave theory to the spiral structure of the Milky Way system, I. Systematic motion of neutral hydrogen', ApJ 158, 871

Yuan C., 1969b, 'Application of the density-wave theory to the spiral structure of the Milky Way system, II. Migration of stars', ApJ 158, 889